

AD-A086 497

TORONTO UNIV DOWNSVIEW (ONTARIO) INST FOR AEROSPACE --ETC F/G 17/4

STUDIES OF LASER SELECTIVE EXCITATION OF ATOMS, (U)

DEC 79 N DREWELL

AFOSR-76-2902

UNCLASSIFIED

UTIAS-229

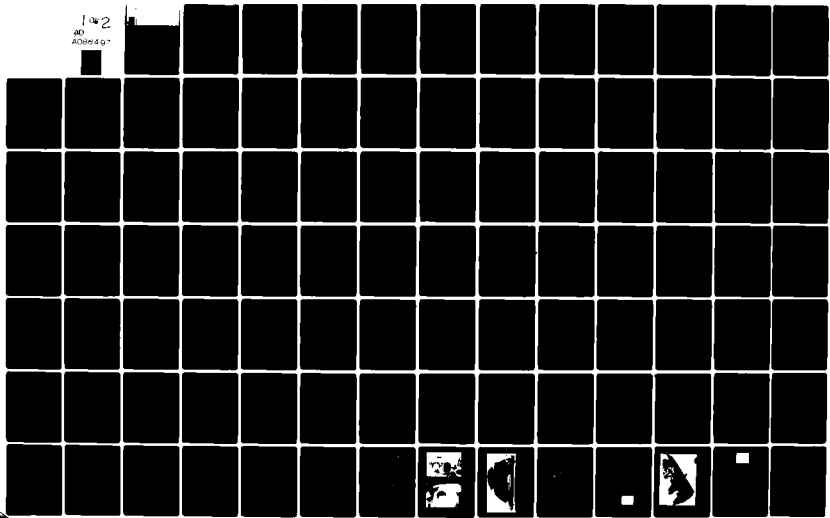
AFOSR-TR-80-0507

NL

142

AD

Added 97





INSTITUTE
FOR
AEROSPACE STUDIES

UNIVERSITY OF TORONTO

ADA 086497

AFOSR-TR- 80-0507 ✓

STUDIES OF LASER SELECTIVE EXCITATION OF ATOMS

LEVEL

by

Norbert Drewell

DTIC
ELECTE
JUL 7 1980

C

October, 1979

UTIAS Report No. 229
CN ISSN 0082-5255

Approved for public release;
distribution unlimited.

80 7 2 100

FILE COPY

Qualified requestors may obtain additional copies from the Defense Documentation Center, all others should apply to the National Technical Information Service.

Conditions of Reproduction:

Reproduction, translation, publication, use and disposal in whole or in part by or for the United States Government is permitted.

8
STUDIES OF LASER SELECTIVE EXCITATION OF ATOMS

by

10

Norbert/Drewell

Submitted June, 1979

15

AFOSR-76-2902

14

UTIAS-229

18

AFOSR

19

TK-84-4597

12

150

11

Dec 1979

AIR FORCE OFFICE OF SCIENTIFIC RESEARCH (AFSC)
NOTICE OF TRANSMITTAL TO DDC
This technical report has been reviewed and is
approved for public release IAW AFR 190-12 (7b).
Distribution is unlimited.

A. D. BLGSE
Technical Information Officer
UTIAS Report No. 229
CN ISSN 0082-5255

178920

Acknowledgement

The author wishes to thank his supervisor, Dr. R. M. Measures, for his guidance and encouragement throughout the program.

It is a pleasure to acknowledge the technical assistance of Messrs. J. L. Bradbury and Ted Mills during the fabrication of the apparatus. Special thanks are due to Mr. H. S. Kwong for the many stimulating discussions and for his help in the early experiments. The calculations of various rate coefficients by Mr. P. Cardinal were very helpful during the theoretical part of this program. Mrs. Winifred Dillon typed the manuscript.

A special thank-you goes to my wife, Loraine, for her patience, understanding, and many helpful suggestions.

This work was supported in part by the USAF/AFOSR under grant No. 76-2902, and the National Research Council.

Accession For	
NTIS GRA&I	<input checked="" type="checkbox"/>
DDC TAB	<input type="checkbox"/>
Unannounced	<input type="checkbox"/>
Justification	
By _____	
Distribution/	
Availability Codes	
Dist	Available/or special
A	

Abstract

Sample preparation through laser ablation of a solid target under vacuum has been combined with short-pulsed laser selective excitation to create a new and convenient experimental technique for measuring atomic radiative lifetimes. The lifetimes of the three resonance states of chromium determined in this way compare very favourably with those found through other experimental means.

In addition, the technique has been extended to demonstrate experimentally the potential for plasma diagnostics using two-wavelength selective excitation with short laser pulses. The ratio of population densities of two energy states of chromium atoms has been measured as a function of time during the expansion of the ablation plasma.

Extended saturation pumping of the resonance transition in sodium vapour has been investigated theoretically. Rate equations for 20 energy levels in the sodium atom, and the rate equations for the free electrons, were integrated numerically. It has been found that multiphoton ionization, combined with superelastic heating of free electrons can account for the rapid and complete ionization of an un-ionized vapour, as reported in the literature. The detailed theoretical results have led to the development of a simple model which accurately predicts the temporal variation of electron density.

CONTENTS

	<u>Page</u>
Acknowledgement	ii
Abstract	iii
1. INTRODUCTION	1
2. THEORETICAL BACKGROUND	5
2.1 Rate Equation for Population Densities	5
2.2 Selective Laser Excitation	8
2.3 Laser Saturation of a Transition	12
2.4 System Relaxation	15
2.5 Extended Saturation Pumping	17
3. LASER ABLATION AND SELECTIVE EXCITATION SPECTROSCOPY FACILITY	22
3.1 Lasers	24
3.1.1 Ruby Laser (The Ablation Laser)	24
3.1.2 Nitrogen Laser	24
3.1.3 Dye Laser Model 1	25
3.1.4 Dye Laser Model 2	26
3.2 Monochromators	26
3.3 Photodetectors	26
3.3.1 Photodiodes	26
3.3.2 Photomultiplier C70042K	27
3.3.3 Photomultiplier C31034	27
4. PRELIMINARY LASES EXPERIMENTS	29
4.1 Plume Emission Spectrum	30
4.2 Plume Resonance Radiation and Dye Laser Interaction	30
4.3 Decay of Intensified Spontaneous Emission (ISE)	34
4.4 Conclusions	35
5. MEASUREMENT OF RADIATIVE LIFETIME OF THE CHROMIUM RESONANCE LEVELS	36
5.1 Experimental Conditions and Procedures	36
5.2 Results	38
5.3 Error Analysis	38
5.3.1 Experimental Errors Associated with LASES	38
5.3.2 Experimental Errors in Data Reduction	41
5.4 Discussion	43

Continued...

	<u>Page</u>
6. SELECTIVE EXCITATION SPECTROSCOPY EXPERIMENT INVOLVING TWO TRANSITIONS	45
6.1 Experimental Layout and Procedure	45
6.2 Experimental Results	47
6.3 Population Ratio Calculation	48
6.4 Discussion	52
7. LASER IONIZATION BASED ON RESONANCE SATURATION - LIBORS	53
7.1 LIBORS Result	55
7.2 Simplified LIBORS Model	56
7.3 Importance of Single Photon Ionization	59
7.4 The LIBORS Electron Temperature	60
7.5 Laser-Plasma Power Flow	64
7.6 Comparison with Laboratory Experiments	65
8. SUMMARY	66
REFERENCES	69
TABLES - 1 to 4	
FIGURES - 1 to 50	
APPENDIX A: COLLISION RATE COEFFICIENTS	
APPENDIX B: PHOTOIONIZATION RATE COEFFICIENT	
APPENDIX C: OSCILLOSCOPE ANALYSIS FOR ISE DECAY TIMES	
APPENDIX D: RAY TRACING ROUTINE	
APPENDIX E: LIBORS COMPUTER PROGRAM	

1. INTRODUCTION

This thesis is concerned with laser selective excitation of atoms and is divided into two main parts, distinguished by the length of the laser pulse. The first part is concerned with the diagnostic possibilities related to short pulse excitation. It involves the development of a new kind of facility for testing some of the diagnostic aspects of this work. The facility makes use of laser ablation to create a suitable medium to be studied by laser selective excitation spectroscopy. The second part of the thesis deals with extensive system perturbation through extended laser pumping of a suitable medium, and concentrates on a theoretical study of laser ionization based on resonance saturation - LIBORS.

The concept of using pulsed laser selective excitation with sufficient laser power to saturate a transition was first suggested by Measures (1968) as a method of plasma diagnostics. The concept was tested experimentally by Rodrigo (1972) and Rodrigo and Measures (1973), who thermally tuned a Q-switched ruby laser to pump the 693.9 nm transition in a DC potassium plasma. The decay of the resultant intensified spontaneous emission (ISE) pulse from the laser-excited level showed the expected dependence on electron density.

Laser selective excitation has subsequently been employed in a wide variety of experiments due to the development of tunable dye lasers. Most of the early experimentalists, such as McIlrath (1969), measured basic atomic and molecular parameters and cross sections, relying on atomic or molecular beams, or DC ovens and vapour cells to provide a sufficient density of the species of interest.

Burrell and Kunze (1972), using a helium DC plasma, verified that their pulsed, 10 kW laser saturated the 447.1 nm transition. They recognized the value of a short* laser pulse and used the decay times of the ISE signals to estimate the radiative lifetime of the 3^3D level of helium, and to estimate various electron collision rate coefficients for their plasma conditions.

The diagnostic possibilities of long*, saturating laser pulses were pointed out by Burgess and Skinner (1974), although their treatment did not consider all possible forms of ISE. In a recent paper, Koopman, McIlrath and Myerscough (1978) have reiterated the advantages of short duration laser selective saturation pumping, including the good spatial and temporal resolution available, and have proposed that this technique could be used to determine the neutral densities in various fusion plasmas. Daily (1976) has done exploratory calculations on a similar diagnostic technique as applied to combustion flows. On the other hand, in another recent paper, Boutilier, Blackburn, Mermet, Weeks, Haraguchi, Winefordner and Omenetto (1978), in analysing the diagnostic potential of steady state saturation of three-level systems, contend that short duration laser selective saturation spectroscopy is difficult to perform experimentally.

Laser ablation of a solid is currently of considerable interest in the areas of inertial confinement fusion and X-ray laser development. In the

*Short (long) in this context refers to a laser pulse whose width (FWHM) is much less (greater) than the time constant of the trailing edge of the ISE pulse.

context of X-ray laser development, laser ablation is particularly attractive because it provides a means of very rapidly creating a pure, high density, high temperature plasma in a vacuum. The subsequent expansion and cooling of this plasma leads to several proposed methods of creating a population inversion in some highly ionized species (Norton and Peacock, 1975; Mahr and Roeder, 1974; Seely and McKnight, 1977; and Dixon and Elton, 1977).

In order to undertake a diverse set of laser selective excitation experiments a new facility was built that combined laser ablation and selective excitation spectroscopy (LASES). Two of these experiments have led very directly to real applications in atomic lifetime determinations and in trace element microanalysis. By using laser ablation, a burst of chromium vapour was conveniently generated within a vacuum chamber. Selective excitation by a tunable dye laser was then used to measure the radiative lifetime of the three resonance levels by recording directly the decay of the intensified spontaneous emission (ISE). A knowledge of radiative lifetimes, particularly of high lying excited states in neutrals and excited states of ions is important in the search for UV and X-ray laser transitions and in the search for higher quantum efficiency visible lasers.

Although other techniques exist for measuring radiative lifetimes, sample preparation using laser ablation is particularly simple and convenient. This would be expected to be particularly true in the case of ions. By recording directly the decay of the ISE pulse, maximum use was made of the information content of the signal, thereby surpassing time-to-height converters (e.g., Bergstedt, Himmel and Pinnekamp, 1975) and the photon counting technique (e.g., Marek, 1975) in the speed of data collection. The results of this experiment have been published in condensed form (Measures, Drewell and Kwong, 1977).

An additional experiment was undertaken in order to demonstrate the feasibility of using short, pulsed laser saturation pumping in a diagnostic role, and to demonstrate the good temporal and spatial resolution obtainable with such a diagnostic technique while at the same time providing insight into the dynamics of an ablation plasma. A two-wavelength laser pumping experiment was undertaken whereby the ratio of population densities in the metastable and ground states of chromium could be evaluated as a function of time during the recombination and expansion of the ablation plasma. Measurements of population ratios are of general interest in laser research, and of particular interest in the current race to achieve X-ray laser action by laser ablation.

A case in point is the research into the copper halide pulsed laser reported by Shukhtin, Mishakov, Fedotov, and Ganeev (1975), Liu, Feldman, Pack, and Weaver (1977), and Tenenbaum, Smilanski, Gabay, Erez, and Levin (1978). In order to get laser action on the 510.6 and 578.2 nm lines of copper, an electrical discharge is required to dissociate the molecule, and after a given optimum time delay a second pulsed discharge is required to create the population inversions. The existence of an optimum delay for the second discharge was conjectured by Chen, Nerheim, and Russell (1973), and Chen (1974) as being due to the production of a substantial population in the lower levels of the laser transitions which had subsequently to be quenched prior to the application of the second pulse and before the disappearance of copper atoms by recombination with the halides.

The experiments of Shukhtin et al (1975) and Liu et al (1977) to measure the relevant ratio of populations suffered from a lack of good spatial and temporal resolution, and as a result the extrapolations of this ratio to zero time delay (after the first electrical discharge) indicated conflicting conclusions. Both groups employed absorption spectroscopy, which in the case of Liu et al (1977) could not be used immediately after the discharge pulse because the spontaneous emission in the relevant lines was more intense than the source used for the absorption measurement. Tenenbaum et al (1978) resolved the matter by also employing absorption spectroscopy. Such a problem does not arise when laser selective saturation pumping is employed.

Germane to the application of laser selective excitation spectroscopy for diagnostic purposes is the concept of momentary saturation. This is necessary to avoid perturbing the medium under investigation. Measures (1970) demonstrated this point by theoretically studying the case of extended laser saturation of the resonance lines of weakly ionized potassium vapour. His analysis suggested that the electron density could be made to jump three orders of magnitude within a few microseconds and that this process of resonance saturation invariably led to almost complete ionization.

Fournier (1972) extended this analysis by representing the laser excited atom by a twenty-level model and setting up a computer program to solve the subsequent set of coupled rate equations.

In the second half of this thesis, Fournier's analysis is expanded to account for several additional features including simulation of much higher densities and the inclusion of both multiphoton ionization from the resonance level and single photon ionization from higher lying levels. This necessitated an extensive revision of this program. Multiphoton ionization was suggested as being necessary (Measures, 1977) to allow these calculations to be applied to un-ionized vapours such as those involved in the recent experiments of Lucatorro and McIlrath (1976) and McIlrath and Lucatorro (1977).

This laser ionization based on resonance saturation, LIBORS, program clearly predicts that almost complete ionization will invariably be produced when one or more resonance lines of any dense ($\geq 10^{14} \text{cm}^{-3}$) atomic vapour is saturated for an extended period of time. The higher the density, the shorter the time needed to achieve ionization burnout. Subnanosecond burnout times might be achieved at around one atmosphere. The implications of this to many laser experiments could be important. Indeed, the superelastic heating aspect of this LIBORS theory could help to account for some of the observations made in the laser pumping experiments of Allegrini, Alzetta, Kopystynska, Moi, and Orriols (1976), Tam and Happer (1977), and Leslie, Verdeyen and Millar (1977). Furthermore, the LIBORS concept could have several applications, including the formation of plasma channels for electron and ion beams that are currently under consideration for inertial fusion (Yonas, 1978; Measures, Drewell and Cardinal, 1979a). The inclusion of other ionization processes in the model will further increase the efficiency of the laser energy coupling to the plasma and thus decrease the time to ionize. It is also possible to show that laser coupling via resonance saturation competes favourably with inverse bremsstrahlung under a range of conditions (Measures, Drewell, and Cardinal, 1979b).

The presentation of this work is organized as follows:

Chapter 2 presents the theoretical background based on rate equation analysis. There has been discussion in the literature about the validity of the rate equation approach to various experimental situations. The applicability of the rate equations to the present work is reviewed at the beginning of Chapter 2. A general rate equation governing the population density of a bound atomic level is introduced, followed by the development of a second order differential equation describing the population density of the upper of two laser coupled levels. A solution is obtained in terms of the initial steady state conditions as opposed to the usual practice of invoking continuity of the sum of the two population densities involved in the laser-atom interaction. The seven possible forms of the solution are presented and interpreted physically. The laser saturation condition is presented, along with the concomitant physical consequences as they apply to plasma diagnostics. System relaxation after turnoff is examined, again with reference mainly to applications in plasma diagnostics.

The final section of Chapter 2 explains the more important physical processes which should be considered when the saturation pumping is intense enough that multiphoton ionization becomes important, and/or long enough that the effects of free electron heating through superelastic atom collisions become important. A simple calculation of power flow on a macroscopic scale between a laser beam and a resonantly interacting atomic vapour is introduced. Finally, rate equations are presented for the power flow and the other important physical processes in preparation for their numerical integration.

Chapter 3 gives an overview of the experimental layout, followed by a brief description of major pieces of apparatus including their calibration where applicable. Three lasers which were built in-house are covered in more depth to include some construction details.

A set of "preliminary" experiments is described in Chapter 4. Various tests were performed on the ablation plasma to determine the suitability of the LASES approach to the plasma diagnostics, and basic atomic measurements role.

Chapter 5 describes the experiment, using the LASES facility, to measure atomic radiative lifetimes. The specific procedures and equipment layout are given, along with results and a discussion about their errors and uncertainties. Potential improvements to the LASES facility are discussed which would allow higher accuracies to be achieved.

Chapter 6 presents a two-wavelength pumping experiment which strives to demonstrate the feasibility and advantages of laser saturation pumping with short laser pulses. The procedure of pumping simultaneously the ground state and the first metastable state of the ablation target material (chromium) while it is recombining and expanding into a vacuum is described. An estimated time variation of the population ratio is obtained from the temporal behaviour of the ISE signals. The chapter closes with a discussion of some of the fine points to be considered when attempting accurate population ratio measurements.

Chapter 7 covers the results of the computer program (LIBORS program) which integrated the rate equations describing extended saturation pumping of the resonance transition in sodium vapour. The values of the parameters employed correspond closely with the experiment performed by Lucatoro and McIlrath (1976), who observed almost complete ionization of sodium vapour in about 500 ns.

First an explanation is given of the integration procedure employed and the initial conditions used. A physical picture of the resultant ionization process is given and incorporated into a simplified mathematical model with an analytical solution describing the electron density time dependence. Finally, the importance of the electron temperature in this process is discussed, as are comparisons with laboratory measurements.

A short summary of results of this study is presented in Chapter 8.

2. THEORETICAL BACKGROUND

The theoretical background for this study is developed in this chapter based on the use of rate equations. Several workers have addressed themselves to the question of the applicability of rate equation analyses to differing experimental conditions; however, the treatment in the literature is incomplete.

The question of applicability arises because rate equations constitute a phenomenological description of a quantum mechanical interaction of a radiation field with a group of atomic systems. With conventional laboratory light sources, no difficulties arise from the use of rate equations, but in some cases of laser light sources the coherence, intensity, monochromaticity and short pulse length require the use of a density matrix approach.

In studying the resonant interaction of multi-mode laser light with an atomic gas, McIlrath and Carlsten (1972) concluded that a rate equation approach is justified when the atom dephasing time is shorter than the laser-pumping time. Judging from their examples of van der Waals broadening and resonance broadening, and a coherence time of the lasers used in this study, we consider the use of rate equations justified for the experimental conditions covered in this study. Recently Daily (1977) has examined this question and come to conclusions that are similar to those of McIlrath and Carlsten (1972) regarding the range of validity of a rate equation analysis.

The fastest pumping time for the conditions encountered in the present work is in the picosecond range, whereas the corresponding dephasing time (McIlrath and Carlsten, 1972) and the laser coherence time are both in the tens of picoseconds range. Under these particular conditions, a rate equation approach may have to be replaced by a density matrix approach, but considering the time resolution of the light collection equipment, it is doubtful any coherency effects would be observed. In the experimental part of this work, the only situation where coherency effects might have played a part was in pumping the chromium resonance transition at 429 nm, but no such effects were observed (see Chapter 6). In the theoretical part of the work, coherency effects may dominate during laser turn-on, when the sodium vapour is first being resonance-pumped. However, in this case we are interested in the long term (relative to the laser pumping time) evolution of the atomic gas on a tens of nanoseconds time scale, while the dephasing rate is estimated to be on a time scale one thousand times faster. In summary, we feel justified in using a rate equation approach.

2.1 Rate Equation for Population Densities

Let us confine our attention to a volume of plasma small compared to gradients of its macroscopic properties, yet large enough that the important

densities can be regarded as continuous functions of position. If we further limit ourselves to an atomic species which has one optically active electron and is at most singly ionized, then we can write a rate equation which describes phenomenologically the behaviour of the population density N_i of an energy level i of the neutral component when it is subjected to laser radiation.

$$\begin{aligned} \dot{N}_i = N_e \sum_j (N_j K_{ji} - N_i K_{ij}) + \sum_{j>i} [N_j (R_{ji} + A_{ji}) - N_i R_{ij}] \\ - \sum_{j<i} [N_i (R_{ij} + A_{ij}) - N_j R_{ji}] + N_e^2 (N_e K_{ci} + \beta_i) \\ - N_e N_i K_{ic} - \sigma_i^{(\kappa_i)} F^{\kappa_i} N_i \end{aligned} \quad (2.1.0)$$

where the summation over j refers to bound energy levels, and where

N_j is the population density (cm^{-3}) of level j ,

N_e is the free-electron density (cm^{-3}),

A_{ij} is the Einstein spontaneous emission coefficient (sec^{-1}),

K_{ij} is the rate coefficient ($\text{cm}^3 \text{sec}^{-1}$) for electron-collision induced transitions,

K_{ci} is the three-body recombination rate coefficient ($\text{cm}^6 \text{sec}^{-1}$) for the reaction $A^+ + 2e \rightarrow A + e + \text{kinetic energy}$,

β_i is the radiative recombination rate coefficient ($\text{cm}^3 \text{sec}^{-1}$) for the reaction $A^+ + e \rightarrow A + h\nu$ where $h\nu$ is the photon energy,

$\sigma_i^{(\kappa_i)}(\nu_0)$ is the photoionization rate coefficient ($\text{cm}^{2\kappa_i} \text{sec}^{\kappa_i-1}$) at laser frequency ν_0 for a κ_i -photon process. κ_i is defined as the smallest integer satisfying $\kappa_i h\nu_0 - \epsilon_{ci} \geq 0$, where $\epsilon_{ci} = \epsilon_c - \epsilon_i$ is the ionization energy of the i th level with the ground state considered as the zero energy level. F is the laser beam photon flux density ($\text{cm}^{-2} \text{sec}^{-1}$),

i.e., $F = 1/h \int I(\nu) d\nu/\nu$ where $I(\nu)$ is the laser spectral irradiance ($\text{Wcm}^{-2} \text{Hz}^{-1}$).

R_{ij} is the radiation-field-induced transition rate coefficient (sec^{-1}) for transitions from level i to j . For $i < j$ we have absorption; for $i > j$ we have stimulated emission.

$$R_{ij} = B_{ij} \int I(\nu) L_{ij}(\nu) d\nu/4\pi \quad (2.1.1)$$

where B_{ij} is the Milne coefficient ($\text{cm}^2 \text{W}^{-1} \text{sec}^{-2}$) and $L_{ij}(\nu)$ is the line shape function (Hz^{-1}) of the transition.

The first term of (2.1.0) describes electron-collision induced rates between level i and all other levels j . The second and third terms describe the radiative transitions between levels i and $j > i$ and between levels i and $j < i$, respectively. The fourth term describes three-body and radiative recombination into level i and the fifth term describes electron-collision induced ionization out of level i . The last term describes the multiphoton ionization (a κ_i -photon process) out of level i .

The rate equation does not take account of auto-ionization from core-excited states (McIlrath and Lucatorto, 1977), associative ionization (e.g., Dobrolezh, Klyucharev and Sepman, 1975; Tam and Happer, 1977), or depression of the ionization energy as a function of electron density (Drawin and Felenbok, 1965). Inelastic collisions with neutrals and ions are not included (see Appendix A). Also, laser coupling of two bound levels is assumed to be a one-photon process. Expansion or contraction of the plasma is not considered - any change in electron density is accounted for by an equal and opposite change in density of neutrals, and vice versa.

Except for the laser-coupled levels, R_{ij} is in general very small compared with collision processes. However, if the lower level i of a particular transition is appreciably populated (and collision processes do not dominate over R_{ij}), then R_{ij} will have to be taken into account. If this reabsorption of the emitted radiation is not too severe, then the radiation "trapping" effect can be simply accounted for (Milne, 1926; Holstein, 1947, 1951) by including an escape factor γ_{ji} with the spontaneous emission coefficient, viz,

$$A_{ji}^{\text{effective}} = \gamma_{ji} A_{ji} \quad (2.1.2)$$

where $\gamma_{ji} \leq 1$.

γ_{ji} is a fairly complex function of the geometry and line broadening mechanisms, but for light propagating through a thin slab of an atomic gas with homogeneous broadening, for example, Milne (1926) derives

$$\gamma_{ji} = [1 + (C/\lambda)^2]^{-1} \quad (2.1.3)$$

where

$$C = \ell \alpha_{ij} N_i \quad (2.1.4)$$

and ℓ is the slab thickness (cm),

α_{ij} is the appropriate absorption coefficient (cm^2), and

N_i is the number density (cm^{-3}) of the lower of the two levels,

λ obeys $\lambda \tan \lambda = C$ where λ is expressed in radians.

This form (2.1.3) of escape factor has been found to agree well with experiment (Kibble, Copley and Krause, 1967). In the present work, both Milne and Holstein escape factors are used; see Subsection 5.3.1 and Appendix E.

For laser-coupled levels the exact value of R_{ij} depends on $\int I(\nu)L_{ij}(\nu)d\nu$ as mentioned previously, but for most cases of practical interest $I(\nu)$ and $L_{ij}(\nu)$ are both complicated functions of ν and the integral cannot be evaluated accurately. In addition, for a pulsed dye laser, Hänsch (1972) has found random fluctuations in $I(\nu)$ in narrow frequency intervals. $L_{ij}(\nu)$ is generally a convolution of a Lorentzian line shape, due to a finite lifetime resulting from dephasing and quenching collisions (McIlrath and Carlsten, 1972) and a Gaussian line shape arising from Doppler broadening due to a Maxwellian velocity distribution. The uncertainty in the value of the integral is further compounded in the case of high laser spectral irradiance (e.g., Hahn and Hertel, 1972). In most of the work treated in this thesis, laser saturation of the transition is achieved so that the exact value of R_{ij} is relatively unimportant (see Section 2.3).

The electron-collision induced rate coefficient K_{ij} and three-body recombination rate coefficient K_{ci} are discussed in Appendix A. Appendix B covers the photo-ionization rate coefficient $\sigma_i^{(ki)}$.

β_i is given by

$$\beta_i = 1.6 \times 10^{-6} \frac{(Z_i)_{\text{eff}}^2}{T_e^{3/2}} \frac{1}{n_i^3} e^{\epsilon_{ci}/kT_e} \int_{\epsilon_{ci}/kT_e}^{\infty} \frac{e^x}{x} dx \quad (2.1.5)$$

where $(Z_i)_{\text{eff}}$ is the effective nuclear charge as seen by an electron in state i with principal quantum number n_i , and is given by

$$(Z_i)_{\text{eff}} = \epsilon_{ci} n_i^2 / hcR$$

where R is the Rydberg constant. Equation (2.1.5) has the same form as that given by Allen (1963) for the hydrogen atom except for the correction factor $(Z_i)_{\text{eff}}^2$.

2.2 Selective Laser Excitation

In this section we investigate the temporal behaviour of the populations of two levels i and $j > i$ of an atomic species subjected to a step function of laser radiation tuned to the transition $i \rightarrow j$. Measures (1968) was the first to formulate the concept of "selective excitation spectroscopy" involving laser saturation and to recognize the importance of various applications of such a "tuned" laser-atom interaction.

The rate equations for levels j and i can be expressed in the form

$$\dot{N}_j = N_i(R_{ij} + N_e K_{ij}) - N_j(R_{ji} + A_{ji} + N_e K_{ji} + D_j) + C_j \quad (2.2.0a)$$

$$\dot{N}_i = N_j(R_{ji} + N_e K_{ji} + A_{ji}) - N_i(R_{ij} + N_e K_{ij} + D_i) + C_i \quad (2.2.0b)$$

where \dot{N}_i and \dot{N}_j are the time derivatives of N_i and N_j , respectively. Figure 1 shows schematically the two laser-coupled energy levels i and j with expressions for the rates (per unit volume) of the various processes under consideration. For simplicity we have assumed that the degeneracies of the two levels are equal. Also, the rate coefficients D_i and D_j have been used to represent all processes which deplete levels i and j respectively, exclusive of those that couple the two levels. In a similar manner C_i and C_j have been employed to represent the rates of populating levels i and j respectively, exclusive of interactions that couple levels i and j .

Introducing time-invariant rates (the C's) and rate coefficients (the D's) in this way simplifies the problem because only the populations N_i and N_j need be considered explicitly. As a result, however, the validity of the solution of (2.2.0) is restricted to times shorter than that required to appreciably alter the populations in the other levels of the atom and the electron density, because the C's and D's are functions of these variables. In a similar fashion, writing K_{ij} and K_{ji} as time invariant implies that we are assuming a constant electron temperature throughout the analysis (the C's and D's are in general also electron temperature dependent), and similarly restricts the validity of the solution of (2.2.0). These points were not raised by Burgess and Skinner (1974), who presented a simplified analysis of the same problem. The restrictions on the C's and D's are removed in Section 2.5 where the effects of extended laser saturation are discussed.

The coupled set of differential equations (2.2.0) can be decoupled to form two second order differential equations. The equation for N_j can be found as follows: rewrite (2.2.0a) in the form

$$N_i = [\dot{N}_j + N_j(R_{ji} + A_{ji} + N_e K_{ji} + D_j) - C_j] / (R_{ij} + N_e K_{ij}) \quad (2.2.1)$$

Differentiate (2.2.0a) to get

$$\ddot{N}_j = \dot{N}_i(R_{ij} + N_e K_{ij}) - \dot{N}_j(R_{ji} + A_{ji} + N_e K_{ji} + D_j) \quad (2.2.2)$$

Use (2.2.0b) to eliminate \dot{N}_i in (2.2.2), then use (2.2.1) for N_i in the resulting equation. The final equation for N_j takes the form

$$\ddot{N}_j + A\dot{N}_j + BN_j = C \quad (2.2.3)$$

where, after some algebra, we find

$$A = N_e(K_{ij} + K_{ji}) + A_{ji} + D_i + D_j + R_{ij} + R_{ji} \quad (2.2.4a)$$

$$B = D_i(R_{ji} + D_j + A_{ji} + N_e K_{ji}) + D_j(R_{ij} + N_e K_{ij}) \quad (2.2.4b)$$

$$C = C_i(R_{ij} + N_e K_{ij}) + C_j(R_{ij} + N_e K_{ij} + D_i) \quad (2.2.4c)$$

The solution to Eq. (2.2.3) can be expressed in the form

$$N_j(t) = C/B + E_1 e^{\lambda_1 t} + E_2 e^{\lambda_2 t} \quad (2.2.5)$$

where

$$\lambda_{1,2} = -A/2 \pm \frac{A}{2} \left(1 - \frac{4B}{A^2} \right)^{\frac{1}{2}} \quad (2.2.6)$$

The form of the solution depends on the particular values of C_i , C_j , D_i , D_j and on the initial conditions. In order to show qualitatively the variety of possible forms of solution we set $N_i(0) = N_0$ and $N_j(0) = sN_0$ where N_0 is the population of the lower level, and s is a free parameter which represents the ratio of N_j/N_i , evaluated prior to laser coupling. Under these initial conditions we obtain

$$E_2 = sN_0 - C/B - E_1 \quad (2.2.7)$$

and

$$E_1 = N_0(R_{ij} - sR_{ji}) + \lambda_2(C/B - sN_0)/(\lambda_1 - \lambda_2) \quad (2.2.8)$$

We assign a value to D_i and define a free parameter Q such that $Q = D_j/D_i$. C_i and C_j could similarly be assigned certain values, however, we use C_i and C_j to impose the steady state condition on the system prior to laser coupling, i.e., we set $\dot{N}_j(t < 0) = \dot{N}_i(t < 0) = 0$ from which it follows that

$$C_i = N_0[D_i + N_e(K_{ij} - sK_{ji}) - sA_{ji}] \quad (2.2.9)$$

and

$$C_j = N_0[s(D_j + A_{ji}) + N_e(sK_{ji} - K_{ij})] \quad (2.2.10)$$

Note that

$$C_i + C_j = N_0(sD_j + D_i) \quad (2.2.11)$$

and since C_i and C_j are greater than zero by definition, (2.2.9) and (2.2.10) show that the values of the variables on the RHS's are not completely arbitrary.

The temporal forms of intensified spontaneous emission (ISE) from level j , for various values of the free parameters, are shown in Fig. 2 on the assumption

that this emission is directly proportional to $A_{ji}N_j(t)$. The laser-induced rate coefficients $R_{ij} = R_{ji}$ were set equal to ten times the rate coefficient D_i . The electron collision quenching probability $N_e K_{ji}$ and the spontaneous emission probability A_{ji} were both set equal to $D_i/10$. The time axis is in terms of D_i^{-1} and the vertical scale has been normalized by the j level population prior to laser saturation so that the spontaneous emission before laser turn-on equals unity. In Fig. 2 the step-function laser irradiation starts at $t = 0$, and the initial sharp change in spontaneous emission reflects the laser induced redistribution of the population between levels i and j .

Positive-going signals refer in general to cases where $N_j < N_i$ for $t < 0$, which apply to all cases of thermal plasmas; curves A, B and C refer specifically to the case where $N_j = N_i/5$ for $t < 0$. Negative going signals refer in general to cases where $N_j > N_i$ for $t < 0$, which apply to all cases of "inverted" populations. These D, E and F curves (shown in Fig. 2) refer specifically to the case where $N_j = 5N_i$ for $t < 0$. The special case of $N_j = N_i$ is represented by curve G, which shows no deflection on laser turn-on.

The positive and negative deflections are further classified according to the ratio $Q = D_j/D_i$. For a given s , Q is a measure of the change in the rate of loss of population from the set of laser coupled levels due to the laser induced internal redistribution. For $Q > 1$ and $s < 1$ (e.g., curve C for $Q = 2$, $s = 0.2$ in Fig. 2), the spontaneous emission declines after the initial jump, because the pair of laser-coupled levels loses population faster (via $N_j D_j$ and $N_i D_i$) than can be supplied by the sum of rates $C_i + C_j$. This form of solution (curve C) has been analysed in detail by Measures (1968) within the context of plasma diagnostics.

The change in loss rate from the set of levels on laser turn-on is given by

$$\frac{L - L_0}{L_0} = \frac{(s - 1)(1 - Q)}{2(1 + sQ)} \quad (2.2.12)$$

where L_0 is the loss rate just before laser turn-on, $L_0 = N_i(0) D_i + sN_i(0) D_j$ and L is the corresponding loss rate after turn-on.

For $Q < 1$ and $s < 1$ (e.g., curve A for $Q = 0.5$, $s = 0.2$ in Fig. 2), the spontaneous emission continues to increase after the initial rise, achieving a steady state value somewhat greater than that for curve B. In this case the population loss rate via $N_j D_j + N_i D_i$ has been decreased by the laser induced redistribution of populations in levels i and j .

When $Q = 1$, $D_j = D_i$ and therefore no change in population loss rate via $N_j D_j + N_i D_i$ occurs due to the laser induced redistribution. Curves D, E, and F are the population inversion equivalents of curves C, B, and A respectively, and represent media which exhibit optical gain. In these cases the onset of laser action in a laser cavity or the penetration of a laser beam in a laser amplifier will cause a sudden decrease in the spontaneous emission from the upper level (and an increase from the lower level if such transitions are allowed). This effect has been observed (Waksberg and Carswell, 1965; Dunn and Maitland, 1967; and Khaikin, 1967) during the course of investigations into lasing media.

The conditions that applied to curve C in Fig. 2 have been used to form a three dimensional plot of normalised ISE signals against time using the logarithm

of the ratio of the laser-induced rate coefficient R_{ij} ($= R_{ji}$) to the loss coefficient D_i as the third dimension. Figure 3 illustrates the change in the temporal variation of the ISE with increasing laser coupling. R_{ij} varies in steps of $10^{1/2} D_i$ from $10^{-7/2} D_i$ at the front to $10^4 D_i$ at the back. Note that at suitably high laser powers ($R_{ij} > 10 D_i$), the shape of the ISE curve has only a weak dependence on R_{ij} - this in fact is what is implied by saturation.

Figure 4 shows the ISE curves for the special case of resonance pumping. In this graph we have assumed that $D_i = D_j = 0$, and therefore the time is given in units of A_{21}^{-1} . In addition, we have assumed that $N_2(0) = 0$ and therefore that $C_i = C_j = 0$. The vertical scale is not normalized and the ISE amplitude is in arbitrary units. Note that since there are no pathways which enable population exchange with other energy levels, the ISE curves exhibit a "flat top".

2.3 Laser Saturation of a Transition

Figures 3 and 4 both show the phenomenon of laser "saturation of a transition", viz, the ISE does not increase indefinitely with laser power but instead approaches an asymptotic value. In this section we investigate this phenomenon and its practical consequences.

Consider solution (2.2.5) of the differential equation (2.2.3) for the upper of the laser coupled levels. Under saturation conditions

$$R_{ji} \gg A_{ji} + N_e K_{ji} + D_j \quad (2.3.0a)$$

and

$$R_{ij} \gg N_e K_{ij} + D_i \quad (2.3.0b)$$

or, alternatively we may write

$$R_{ij} + R_{ji} \gg N_e (K_{ij} + K_{ji}) + A_{ji} + D_i + D_j \quad (2.3.0c)$$

c.f. (2.2.4); in either case the solution (2.2.5) takes the form

$$N_j(t) = C/B = E_1 e^{-t/\tau_p} + E_2 e^{-t/\tau_f} \quad (2.3.1)$$

where

$$\tau_p \approx [(1 + g)R_{ji}]^{-1} \quad (2.3.2)$$

and

$$\tau_f \approx \frac{(1 + g)}{D_i + gD_j} \quad (2.3.3)$$

with

$$\tau_p \ll \tau_f \quad (2.3.4)$$

In (2.3.2) we have used the general relation

$$g_1 R_{ij} = g_j R_{ji} \quad (2.3.5)$$

and have defined

$$g = g_j / g_1 \quad (2.3.6)$$

as the ratio of degeneracies of the two laser coupled levels.

τ_p is the characteristic time for laser induced redistribution of the populations in levels i and j (the laser pumping time), and τ_f is the relaxation time of the system in the presence of the laser radiation field. The implications of this relaxation process in the context of plasma diagnostics has been treated by Measures (1968) and Burgess and Skinner (1974).

Under the conditions indicated by (2.3.0c) and for times greater than τ_p we may rewrite Eq. (2.2.0a) as

$$0 \approx N_i R_{ij} - N_j R_{ji} \quad (2.3.7)$$

Consequently, making use of (2.3.5), we have the important result that

$$N_j / N_i = g_j / g_1$$

under saturation conditions. This radiative balance condition corresponds to an equivalent infinite temperature.

An important practical consequence of (2.3.4) is that there exists a time domain

$$\tau_p \ll t \ll \tau_f \quad (2.3.8)$$

where

$$N_j(t) / N_i(t) = g_j / g_1 \quad (2.3.9)$$

and

$$N_j(t) + N_i(t) = N_j(0) + N_i(0) \quad (2.3.10)$$

apply simultaneously. $t = 0$ refers to the time just prior to laser irradiation. Combining (2.3.9) and (2.3.10) we obtain

$$\frac{N_j(t)}{N_j(0)} = \left(1 + \frac{N_i(0)}{N_j(0)} \right) \left(1 + \frac{g_1}{g_j} \right)^{-1} \quad (2.3.11)$$

when $\tau_p \ll t \ll \tau_f$.

Thus by observing the change in spontaneous emission resulting from the sudden application of a saturating laser pulse, we can evaluate $N_i(0)/N_j(0)$. Under conditions of thermal (or collisional) equilibrium this ratio can be used to derive the temperature T_0 prior to laser irradiation since T_0 is related to this population ratio through the Boltzmann relation

$$N_i(0)/N_j(0) = g_i/g_j e^{\epsilon_{ji}/kT_0}$$

If the gas has a degree of ionization in excess of a few percent, then T_0 is probably equivalent to T_e , the free electron temperature (Griem, 1964).

Note that in general we can write

$$N_j(t) = GN_0 \quad \text{for } \tau_p \ll t \ll \tau_f \quad (2.3.12)$$

where

$$G = \frac{g_j}{g_i + g_j} \quad (2.3.13)$$

and $N_0 = N_i(0) + N_j(0)$. On the other hand, if $N_j(0) \ll N_i(0)$, then (2.3.12) still applies but now $N_0 = N_i(0)$ as introduced in Section 2.2. In this case it follows from (2.3.12) that the population of any two levels can be compared by laser pumping two appropriate transitions.

With reference to Fig. 2 we may note parenthetically that substitution of $N_j(0) = N_i(0)/5$ and $g_i = g_j$ into (2.3.11) yields in the saturation limit $N_j(t)/N_j(0) = 3$. By comparison, curves A, B, and C in Fig. 2 rise initially to just below 3 in the time interval (2.3.8) because the saturation conditions are not strictly fulfilled here.

The laser spectral irradiance $I(\nu)$ required for saturation of the transition can be calculated from (2.1.1), which is repeated here for convenience:

$$R_{ij} = \frac{B_{ij}}{4\pi} \int I(\nu) L_{ji}(\nu) d\nu \quad (2.3.14)$$

We define a "saturated spectral irradiance" I_{SO} by setting

$$A_c = N_e(K_{ij} + K_{ji}) + A_{ji} + D_i + D_j \quad (2.3.15)$$

[c.f. (2.3.0c)]. If now we assume that the laser is broadband relative to the absorption line width and that the centre frequencies of the two are coincident, we can write

$$\int I(\nu) L_{ji}(\nu) d\nu \rightarrow I_s^l$$

where I_s^l is the laser spectral irradiance ($\text{Wcm}^{-2}\text{Hz}^{-1}$) corresponding to the peak value of the $I(\nu)$ curve. The laser spectral irradiance I_s^l is equal to the "saturated spectral irradiance" I_{s0} when

$$R_{ij} + R_{ji} = A_c \quad (2.3.16)$$

i.e.,

$$\frac{(1 + g)c^2 A_{ji} I_s^l}{8\pi h\nu^3} = A_c$$

where we have used $R_{ij} + R_{ji} = R_{ji}(1 + g)$ and

$$B_{ji} = \frac{c^2 A_{ji}}{2h\nu^3} \quad (2.3.17)$$

for the Milne coefficient. That is to say $I_s^l = I_{s0}$ where

$$I_{s0} \equiv \frac{8\pi h\nu^3}{(1 + g)c^2} \frac{A_c}{A_{ji}} \quad (2.3.18)$$

We can therefore expect saturation conditions to apply when

$$I_s^l \gg I_{s0} \quad (2.3.19)$$

In Fig. 4, which shows the ISE curve for the special case of resonance pumping, the particular curve corresponding to $I_s^l = I_{s0}$ has been identified by the symbol I_{s0} , which for this case equals $3.5 \times 10^{-10} \text{ Wcm}^{-2} \text{ Hz}^{-1}$. For a laser with a bandwidth of about 0.05 nm this corresponds to an irradiance I^l of about 15 Wcm^{-2} . Note that in the case of Fig. 4 we have set $D_i = D_j = 0$ and we have assumed $N_e = 0$ so that $A_c = A_{ji}$ in (2.3.18).

2.4 System Relaxation

On extinguishing the laser radiation, the populations of the various energy levels will redistribute to form a new equilibrium distribution. In this section we investigate the characteristics of this relaxation as a function of the various system parameters for a step function termination of the laser radiation. The differential equation (2.2.3) for $N_j(t)$ still holds, but now R_{ij} and R_{ji} must be set to zero in the equations (2.2.4) for the coefficients A, B and C of the differential equation. The solution, Eq. (2.2.5), is repeated here for convenience:

$$N_j(t) = C/B + E_1 e^{\lambda_1 t} + E_2 e^{\lambda_2 t} \quad (2.4.0)$$

where

$$\lambda_{1,2} = -A/2 \pm \frac{A}{2} \left(1 - \frac{4B}{A^2} \right)^{1/2} \quad (2.4.1)$$

and after laser termination

$$\left. \begin{aligned} A &= N_e(K_{ij} + K_{ji}) + A_{ji} + D_i + D_j \\ B &= D_i(D_j + A_{ji} + N_e K_{ji}) + D_j N_e K_{ij} \\ C &= C_i N_e K_{ij} + C_j(N_e K_{ji} + D_i) \end{aligned} \right\} \quad (2.4.2)$$

Under these circumstances E_1 and E_2 will be defined by the populations N_i and N_j at the moment the laser radiation terminates. For the general case, the decay characteristic of N_j is a complex function of the system parameters, but for the case of $N_e(K_{ij} + K_{ji}) + A_{ji} \gg D_i + D_j$, the decay rates $\lambda_{1,2}$ take on simple forms:

$$-\lambda_1 \approx B/A \ll 1$$

$$-\lambda_2 \approx A \gg 1$$

where

$$A \approx N_e(K_{ij} + K_{ji}) + A_{ji}$$

In fact, if we set $D_i = D_j = 0$ and consequently $C_i = C_j = 0$, then the form of the differential equation (2.2.3) changes to first order with a solution

$$N_j(t) = E_3 e^{\lambda_3 t} + E_4$$

where

$$\lambda_3 = -[N_e(K_{ij} + K_{ji}) + A_{ji}]$$

and where E_3 and E_4 are constants which can be related to conditions before laser turn-on. The important thing to note is that the time constant for relaxation of the population in level j

$$\tau_3 = -\lambda_3^{-1} \quad (2.4.3)$$

and therefore the decay characteristic of the ISE can be used to calculate N_e if K_{ij} and K_{ji} are known along with A_{ji} . This assumes that radiation

trapping can be safely ignored. If $N_e = 0$, then

$$\tau_3 = A_{ji}^{-1} \quad (2.4.4)$$

and the lifetime of the upper state can be measured directly. Note that if alternative radiative decay modes exist for the laser enhanced population, we can choose to monitor the ISE at a wavelength other than the laser wavelength, thereby eliminating Rayleigh, Mie, and apparatus scattering. In this case, however, (2.4.4) must be replaced by

$$\tau_3 = \left(\sum_i A_{ji} \right)^{-1} \quad (2.4.5)$$

where the sum extends over all allowed transitions from level j .

2.5 Extended Saturation Pumping

In the case of laser saturation that persists for times $> \tau_f$, the distributions of the electrons in all of the energy levels of the atoms within the laser beam will eventually be perturbed. This will inevitably lead to an increase in the degree of ionization as the free electrons come into a new equilibrium with the larger population of excited atoms. This effect will be particularly pronounced if the lower of the laser coupled levels is the ground state, thereby ensuring that a majority of the atoms in the laser beam participate in the laser pumping process. In this section we investigate theoretically the extended saturation pumping of the $3^2S_{1/2} - 3^2P_{1/2}$ resonance transition in un-ionized sodium vapour at an irradiance $I_l = 1 \text{ MW cm}^{-2}$ and an atom density of about $N_0 = 10^{16} \text{ cm}^{-3}$. These are the conditions under which Lucatorto and McIlrath (1976) observed almost total first degree ionization in approximately 500 ns.

Measures (1970) showed that in the case of a weakly ionized gas, the large reservoir of resonance state atoms (created by the laser pumping) can very quickly increase T_e via electron superelastic collision quenching of the resonance level. This increase of T_e , combined with the large number of resonance state atoms was shown to rapidly increase the free electron density N_e to above 95% ionization.

In order to evaluate these effects in detail and to determine the time scale involved, it will be necessary to solve the rate equations (2.1.0) for all bound levels simultaneously, along with a rate equation for N_e . Furthermore, to account for the electron temperature dependence of the various collision rate coefficients, the rate equation for T_e will also have to be solved.

Before proceeding with this analysis, let us consider the physics involved. In general, saturation of the transition to which the laser is tuned will not be the only influence of the radiation field. Multiphoton effects are possible and if a laser irradiance of about 1 MW cm^{-2} is used multiphoton ionization can become an important source of free electrons. We recall that the original work by Measures (1970) was based on the existence

of an initial pool of free electrons. In the case of cold (i.e., un-ionized) sodium vapour excited by 1 MW cm^{-2} of laser radiation tuned to the $3^2S_{1/2} - 3^2P_{1/2}$ transition (589 nm), the rate of two-photon ionization of the resonance level can be approximately 10^{16} sec^{-1} when $N_0 = 10^{16} \text{ cm}^{-3}$ (Cardinal, 1979; Geltman, 1977). These electrons are produced with a kinetic energy of approximately 1.2 eV, which is certainly above the threshold level for electron impact excitation from the resonance state to the next higher lying excited state. In this analysis we neglect fine structure and, for example, consider the $3^2P_{1/2}$ and $3^2P_{3/2}$ states as one state with a degeneracy of 6. This is justified by the large mixing cross-sections ($8 \times 10^{-14} \text{ cm}^2$) reported by Krause (1966).

Let us follow for a moment longer this 1.2 eV electron in order to understand some of the physics involved. Due to the ratio of degeneracies, a collision with a resonance state atom is three times as probable as one with a ground state atom. A "ground state" collision is uninteresting in that the collision is elastic with insignificant energy loss by the electron due to the mass disparity. (The atoms are assumed initially to have a kinetic energy of only 0.06 eV consistent with the temperature required to provide an equilibrium sodium vapour density of about 10^{16} cm^{-3} .) An "excited state" collision, however, produces one of two results: (a) the electron excites the atom further to a higher energy level at the expense of some of its kinetic energy, or (b) the atom is de-excited in a superelastic collision, transferring the energy difference to the free electron. Consider case (a); if the electron excites the atom further, then the expended energy leaves the electron with insufficient energy to cause subsequent further excitation (Gryzinski, 1965) and the electron will in all likelihood suffer a superelastic collision the next time it encounters a resonance state atom and thereby recover at least part of its energy. In the case of (b), the electron will have about 3.3 eV of energy and the chance of the next collision being inelastic with consequent further atomic excitation, or ionization, is much enhanced. From these considerations, it is obvious that extended saturation pumping of the resonance state produces free electrons and that these electrons in turn exert a "pressure" to excite higher lying states (including the continuum) of the atom. In summary, the laser delivers energy to the vapour because the laser photo-ionizes some atoms directly through two-photon ionization from the resonance level, and the laser maintains an infinite temperature distribution against the differential depletion of the ground and resonance states due to electron collisions and spontaneous emission.

The concept of power flow from the laser to the atomic system due to a differential depletion of the laser coupled levels is easily visualized without recourse to detailed calculations. Consider the saturation condition (2.3.9), repeated here for convenience:

$$g_i N_j \cong g_j N_i \quad (2.5.0)$$

from which it follows that

$$g_i \dot{N}_j \cong g_j \dot{N}_i \quad (2.5.1)$$

for time variations much slower than the laser-induced pumping rate, $N_i R_{ij}$.

At any instant in time we may in principle rewrite the rate equations (2.2.0) as

$$\dot{N}_j = \dot{N}_{jE} - R + P_a \quad (2.5.2)$$

$$\dot{N}_i = \dot{N}_{iE} + R - P_a$$

where the subscript E signifies a rate ($\text{cm}^{-3} \text{sec}^{-1}$) due to interactions with energy levels external to i and j, R is the net downward rate ($\text{cm}^{-3} \text{sec}^{-1}$) from level j to i in the absence of laser coupling, and P_a is the laser-induced net upward rate ($\text{cm}^{-3} \text{sec}^{-1}$) from level i to j.

Solving (2.5.2) for P_a using (2.5.1), we get

$$P_a \cong R + (g_j \dot{N}_{iE} - g_i \dot{N}_{jE})(g_i + g_j)^{-1} \quad (2.5.3)$$

If $(g_i + g_j)R + g_j \dot{N}_{iE} > g_i \dot{N}_{jE}$, then $P_a > 0$ and power flows from the laser beam to the atomic system, as for example in LIBORS where $\dot{N}_{jE} \ll 0$. The generalization to a power flow from the atomic system to the laser beam follows easily. If $(g_i + g_j)R + g_j \dot{N}_{iE} < g_i \dot{N}_{jE}$, the $P_a < 0$ and power flows from the atomic system to the laser beam as in a laser amplifier. The power exchanged per unit volume is given by

$$P = P_a h\nu$$

The rate equations presented below model the various processes which should be taken into account under the conditions of extended saturation pumping of the sodium resonance level. A twenty-level model of the sodium atom was adopted (see Chapter 7) and the rate equations reflect this fact.

The rate equation for the kinetic energy content (ergs cm^{-3}) of the free electrons can be written as

$$\begin{aligned} \frac{d}{dt} (N_e \epsilon_e) = & N_2 N_e K_{21} \epsilon_{21} + (2\epsilon_{21} - \epsilon_{c2}) N_2 \sigma_2^{(2)} F^2 \\ & + \sum_{i>2}^{20} (\epsilon_{21} - \epsilon_{ci}) N_i \sigma_i^{(1)} F - N_e \sum_{i=1}^{20} N_i K_{ic} \epsilon_{ci} \\ & - N_e C - N_e^2 H_{ei} - N_e N H_{en} \\ & + N_e^2 \sum_{i=1}^{20} (N_e K_{ci} \epsilon_{ci} - \beta_i \epsilon_e) \end{aligned} \quad (2.5.4)$$

where ϵ_e represents the mean translational energy of a free electron, C represents the loss of energy per electron due to the collisionally induced net upward movement of bound electrons (exclusive of the resonance super-elastic term)

$$C = \sum_{i=1}^{19} \sum_{j>1}^{20} (N_i K_{ij} - N_j K_{ji}) \epsilon_{ji} + N_2 K_{21} \epsilon_{21}$$

where $N_2 K_{21} \epsilon_{21}$ represents the superelastic heating term for the free electrons due to laser saturation of the resonance transition, H_{ei} represents the rate of elastic energy transfer to ions through Coulomb scattering collisions and if the electrons and ions have Maxwellian velocity distributions,* H_{ei} takes the form (Morgan and Morrison, 1965)

$$H_{ei} = \frac{e^4}{m_i} \left(\frac{8\pi m_e}{kT_e} \right)^{1/2} \frac{T_e - T_i}{T_e} \ln \left[\frac{9(kT_e)^3}{8\pi N_e \sigma} \right] \quad (2.5.5)$$

where e is the electronic charge in esu, m_i and m_e are the ion and electron masses (g), and T_e and T_i are the electron and ion kinetic temperatures ($^{\circ}K$), N represents the total neutral atom density (cm^{-3}), and H_{en} represents the rate of elastic energy transfer to neutral atoms from the free electrons, and is given by

$$H_{en} = \left(\frac{8kT_e}{\pi m_e} \right)^{1/2} k(T_e - T_n) \sigma_{en} \frac{4m_e}{m_n} \quad (2.5.6)$$

where σ_{en} is the relevant electron-atom cross-section (cm^2).

Equation (2.5.4) may be written in the form

$$\frac{d}{dt} (N_e \epsilon_e) = \epsilon_e \dot{N}_e + N_e \dot{\epsilon}_e \quad (2.5.7)$$

and divided into two equations, one for the rate of growth of the free electron density

$$\epsilon_e \dot{N}_e = \epsilon_e \left[N_2 \sigma_2^{(2)} F^2 + \sum_{i>2}^{20} N_i \sigma_i^{(1)} F + N_e \sum_{i=1}^{20} N_i K_{ic} - N_e^2 \sum_{i=1}^{20} (N_e K_{ci} + \beta_i) \right] \quad (2.5.8)$$

and the second for the variation of the free electron temperature,

*The validity of this assumption is discussed in Section 7.4.

$$\begin{aligned}
N_e \frac{3}{2} kT_e \dot{\epsilon}_e &= N_e N_2 K_{21} \epsilon_{21} + \left[2\epsilon_{21} - \epsilon_{c2} - \frac{3}{2} kT_e \right] N_2 \sigma_2^{(2)} F^2 \\
&+ N_e^3 \sum_{i=1}^{20} K_{ci} \left(\epsilon_{ci} + \frac{3}{2} kT_e \right) - N_e \sum_{i=1}^{20} N_i K_{ic} \left(\epsilon_{ci} + \frac{3}{2} kT_e \right) \\
&+ \sum_{i \geq 2}^{20} \left[\epsilon_{21} - \epsilon_{ci} - \frac{3}{2} kT_e \right] N_i \sigma_i^{(1)} F - N_e C \\
&- N_e^2 H_{ei} - N_e N H_{en}
\end{aligned} \tag{2.5.9}$$

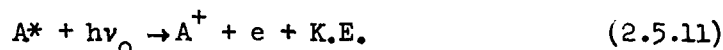
where we have used $\dot{\epsilon}_e = \frac{3}{2} kT_e$.

In Eqs. (2.5.4) and (2.5.9) we have chosen to present separately the superelastic heating term, $N_2 K_{21} \epsilon_{21}$, and the cooling term, C , in order to draw attention to their opposite effect on electron temperature.

The first term in Eq. (2.5.8) accounts for two-photon ionization from the resonance level:



and the second term accounts for photo-ionization from all the higher lying states:



The third term describes electron impact ionization



and the last term describes three-body and radiative recombination, respectively given by



and



In (2.5.10) to (2.5.14) we have used ν_0 as the laser frequency, A^+ as the singly ionized atom, A^* as the neutral atom in any energy state, e as the electron, and K.E. as the excess of kinetic energy associated with the free electron.

The second term of (2.5.9) represents two photon ionization, the third term represents three-body recombination, and the fourth term accounts for radiative recombination. The fifth term of (2.5.9) accounts for photo-ionization from the higher lying ($i > 2$) states. The last two terms represent energy transfer to ions and neutrals through Coulomb and elastic collisions, respectively.

Various other processes have not been included in these rate equations; these are enumerated in Section 2.1.

The kinetic temperature of the neutral atom, T_n , and the ion, T_i , can be derived by using rate equations for the respective kinetic energies. We define E_n as the kinetic energy per unit volume (ergs cm^{-3}) deposited in the neutral atoms and similarly E_i for the ions. Then we have

$$\dot{E}_n = N_e H_{en} N_n - X \quad (2.5.15)$$

$$\dot{E}_i = N_e^2 H_{ei} + X \quad (2.5.16)$$

where

$$X = \begin{cases} \frac{E_n}{N_n} \dot{N}_e & \text{if } \dot{N}_e > 0 \\ -\frac{E_i}{N_i} \dot{N}_e & \text{if } \dot{N}_e < 0 \end{cases} \quad (2.5.17)$$

and we have assumed that an atom's kinetic energy is preserved during the process of ionization and likewise that an ion's kinetic energy is preserved upon recombination.

The results of the numerical integration of the various rate equations are presented in Chapter 7, along with physical interpretations. Details of the actual computer program are left to Appendix E.

3. LASER ABLATION AND SELECTIVE EXCITATION SPECTROSCOPY FACILITY

A Laser Ablation and Selective Excitation Spectroscopy (LASES) facility was assembled in order to test experimentally some of the concepts advanced in the previous chapter. In this chapter we outline the features of the LASES facility and describe in more detail major pieces of apparatus, including performance features and calibration.

The LASES facility consisted basically of a high power, pulsed laser which ablates a target material under vacuum. After an adjustable time delay, a tunable dye laser sent a probe pulse of appropriate wavelength through the ablation plume. (In this thesis we prefer to use the term 'ablation plume' as opposed to 'ablation plasma' in order to draw attention to the fact that in the case of our experimental conditions the ablated material at the time delays

of interest was in general only very weakly ionized, if at all.) Collection optics captured some of the general background emission and the intensified spontaneous emission (ISE) generated by the interaction of the probe pulse and the ablation plume. A choice of instruments provided flexibility in the method of recording this radiation; a spectrograph was available, as well as monochromator and photomultiplier tubes. A schematic of two versions of the LASES facility is shown in Fig. 5, a detailed description of which follows.

The optical paths are indicated by dotted lines; electrical connections are shown with solid lines. Figure 5a represents the LASES facility as it was comprised during most of the experiments reported in Chapters 4 and 5. The figure shows the nitrogen laser and a tunable dye laser (see Subsections 3.1.2 and 3.1.3 for details). For tuning purposes, part of the output of the dye laser was intercepted by a beamsplitter (all beamsplitters were simple microscope slides) and directed to the Heath monochromator (see Section 3.2). The light from a chromium resonance lamp was merged with that of the dye laser at the entrance slit of the monochromator. The monochromator served simply to remove interfering chromium spectral lines from the final interferogram. The output of the monochromator was sent through a Fabry-Perot interferometer (finesse = 15) and into the 1400 mm focal length camera. The resulting split field interference pattern was recorded on Polaroid type 410 film (10,000 ASA).

During experiments, the tunable laser system was triggered by a laser pulse arriving at a photodiode from the ablation laser. All photodiodes were H.P. No. 5082-4220 PIN photodiodes in special mounts (see Subsection 3.3.1). The electrical signal from the photodiode triggered a Tektronix 556 oscilloscope which acted as a delay unit. The desired delay could be set to any value above 150 ns. The delayed trigger output in turn triggered the nitrogen laser. The minimum delay possible between ablation laser pulse and dye laser pulse(s) was about 950 ns.

The ablation laser was a passively Q-switched ruby laser (see Subsection 3.1.1). The laser pulse entered the ablation chamber through a lens, which focussed the pulse onto a small area of the chromium target. The ablation chamber was maintained at about 5×10^{-5} torr. The temporal pulse shape and amplitude of the ablation laser was monitored on a L.R.S. model WD 2000 transient digitizer with 1 ns resolution, whose input and trigger signals came from separate photodiodes, each of which viewed part of the ablation laser pulse through beam splitters, neutral density filters, and diffusers. For the sake of clarity, this unit is not represented in Fig. 5a.

Part of the light from the ablation plume was collected by a lens and focussed onto the slit of a Spex No. 1700-II Czerny-Turner monochromator (see Section 3.2), whose output was detected by a photomultiplier tube PMT. The two photomultipliers which were used are discussed in Section 3.3. The output of the PMT served as the input signal for the Tektronix 7704 oscilloscope with a 7A24 vertical amplifier. The published risetime of the mainframe-plug-in combination was 2.1 ns.

Some of the atoms of the ablation plume were selectively excited by sending a dye laser pulse vertically through the plume parallel to the target surface. This was done by using two mirrors, one of which was located above the ablation chamber; this mirror is not shown in the figure. Part of the dye laser beam was directed to a photodiode PD through a lens and neutral density filter. The

signal from the photodiode was used variously to monitor the performance of the laser or to trigger the 7704 oscilloscope. A photograph of the ablation chamber is shown in Fig. 6, which shows also the mirror above the chamber used to deflect the dye laser beam through the plume.

Figure 5b shows a schematic of the LASES facility used for the two-wavelength pumping experiment reported in Chapter 6. Only the essential features are shown in this figure. A 6-armed glass cross was used as an ablation chamber in order to accommodate two dye laser beams arriving from opposite directions. This facility also incorporated broad-band, high-efficiency collection optics (see Chapter 6 for details).

The detailed composition of the LASES facility varied from experiment to experiment. The variations are discussed in the appropriate chapters.

3.1 Lasers

3.1.1 Ruby Laser (The Ablation Laser)

The ruby laser was manufactured by TRG Inc. and consisted of a model 104 Power Source and a model 104A Laser Head. The laser had previously been modified in this laboratory to incorporate a passive Q-switch consisting of a cylindrical cell of cryptocyanine dye in acetonitrile. Lasing wavelength was 694.3 nm and pulse length varied between 18 and 30 ns, and energy between 20 and 400 mJ, depending on the condition of the Q-switch solution and the optical alignment. The energy was measured with a Hadron 102A Energy Meter connected to a Hadron TRG 100 Thermopile. No calibration of the thermopile was attempted.

The alignment of the laser components was done interferometrically using the beam of a helium-neon laser. The alignment of the outcoupling flat was found to be very sensitive to vibration and consequently the mount for this flat was redesigned. During experiments the laser was manually triggered at about 5 minute intervals, which was sufficient time to allow the ruby crystal to cool and achieve a homogeneous temperature distribution with the aid of the forced air ventilation.

3.1.2 Nitrogen Laser

The double-pass nitrogen laser, used to optically pump the dye laser(s), was constructed in the laboratory using plans based in large part on the design of Schenck and Metcalfe (1973). Figure 7 gives an overview of the laser and Fig. 8 illustrates some of the details of construction. The laser exhibited an 8 ns FWHM pulse with peak power of 125 kW, in a spectral band 0.1 nm wide centered on a wavelength of 337.1 nm. The 125 kW figure was achieved at an electrode voltage of 12.5 kV and a channel pressure of 16 torr which corresponded to an E/p value of 205 V cm⁻¹ torr⁻¹. Maximum pulse repetition rate was 10 Hz. The divergence of the main beam was 30 mrad in the horizontal plane and 2 mrad in the vertical plane. The output also contained secondary beams displaced vertically from the main beam by small angles. These secondary beams were attributed to the closely spaced, smooth upper and lower glass surfaces of the laser channel.

After some hours of operation, the glass developed cracks and broken glass lying on the floor of the laser channel interfered with the beam. Subsequently

the channel was redesigned and rebuilt. A cross-sectional view of the new channel is shown in Fig. 9. The glass was replaced by lucite, and the separation of the two lucite strips was increased to 25 mm. In addition, the two inward facing surfaces of the lucite strips were roughened to prevent grazing-angle reflections which cause secondary output beams from the channel. The electrodes were machined from single pieces of aluminum for optimum electrical conductivity between channel and the dumping capacitors. This particular channel was used for all the experimental work detailed in this thesis. A recent paper discussing improvements to the laser of Schenck and Metcalfe (1973) shows a channel cross section very similar to that shown in Fig. 9, though the gas flow had also been changed to transverse from longitudinal (Feldman, Lebow, Raab and Metcalfe, 1978).

The new channel generated about 30 kW peak power during an 8 ns pulse when operated at 13 kV and 33 torr of nitrogen (E/p ratio = $160 \text{ V cm}^{-1} \text{ torr}^{-1}$). An oscilloscope display of the laser pulse is shown in Fig. 10.

During the course of the experiments an attempt was made to reduce the time delay between the arrival of a trigger pulse at the control box and the arrival of the laser pulse. The delay was 950 ns, of which 700 ns were due to the turn-on time of the 2N4443 SCR. The SCR was then replaced by a set of six 2N2405 transistors, and a hand-wound transformer, which reduced the delay to 800 ns. The lifetime of these transistors was short, however, due to the large voltage transients present. This approach was abandoned.

3.1.3 Dye Laser Model 1

Dye laser No. 1 was built in the laboratory according to the design of Hänsch (1972) but without an intra-cavity polarizer. A photograph of the laser is shown in Fig. 11. The laser used a cylindrical uncoated quartz dye cell 1 cm long with parallel end windows. In order to prevent cavity effects, the cell was rotated slightly about an axis parallel to the optical axis of the pump light. The outcoupling flat, 6 cm from the dye cell, had a dielectric coating on the inner surface which reflected approximately 50% of the blue light. Alignment of the flat was facilitated by a special mount which incorporated very stable, fine angle adjustments in the vertical and horizontal planes.

The beam expander was a Jodon Engineering Associates model LC-25 used at a beam expansion of $\times 10$. The beam expander was mounted on a translation stage which provided adjustment of the device in a direction transverse to the optical axis of the dye laser. Vertical adjustment of the translation stage was also provided.

The intracavity etalon was a TRG (Hadron) No. EZ00-ZB-101 with a spacing of 3 mm and a finesse of about 20 at 600 nm. The grating was a PTR Optics TF-R2 with 316 lines per mm, blazed at $63^\circ 35'$, and used in the 7th order. The etalon was removed after preliminary tests with Rhodamine 6G and the laser was used without etalon in all the experiments reported here because the etalon finesse was insufficient at the chromium resonance wavelengths.

A typical oscilloscope (No. 7704) display of the dye laser pulse is shown in Fig. 12; in this case the dye was dimethyl POPOP in toluene lasing at 425.4 nm. The pulse FWHM is seen to be 4 ns as detected by an HP photodiode. Bandwidth of the pulse was typically 0.02 nm at a wavelength of 425 nm.

An attempt was made to measure the peak power output of the dye laser. The Hadron energy meter used for the ruby and nitrogen lasers had insufficient sensitivity to detect the energy of the dye laser pulse. As a result one of the HP photodiodes (see Section 3.3.1) was used in conjunction with the quantum efficiency curve supplied by the manufacturer. The power of the laser was estimated by exposing the active area of the photodiode (measured with the aid of a travelling microscope) to the collimated dye laser beam of a known cross-sectional area and known attenuation, and extrapolating the power incident on the photodiode to the full, unattenuated beam. The extrapolation yielded 3 kW peak power. Carbostryl 165 in methanol and dimethyl POPOP in toluene both produced about the same power, and therefore Cl65 was used for the experiments because its solvent (methanol) was easier to use in the laboratory.

3.1.4 Dye Laser Model 2

Dye laser No. 2 was built in the laboratory and resembled closely No. 1. Some improvements were implemented, however. An Oriel No. 1592 beam expander was used at x20 expansion, and a Hellma No. 131.037 flow-through dye cell with wedge-angled windows were employed. Pulse length was 4 ns FWHM, unchanged; but the bandwidth was reduced to 0.015 nm when coumarin 120 in methanol was used at a wavelength of 450 nm. The peak output power as measured with the HP photodiode and Tektronix 7704 oscilloscope was approximately 3 kW.

3.2 Monochromators

Two monochromators were used as part of the LASES facility - a Spex model 1700-II 3/4 m Czerny-Turner monochromator and a smaller Heath monochromator of similar design. The Spex monochromator was used to select the collection optics' spectral window during the preliminary experiments outlined in Chapter 4 and during the atomic lifetime experiments described in Chapter 5. The Heath monochromator was used only for dye laser tuning purposes to prefilter the light from the chromium resonance lamp in order to prevent light from other chromium emission lines from reaching the Fabry-Perot interferometer and producing extraneous ring patterns. Both monochromators had a dispersion of about 1 mm per nm and both were operated with approximately 1 mm slit widths to yield a bandpass of about 1 nm. No detailed calibrations were conducted. However, the chromium spectral lamp was always used to provide reference wavelengths for purposes of tuning the monochromators.

3.3 Photodetectors

3.3.1 Photodiodes

All photodiodes were Hewlett Packard No. 5082-4220. They were installed in special high speed mounts whose designs were based on those of McCall (1972) but containing BNC connectors suitable for use with 50 Ω RG58-U coaxial cable. A battery was connected to the diode through two 100 k Ω resistors to provide a back bias of 45 V.

Accurate calibration of the photodiodes was not attempted because the diodes were not used to make accurate quantitative measurements; however, general performance features were checked. An indication of response time, for example, can be gained by reference to Fig. 12. The dye laser pulse (@ 425 nm) depicted has an indicated FWHM width of 4 ns as displayed on the Tektronix 7704 oscilloscope, which has a quoted risetime of 2.1 ns. The same

laser pulse as detected by the RCA C70042K photomultiplier, with a quoted pulse risetime of 1.6 ns, shows a 5 ns FWHM. It is therefore reasonable to suppose that the pulse response of the photodiode assembly is faster than 1.6 ns.

The linearity of the photodiode assembly was checked by using the dye laser as a pulsed source at 425 nm, and introducing attenuation with neutral density filters. No accurate measurement was attempted, however the non-linearity of the diode was about 10% at 1.5 V peak output. Since the largest output signal encountered during the experiments was about 0.8 V, the departure from linearity of the photodiode assembly was considered negligible.

3.3.2 Photomultiplier C70042K

An RCA C70042K photomultiplier tube (PMT) with a No. 131 spectral response was available in the laboratory, and was rewired for maximum response speed (1.6 ns anode pulse risetime at 2100 V) according to a circuit in the RCA specification sheet for the tube.

The tube risetime using a step input could not be accurately measured because a suitable light source was not available. In any case, it was not possible to separate the tube response from the oscilloscope response because the oscilloscope was the only means of displaying the PMT output. A conservative estimate of the risetime of the tube-'scope system for a step function input was obtained by using the intensified spontaneous emission (ISE) signal obtained during the course of the preliminary experiments described in Chapter 4. Some of these ISE signals were characterized by both a rapid initial rise and a much slower decay. Although the risetime of the dye laser was also involved, these ISE signals nonetheless provided a first approximation to the system (i.e., PMT-'scope) risetime. The risetime thus indicated was about 5 ns at a supply voltage of 1800 V.

The linearity of the C70042K PMT was checked at a supply voltage of 1800 V by using the dye laser as a source of 425 nm light and introducing neutral density filters into the laser beam. Accurate measurements were not required; however a deviation of about -10% was found at an output level of about 2 V. All signal levels during the experiments were below 1 V and the nonlinearity of the tube was therefore not considered to be an important factor.

3.3.3 Photomultiplier C31034

An RCA C31034 photomultiplier tube was used to detect the ISE signal during the atomic lifetime measurements reported in Chapter 5. The tube had a No. 128 spectral response which resulted in a quantum efficiency of 19% at 427 nm, considerably higher than the 4.5% of the C70042K, however the quoted anode pulse risetime was longer (2.5 ns).

The risetime of the C31034-'scope system for a step input was estimated using the technique as outlined in the previous subsection. In this case the supply voltage was 1500 V in order to conform with the operating conditions during the atomic lifetime experiments. The figure adopted was 6 ns.

A knowledge of the linearity of this PMT was important in analysing the results of the lifetime experiment. Consequently a two-filter technique (shortly to be described) was employed.

In order to achieve high output levels, a pulsed source was required in order to keep the average anode current below the specified maximum for the tube. A light-emitting diode was driven by a pulse generator to produce 1 μ s long pulses at a repetition rate of 60 Hz. The linearity check proceeded as follows.

For various source intensities, four separate PMT output levels were recorded using all combinations of two neutral density filters between the source and the photocathode of the PMT:

- (a) y_A - using filter 1 and filter 2,
- (b) y_B - using filter 2 only,
- (c) y_C - using filter 1 only,
- (d) y_D - using no filters,

where filter 1 had a transmission of $T_1 = 51\%$ and filter 2 had a transmission of $T_2 = 25\%$. A typical plot of photomultiplier output versus input would appear as shown in Fig. 13 where the nonlinearity of the PMT has been exaggerated for clarity. If we define

$$r_1 = \frac{y_C}{y_D}, \quad r_2 = \frac{y_A}{y_B}$$

then we have $r_1 = T_1$ and $r_2 = \eta T_1$ where $\eta > 1$ and accounts for multiple reflections between the neutral density filters which effectively raise the transmission of the second filter. Therefore

$$\frac{r_1}{r_2} = \frac{1}{\eta T_1} \frac{y_C}{y_D}$$

and if the PMT is linear

$$\frac{r_1}{r_2} = \frac{1}{\eta} \tag{3.3.3.0}$$

If the tube is nonlinear due to space-charge effects, then

$$y_{DN} = y_{DL} = \delta$$

where y_{DN} is the nonlinear (real) output and y_{DL} is the theoretical (linear) output and $\delta > 0$. Then

$$\frac{r_1}{r_2} = \frac{1}{\eta T_1} y_C \frac{1}{y_{DL} - \delta} \tag{3.3.3.1}$$

We are only interested in small departures from linearity, i.e., $y_{DL} \gg \delta$ and we can therefore approximate (3.3.3.1) by

$$\frac{r_1}{r_2} = \frac{1}{\eta^2} \frac{y_C}{y_{DL}} \left(1 + \frac{\delta}{y_{DL}} \right)$$

and if we have established that the PMT is linear at the point y_C , we may write

$$R_r = \frac{1}{\eta} \left(1 + \frac{\delta}{y_{DL}} \right) \quad (3.3.3.2)$$

or

$$\frac{\delta}{y_{DL}} = R_r \eta - 1 \quad (3.3.3.3)$$

where we have introduced $R_r = r_1/r_2$. Note that if the tube is operating in its linear range, then $\delta/y_{DL} = 0$ and (3.3.3.2) is equivalent to (3.3.3.0).

Four values of R_r were found corresponding to values of y_{DN} equal to 0.7, 1.6, 3, and 4.65 volts. The respective R_r values were 0.976, 0.972, 1.015, and 1.313. Thus we have $\eta \cong 1.03$, and for $y_{DN} = 3$ V we have $\delta/y_{DL} \approx 4\%$. For $y_{DN} = 1.6$ V we have no discernable nonlinearity; however, considering the accuracy of the attenuation measurements, we have assigned a value of 1% maximum nonlinearity for output signals below 1 V.

4. PRELIMINARY LASES EXPERIMENTS

Preliminary experiments using the LASES facility were conducted to determine some of the more obvious features of the laser ablation plume and the plume-dye laser interaction in order to determine the potential and the limitations of the LASES facility.

Three sets of experiments are described. The first involved photographing the time-integrated emission spectrum of the plume to determine which stages of ionization were involved (if any), and to find out the degree of contamination of the plume by impurities in the chromium sample. The second set of experiments consisted of recording the time history of the resonance radiation of the (chromium) plume in order to gain an understanding of the dynamics and time scale involved. Some of the more obvious effects of the tuned dye laser-plume interaction were also observed. The third set involved studying the decay characteristics of the ISE pulse in order to better understand the plume expansion and recombination processes.

The target material for the ablation process was chosen to be chromium. Chromium is easy to handle in the laboratory and it contains resonance transitions in the visible part of the spectrum. Chromium can therefore be optically pumped with readily available laser dyes. A partial energy level diagram of the metal is presented in Fig. 14. Another attractive feature of chromium is associated with its low-lying metastable energy levels which are connected to higher lying excited states via transitions whose wavelengths are in the same

part of the spectrum (blue) as those of the resonance transitions. Thus various transitions of interest can be optically pumped without changing the laser dye. The chromium sample used in this work was obtained from a local electroplating company.

In keeping with the exploratory nature of these experiments, extensive data collection and processing was not undertaken. Nevertheless, a significant insight into the LASES phenomenon was gained from these experiments. A more detailed description of the various experiments follows.

4.1 Plume Emission Spectrum

The experimental arrangement was similar to that outlined in Chapter 3 except for the following differences. The four-armed glass cross shown in Fig. 6 was used as the vacuum chamber. The background pressure was maintained at about 10^{-4} torr. The dye laser system was not required and was therefore not operated. The monochromator was replaced by a Jarrel Ash 1.5 m Wadsworth spectrograph which had a dispersion of 1.09 nm per mm, and which was operated with a 100 μ slit.

A spectrogram of the ablation plume was taken by accumulating 10 events on film. Each ablation laser shot delivered approximately 200 mJ of energy in about 20 ns to yield a peak irradiance on target of 2.5×10^8 Wcm⁻².

The time integrated chromium plume spectrum was analysed at wavelengths between 414.5 and 484.7 nm. Line positions were measured with a travelling microscope and converted to nanometers by using the 425.44 and 440.35 nm lines (whose exact wavelengths were obtained from Corliss and Bozman, 1962) as benchmarks. The results, along with visual estimates of intensities on an arbitrary scale, are presented in Table 1. Table 1 also shows the most probable identity of each measured line according to species and wavelengths as given by Corliss and Bozman (1962) and/or by Harrison (1956). The lines that were left unidentified were probably either CrI or CrII lines. Harrison (1956) shows such lines within 0.03 nm of the measured wavelengths for all cases but one, but they are very weak. The spectrogram also showed a continuum between about 425 and 440 nm. The appearance of at least one strong CrII line indicates that some degree of ionization occurred in the ablation plume for an ablation beam intensity of 2.5×10^8 Wcm⁻². This is supported by the appearance of the continuum radiation which was probably the result of radiative recombination.

4.2 Plume Resonance Radiation and Dye Laser Interaction

In this section we describe a set of experiments which were carried out in order to ascertain the general characteristics of the ablation and plume expansion process, and the dye laser beam-plume interaction. The general character of the ablation plasma emission is described, and related to experimental parameters. The effect of the ablation plume on the propagation of the dye laser pulse is noted, as is the effect of the dye laser pulse on the emission from the ablation plume.

The layout of the equipment was similar to the general description given in Chapter 3, using the four-armed glass cross as the vacuum chamber.

Pressure was again about 10^{-4} torr, but the ablation laser energy in this case was about 30 mJ due to the deterioration of the Q-switch solution. The RCA photomultiplier C70042K, mounted at the exit slit of the Spex monochromator, was used as the resonance radiation signal detector, operating at 1800 V. The chromium resonance lines of interest were selected with the monochromator, which operated with 1 mm wide slits to yield an instrument bandpass of about 1 nm. The collection optics provided a x2 magnified image of the target area at the entrance slit of the monochromator. The slit height of the monochromator was 10 mm, and therefore the field-of-view of the photomultiplier tube (PMT) was a slice through the plume 5 mm wide, 0.5 mm thick, parallel to and 5 mm in front of the target surface.

The geometry of the situation is shown schematically in Fig. 15, which presents a plan view of the target area of the ablation chamber. Reference to Fig. 15 shows that the PMT field-of-view was intersected by the dye laser beam, of 2 mm diameter, located at one of the three indicated positions.

The chromium resonance radiation was recorded at 425.44, 427.48, and 428.97 nm (only one wavelength at a time). The temporal behaviour of the 425 nm radiation as detected by the PMT is depicted in Fig. 16. The radiation of the other two wavelengths exhibited a similar time variation, and is not shown. The sudden increase in the spontaneous emission 3.5 μ s after the ablation event is due to the ISE pulse, which will be discussed later in this section. The ablation spot size was 7×10^{-2} cm² and the ablation laser irradiance was about 2×10^7 Wcm⁻². The general character of the line radiation as represented in Fig. 16 is consistent with the expansion into vacuum of an ionized wavefront as observed by Rumsby and Paul (1974). They measured the electron density profile (as a function of distance from the ablation point) at various points in time after the ablation event. The laser irradiance used by Rumsby and Paul was about 7×10^{14} Wcm⁻², which was applied to a carbon target; thus their results are not strictly applicable to the results obtained in this work, however they observed a thin shell of plasma expanding at a constant speed of about 10^7 cm sec⁻¹.

Reference to Fig. 16 shows a faint pulse of light at the beginning of the oscilloscope sweep. This pulse was found to be coincident with the arrival of the ablation laser pulse, however the slow decay of the initial pulse shown in Fig. 16 rules out scattered ablation laser light (which has a FWHM of only 20 ns). A probable explanation is scattered light from the intense emission arising from the small dense ablation plasma. The original colour photograph from which Fig. 6b was derived also showed an intense, white light source adjacent to the target. The large signal evident in Fig. 16 at approximately 500 ns after the ablation event is probably due to the arrival of the expanding plasma within the field of view of the photomultiplier tube (see Fig. 15). The photograph on which Fig. 6b is based also shows a halo of blue light centred roughly on the ablation spot.

The peak value of the line radiation at 427 nm (exclusive of the ISE) has been plotted against ablation laser power for two different focal spot sizes in Fig. 17. The straight lines are meant only to indicate the trend of the data. The spatial resolution of these data was poor because the region of observation was a slice through the plume (see Fig. 15), however, the data are useful in indicating two characteristics of the ablation event.

The first characteristic to note is the indication of reproducibility of the event on a shot-to-shot basis. This is significant in view of the fact that each ablation event involved the same region of the target surface. There was no provision in the ablation chamber for exposing a fresh target surface to the ablation laser at each shot. The second characteristic indicated is the existence of an ablation laser threshold power, unique for each focal spot size, below which no line radiation is observed. Such a threshold effect has been observed by others (e.g., Ready, 1971).

Using Fig. 16 as a reference, we can calculate roughly the number of atoms ablated in one shot by applying energy considerations. A significant number of atoms were present 5 mm from the target 0.5 μ s after ablation. The implied kinetic energy per chromium atom is therefore at least 27 eV (corresponding to a speed of 5 mm/0.5 μ s). If all the ablation laser energy of 30 mJ went into creating 27 eV chromium atoms, about 8×10^{15} would be ablated. For the 7×10^{-2} cm² spot size used, this would correspond to a layer of atoms 1×10^{-5} mm thick. Ablation of such a thin layer lends credence to the reproducibility of the ablation event described earlier.

Investigation of the effect of the ablation plume on the dye laser beam revealed two phenomena. The beam power appeared to be attenuated on passing through the plume, and the beam was no longer collimated. These effects varied with the time delay, being most pronounced at the shortest delays (around 1 μ s). The loss of collimation was undoubtedly due to self-focussing and/or defocussing of the beam as a result of refractive index changes caused by the dye laser beam. These changes result in nonlinear interactions between the beam and the plume (see, for example, Grischkowsky and Armstrong, 1972). In order to measure the drop in beam power, the beam was sampled with beamsplitters before and after traversing the ablation plume. The secondary beams thus derived were directed to two photodiodes fitted with diffusers. A lens was required to focus the divergent beam from the plume onto the diffuser of the second photodiode. To make the power measurement as insensitive as possible to the collimation characteristic of the beam, the lens was positioned such that the spot size on the diffuser did not vary significantly with beam divergence created in the plume. (The maximum divergence created by the interaction was estimated visually to be about 10°.) An oscilloscope photograph showing the attenuated beam and the reference beam without, then with the ablation plume, is presented as Fig. 18. Three separate traces are shown for the case of no plume in order to demonstrate that the two dye laser sensors tracked each other. Attenuation of about 65% is apparent at the quoted delay of 950 ns. This represents the maximum attenuation observed. Detuning the laser by ± 0.05 nm removed all interaction; and with the dye laser tuned to within 0.01 nm of the resonance line, attenuation was observed to decrease with increasing time delay - becoming unobservable at time delays greater than about 5 μ s.

In light of the observed on-line attenuation and the natural line width of the chromium resonance lines (about 10^{-5} nm), it is apparent that some line broadening mechanism must be at work (and a sufficient density must exist) to give an absorption line equivalent width that is comparable to the FWHM of the dye laser. The spread in the absorption frequencies due to the shift associated with the rapid plume expansion is one possible mechanism.

Consider Fig. 19, which shows schematically the geometry of the situation near the chromium target as seen from the side (i.e., at right angles to the dye laser beam), in a direction parallel to the surface of the target.

The dye laser beam passes vertically through the plume 1 μ s after the ablation event. A self-similar expansion of the outer part of the plume is assumed (Rumsby and Paul, 1974), and the outer shell of 27 eV atoms is represented by the arc in Fig. 19. At an elapsed time of 1 μ s the atoms have travelled 10 mm. The two parts of the shell intersected by the laser beam will contain atoms of speed $v \approx 10^6$ cm/sec whose components parallel to the beam will be $\pm \sqrt{3}/2 v$ respectively, with a total speed spread $\Delta v = \sqrt{3} v$. This would imply an absorption width of $\Delta\lambda \approx \lambda\Delta v/c$ which is 0.025 nm at a wavelength of 425 nm. This equals the laser 0.025 nm FWHM.

A lower bound on the density of chromium atoms in the dye laser beam can be estimated by assuming that each atom resonantly scatters one dye laser photon. The total number of photons delivered by the 3 kW, 4 ns pulse is about 2.6×10^{13} and the beam volume in common with the plume at 1 μ s delay is about 0.2 cm³. The implied chromium density is therefore about 1.3×10^{14} cm⁻³, which is consistent with the total number of atoms ablated as calculated earlier in this section.

An ISE signal was observed, superimposed on the line radiation, when the dye laser fired, as shown in Fig. 16. The indicated presence of ground state atoms is understandable in view of the observed line radiation, which itself is indicative of excited atoms decaying to the ground state. ISE signals were also observed when the ablation laser power density (15 mJ over 7×10^{-2} cm²) was low enough that no plasma line emission was detectable from the plume 5 mm away from the target. This indicates that laser ablation of atoms is not necessarily accompanied by extensive excitation or ionization of these atoms. Figure 20 represents the PMT signal for such an event. The two narrow positive pulses represent the ablation and dye lasers; the negative pulse is the ISE signal as detected by the PMT. The ISE signal in this case was time delayed in order to show all the pulses on a single trace without interference.

The shot-to-shot reproducibility of the ISE signal was poor, which contrasts sharply with that of the plasma self-emission as plotted in Fig. 17. There are several possible reasons for the poor reproducibility of the ISE signal. One explanation may be irreproducible fine structure in the density of the plume which will cause the density of laser-excited atoms to vary from shot to shot. The absorption of part of the ISE within the plume between the region of laser excitation and the collection optics will also vary between shots, in this case. Another explanation may be the shot-to-shot variability of the dye laser power, with a resultant variability in the degree of excitation of the atoms in the field of view. The real explanation is likely a combination of the two, which introduces a further complicating factor - a variation in the ability of the dye laser pulse to penetrate the plume to excite the atoms in the volume of observation.

A typical ISE signal has been plotted in Fig. 21 to show the time scales in more detail than is apparent from Fig. 20. The ablation laser was operating unattenuated and was delivering approximately 30 mJ pulses to the target. The ISE is characterized by a sudden turn-on (< 4 ns) and a much slower, apparently exponential, decay. The decay of the ISE is discussed in Section 4.3.

Evidence of collisional mixing between the resonance fine structure levels was obtained from observations of ISE arising at 427 nm when the dye laser was tuned to pump the 425 nm line. The rate of this collisional mixing can be appreciated by noting the slow rise of the ISE signal at 427 nm, see Fig. 22, as opposed to the relatively sudden onset of the ISE signal at 425 nm (see Fig. 21). The dye laser delay in the case of Fig. 22 was 1.1 μ s. No collisional mixing was observed at delays beyond 2 μ s, and no direct comparison of amplitudes at the two wavelengths was possible because only one line could be monitored at one time. A rough estimate of the relative amplitudes of the 425 nm ISE and the 427 nm ISE at 1.1 μ s delay yields a ratio of ten to one, based on alternately observing one, then the other, transition. This estimate is crude, however, due to the large shot-to-shot fluctuations of each ISE signal.

4.3 Decay of Intensified Spontaneous Emission (ISE)

The measurement of the decay of the ISE was conducted using the facility as described in Section 4.2 with the exception of the dye laser monitors. Both of them were removed, along with their associated beam splitters.

Figure 21 shows ISE at 427.48 nm recorded at 20 ns/cm in order to display in detail its decay characteristic. The signal is shot-noise limited and no accurate measure of its decay constant was attempted. The decay was assumed to be exponential based on Eqs. (2.4.3) and (2.4.4) and was therefore plotted in semi-log form. The decay constant was found by visually fitting a straight line to these data, and was repeated for other ISE signals obtained at the various time delays. A plot of decay constant versus delay time is shown in Fig. 23, where ablation laser irradiance was approximately 4×10^7 Wcm⁻² with a 20 ns, 60 mJ pulse. The natural lifetime indicated in Fig. 23 was obtained from a later experiment (see Chapter 5). The curve drawn through the data points is intended to show only the trend of the data. Dye laser beam position A (Fig. 15) was used throughout. With reference to Eq. (2.4.3), which is restated here in the context of the present experimental conditions,

$$\tau_{\text{DECAY}} = [N_e(K_{12} + K_{21}) + \gamma A_{21}]^{-1} \quad (4.3.0)$$

it is obvious from Fig. 23 that at early times, i.e., $t < 1.3 \mu$ s, collision quenching of the $z^7P_3^o$ level occurs due to a finite electron density N_e to yield $\tau_{\text{DECAY}} < \tau_{\text{RAD}} \equiv A_{21}^{-1}$. Quenching is less severe as $t \rightarrow 1.3 \mu$ s, where $\tau_{\text{DECAY}} \approx \tau_{\text{RAD}}$. For $t > 1.3 \mu$ s we obviously have radiation trapping where $\tau_{\text{DECAY}} = \tau_{\text{RAD}} \gamma^{-1}$.

It should be emphasized that the data of Fig. 23 were collected at a fixed point in space (i.e., 5 mm in front of the target) and were not a result of following the streaming motion of a small volume of the ablation plume. Therefore the observed change in decay time constant and the implied change in electron density with time may be due to recombination alone, however, electron density gradients carried past the field of view by the bulk motion (expansion) of the plume will also contribute if such gradients exist. In fact, the data of Rumsby and Paul (1974) show such gradients. Therefore care is required in interpreting the data of Fig. 23.

With the above qualification, we may speculate on the actual plume dynamics involved. Figure 23 seems to indicate continued recombination up to about 1.3

μsec where the decay time constant is approximately equal to the natural lifetime. In the region between about 1.3 μsec and the maximum of the curve at about 2.3 μsec two limiting interpretations are possible:

- (a) The electron density is close to zero at the start of the period and stays low, but the density of ground state atoms increases over the period with a concomitant increase in decay time of the pumped level due to radiation trapping.
- (b) The density of ground state atoms is high enough during the entire period to yield a decay constant of the upper level of at least 60 ns (due to radiation trapping) but the electron density is significant at the start of the period then decays to about zero during the period.

The real explanation is probably somewhere between these two limiting cases.

The large spread in the data, especially obvious in this region of the graph, is due to ablation laser power fluctuations and irreproducible fine structure in the ablation plume. The drop in the ISE decay time constant at successively longer delays beyond 2.3 μs is due to a general drop in chromium vapour density as the plume expands. The presence of radiation trapping may seem surprising considering the large Doppler spread (~ 0.025 nm) within the plume as compared to a natural linewidth of about 2×10^{-5} nm. In the plume expansion model which we are using, each atom recedes from its neighbours (much as the galaxies in an expanding universe), and natural line profiles of neighbouring atoms could be expected to be Doppler shifted enough that a photon emitted by one atom cannot be absorbed by a nearby neighbour. However, a simple order-of-magnitude calculation shows this concept to be incorrect. Using Milne's (1926) formula (2.1.3) for the escape factor, we can calculate by iteration the value of C , given that $\tau_{\text{OBSERVED}} \approx 50$ ns (at a time delay of 3 μs , for example) and $\tau_{\text{RADIATIVE}} \approx 32$ ns (see Chapter 5). By using (2.1.4) for C and by assuming a density of 10^{14} cm^{-3} and a cross-section of 10^{-12} cm^2 , we get a required slab thickness, l , of 5×10^{-4} cm to account for the observed radiation trapping. At a density of 10^{14} cm^{-3} , such a slab would contain 23 layers of evenly spaced atoms, and the Doppler shift of the natural line profiles between the two surfaces of this slab located at the centre of symmetry of the plume 5 mm from the target would be 1.6×10^{-5} nm compared with the natural FWHM of 2×10^{-5} nm. Radiation trapping is therefore possible under these conditions.

A few observations of the decay time constant of the ISE were carried out using dye laser beam positions B as shown in Fig. 15. The time delay was set to 950 ns and the decay time was observed to be 14 ns, which indicates a lower electron density than at beam position A at the same time delay. Qualitatively this agrees well with the observation of an expanding ionized wavefront by Rumsby and Paul (1974) if we assume that the dye laser beam at positions B has intercepted the leading edge of this front whereas position A was located inside the front at the 950 ns delay. This assumption is reasonable considering that locations B are further from the ablation spot than is location A.

4.4 Conclusions

The results of the preliminary experiments indicate that an ablation plume which is initially dense and at least partially ionized, recombines as it expands into vacuum. However, there exists an ablation laser intensity regime where

ablation takes place without ionization being observable 5 mm from the target surface. In either case, the plume density and dwell-time are sufficiently large to make possible selective excitation experiments using pulsed lasers of appropriate wavelength.

5. MEASUREMENT OF RADIATIVE LIFETIME OF THE CHROMIUM RESONANCE LEVELS

An experiment to measure the radiative lifetimes of the three resonance states $z^7P_4^0$, $z^7P_3^0$, $z^7P_2^0$, of chromium at 23499, 23386 and 23305 cm^{-1} above the ground state was undertaken with the LASES facility. The experiment served at once as a contribution to basic knowledge and as a test of three performance aspects of the facility:

- (1) feasibility of preparing a group of atoms in a state where the atoms are unperturbed by their environment such that Eq. (2.4.4) is valid;
- (2) feasibility of generating a sufficiently large intensified spontaneous emission (ISE) signal (from atoms in that state) in order that it be easily detectable;
- (3) feasibility of recording the signal with enough fidelity such that its characteristics can be reliably measured.

This experiment, using only the decay characteristic of the ISE, does not require a saturating laser pulse. The tunable dye laser is used simply to perturb the system of atoms by "momentarily"* raising some atoms to an excited state. Beyond generating a sufficiently large ISE signal to attain a good signal/noise ratio, the tuning, bandwidth, and irradiance of the dye laser, and the energy and irradiance of the ablation laser are not critical.

5.1 Experimental Conditions and Procedures

The experiment to measure the natural lifetimes of the three resonance levels of chromium was carried out using the experimental layout described in Chapter 3, except for one modification. The collection optics was contained within an aluminum tube that was suspended inside the vacuum chamber by means of a wall mount, see Fig. 24. The purpose of this tube was to reduce to a minimum the path length (through chromium vapour) of the photons emitted in the ISE pulse, and thereby reduce radiation trapping effects which were evident in the preliminary experiments. The modification reduced the photon path length through the plume from 135 mm to 2.5 mm.

The delay time between ablation and dye laser firing was set between 40 and 50 μs . This delay provided sufficient density of chromium atoms to yield reasonable signal-to-noise ratios of the ISE signal, and at the same time a low enough density to reduce radiation trapping effects to insignificant levels.

*"Momentarily" refers to a dye laser pulse which is short enough that the populations of other energy levels do not become perturbed appreciably during the laser pulse. In addition, the laser turn-off time should be sufficiently fast that it does not interfere with the intrinsic decay characteristic of the ISE pulse.

The central portion (selected by a 0.5 mm diameter aperture) of the collimated dye laser beam was directed through the plume in such a fashion that it passed through the mid-plane of the 1 mm wide field of view of the collection optics.

The dye laser, using carbostryl 165 in methanol, was successively tuned to the three resonance lines at 425.44, 427.48 and 428.97 nm with the aid of the Heath monochromator and a Fabry-Perot interferometer with a free spectral range of about 0.1 nm and a finesse of about 15 at 425 nm. The procedure used was as follows. The light from a hollow cathode chromium spectral lamp was prefiltered with the Heath monochromator to select the resonance line of interest, and then directed to the interferometer. A split-off portion of the dye laser beam was merged with the lamp light at the entrance slit of the monochromator to form a final split-field interferometric coaxial ring pattern of the two sources. In this way the dye laser was observed to have a spectral width of about 0.025 nm and was tuned to within 0.01 nm of the chromium line of interest.

The ISE from the plume-dye laser interaction passed through the Spex monochromator (using slits 2 mm wide to form a bandpass of about 2 nm, 10 mm high, and tuned to the dye laser wavelength) and was collected by the photocathode of the RCA C3103⁴ photomultiplier operating at 1500 V. The signal was displayed on the model 770⁴ oscilloscope using the 7A2⁴ vertical plug-in at 50 mV/cm. The oscilloscope was triggered by the signal from a photodiode that intercepted part of the dye laser beam and used a sweep of 10 ns/cm. Since at the time delays involved there was no background radiation from the plume, a zero signal reference baseline could be conveniently added to each intensified emission trace immediately before the ablation event by simply opening the oscilloscope camera shutter to record a single sweep generated by the dye laser, without firing the ablation laser.

The oscilloscope traces thus photographed were subsequently digitized with a Tektronix 4662 Interactive Plotter attached to a Tektronix 4051 Graphic Display System (with 8k of RAM) using a program developed for the purpose (see Appendix C). Thirty-one data points per photograph were digitized and transferred to the 4051 for storage on cassette tape. The data points spanned a 60 ns time interval in steps of 2 ns starting about 15 ns after the peak of the ISE pulse. The particular values of the above parameters were chosen after the following points were considered.

- (a) The memory capacity of the 4051 limited the number of data points to a maximum of 31.
- (b) The signal-to-noise ratio in the ISE precluded using data much beyond 75 ns past the ISE peak.
- (c) 15 ns was sufficient time to reduce the effects of ISE recording system response time to negligible levels. This finite system response time (6 ns-see Subsection 3.3.3) also made the use of digitization steps of less than 2 ns unattractive.

After the data were averaged (with equal weighting) over all photographs obtained for a given energy level, they were plotted by the 4051 Display System using a logarithm scale versus time. Parameters were calculated for a straight line which best fit these data in a least squares sense with each data point

having equal weight. The linear regression routine written into the 4051 worked on any connected subset of the set of 31 data points and the values of lifetimes finally adopted represent those subsets of data which produced the smallest standard deviations of the respective lifetimes. Details of the analysis programs and their operation appear in Appendix C; a listing appears in Fig. C2.

5.2 Results

A typical decay curve of the ISE at 425.44 nm from the $z^7P_4^0$ level is shown in Fig. 25. The noise in the signal is mainly shot noise due to the low photon flux. Fifty-five such photographs were averaged and plotted on a logarithm scale versus time. The result is Fig. 26 which shows in addition a straight line fitted to the data in a least-squares sense.

The hash marks appearing below the line indicate the range of the experimental data used in the fitting procedure. The standard deviation σ_τ was calculated according to $\sigma_\tau = \sigma_S S^{-2}$ where σ_S is the standard deviation of the slope and S is the regression coefficient representing the slope. Each datum point within the hash marks was given equal weight in the linear regression routine (Baird 1962). The calculated lifetime of the $z^7P_4^0$ level is 31.17 ± 0.07 ns.

The experimental decay curves for the populations of the $z^7P_3^0$ and $z^7P_2^0$ levels of chromium, averaged over 30 and 19 ablation events respectively, and plotted on a log scale are shown in Figs. 27 and 28. The hash marks again indicate the range of data which produced the lowest value for the standard deviation of the lifetimes; in these cases inclusion of all data points was required. The corresponding radiative lifetimes are 32.22 ± 0.17 ns and 31.42 ± 0.25 ns for the $z^7P_3^0$ and $z^7P_2^0$ levels, respectively.

The results are summarized in Table 2 along with those of previous workers. The agreement in all cases is well within estimated experimental uncertainties.

5.3 Error Analysis

A discussion of sources and sizes of experimental errors is particularly pertinent because these lifetime measurements involve a new technique. Accordingly, the error sources have been divided into two groups: those peculiar to the LASES technique, and those arising from the particular data reduction techniques employed. The output terminal of the photomultiplier tube is the natural dividing line between the two groups of errors. On the one hand, the experimental layout and the photomultiplier tube signal are unique for this type of measurement, while the data handling of this signal is conventional. In the following two subsections, the errors in the two groups are enumerated, and their sizes are estimated. A discussion of potential improvements is left to Section 5.4.

5.3.1 Experimental Errors Associated with LASES

Inspection of Fig. 25 shows one obvious source of error - noise in the recorded ISE signal. The major contributions to this noise are the photon arrival statistics and photoelectron emission statistics at the photocathode of the PMT (RCA Photomultiplier Manual). Also present is the noise generated

by the oscilloscope electronics and radio frequency interference (RFI) pick-up from the electrical discharge in the nitrogen laser channel. Unlike the first two noise sources, the latter two show up in the zero reference signal baseline as well as the ISE signal, making possible a comparison of the relative magnitudes of noise generated by these two groups of noise sources. Figure 25 shows the large amount of noise in the ISE signal as compared to that in the zero signal reference baseline. Clearly the statistical noise sources associated with the photons and the PMT photocathode dominate the other noise sources and therefore the oscilloscope noise and the RFI pick-up were not considered.

Although the photoelectron emission is Poisson distributed with the variance of the emission during any time interval equalling the mean of that emission, the output of the PMT is not in general Poisson distributed due to other statistical processes occurring at each dynode (RCA Photomultiplier Manual). Nevertheless, by assuming a Poisson distribution, we can calculate approximately the signal-to-noise ratio (SNR) to be expected at the ISE signal levels used in the experiment.

A system pulse response time of about 6 ns and an output current of 2 mA implies an average photoelectron emission rate of 156 per 6 ns when the PMT is operated at 1500 V with a gain of 4.8×10^5 . The corresponding SNR is 13. Thus the data such as presented in Fig. 25 fall into the shot-noise-limited regime. The effect of this noise was reduced by averaging over many such ablation events, and in the case of the $z^7P_4^0$ level, the standard deviation of the lifetime was only 0.07 ns. By using the t statistic with 30 degrees of freedom (Freund 1967) the 90% confidence limits were calculated to be ± 0.119 ns, and represent a probable upper bound on the uncertainty in the lifetime attributable to shot noise. The 90% confidence limits corresponding to the lifetimes of the $z^7P_3^0$ and $z^7P_2^0$ levels are ± 0.288 and ± 0.424 ns respectively.

A second source of error is the directed motion of excited atoms out of the field of view during the 60 ns data acquisition time. With reference to Fig. 29, which shows schematically the position of the dye laser beam relative to the field of view of the collection optics, it is obvious that atoms escaping sideways out of the field of view need a minimum speed of $0.25 \text{ mm}/75 \text{ ns} = 3 \times 10^5 \text{ cm/sec}$ directed away or towards the ablation point. The observations of Rumsby and Paul (1974) and the analysis of Zel'dovich and Raizer (1966) applied to the present situation indicate a maximum directed velocity away from the ablation point (at a 40 μsec delay time) of about $0.5 \text{ cm}/40 \mu\text{sec} = 1.3 \times 10^4 \text{ cm sec}^{-1}$, which is a factor of 30 below the required minimum. The only regions where a speed of $1.3 \times 10^4 \text{ cm sec}^{-1}$ could be significant would be at the top and bottom edges of the field of view of the collection optics as shown in Fig. 29. If the motion of the atoms could be considered as random, then no error would be introduced, but as noted earlier, some directed motion is involved. At the top and bottom edges, the atoms have a velocity component out of the field of view of approximately one half of their directed velocity. Thus at most an $8 \times 10^{-4} \text{ cm}$ thick slice of the column of atoms is lost to the collection optics during the 60 ns data acquisition time. This can reasonably accurately be expressed as a constant rate of $r = 2.6 \times 10^{-7} \text{ ns}^{-1}$ over the 60 ns. When compared with the natural transition probability of 0.031 ns^{-1} for the resonance levels of chromium, this is seen to introduce an error of less than $10^{-3}\%$ in the calculated lifetime. This source of error can be dismissed.

A third source of error is the general response characteristic of the photomultiplier tube (PMT), including its transient response and linearity. As a result of the calibration of the PMT C31034 described in Subsection 3.3.3, a PMT-oscilloscope risetime of 6 ns was assigned because it was difficult to accurately separate the responses of the PMT and oscilloscope since the oscilloscope was the only means of displaying the output of the PMT. The effects of the risetime of the PMT-'scope combination can be (and have been) avoided by simply waiting for the turn-on transient of the ISE to disappear before beginning data acquisition. The data presented in Figs. 26, 27 and 28 were acquired starting 15 ns after the indicated peak of the intensified emission curve. Under these circumstances, it is safe to assume that errors introduced as a result of PMT-oscilloscope risetime are insignificant.

The nonlinearity of the C31034 PMT response was difficult to quantify, but as indicated in Subsection 3.3.3, the nonlinearity was assumed to be characterized by a maximum deviation of 1% from linear response using signal levels comparable to those of the lifetime measurements. The effect on calculated lifetime of a nonlinearity in the PMT depends on the form which the nonlinearity takes, however; in order to establish roughly the magnitude of this effect, consider a nonlinear PMT output of the form

$$Y_R(t) = Y_{TH}(t) - \gamma Y_{TH}^2(t)/Y_{TH}(0) \quad (5.3.1.0)$$

where $Y_R(t)$ is the real output of the PMT, $Y_{TH}(t)$ is the theoretical output assuming a linear relation between photon flux at the photocathode and PMT output, γ is a measure of the degree of nonlinearity (a dimensionless constant), $Y_{TH}(0)$ is the theoretical output at $t = 0$, where the time coordinate of the first data point has been defined as equal to zero, and the effects of PMT risetime and noise have been neglected. The particular form (5.3.1.0) of $Y_R(t)$ was chosen because it represents approximately the type of departure from linearity due to space charge limiting effects (RCA Photomultiplier Manual) when these effects are small. The quadratic term in (5.3.1.0) has been normalized such that $\gamma \times 100$ represents the percentage (of the theoretical output) by which the real output falls short at the first data point in the digitized photograph. On the basis of the PMT calibration, γ was set at 0.01, and theoretical data were analysed for lifetime before, and after introducing the nonlinear response. In the case of noise-free data with $\tau_{TH} = 32.00 \pm 0.00$ ns, the inclusion of the nonlinearity resulted in $\tau_R = 32.14 \pm 0.00$ ns and in the case of noisy data with $\tau_{TH} = 32.22 \pm 0.15$ ns, the nonlinearity resulted in $\tau_R = 32.36 \pm 0.15$ ns. An increase in calculated lifetime of about 0.14 ns with no concomitant increase in standard deviation is observed in each case. Thus the standard deviation cannot be used as a reliable indicator of the size of this error, but based on the change in calculated lifetime noted above, an uncertainty of 0.5% due to PMT nonlinearity was adopted.

A fourth source of error inherent in the LASES technique is the "trapping" of the ISE radiation from the laser-excited atoms by repeated absorption and re-emission of the original ISE radiation. Formulae are available for calculating the effect of radiation trapping on observed lifetime, however, these formulae incorporate simplifying assumptions about the line broadening mechanisms, the geometry of the situation, and density distribution of absorbing atoms (Holstein 1947 and 1951; Milne 1926). Because of these simplifications and because the density and line-broadening mechanisms are not known in the

present experiment, these formulae are of limited use in calculating the "radiation escape" factor. A technique was therefore devised which utilized only the functional form of the escape factor, i.e., the variation of escape factor with slab thickness [see Eqs. (2.1.3), (2.1.4)]. The lifetime observed with the aluminum tube in place (Section 5.1 and Fig. 24) was compared with the observed lifetime with the tube removed, with a resultant factor of 54 increase in the photon path length between the region of laser excitation and the collection optics. The observed lifetimes of the three energy states were an average 11% longer with the tube removed. Since the ablation laser power and energy were approximately the same in the two sets of measurements (to within a factor of two), equal densities can be assumed for the two cases, and by using Eq. (2.1.3) for the Milne escape factor, it can be shown that the observed increase in lifetime is consistent with the increase in photon path length only if the original escape factor is 0.9980. This means the observed lifetimes are 0.2% too long. The removal of the aluminum tube from the chamber undoubtedly changed the character of the plume expansion, allowing the plume to disperse quicker and resulting in a lower density of atoms at comparable ablation laser powers and time delays. If the resultant drop in density is a factor of 2, for example, then the original escape factor would have had to be 0.9960. A factor of two change in density between the two cases is probably a maximum, and the maximum error assigned to this source has been set at 0.4%.

A fifth source of experimental error connected with the LASES technique is the distortion of the ISE signal due to its convolution with the laser pulse. This would be expected to be particularly so under laser saturation conditions. The ISE decay would in general have to be carefully deconvoluted from the laser pulse, especially if the fall time of the laser is comparable to the decay time of the excited energy level (Shaver and Love 1975). In the case of the chromium levels under consideration, the decay time is at least 10 times longer than the laser fall time, so that this problem is not important. Furthermore, the 15 ns delay between the ISE peak and the start of data acquisition further ensures a convolution-free ISE decay measurement.

5.3.2 Experimental Errors in Data Reduction

The errors introduced in the data reduction can be grouped under three broad categories: errors in the oscilloscope-camera system; errors in digitizing the oscilloscope photographs; and errors introduced by the mathematical procedure to calculate the lifetimes.

Errors in the oscilloscope-camera system arise from three sources. The first source is the error in position of the graticule lines on the face of the CRT. The second source is the error in the camera imaging system which introduced nonlinearities in the image of the graticule and trace, and the third source is the nonlinear electron beam deflection in the cathode ray tube.

Errors introduced by the graticule inaccuracies can be safely neglected as they were found to be one tenth those of the second source (i.e., the imaging system, whose errors are meant to include distortion of the photographic paper after the image has been deposited).

Errors in the imaging system can be further subdivided according to vertical (i.e., signal) and horizontal (time) errors. The vertical errors

were evaluated by measuring the nonlinearity in the vertical displacements of the graticule lines, which was found to be approximately of the form

$$Y_i = iY_2[1 - \eta \sin(Y_i \pi/2Y_5)]$$

where Y_i is the distance from the first graticule line (one cm above the bottom of the graticule) to the i^{th} line, and $\eta = 0.01$. This information was combined with the vertical deflection data of the oscilloscope and analysed for its effect on calculated lifetimes in a manner similar to the analysis of the PMT nonlinearity. The error was found to be 1%.

The horizontal (time) errors were partially compensated for by the design of the digitization program (see Appendix C).

Errors in digitizing the photographs can be grouped into two categories: those involved in incorrectly positioning the cursor, and those due to the finite resolution of the electronic position resolvers in the 4662 Plotter. The errors in both categories apply to both the signal trace and the "zero signal" baseline. Consideration of the spatial resolution of the 4662 Plotter as given by Tektronix, and the physical size of the oscilloscope photograph leads to an estimate of ± 0.13 ns for the maximum error (due to finite spatial resolution) in the time coordinate, and to $\pm 0.3\%$ to $\pm 2\%$ of the signal, depending on signal size. These errors are small when compared to the shot noise content of any given photograph, and are random; therefore they would be reduced by the averaging process and would in any case be reflected in the standard deviation figure calculated with the lifetime. Therefore these errors need not be considered further.

During data point entry, the horizontal position of the cursor is not critical and no error ensues from "incorrect" horizontal positioning because the digitization program records the actual horizontal position - not some target value (see Appendix C for details). However, for the given horizontal position there will in general be a vertical cursor position error. Tests showed this error to be random and much smaller than the noise in the signal, thus it too would show up in the standard deviation of the lifetime and need not be considered further.

Some error is introduced into the calculated lifetime by the mathematical procedure of fitting a straight line to the semi-log data (as, for example, those shown in Figs. 26, 27 and 28) in a least squares sense, whenever there is noise in the data. An error shows up as a negative bias in the lifetime estimate and arises from the singularity of the logarithm function at zero. This tends to emphasize data points smaller than the average, especially in the tail of the decay curve, where the shot noise is worst. Sterlinski (1967) has analysed this problem for radioactive decay data containing a "background" contribution which cannot be accurately subtracted from the data. His data, which consist of counts in a number of channels (time windows) are assumed to be uncorrelated between channels (except to the extent that they are part of the same decay curve). In addition the count c_i in each channel i is assumed to be a random sample from a Poisson distribution with mean and variance of c_i . Even though the data of Figs. 26, 27 and 28 do not conform exactly to the above stated assumptions, it is worth noting that Sterlinski

(1967) calculates a typical bias of less than 0.1% in the lifetime calculation, depending on the size of the background count. A crude extrapolation to the conditions of the lifetime measurements presented in this work would indicate a bias which is at least one order of magnitude smaller, and therefore this source of error can be safely ignored.

Note that the establishment of an accurate zero signal reference baseline as discussed in Section 5.1 is somewhat analogous to the accurate subtraction of a background count as considered by Sterlinski (1967). The high accuracy achieved by the technique as outlined in Section 5.1 is attested to by the linearity of the log plots (Figs. 26, 27 and 28) near the tail of the curves.

By combining the errors discussed in Subsections 5.3.1 and 5.3.2, an estimate of the total experimental uncertainty can be made. The contribution of PMT nonlinearity and radiation trapping are 0.5 and 0.4% respectively. The 'scope-camera contributions are 0.5 and 1% respectively, due to horizontal and vertical distortions. The sum, 2.4%, is added to the contribution due to noise in the signal, i.e., 0.12, 0.29, and 0.43 ns, to give a final result of 31.17 ± 0.87 , 32.22 ± 1.06 , 31.42 ± 1.18 ns for the lifetimes of the $z^7P_4^0$, $z^7P_3^0$, and $z^7P_2^0$ levels in chromium.

5.4 Discussion

The combination of laser ablation and selective excitation spectroscopy (LASES) has been shown to represent a new approach in the measurement of basic atomic parameters. Our LASES facility has demonstrated its capability of generating a reasonably large, noise-free ISE signal from atoms in vapour form. This has resulted in the ability to accurately measure the lifetime of resonance energy levels of a refractory metal (chromium in this case) by selective laser excitation.

The LASES technique is inherently simpler than the beam-foil, atomic beam-dye laser, and absolute absorption techniques in sample preparation. It is inherently more accurate than the beam-foil method because the latter requires cascade corrections. The data acquisition rate of an optimized LASES technique (see discussion below) may be superior to that of the atomic beam-dye laser technique because the low density of atomic beams requires that photon counting be used.

The results of our lifetime experiment, along with those of other workers using different techniques, are shown in Table 2. The results themselves, as well as the associated experimental uncertainties, compare favourably with those of the other techniques, even though little attempt was made to maximize the accuracy of the results as would be the case if a LASES facility were to be dedicated to measuring excited state lifetimes. A brief discussion of some improvements along this line is warranted.

The largest single source of error is the shot noise in the ISE signal. This noise can be reduced to arbitrarily low levels by averaging the data over a sufficiently large number of events. However, the time involved becomes prohibitive and a better approach is to reduce the noise in the original signal. This can be accomplished by increasing the photon flux at the photocathode of the PMT and/or increasing the photocathode quantum efficiency. The largest improvement comes from increasing the photon flux because the quantum

efficiency is already quite high (19%) in the present PMT. The photon flux cannot be materially improved by increasing the atom density, nor the depth of the volume under observation, because radiation trapping then becomes a problem if the lower of the laser coupled levels is appreciably populated. The cross-sectional area of the volume could be increased but a limit is set by the size of the PMT photocathode, and also by the radiation trapping restriction, particularly if a fast collection lens is used. If a stepwise excitation technique with two lasers is employed (for example, Marek 1975) or if two photon excitation is employed (for example, Cagnac 1975) to excite a high lying energy level not optically connected to the ground state, then radiation trapping can be expected to be less severe.

The photon flux can be improved by ensuring that the ISE detection system has a broad enough bandwidth to cover all the wavelengths at which radiative decay from the laser-pumped level occurs. Care must always be exercised to provide enough spectral discrimination in order that the PMT not become overloaded by scattered light from the ablation laser; hysteresis effects may then be important (Yamashita 1978). Perhaps gating of the PMT will also be required (see, for example, Jameson and Martin 1975, and Martini and Wacks 1967). In the present experiment, only one decay mode was possible so that spectral bandwidth considerations were of minor importance.

An improvement in the efficiency of the collection optics will increase the photon flux at the PMT photocathode. The optical system used in the present experiment was approximately $f/7$ with a collection efficiency of just over 0.1%. With a fast lens-mirror combination, the efficiency could be pushed to about 20% (She, Fairbank, and Billman 1978), and 60% has been achieved using an ellipsoidal collector (Kaufman, Greenless, Lewis, Tonn, Broadhurst, and Clark 1977). This factor alone would increase the single shot signal-to-shot-noise ratio by a factor of almost 25! No improvement in photon flux accrues from increasing dye laser intensity since the transition is already saturated at the power levels used in the present experiment.

Other improvements that could be made in a LASES facility devoted to lifetime measurements are in the ISE signal recording apparatus. The distortions produced by the oscilloscope-camera system were significant. These could be reduced by using better cameras or by doing away with the 'scope-camera combination altogether and replacing it with a multi-channel transient digitizer. Use of a transient digitizer would at the same time eliminate the reading errors in the presently employed method of manual digitization of the ISE decay trace. A further benefit of the use of a transient digitizer is the much shorter risetimes which are possible with such devices, as compared with real-time oscilloscopes. If such devices were to be used in conjunction with shorter dye laser pulses (as from mode-locked lasers), then the measurement of much shorter natural lifetimes would be possible without the necessity of complicated deconvolutions.

The method of calculation of the lifetime could be improved; however, the improvement possible decreases as the noise in the signal decreases. Robinson (1970) has considered the effect of weighting the individual data points, before applying them to a curve-fitting procedure, as applied to half-life measurements of nuclear decay processes. In addition he has found improved accuracy by fitting an exponential curve to the original data rather than fitting a straight line to the logarithms of the data. Because Robinson

(1970) used unequal weighting of the data points, his results are not easily extrapolated to the conditions of our lifetime experiment, but it becomes obvious that further theoretical work in this area may be fruitful.

6. SELECTIVE EXCITATION SPECTROSCOPY EXPERIMENT INVOLVING TWO TRANSITIONS

An experiment was undertaken to test the behaviour of the ISE signal peak under conditions which, according to the considerations presented in Section 2.3, correspond to laser saturation of two transitions. This was done in order to ascertain whether in plasma diagnostics the benefits of laser saturation [exploitation of (2.3.12)] can be realized. Specifically, an experiment was conducted wherein two separate transitions were simultaneously "saturation pumped" by two separate dye lasers. The two ISE signal peaks were recorded and their ratio was evaluated as a function of delay time between the ablation event and the dye laser firings. According to the arguments of Section 2.3, laser saturation of the respective transitions leads to a simple relation between the ratio of the ISE signal peaks and the ratio of the relevant population densities.

Therefore the practical feasibility of plasma diagnostics using laser saturation pumping was investigated in two steps:

1. The ratio of the ISE signal peaks was checked for shot-to-shot consistency at various delay times, since a lack of consistency can be interpreted as a lack of laser saturation.
2. The simple relationship between population density and ISE signal peak (assuming laser saturation) was applied in order to evaluate the ratio of the relevant population densities. The consistency of this population ratio with other observations of the ablation plume was then investigated.

6.1 Experimental Layout and Procedure

The experimental layout used to measure the ratios of two different ISE signals from the ablation plume was similar to the general arrangement which is described in Chapter 3, and which appears in schematic form in Fig. 5. Both tunable dye lasers (see Fig. 5b) were pumped by the same nitrogen laser; one half of the 2 cm wide nitrogen laser beam was deflected by a metallic front-surface mirror to the second dye laser (dye laser No. 2, Subsection 3.1.4) while the other half of the nitrogen laser beam travelled unimpeded to the first dye laser (Subsection 3.1.3). By pumping both dye lasers with the same nitrogen laser, time synchronization of the two dye laser pulses was automatically assured.

Dye laser No. 1, using carbostryl 165 in methanol, had a bandwidth of 0.02 nm (30 GHz) and was tuned to within 0.01 nm of the 428.97 nm resonance transition, which connects the a^7S_3 ground state of chromium to the $z^7P_2^0$ resonance state. Dye laser No. 2 used coumain 120 in methanol, had a bandwidth of 0.015 nm (22 GHz), and was tuned to within 0.005 nm of the 449.69 nm line which connects the a^5S_2 metastable state to the $y^5P_3^0$ excited state.

A schematic of the relevant transitions and chromium energy levels appears as Fig. 30. In this figure, the solid arrows represent the transitions suffering a population redistribution induced by the two dye lasers,

and the broken arrows represent the most important radiative decay modes from the laser-pumped levels.

The four-armed glass cross previously used as the ablation chamber was replaced by a six-armed glass cross in order to accommodate the second dye laser beam. Figure 31 shows a photograph of the new chamber and Fig. 32 shows a close-up view of the target area. The two dye laser beams were sent coaxially and horizontally through the chamber in opposite directions, passing 20 mm above the horizontal target surface and 2 mm in front of the collection optics window.

Before entering the vacuum chamber, the 449.69 nm laser pulse was collimated and the central portion selected by a 2 mm diameter aperture. The estimated irradiance of the pulse was $6 \times 10^4 \text{ Wcm}^{-2}$ which corresponds to a spectral irradiance of $3 \times 10^{-6} \text{ Wcm}^{-2} \text{ Hz}^{-1}$. The collimated 428.97 nm laser pulse was reflected by two mirrors to generate a 20 ns propagation delay; subsequently it was trimmed by a 2 mm aperture, then focussed to 0.2 mm within the plume by a 500 mm focal length lens. The time delay was required in order to display separately the peaks of the two ISE signals with the single sweep of the single beam 7704 oscilloscope. This was the only oscilloscope available with the required risetime and writing speed. The 428.97 nm laser pulse was focussed to a small diameter within the plume in order to keep the two ISE signals at comparable amplitudes on the oscilloscope screen; since the 428.97 nm pulse pumped from the ground state and since the ground state was much more heavily populated than the metastable a^3S_2 state, the ISE produced by the 428.97 nm pulse was much more intense than that produced by the 449.69 nm pulse. The resultant laser irradiance in the plume was $6 \times 10^6 \text{ Wcm}^{-2}$ and the spectral irradiance was $2 \times 10^{-4} \text{ Wcm}^{-2} \text{ Hz}^{-1}$. For the same reason, the time delay was inserted in the 428.97 nm laser pulse (as opposed to the 449.69 nm pulse) in order to prevent the resultant population redistribution from appreciably changing the metastable state population (through radiative decay on the 636.29 nm line) before that state could be probed by the 449.69 nm laser pulse.

The ablation laser beam was directed vertically onto the horizontal target by a total-internal-reflection prism after passing through a focussing lens of 400 mm focal length. Spot size on target was about 1 mm in diameter, and ablation laser pulses had an energy of about 40 mJ and a duration of 20 ns. The peak ablation irradiance was $6 \times 10^7 \text{ Wcm}^{-2}$.

The collection optics (f/1.1) of Fig. 5b is described mathematically in Appendix D. This relatively fast optical system was necessitated by the weak ISE signal which resulted from laser-pumping the a^3S_2 metastable state. In order to provide the system with enough spectral bandwidth to cover all ISE lines (except for uv lines) from the plume, the monochromator had to be removed. This in turn removed the restriction on the speed of the optical system, allowing for much faster optics. The collection optics did, however, contain one blocking filter to reduce, by a factor of about 50, the sensitivity of the PMT to the scattered ablation laser light at 694.3 nm. The detection PMT (RCA C70042K) was run between 1400 V and 1700 V depending on the size of the ISE signal.

6.2 Experimental Results

Figure 33 shows a typical composite ISE signal from the two chromium lines at 449.69 and 428.97 nm respectively. The small 449.69 nm ISE pulse appears about 20 ns before the larger 428.97 nm ISE signal due to the optical delay built into the path of the latter dye laser beam. The effect of the improved collection optics in reducing shot noise is apparent when this photograph is compared to that of Fig. 21, which shows a typical ISE signal used in the lifetime determinations.

The ISE signal represented in Fig. 33 shows no signs of coherency effects. One such effect is a Rabi oscillation (e.g., McIlrath and Carlsten 1972) during periods of intense laser pumping; its frequency is in the gigahertz range and well beyond the capabilities of the collection optics system and associated instrumentation. Other coherency effects arise from various mechanisms which generate quantum beats (Haroche 1976) in the decay of the ISE signal. These effects are likewise unobservable in the present experiment (or in the lifetime experiments reported in Chapter 6) because the combination of conditions required to make them observable have not been met (e.g., Haroche 1976; Corney 1977).

The peaks of the ISE signals at the two wavelengths are plotted as a function of delay time (after ablation) in Fig. 34 for 28 ablation events. The vertical scale represents deflection of the trace in mm, normalized to a constant PMT voltage of 1400 V and a constant vertical deflection factor of 100 mV cm^{-1} . The data points without error bars (one standard deviation) are single measurements, i.e., results of single ablation events. There is considerable scatter in the data due to ablation laser power fluctuations and irreproducible fine structure in the plume. In addition, multiple pulsing of the ablation laser may have occurred. Multiple pulsing had been observed on occasions previous to this experiment, but the necessary monitoring equipment was not in place during this experiment. The ablation laser peak power as recorded on the transient digitizer is shown in Fig. 35. The power figures are grouped according to delay time, with the resultant average and standard deviation plotted in a manner which allows easy comparison of the ISE peak signal averages and standard deviations (Fig. 34) with those of the corresponding ablation laser peak power at any given time delay. In an effort to reduce the scatter of the ISE data of Fig. 34, normalized graphs of these ISE data were prepared (normalized with respect to ablation laser peak power) but no improvement was found with respect to scatter. Note that both ISE signals are small at short delay times, maximum at approximately 3 μs , and then tend to small values at longer delay times.

Figure 36 shows a graph of the ratios of the ISE peaks plotted separately in Fig. 34. The error bars (one standard deviation) are smaller on a percentage basis than those of either ISE signal individually or the ablation laser peak power. This obviously implies a strong correlation between the two ISE signals during any given ablation event. The trend of the ratio is from relatively large values at short delays to a smaller but non-zero value at long delay times.

The decay time constant of the combined ISE signals is shown in Fig. 37 as a function of delay time. The natural lifetime of the $z^7\text{P}_2^0$ state (from which most of the observed transitions occur due to the large number of originally

ground state atoms) is indicated by a horizontal line at the top of the graph. The decay constant of the combined ISE signal was derived in a manner entirely analogous to that described in Chapter 5, except that the output display in this case is linear instead of logarithmic. A digitized output with the fitted exponential curve is shown in Fig. 38. This is the same ablation event whose ISE curve is shown in Fig. 33. Note that a single exponential describes the decay very well for the first twenty nanoseconds after the peak. The decay constant of only 11 ISE signals could be calculated because the other 17 were not recorded at a sufficiently fast sweep on the oscilloscope. Nevertheless, the data indicate that a combination of electron collision quenching, and bulk motion of the atoms out of the field of view, reduced the ISE decay time constant.

6.3 Population Ratio Calculation

Given the observed ISE signal peak ratio, we can calculate the ratio $N_M(t_0)/N_G(t_0)$ where $N_M(t_0)$ is the population (cm^{-3}) of the a^5S_2 metastable state and $N_G(t_0)$ is the population (cm^{-3}) of the a^7S_3 ground state - both values referring to the time t_0 just prior to laser excitation. Figure 30 shows the relevant energy states and transitions in chromium. The lines indicate the laser-induced transitions; the other arrows indicate the prominent allowed transitions from the y^5P_2 and z^7P_2 excited states. The calculation of the ratio $N_M(t_0)/N_G(t_0)$ proceeds in two steps: (a) we relate the populations $N_M(t_0)$ and $N_G(t_0)$ to the populations $N_M(t_p)$ and $N_G(t_p)$ existent at the time t_p when the ISE signals are at their peak (we disregard the 20 ns time difference between the two dye laser pulses and we disregard the effects of dye laser and collection system risetime), and (b) we relate the ratios of the peaks of the ISE signals $S_M(t_p)$ and $S_G(t_p)$ to the ratios of these two populations.

Step (a) is possible by using appropriate values for spectral irradiance, linewidth, duration and risetime of the dye laser pulses. The spectral irradiances of the two laser beams has already been calculated to be 3×10^{-6} and $2 \times 10^{-4} \text{ W cm}^{-2} \text{ Hz}^{-1}$ respectively for the 449 and 429 nm wavelengths based on the measured laser intensities and linewidths. The "saturated spectral irradiance" for the two transitions can be calculated using Eq. (2.3.18) repeated here for convenience:

$$I_{SO} = \frac{8\pi h\nu^3}{(1+g)c^2} \frac{A_c}{A_{\text{radiative}}} \quad (6.3.0)$$

but first the ratio A_c/A_{rad} must be estimated for both transitions. A_{rad} is the transition probability for radiative decay from the upper to the lower of the laser coupled levels and A_c is the total transition probability for all processes of decay from the upper level.

For the case of the z^7P_2 resonance state the determination of the A_c/A_{rad} ratio is fairly straightforward. The decay of the combined ISE signal after laser turn-off is due mainly to the decay of the z^7P_2 state, whose main components are radiative decay to the ground state and collision-induced decay to all lower states including the ground state. Thus the ratio $A_{\text{rad}}/A_{\text{decay}}$ represents the upper bound of the ratio A_c/A_{rad} . Using the decay time plotted in Fig. 37, we estimate this ratio to be a maximum of 1.5. Thus,

$$I_{SO}(429) = \frac{8\pi h\nu^3 1.5}{c^2 12/7} = 1 \times 10^{-8} \text{ W cm}^{-2} \text{ Hz}^{-1}$$

For the case of the y^5P_3 state, five radiative decay modes are possible with the 449 nm transition having a branching ratio of only 0.23 (Corliss and Bozman 1962). We can account for the branching ratio approximately by multiplying the A_c/A_{rad} ratio calculated above by 4. Thus,

$$I_{SO}(449) = \frac{8\pi h\nu^3 6}{c^2 12/5} = 1 \times 10^{-8} \text{ W cm}^{-2} \text{ Hz}^{-1}$$

where we have in addition assumed that A_c associated with this level is approximately equal to A_c for the z^7P_2 level, and that the radiative lifetime of the y^5P_3 level is approximately equal to that of the z^7P_2 level (Corliss and Bozman 1962). We see that

$$I_v^l/I_{SO} = 2 \times 10^4 @ 429 \text{ nm} \quad (6.3.1)$$

and

$$I_v^l/I_{SO} = 3 \times 10^2 @ 449 \text{ nm} \quad (6.3.2)$$

Whether or not the lasers actually saturate the transitions depends on them having sufficient linewidth to cover the atomic absorption features. However, this has already been shown to be the case; indeed, the calculation of spectral irradiance was based on a measured laser linewidth so broad that the spectral irradiance could be assumed constant over the absorption line profile.

The question of laser saturation of the respective transitions in the region of observation depends in addition on the laser pulse lengths. By reference to curve C of Fig. 2, it becomes clear that the laser pulse must last long enough that the peak value of curve C can be attained. Furthermore, the laser pulses must contain enough energy (or photons) to saturate the transition after suffering attenuation in passing through the ablation plume. In the frequency interval corresponding to that of the natural absorption line width for each transition (30 MHz), both laser pulses contain about 2×10^{10} photons (on the assumption of 8 μ j pulses 30 GHz wide). This compares with 2×10^7 excited atoms (i.e., $z^7P_2^0$ state) in the field of view as calculated from the size of the ISE signal; such a calculation assumes a 4 mA signal, a tube gain of 2×10^4 and a quantum efficiency of 4%, a collection efficiency of 0.054, and a radiative transition probability of $3.1 \times 10^7 \text{ sec}^{-1}$.

A calculation of the beam attenuation would have to take into account the number of atoms in the beam before the light reaches the region of observation. For the 428.97 nm laser pulse which pumps the $z^7P_2^0$ state, such a number can be calculated approximately by extrapolating the number of atoms in the field of view (which is a segment of a column defined by the laser beam) to a column length which equals the radius of the plume. The segment of the column of atoms seen by the collection optics was about 0.4 mm long (which contained

about 2×10^7 excited atoms), and extrapolating this number of atoms to a column 10 cm long (the worst case) would imply that about 5×10^8 atoms are excited in the laser beam before the beam reaches the collection optics' viewport. This is an insignificant number when compared with the number of laser photons contained within the natural absorption profile of the transition (3×10^{10}). Thus it becomes apparent that even without relying on arguments concerning stimulated emission, and Doppler shifts of absorption line profiles due to bulk motion (expansion) of the plume (see Section 4.2), attenuation of the dye laser pulse can be neglected when considering laser irradiance in the region of observation. In fact, the laser saturation condition has been verified experimentally by Kwong (1979) in a related experiment using the same apparatus as described in this thesis.

The same argument about laser penetration at 449.69 nm can be made a posteriori for the second dye laser. The absorbing volume is 100 times larger for this pulse, but the relevant population density turns out to be about 1000 times smaller.

The laser spectral irradiances are thus sufficiently high in both cases (in the region of observation) that the saturation conditions are satisfied. From (6.3.1) and (6.3.2) it follows that the laser pumping times are in the subnanosecond range, and the laser pulse lengths of 4 ns are sufficiently long that the aforementioned peak of curve C of Fig. 2 can be attained.

With these indications of saturation, we can use (2.3.9) and (2.3.10), which can be combined to yield Eq. (2.3.12) for the population $N_M^L(t_p)$ of the $5P_3^0$ state which is laser-coupled to the a^5S_2 metastable state:

$$N_M^L(t_p) = \frac{7}{12} N_M(t_0) = \frac{7}{5} N_M(t_p) \quad (6.3.3)$$

and similarly for $N_G^L(t_p)$:

$$N_G^L(t_p) = \frac{5}{12} N_G(t_0) = \frac{5}{7} N_G(t_p) \quad (6.3.4)$$

where we use the assumptions $N_M^L(t_0) \ll N_M(t_0)$ and $N_G^L(t_0) \ll N_G(t_0)$ respectively, and t_0 and t_p refer to times prior to laser turn-on and at the time of ISE peak, respectively. The above assumptions are certainly justified if no line radiation is observable before laser turn-on (i.e., no background radiation); this is the case for time delays greater than about 4 μ s. However, even at the short delay times (for example, the ISE in Fig. 33) of 2.3 μ s, the background can be considered insignificant when account is taken of the much larger plume volume which contributes to this radiation, as compared to the relatively small volume responsible for the ISE, i.e., the so called "volume dilution effect" (Measures, 1968).

In both equations (6.3.3) and (6.3.4) we have assumed that the laser risetime is fast enough that condition (2.3.10) holds, i.e., that negligible loss of population from the two systems of laser-coupled levels occurs before the peaks of the ISE signals occur. This assumption is justified by the relatively slow decays of the ISE signals as compared to the risetimes of these signals.

We continue the calculation of the ratio of populations by considering step (b), which requires finding a relationship between the excited state populations $N_M^L(t_p)$ and $N_G^L(t_p)$ and the ISE signal peaks. In general, the output of a photomultiplier tube (considering a given load resistor) can be written

$$S_j = N_j V_j \left(\sum_i U_i Q_i A_{ji} \right) \quad (6.3.5)$$

where S_j is the signal (mV) due to the laser-excited number density N_j (cm^{-3}) in the region of observation,

V_j is the effective volume (cm^3) under observation and represents a convolution of the excitation volume and the absolute collection efficiency of the optical system,

U_i is the branching ratio of transition $j \rightarrow i$,

Q_i is a number representing the product of the quantum efficiency of the PMT at wavelength λ_{ji} and the gain of the tube (mV/photon),

and A_{ji} is the Einstein transition probability (photons/sec).

The sum over i assumes that the signal S_j arises from emission on several lines.

By writing Eq. (6.3.5) for both populations of interest and taking the ratio, we get

$$\frac{N_M^L(t_p)}{N_G^L(t_p)} = \frac{S_M^L V_G}{S_G^L V_M} \frac{Q_G^L A_G^L}{\sum_i U_i Q_{Mi}^L A_{Mi}^L} \quad (6.3.6)$$

where the symbols are self explanatory and we have used the fact that only one decay mode is available to N_G^L . Equation (6.3.6) can be rewritten to define the initial populations in the metastable and ground states:

$$\frac{N_M(t_o)}{N_G(t_o)} = \frac{5}{7} \frac{S_M^L V_G}{S_G^L V_M} \frac{Q_G^L A_G^L}{\sum_i U_i^L Q_{Mi}^L A_{Mi}^L} \quad (6.3.7)$$

In order to find the conversion factor between the ordinates of the ISE ratio plot (Fig. 36) and the ratio of populations $N_M(t_o)/N_G(t_o)$, we evaluate the RHS OF (6.3.7) with $S_M^L/S_G^L = 1$. V_G/V_M has been evaluated for the geometry of this experiment by using a ray tracing technique, and found to be 0.023 (see Appendix D). The remaining factor was calculated by using the published spectral response data of the C70042K PMT and the gA values tabulated in Corliss and Bozman (1962) for the relevant transitions. Although a comparison with other experimental data (see Table 2) shows the Corliss and Bozman (1962) figures to be in considerable error, we assume that the ratios of given gA

values are reasonably correct. Thus the value of the last factor on the RHS of (6.3.7) is 0.63. The conversion factor between signal ratio and population ratio $N_M(t_0)/N_G(t_0)$ is therefore 0.010, i.e., the population ratio is 0.010 times the indicated ISE signal ratio. A typical population ratio is seen to be $N_M/N_G = 10^{-3}$.

6.4 Discussion

The behaviour of the two separate ISE signals under saturating laser conditions is marked by a pronounced correlation between these signals. At a given time delay after laser ablation, the two ISE signals are seen to bear a constant amplitude relation to each other even though on a shot-to-shot basis, the amplitudes of the individual signals fluctuate widely. This suggests that the benefits of laser saturation in selective excitation spectroscopy can be realized in practice.

A different interpretation of the correlation between the two ISE signal amplitudes is possible. Saturation may not have been achieved, but in its place, "tracking" of the amplitudes of the two dye laser pulses may have occurred. That is, there may have existed a constant relation between the peak powers of the two dye lasers - and this sounds reasonable in light of the fact that both lasers were optically pumped by the same nitrogen laser. Since the laser peak powers were not recorded during the experiment, this cannot be ruled out; however, in separate tests the lasers were found to fluctuate by a factor of at least two in power on a shot-to-shot basis with no apparent correlation between the lasers. The power output of the nitrogen laser was found to fluctuate, as did the spatial distribution of the beam, due to irreproducible nitrogen laser channel discharges. Thus it is not reasonable to suppose that the two dye lasers "tracked" each other during the present experiment.

In either case, the strong correlation between the ISE signals at the two wavelengths (as implied by the data of Fig. 36) is remarkable, considering the relatively large ablation laser power variations obvious from Fig. 35, and the large density variations indicated by Fig. 34.

An experiment which uses selective laser saturation as a diagnostic tool requires that the ISE peak can be accurately related to a population density. In order for this to be true several conditions must be met or at least taken into account. The laser beam diameter must be known with some precision. Corrections must be applied to beam diameters calculated by using geometric optics. The diffraction pattern of the aperture which defines the beam size should be considered. The resultant spatial averaging (Rodrigo and Measures, 1973; Daily, 1978) of the ISE must be considered, especially when the laser spectral irradiance is well above the saturation requirement for the transition. Self-focussing or defocussing of the laser beam may be a serious problem depending on laser linewidth and atom density. In the present experiment no account was taken of these three effects. Another required condition is that the observed volume be optically thin for all ISE lines. If this condition is not met, then the population density cannot be accurately related to the observed ISE peak due to radiation trapping. The requirement of an optically thin region has been met in the present experiment by using a photon path length of only 2 mm. Note that in the limit of optically thick regions, amplified spontaneous emission may prevent the attainment of the saturation condition.

In light of these points, the interpretation of the ISE signal ratio in terms of the metastable/ground state population ratio must be viewed with some degree of caution. Nevertheless, inferences can be made from the relative variation of the population ratio with delay time and from the absolute size of this ratio. The most obvious conclusion is that the degree of excitation of the atoms tends to "freeze out" at some time during the plume expansion, as evidenced by the constant ratio of the ISE signals (i.e., metastable $^5S_2/7S_3$ ground state populations) after about $3\mu s$. For delay times greater than about $3\mu s$, the ISE decay constant is close to the natural lifetime (the residual can be accounted for by bulk motion of the excited atoms out of the field of view of the collection optics) and this observation is consistent with a lack of collision quenching implied by the "freeze out". The lack of background emission after $4\mu s$ is further evidence that encounters with free electrons become very rare at about this time. In the time between $0.6\mu s$ and $3\mu s$ after ablation, collision mixing and quenching occurs as evidenced by the relatively strong background emission. This is consistent with the observation of a drop in population ratio during the same period.

The absolute value of the frozen population ratio may be used to estimate the free electron temperature in the plume at the time that collisions between the free electrons and the atoms rarefied. If we can assume LTE conditions at that time (no data were collected which support or refute this assumption), then the Boltzmann relation implies $T_e = 10^3$ °K.

The observations of the present experiment cannot be compared in detail with the results reported in Chapters 4 and 5 because the region of observation is 4 times further from the target in the present case. This change was necessitated by the present much higher overall sensitivity of the collection optics to radiation, and therefore to scattered ablation laser light. A further factor complicating the comparison is the present projection of the collection optics into the vacuum chamber (see Figs. 31 and 32), with a resultant distortion of the plume expansion, recombination, and decay processes. Nevertheless, the picture of an expanding, decaying plasma indicated by the results of the preliminary experiments is corroborated by the results of this experiment.

7. LASER IONIZATION BASED ON RESONANCE SATURATION - LIBORS

In a recent experiment, Lucatoro and McIlrath (1976) observed almost 100% ionization of sodium vapour (at a density of 10^{16} cm⁻³) when a laser was used to saturate the D_1 resonance transition for about 500 ns. Their flash-lamp-pumped dye laser had a mean irradiance of about 1 MW cm⁻² and a 0.05 nm bandwidth. Although no satisfactory explanation for the very rapid ionization was advanced at the time, Measures (1977) suggested that superelastic electron heating, combined with seed electron creation by multiphoton ionization was the most plausible mechanism. We have undertaken a detailed computer study of this interaction employing a 20-level model of the laser-pumped sodium atom. Subsequent to this work, Geltman (1977) has shown that associative ionization can create seed electrons as efficiently as multiphoton ionization. Thus our predicted ionization times are probably an upper bound.

The necessary rate equations required to describe in detail the results of extended selective laser saturation pumping of a vapour were developed in Chapter 2. In this chapter we describe the results of numerical integration

of these equations as applied to resonance saturation pumping of sodium atoms under the title of Laser Ionization Based on Resonance Saturation - LIBORS.

The details of the LIBORS program are left to Appendix E, however a brief discussion of the method of solution, assumptions, and approximations made, is helpful in establishing the context within which the results should be viewed.

A model of the sodium atom was used which consisted of the ground state and the first 19 excited states. On the basis of the large cross-sections ($8 \times 10^{-14} \text{ cm}^2$) for collisional mixing of the fine-structure states (Krause, 1966), the fine structure was neglected and each state was instead assigned a degeneracy which was the sum of the degeneracies of its fine structure components. A diagram showing the energy level system used by the LIBORS program is shown in Fig. 39. For ease of reference the levels have been numbered from 1 to 20 in ascending order of energy.

A fourth-order Runge-Kutta integration technique (Ralston, 1965) was used to solve simultaneously the twenty rate equations (2.1.0) for the population density of each bound level, the rate equation for the free electron density (2.5.8), and the three rate equations for kinetic energy of the electrons (2.5.9), neutrals (2.5.15) and ions (2.5.16), respectively. We employed the experimentally based (Crandall et al, 1974) electron collision rate coefficient for the resonance transition and a combination of Gryzinski (1965) and Seaton (1962) cross sections for evaluating the electron collision rates for optically forbidden and allowed transitions, respectively. All the collision rate coefficients were updated by the program at each integration step to take account of their temperature dependence.

The two-photon ionization rate coefficient was calculated (Cardinal, 1979) based on the theoretical work of Bebb (1966, 1967), and Teague and Lambropoulos (1976). Self absorption for all transitions terminating on either the resonance or ground state was taken into account by the use of Holstein (1951) escape factors. In all instances step excitation was assumed with initial conditions $N_e(0) = 0$, $N_i(0) = 0$ for $i > 2$ and $N_1(0) = N_0 g_1 / (g_1 + g_2)$ and $N_2(0) = N_0 g_2 / (g_1 + g_2)$ which corresponds to the strong saturation limit. Subsequently, $N_1(t)$ and $N_2(t)$ were re-apportioned at each integration step such that $N_1(t)g_2 = N_2(t)g_1$, where $g_1 = 2$ and $g_2 = 6$, in the case of sodium.

The output of the program comprises the population densities of the 20 levels, N_e , T_e , neutral and ion kinetic temperature T_n and T_i respectively, power absorbed from the laser beam Q^l (W cm^{-3}), and the power radiated due to radiative recombination to the 3p state (W cm^{-3}).

During the course of this investigation, the LIBORS program was run more than one hundred times using various input parameters. In the discussion which follows, only a small sample of the outputs is presented, however, the emphasis has been on describing the essential features of LIBORS (which is common to all the outputs presented), and on describing the large variation in predicted ionization time. The range of conditions simulated by the LIBORS program were dictated by variations in the experimental variables such as laser irradiance and vapour density. The accuracy of the LIBORS predictions are, however, conditioned by the uncertainty in many of the collision rate coefficients and various cross-sections used by the LIBORS program.

For cost-efficiency reasons, most runs of the LIBORS program were terminated at the 75% ionization point, but some ran to well past 99.8% ionization.

7.1 LIBORS Result

Figure 40 shows a typical output of the LIBORS program using collision rate coefficients as discussed in Section 7, and using the following parameters:

$$N_0 = 10^{16} \text{ cm}^{-3},$$

Photon flux density $F = 2.97 \times 10^{24} \text{ cm}^{-2} \text{ sec}^{-1}$ which corresponds to an irradiance of 10^6 W cm^{-2} ,

$$\sigma_2^{(2)} = 5 \times 10^{-49} \text{ cm}^2 \text{ sec},$$

$$\sigma_1^{(3)}, \sigma_3^{(1)}, \dots, \sigma_{20}^{(1)} = 0.$$

Indicated in Fig. 40 are the temporal behaviours of the 3p and 3d population densities (i.e., levels 2 and 4), and the electron density, N_e , relative to the scale on the left hand side of the figure. Also plotted is the electron temperature, T_e , relative to the scale on the right. The run terminated at 75% ionization. For the sake of clarity the population densities of the other bound levels have not been plotted but they display essentially the same temporal behaviour as that of the 4d state, although they differ in absolute magnitude.

Almost complete (> 75%) ionization occurs within 430 ns of laser turn-on which is consistent with the experimental observations of Lucatoro and McIlrath (1976). Note that the electron temperature T_e varies little over most of the time interval even though the electron density N_e increases many orders of magnitude during this time. This remarkably constant electron temperature can be understood by considering the electron temperature dependence of the electron collision rate coefficient for excitation and ionization (inelastic collisions) and for de-excitation (superelastic collisions). See Appendix E and Section 7.3.

Because of the choice of scale, the early time variations of N_e and N_{3d} are not shown; both are zero at $t = 0$ and N_e increases linearly with time in this region due to a constant two-photon ionization rate from the 3p level. During the time interval from 100 to 300 ns both N_e and N_{3d} (and the population densities of levels 3 to 20, in general) increase exponentially with time as indicated by the constant slope of their logarithm plots in Fig. 40. At about 380 ns the rate of growth of N_e is seen to increase dramatically, followed shortly afterwards by a sudden drop in N_{3d} . At this time N_{3p} and T_e , which had both been constant, also decrease. This set of computations was terminated at the 75% ionization point. An understanding of these basic features can be attained by considering a simplified LIBORS model of sodium such as presented in Fig. 41. This shows all excited states above the resonance level collapsed into one level (call it level No. 3), and in addition shows the dominant population exchange processes involved between the various energy levels, and between these levels and the continuum.

The next section relates the LIBORS results to the behaviour of this simplified model.

7.2 Simplified LIBORS Model

The discussion in the previous section of the temporal behaviour of the electron density N_e can be put into mathematical form by considering the simplified energy level diagram of Fig. 41. The rate equation for free electrons can be written:

$$\dot{N}_e = N_2 \sigma_2^{(2)} F^2 + N_2 N_e K_{2c} + N_3 N_e K_{3c} \quad (7.2.0)$$

We recall that N_2 and T_e are relatively constant up to about 1% ionization (or 414 ns). Therefore if we restrict our attention to times less than about 400 ns, Eq. (7.2.0) is a first order differential equation in N_e where the only variables are N_e , N_3 , and \dot{N}_e . The first term of the equation represents 2-photon ionization of level 2 (the laser-pumped resonance level) and this term is constant as F is assumed constant. Immediately after laser turn-on, this term dominates the RHS of (7.2.0) because N_e and N_3 are very small, and so N_e rises linearly with time. Between about 100 and 300 ns the middle term dominates the RHS of (7.2.0) and we have exponential growth in N_e with a time constant of $\tau_E = (N_2 K_{2c})^{-1}$. Clearly, after about 300 ns, the third term in (7.2.0) dominates over the others due to the increase of N_3 . The equation for N_3 can be written:

$$\dot{N}_3 = N_2 N_e K_{23} - N_3 / \tau_3 \quad (7.2.1)$$

where τ_3 is the effective lifetime of level 3. τ_3 can be assumed to be determined by radiative losses (which occur at a constant per-atom rate) until the free electron density increases to the point where collisional effects become important. At $N_0 = 10^{16} \text{ cm}^{-3}$, this is reasonable for times less than about 400 ns, so we may treat τ_3 as a constant during the initial ionization stages.

Consequently, we can assume

$$N_3 \approx N_2 K_{23} N_e \tau_3 \quad (7.2.2)$$

and thus we may rewrite (7.2.0) as

$$\dot{N}_e = S + A N_e + B N_e^2 \quad (7.2.3)$$

where

$$\left. \begin{aligned} S &= N_2 \sigma_2^{(2)} F^2 \\ A &= N_2 K_{2c} \\ B &= N_2 K_{23} K_{3c} \tau_3 \end{aligned} \right\} \quad (7.2.4)$$

and where S , A , and B are all constant over the time interval 0 to 400 ns.

Recombination processes are not considered in Eq. (7.2.0) because these processes, exhibiting N_e^2 and N_e^3 dependencies, do not become important until almost full ionization has occurred.

Equation (7.2.3) has two forms of analytical solution depending on the relative values of A, B and S.

(i) If $A^2 < 4SB$, which corresponds to strong multiphoton ionization,

$$t = \frac{2}{\sqrt{q}} \left[\tan^{-1} \left\{ \frac{2BN_e + A}{\sqrt{q}} \right\} - \tan^{-1} \left\{ \frac{A}{\sqrt{q}} \right\} \right] \quad (7.2.5)$$

where $q \equiv 4SB - A^2$.

(ii) If $A^2 > 4SB$, which corresponds to weak multiphoton ionization,

$$t = \frac{1}{\sqrt{Q}} \left[\ln \left\{ \frac{2BN_e + A - \sqrt{Q}}{2BN_e + A + \sqrt{Q}} \right\} - \ln \left\{ \frac{A - \sqrt{Q}}{A + \sqrt{Q}} \right\} \right] \quad (7.2.6)$$

where $Q \equiv A^2 - 4SB$.

For modest values of laser irradiance, i.e.,

$$I^h \ll h\nu \left\{ \frac{K_{2c}^2}{4\sigma_2^{(2)} K_{3c} K_{23} \tau_3} \right\}^{1/2} \quad (7.2.7)$$

$$\sqrt{Q} \approx A - 2SB/A$$

and

$$t \approx \frac{1}{A} \left[\ln \left\{ \frac{A^2}{SB} \right\} + \ln \left\{ 1 + \frac{S}{AN_e} \right\} - \ln \left\{ 1 + \frac{A}{BN_e} \right\} \right] \quad (7.2.8)$$

We can introduce two characteristic electron densities:

N_e^* $\left(\equiv \frac{S}{A} \right)$ represents the electron density for which the rate of ionization based upon multiphoton ionization equals the rate of ionization based on direct electron collisional ionization of the resonance level.

N_e^{**} $\left(\equiv \frac{A}{B} \right)$ represents the electron density for which the rate of ionization based on direct electron collisional ionization equals the rate of ionization involving the intermediate level.

In which case,

$$t \approx \frac{1}{A} \left[\ln \left\{ \frac{N_e^{**}}{N_e^*} \right\} + \ln \left\{ 1 + \frac{N_e^*}{N_e} \right\} - \ln \left\{ 1 + \frac{N_e^{**}}{N_e} \right\} \right] \quad (7.2.9)$$

The form of the ionization curve (N_e against t) can be seen by reference to Fig. 42. Here Eq. (7.2.9) has been evaluated for sodium with $N_0 = 10^{16}$ and assuming $B = 7.40 \times 10^{-6}$, $A = 1.65 \times 10^7$ and $S_0 = 3.28 \times 10^{16}$. These values were obtained by fitting this curve to the computer evaluated ionization curve for the same value of N_0 and S_0 . The great virtue of the simple model is that it enables the computer generated ionization curve to be interpreted in terms of several basic processes. Furthermore, although Eq. (7.2.9) is strictly only valid for a degree of ionization of less than 1%, the steepness of the ionization curve for $N_e > N_e^{**}$ is such that negligible error is incurred by equating the ionization time, τ_I , to the limiting value of Eq. (7.2.9), viz,

$$\tau_I \approx \frac{1}{A} \ln \left\{ \frac{N_e^{**}}{N_e^*} \right\} \quad (7.2.10)$$

or

$$\tau_I \approx \frac{1}{GN_0 K_{2c}} \ln \left\{ \frac{K_{2c}^2}{\sigma_2^{(2)} F^2 K_{23} K_{3c} \tau_3} \right\} \quad (7.2.11)$$

In order to account for variations in laser power, the degree of spectral overlap, or the effective cross section for multiphoton ionization, we introduce the multiphoton factor, ζ , defined by the relation

$$S = \zeta S_0 \quad (7.2.12)$$

where S_0 represents the multiphoton ionization rate corresponding to some given set of conditions. In which case,

$$\tau_I = \tau_I^0 - \frac{1}{A} \ln \zeta \quad (7.2.13)$$

where

$$\tau_I^0 = \frac{1}{A} \ln \left\{ \frac{A^2}{S_0 B} \right\} \quad (7.2.14)$$

In the case of two photon ionization from the resonance level we can write

$$\tau_I = \tau_I^0 - \frac{2}{A} \ln \{ I^h / I_0^h \}$$

The degree of agreement between the computer predicted ionization curves and those obtained from Eq. (7.2.9) (i.e., on the basis of the simple 3 level

model) for various values of ξ can be gauged by reference to Fig. 43 and the value of Eq. (2.7.10) in predicting the variation in τ_I as a function of ξ can be seen from Fig. 44.

One of the most important features to emerge from the simple model is the dependence of the ionization time upon the initial atom density, N_0 , and the electron collisional ionization coefficient of the resonance level, K_{2c} . According to (7.2.11) the ionization time τ_I should be inversely proportional to the initial density N_0 . A comparison with the computer predicted variation presented in Fig. 45 shows this to be approximately true.

We see that the simplified LIBORS model predicts well the variation of ionization time with initial atomic density and with the multiphoton factor. However, the exact value of A and B had to be determined by fitting the model curve to a reference ionization curve from the numerical integration procedure and thus cannot predict accurately the ionization time without this initial comparison. Nevertheless the simplified model is easy to use, and provides insight into the physical processes that play a key role in the LIBORS interaction.

7.3 Importance of Single Photon Ionization

The calculations presented so far and the simplified model developed are appropriate to modest values of laser irradiance. One important process neglected to this point is single-photon ionization of the collision excited upper levels. This can become important at high laser powers.

Marr (1967) gives theoretical cross-sections for single photon ionization for hydrogen-like ions. On the basis of these data, a series of LIBORS programs were run with $\sigma_{3,\dots,20}^{(1)} = 10^{-18} \text{ cm}^2$. The results of one such run are shown in Fig. 46, which for comparison purposes shows also the case $\sigma_{3,\dots,20}^{(1)} = 0$, where T_e , N_e and Q^l are plotted up to 75% point. Note that in this run $N_0 = 10^{16} \text{ cm}^{-3}$ and the laser irradiance is 1 MW cm^{-2} as previously stated. Note also that the electron temperature, taking account of the different ionization times involved, has the same profile in each case.

Two aspects of the results in Fig. 46 deserve special mention: The N_e profile which includes photoionization from upper levels is still characterized by three growth regimes as shown in Fig. 42, however, the exponential growth regime in this case involves a shorter time constant. This is easily visualized by reference to (7.2.3) and Fig. 41. With the introduction of single photon ionization, a term of the form $A_1 N_3$, where A_1 is a constant, should be added to (7.2.3), but by using the proportionality argument (7.2.2), this term could be rewritten in the form $A_0 N_e$, where A_0 (A_1) is a constant. The revised equation for \dot{N}_e takes the form

$$\dot{N}_e = S + (A + A_0) N_e + B N_e^2 \quad (7.3.0)$$

Note that B, to first order, is not affected and this is seen to be the case in Fig. 46 which shows that both N_e profiles do not begin to "burn out" until $N_e \approx 10^{13}$.

The second aspect of Fig. 46 is the equal peak values of Q^l in the two cases. Within at least an order of magnitude of its peak value, Q^l varies approximately as $N_2 N_e K_{21} \epsilon_{21}$ due to the superelastic heating of electrons, reaching a peak when $N_e \approx N_0/2$. Q^l is discussed further in Section 7.5.

7.4 The LIBORS Electron Temperature

The discussions in Section 7.2 have been based on the assumption of a constant electron temperature, T_e , at least up to 1% ionization. This section deals with the assumption of being able to use an equilibrium temperature for the free electrons, and with the factors that determine the temperature and its stability over much of the ionization curve. We explain the time variation of T_e over the whole ionization period, and we investigate the influence of the electron temperature on the ionization time.

The question of using a thermodynamic electron temperature arises because its use implies that the speed distribution is assumed Maxwellian. However, the electron loss and gain mechanisms will tend to generate peaks and holes in the speed distribution corresponding to the particular inelastic and superelastic collision energies involved. In particular, during early times in the LIBORS process - i.e., when the generation of free electrons is dominated by the multiphoton process - the electron speed distribution will contain many peaks and valleys because such fine structure cannot be smeared out fast enough by electron-electron collisions.

Alfvén and Fálthammer (1963) cite an equation for the "self-collision time" of electrons, which is the characteristic time to remove anisotropies in the velocity distribution through Coulomb collisions:

$$\tau_{ee} = 2.28 \times 10^5 N_e^{-1} (\ln \Lambda)^{-1} \quad (7.4.0)$$

where we have taken the liberty of evaluating various constants in the cited equation to arrive at the numerical factor. τ_{ee} is in seconds and N_e is in cm^{-3} . The factor $\ln \Lambda$ is the "Coulomb logarithm", whose value for our electron densities and temperatures lies between 5 and 15.

By using an electron temperature of 9500 K (see Fig. 46), we have evaluated $\tau_{ee}(N_e)$ for various values of N_e :

$$\left. \begin{aligned} \tau_{ee} (10^{10}) &\approx 1.9 \mu\text{s} \\ \tau_{ee} (10^{12}) &\approx 23 \text{ ns} \\ \tau_{ee} (10^{13}) &\approx 2.5 \text{ ns} \end{aligned} \right\} \quad (7.4.1)$$

By comparison, the typical collision time for superelastic collisions (with the sodium resonance level, and with $N_0 = 10^{16}$) is 0.8 ns as discussed elsewhere in this section. According to this reasoning an equilibrium temperature is not attained for the free electrons until the ionization process is close to completion.

Let us investigate in more detail the early development of the electron speed distribution function. Consider the trajectory of a newly created free electron in the kinetic energy space. If the electron is a result of a resonant multiphoton ionization event in sodium vapour, then its initial energy is 1.17 eV. There will exist a certain probability χ that the following encounter with an atom will result in an inelastic collision with a loss in its energy of $\epsilon_{32} = 1.09$ eV due to impact excitation of an atom from level 2 to level 3. This is the only energetically allowed inelastic collision if we assume that at early times the population density of states 3 to 20 is orders of magnitude smaller than those of levels 1 and 2. There will exist a probability $1-\chi$ that the collision will be superelastic involving a level 2 atom, with a consequent gain of energy of 2.10 eV. In this case the energy of the electron becomes 3.27 eV and the subsequent collision will be characterized by a host of probabilities, all but the superelastic $2 \rightarrow 1$ transition referring to excitation of the atom. Clearly, as the number of collisions of a given electron grows, its initially well defined energy of 1.17 eV becomes characterized by a probability distribution over a finite number of discrete energies. If this effect is averaged over many electrons (about 6×10^6 electrons are created by this multiphoton process during the 0.8 ns collision time under typical LIBORS conditions), including their interaction, a smooth distribution results.

Until the form of the actual distribution function of electron speeds is found either theoretically or experimentally, we can do little but use a Maxwellian distribution. In light of the poor precision with which the electron collision rate coefficients are presently known for any given electron temperature, the use of a Maxwellian instead of the actual distribution may well cause less error in modelling the LIBORS process than does the error in the rate coefficients. Nonetheless, an attempt was made to establish the magnitude of these errors, as reported elsewhere in this section. Considering the above comments, it may be more appropriate to view the word "temperature" in the following discussion as referring to the average electron kinetic energy.

The temperature of the electrons immediately following laser turn-on is determined by the excess energy of the two photon ionization process over that required to ionize from the resonance level. For sodium this temperature is about 9050 K when the laser is tuned to the resonance transition. Once free electrons exist due to this two-photon effect, superelastic and inelastic electron collisions with the neutrals tend to heat and cool the electrons, respectively.

The superelastic collision heating per electron occurs at a rate of

$$r_H = \epsilon_{21} N_2 K_{21} \quad (7.4.2)$$

which for sodium at 10^{16} density and $T_e = 9050$ K corresponds to 4.2×10^{-10} W per electron, where we have used $\epsilon_{21} = 3.36 \times 10^{-19}$ J, $N_2 = 0.75 \times 10^{16}$, and $K_{21} = 1.68 \times 10^{-7}$ cm³/sec. This occurs on a time scale of

$$\tau_H = (N_2 K_{21})^{-1} = 0.8 \text{ ns} \quad (7.4.3)$$

In theory, superelastic collisions with atoms in all excited states must be considered (they are taken into account in the LIBORS program), however, at times before about 1% ionization the population density of these other excited states is insufficient to significantly affect the overall superelastic collision rate.

At early times, inelastic collision cooling occurs at a rate of

$$r_c = \sum_{i=3}^{21} \epsilon_{i2} N_2 K_{2i} + \sum_{i=2}^{21} \epsilon_{i1} N_1 K_{1i} \quad (7.4.4)$$

which, according to the values of K_{2i} and K_{1i} given in Table 3, is

$$r_c = 3.7 \times 10^{-10} \text{ W per electron} \quad (7.4.5)$$

Therefore in a time of order τ_H the electron temperature rises to a point (9590 K according to the LIBORS program) where $r_c = r_H$; this temperature is maintained thereafter with very high stability due to the fact that r_H is almost independent of T_e , while r_c is very sensitive to T_e through exponential factors of the form $e^{-\epsilon_{i2}/kT}$. This "equilibrium" electron temperature is not affected by changing the laser irradiance and consequently the multiphoton rate, or N_0 . It is an intrinsic property of the particular species of atom.

A constant T_e is maintained until the rate of heating via superelastic collisions cannot keep up with the cooling rate which occurs at the time of ionization "burn-out". At this time the rate of electron impact ionization from the high lying states is extremely rapid and Eq. (7.4.4) for r_c would have to include a summation of the form

$$+ \sum_{i=3}^{21} \epsilon_{ci} N_i K_{ic} \quad (7.4.6)$$

Under such conditions r_c exceeds r_H at the "equilibrium" temperature of 9590 K and the temperature drops towards a new equilibrium. Reference to Fig. 40 shows the point of departure from a constant temperature is at about 380 ns in the absence of single photon ionization, the same point at which the log N_e curve departs from a straight line. The drop in T_e at this time is reinforced by a drop in r_H [see Eq. (7.4.2)] because N_2 begins to decrease appreciably.

The decrease in T_e comes to a halt after the sudden impact ionization from upper levels has diminished, i.e., when ionization has reached about 99.5%, but the recovery of the temperature is now very slow by comparison as seen by reference to Fig. 47. At this time $\tau_H = 300$ ns (as opposed to the 0.8 ns for early times) due to the relatively low value of N_2 . In addition, ion heating [see Eq. (2.5.16)] becomes relatively important. This can be seen by reference to Fig. 47, where the temporal behaviour of the electron and ion temperatures T_e and T_i , respectively, are plotted. Also plotted in Fig. 47 are N_e and N_2 for reference purposes. This figure represents the same LIBORS conditions as those which generated the curves appearing on the LHS of Fig. 46, except in this case data extend to a time of 240 ns and 99.9% ionization.

Recombination processes, and the resultant radiative energy loss, become important in this time domain and inaccuracies in modelling these processes will affect the accuracy of the data in Fig. 47, and the ultimate equilibrium conditions of the LIBORS plasma.

Various LIBORS runs were executed with manipulated values of selected collision cross-sections that were deemed to play an important role. In this manner it was possible to determine the sensitivity of T_e to changes in value of specific collision cross-sections. This observation is of interest because of the present uncertainty in the values of these cross-sections.

Changes in T_e (through changes in specific cross sections) enabled us to evaluate the dependence of the ionization time upon T_e . The two upward collision rate coefficients corresponding to the two transitions in Fig. 39 marked "collisional excitation bottlenecks" were changed in value separately and as a set. As a reference, the set of conditions applying to the ionization graph of Fig. 40 was used, i.e., $N_0 = 10^{16} \text{ cm}^{-3}$, laser irradiance = 1 MW cm^{-2} , $\sigma_2^{(2)} = 5 \times 10^{-49} \text{ cm}^4 \text{ sec}$, and $\sigma_1^{(3)}, \sigma_3^{(1)}, \dots, \sigma_{20} = 0$. The ionization time was taken as the 75% point. The results are shown in Table 4, which indicates the change in K_{23} and/or K_{24} , the resulting "equilibrium" running temperature, and the time to ionize. The three cases in which the rate coefficients were increased failed to get close to ionization in 600 ns because the electron temperature was very low. The two cases in which the coefficients were decreased ionized faster; in fact, a small decrease in each coefficient has a bigger effect than a relatively large decrease in only one of them. The reduced ionization time resulted from the higher electron temperature.

These apparently contradictory results can be explained as follows. When the bottleneck pathways (see Fig. 39) are opened up, more electrons "flow" into the lower excited states and r_c is increased, with a resultant decrease of T_e . The "flow" of electrons out of levels 1 and 2 is larger, but the rate of impact ionization is lower than in the reference case due to the lower T_e . The atoms are hence excited into the lower excited states at a higher than usual per electron rate, but because the per electron rate of ionization is smaller, the exponential increase in N_e is characterized by a longer time constant. In terms of the simple model K_{2c} is reduced and, consequently, τ_I is increased according to Eq. (7.2.11).

The opposite is true in the case of the bottleneck transitions being closed further by a reduction in the appropriate cross sections. In this case the per electron "flow" out of levels 1 and 2 is reduced which reduces r_c and so T_e rises. The extreme T_e -sensitivity of the rate at which electrons go to high-lying excited states or become free electrons ensures that there is an increase in the electron collisional ionization rate coefficient K_{2c} and so the time constant characterizing the exponential growth is reduced and the ionization time is shorter than that of the reference condition.

The data of Table 4 also serve to indicate qualitatively the effect of using some electron speed distributions other than Maxwellians. The important impact ionization rate coefficient K_{2c} is very sensitive to the number of free electrons with energies greater than the threshold value of $\epsilon_{c2} = 3.27 \text{ eV}$, and thus depends strongly on the characteristics of the high-energy tail of

any electron speed distribution. For example, if the high-energy tail were insignificant, ionization time would be considerably longer.

7.5 Laser-Plasma Power Flow

In this section we investigate the general features of the power flow profile and the dependence of the peak value of this flow on initial density N_0 .

Figure 48 shows among other things the power flow Q^l from the laser to the plasma in $W\text{ cm}^{-3}$ as a function of time. Q^l contains the collision, and single- and multi-photon ionization effects. The LIBORS conditions are the same as those for the solid curves appearing in Fig. 46, i.e., $N_0 = 10^{16}$, $I^l = 1\text{ MW cm}^{-2}$, $\sigma_2^{(2)} = 1.7 \times 10^{-49}\text{ cm}^4\text{ sec}$, and $\sigma_{3,\dots,20}^{(1)} = 10^{-18}\text{ cm}^2$. N_2 and N_e are also plotted for comparison purposes. Reference to Fig. 48 indicates that the power flow is constant during the time that N_e grows due to multiphoton ionization alone, turning to an exponential increase while N_e increases exponentially. A further sudden increase in Q^l is observed close to ionization burn-out (i.e., at the time the N_e curve increases dramatically). The power flow peaks at approximately 50% ionization, then just as quickly drops more than an order of magnitude, following the profile of the N_2 curve. This temporal behaviour is what would be expected of the superelastic heating term, and suggests that the power flow is predominantly due to superelastic collisions, i.e.,

$$Q^l \approx N_e N_2 K_{21} \epsilon_{21} \quad (7.5.0)$$

Continuity and assumption of radiative balance between N_1 and N_2 yields

$$N_2 = G[N_0 - N_e(1 + x)] \quad (7.5.1)$$

where x is the fraction

$$\frac{\sum_{i=3}^{20} N_i}{N_e} \quad \text{and} \quad G = \frac{g_2}{g_2 + g_1}$$

If x can be assumed to be approximately constant, then Q^l will be a maximum for

$$N_e = \frac{N_0}{2} (1 + x)^{-1} \quad (7.5.2)$$

A check of the complete LIBORS output indicates that $x = 0.08$ in the region of maximum Q^l . According to (7.5.2), this implies that Q^l_{max} occurs at about 46% ionization (and this is indeed observed).

Equation (7.5.0) may be rewritten

$$Q_{\max}^l \approx \frac{3}{16} N_0^2 K_{21} \epsilon_{21} (1 + x)^{-1} \quad (7.5.3)$$

and this value of Q^l as a function of N_0 is presented as the full line in Fig. 49 for range of N_0 from 10^{14} to 10^{18} cm^{-3} . The circles shown in Fig. 49 represent outputs of the LIBORS program using other parameters equal to those of the case just mentioned (e.g., Fig. 48). From Fig. 49, Q_{\max}^l is seen to vary as N_0^2 as could be inferred from (7.5.0). Indeed, the agreement between (7.5.3) and the computer predicted Q_{\max}^l values is excellent and provides convincing evidence that superelastic heating of the free electrons represents the major source of laser power absorption, just prior to ionization burn-out.

7.6 Comparison with Laboratory Experiments

The ionization results of Lucatorto and McIlrath (1976) have been mentioned previously, and presently preparations are underway in this laboratory to study LIBORS experimentally. A question naturally arises about the validity of these theoretical results in the laboratory. In the LIBORS analysis, many simplifying assumptions have been made. In this section we discuss the relationship between the theoretically predicted results and some laboratory observables.

One assumption which has been implicit throughout the analysis is that the laser irradiance, I^l , is constant throughout the beam volume. This assumption neglects two effects which may occur in an actual experiment. One is self-(de)focussing or filamenting, which has already been mentioned in Section 6.4; the other is beam absorption which causes the irradiance to decrease with depth of penetration. Thus the N_e time history such as shown in Fig. 48, for example, may become significantly distorted when averaged across and/or along the laser beam.

Another assumption which has been implicit in the analysis is that there is at all times sufficient laser spectral irradiance and laser bandwidth to saturate the resonance transitions, in fact, these quantities have been assumed independent of time. We note, however, that in the case of $N_0 = 10^{16} \text{ cm}^{-3}$, the peak power absorbed from the laser is 1 MW cm^{-3} for a brief time near the 50% ionization point (see Figs. 48 and 49). Thus a 1 MW laser beam with appropriate bandwidth and 1 cm^2 area would not satisfy the saturation condition except for the first millimeter or so penetration of the vapour at this point of the N_e time history curve. In such a case the beam intensity "downbeam" will drop and the plasma there will decay. It is easy to visualize that an ionization wavefront will travel down the beam with a laser-intensity-dependent speed. This effect will alter the N_e time history at a given cross-section of the beam.

The first experiment with which the LIBORS results, and the arguments just given, could be tested is that of Lucatorto and McIlrath (1976); but alas, they do not present time-resolved data. In a subsequent, similar experiment, McIlrath and Lucatorto (1977), (ML), present time-resolved results for lithium vapour. On the basis that the general LIBORS features apply equally to lithium, we may use their results as an approximate check of these features and of the

validity arguments given above. ML show an approximately linear rise with time of N_e between about 10% and 80% ionization over a time from 150 to 400 ns after laser turn-on. This is a much slower rise than might be inferred from Fig. 48, for example, where the electron density is shown to increase the final three orders of magnitude in about 30 ns. The 10% and 80% points occur within a period of 8 ns.

Because they were looking at Li^+ absorption features, the data of ML are averaged over beam diameter and beam length within the lithium plasma, and thus the arguments about spatial averaging over filaments and ionization front propagation probably apply. The authors ML speculate that beam filamentation may be taking place, on the basis of their absorption measurements to find the Li resonance level population. In this case the atoms within the filaments will ionize, perhaps even faster than our LIBORS results would predict because the higher laser irradiance within the filaments will cause significantly faster multiphoton ionization. Once such ionization has taken place, the filament will grow in diameter due partially to diffraction, refraction, and diffusion. A combination of this relatively slow growth in filament size, and the possible propagation of an ionization front may explain the spatially averaged ML results for the N_e growth curve between 10% and 80% ionization.

It is interesting to note that ML show 100% ionization being maintained after the laser intensity has dropped to less than 1% of its peak value. This observation is supported by the LIBORS prediction of the amount of laser power absorbed from the beam after 99% ionization is achieved (see Fig. 48). A typical output of the LIBORS program predicts a two-orders-of-magnitude drop in the absorbed power during the time between about 50% and 99.5% ionization due to the reduction in the superelastic collision rate involving the resonance level.

A quantity which should be easily observable in the laboratory is the continuum radiation due to radiative recombination in the LIBORS plasma. Accordingly, one of the LIBORS program outputs was chosen to be the power emitted ($W\text{ cm}^{-3}$) due to radiative recombination onto the resonance level of sodium. As in the case of the other LIBORS outputs, the quantity actually observed will depend on spatial averaging, etc., as discussed above. The predicted recombination as a function of time is shown in Fig. 50, along with the N_e curve for reference purposes. Experimental parameters are the same as those used for Figs. 47 and 48, i.e., $N_0 = 10^{16}\text{ cm}^{-3}$, $\sigma_2^{(2)} = 1.7 \times 10^{-49}\text{ cm}^4\text{ sec}$, $I^l = 1\text{ MW cm}^{-2}$ and $\sigma_{3,\dots,20}^{(1)} = 10^{-18}\text{ cm}^2$. The weak T_e dependence of the radiative recombination rate is indicated by the flat top after about 180 ns, and the recombination rate can be seen to vary as N_e^2 . According to the energy level diagram for sodium (Fig. 39), and without taking into account the depression of the ionization energy due to free electrons, it is apparent that this radiative recombination continuum lies in the UV part of the spectrum with the long-wavelength limit at approximately 408 nm. As regards the experiments to be performed in this laboratory, this wavelength range is easily accessible with photomultiplier tubes on hand. These experiments will provide further insight into the LIBORS phenomenon.

8. SUMMARY

Various aspects of laser selective excitation of atoms have been investigated theoretically and experimentally. The experimental work has concentrated

on short-pulse laser excitation of an atomic gas generated by laser ablation, while the theoretical work concerned the investigation of the behaviour of a sodium vapour subjected to extended resonance saturation pumping by a laser.

The experimental work started with the construction of a Laser Ablation and Selective Excitation Spectroscopy (LASES) facility which consisted basically of an ablation laser, vacuum chamber, and nitrogen laser-pumped dye laser(s). Two separate experiments were conducted with this facility.

In the first experiment, the radiative lifetimes of the three resonance levels of chromium were determined to be 31.17 ± 0.87 , 32.22 ± 1.06 and 31.42 ± 1.18 nanoseconds, respectively, for the $z^7P_4^0$, $z^7P_3^0$, and $z^7P_2^0$ levels. This was accomplished as follows. Chromium atoms were ablated from a solid chromium target under vacuum with a focussed, moderate power laser pulse. At a suitable time delay following ablation, the atoms were excited by a short, tuned dye laser pulse. The time evolution of the intensified spontaneous emission (ISE) which resulted was recorded on an oscilloscope screen and photographed. A mathematical analysis of the decay of the ISE yielded the natural lifetimes of the appropriate energy states.

Even though the LASES facility was not optimized for making such a measurement, the results and the precision of this new technique compare favourably with those of other, less convenient techniques. This method of radiative lifetime determination has therefore been shown to be an attractive alternative to more conventional techniques.

In the second experiment, the ratio of population densities of the ground and metastable states of chromium was determined in the ablation plume as a function of delay time after the ablation event. This was accomplished by pulsed saturation pumping with two separate, synchronized, dye lasers, and recording the heights of the two ISE signals. Each height was proportional to the population density of the lower of the two states coupled by the laser radiation. The ratio of heights was then converted to a ratio of population densities by taking account of two variables: (a) the relative efficiency of the collection optics at the appropriate wavelengths of the ISE's, and (b) the relative volumes of excitation by the two dye lasers.

This experiment demonstrated the feasibility of using laser selective excitation as a plasma diagnostics tool with spatial resolution on the order of 1 mm and temporal resolution on the order of 20 ns. The ratio of population densities (i.e., metastable/ground) was shown to decrease rapidly during the ablation plasma expansion, approaching a small, but non-zero value after some time.

A theoretical treatment of laser ionization of a cold sodium vapour through extended resonance saturation pumping has been given. It has been shown that by taking account of multiphoton ionization and superelastic collision heating of free electrons, ionization of sodium vapour occurs on a time scale (0.5 μ s) equal to that reported in the literature for the same set of conditions. The theoretical treatment involved numerical integration of rate equations governing the twenty lowest energy levels of the sodium atom, and the free electrons.

Detailed examination of the results led to the development of a simple differential equation for the free electron density. The analytical solution of this equation is in excellent agreement with the results of the numerical integration.

The physical picture which emerged can be described as follows. At the instant of laser turn-on, multiphoton ionization creates free electrons at a constant rate. Thus, initially the electron density rises linearly with time. These electrons are heated by superelastic collisions with resonance-state sodium atoms, and cause general collision impact excitation and ionization of the atoms giving rise to an exponential growth of free electrons. After some time, the internal excitation of the atoms has reached a point where impact ionization and photoionization from high-lying levels become important. At this point ionization proceeds extremely rapidly between about 0.1% and 99.9% ionization.

The theoretical treatment described above has included the most important physical processes. However, inclusion in the rate equations of additional ionization processes and changes in the calculation of various rate coefficients will alter the detailed predictions of the theory. It has nevertheless been shown that rapid ionization follows from multiphoton, and superelastic heating effects generated by a suitably tuned laser pulse.

REFERENCES

- Alfvén, H., Fälthammer, C. G., 1963. "Cosmical Electrodynamics", 2nd Ed., Clarendon Press, Oxford.
- Allegrini, M., Alzetta, G., Kopystynska, A., Moi, L., Orriols, G., 1976. Opt. Commun. 19, 96.
- Allen, C. W., 1963. "Astrophysical Quantities", 2nd Ed., Athlone Press, London.
- Baird, D. C., 1962. "Experimentation: An Introduction to Measurement Theory and Experimental Design", Prentice-Hall.
- Bebb, H. B., 1966. Phys. Rev. 149, 25.
- Bebb, H. B., 1967. Phys. Rev. 153, 23.
- Becker, U., Bucka, H., Schmidt, A., 1977. Astron. & Astrophys. 59, 145.
- Bergstedt, K., Himmel, G., Pinnekamp, F., 1975. Phys. Lett. 53A, 261.
- Bieniewski, T. M., 1976. Astrophys. J., 208, 228.
- Boutillier, G. D., Blackburn, M. B., Mermet, J. M., Weeks, S. J., Haraguchi, H., Winefordner, J. D., Omenetto, N., 1978. Appl. Opt. 17, 2291.
- Burgess, D. D., Skinner, C. H., 1974. J. Phys. B: Atom & Molec. Phys. 7, L297.
- Burrell, C. F., Kunze, H.-J., 1972. Phys. Rev. Lett. 28, 1.
- Cagnac, B., 1975. "Laser Spectroscopy", Ed. Haroche, S., Springer Verlag.
- Cardinal, P., 1979. Private Communication.
- Chen, C. J., Nerheim, N. M., Russell, G. R., 1973. Appl. Phys. Lett. 23, 514.
- Chen, C. J., 1974. Appl. Phys. Lett. 24, 499.
- Chen, C. J., 1974. J. Appl. Phys. 45, 4663.
- Cocke, C. L., Curnutte, B., Brand, J. H., 1971. Astron. & Astrophys. 15, 299.
- Corliss, C. H., Bozman, W. R., 1962. "Experimental Transition Probabilities for Spectral Lines of Seventy Elements", NBS Monograph 53.
- Corney, A., 1977. "Atomic and Laser Spectroscopy", Clarendon, Oxford.
- Crandall, D. H., Dunn, G. H., Gallagher, A., Hummer, D. G., Kunasz, C. V., Leep, D., Taylor, P. O., 1974. Astrophys. J. 191, 789.

- Daily, J. W., 1976. Appl. Opt. 15, 955.
- Daily, J. W., 1977. Appl. Opt. 16, 2322.
- Daily, J. W., 1978. Appl. Opt. 18, 225.
- Dixon, R. H., Elton, R. C., 1977. Phys. Rev. Lett. 38, 1072.
- Dobrolezh, B. V., Klyucharev, A. N., Sepman, V. Yu., 1975. Opt. Spectrosc. 38, 630.
- Dunn, M. H., Maitland, A., 1967. Proc. Phys. Soc. 92, 1106.
- Drawin, H. -W., Felenbok, P., 1965. "Data for Plasmas in Local Thermodynamic Equilibrium", Gauthier-Villars, Paris.
- Elton, R. C., 1970. "Plasma Physics", Vol. 9, Ed. Griem, H. R. and Loveberg, R. H., Academic Press, New York.
- Feldman, M., Lebow, P., Raab, F., Metcalfe, H., 1978. Appl. Opt. 17, 774.
- Fournier, G., 1972. Private Communication.
- Freund, J. E., 1967. "Modern Elementary Statistics", 3rd Ed., Prentice-Hall, Englewood Cliffs, N.J.
- Geltman, S., 1977. J. Phys. B: Atom & Molec. Phys. 10, 3057.
- Griem, H. R., 1964. "Plasma Spectroscopy", McGraw-Hill, New York.
- Grischkowsky, D., Armstrong, J. A., 1972. Phys. Rev. A, 6, 1566.
- Gryzinski, M., 1965. Phys. Rev. 138, A305 and A322 and A336.
- Hahn, L., Hertel, I. V., 1972. J. Phys. B: Atom. & Molec. Phys. 5, 1995.
- Hänsch, T. W., 1972. Appl. Opt. 11, 895.
- Haroche, S., 1976. "High-Resolution Laser Spectroscopy", Ed. Shimoda, K., Springer-Verlag, New York.
- Harrison, G. R., 1956. M.I.T. Wavelength Tables.
- Holstein, T., 1947. Phys. Rev. 72, 1212.
- Holstein, T., 1951. Phys. Rev. 83, 1159.
- Jameson, D. G., Martin, J. J., 1975. J. Phys. E: Sci. Instrum. 8, 635.
- Jaskolka, A. I., 1969. Private Communication.
- Kaufman, S. L., Greenless, G. W., Lewis, D. A., Tonn, J. F., Broadhurst, J. H., Clark, D. L., 1977. "A Novel and Sensitive Technique for High Resolution Spectroscopy", International Conference on Hyperfine Interactions (June 1977).

- Khaikin, A. S., 1967. Sov. Phys. JETP. 24, 25.
- Kibble, B. P., Copley, G., Krause, L., 1967. Phys. Rev. 153, 9.
- Koopman, D. W., McIlrath, T. J., Myerscough, V. P., 1978. J. Quant. Spectrosc. Radiat. Transfer, 19, 555.
- Krause, L., 1966. Appl. Opt. 5, 1375.
- Kwong, H. S., 1979. "Laser Ablation and Selective Excitation Directed to Trace Element Analysis", UTIAS Report No. 234.
- Leslie, S. G., Verdeyen, J. T., Millar, W. S., 1977. J. Appl. Phys. 48, 4444.
- Liu, C. S., Feldman, D. W., Pack, J. L., Weaver, L. A., 1977. IEEE J. Quant. Electr. QE-13, 744.
- Lucatorto, T. B., McIlrath, T. J., 1976. Phys. Rev. Lett. 37, 428.
- Mahr, H., Röder, V., 1974. Opt. Commun. 10, 227.
- Marek, J., 1975. Astron. & Astrophys. 44, 69.
- Marek, J., Richter, J., 1973. Astron. & Astrophys. 26, 155.
- Marr, G. V., 1967. "Photoionization Processes in Gases", Academic Press.
- Martini, F. De., Wacks, K. P., 1967. Rev. Sci. Instrum. 38, 866.
- McCall, G. H., 1972. Rev. Sci. Instrum. 43, 865.
- McIlrath, T. J., 1969. Appl. Phys. Lett. 15, 41.
- McIlrath, T. J., Carlsten, J. L., 1972. Phys. Rev. A, 6, 1091.
- McIlrath, T. J., Lucatorto, T. B., 1977. Phys. Rev. Lett. 38, 1390.
- Measures, R. M., 1968. J. Appl. Phys. 39, 5232.
- Measures, R. M., 1970. J. Quant. Spectrosc. Radiat. Transfer, 10, 107.
- Measures, R. M., Drewell, N., Kwong, H. S., 1977. Phys. Rev. A, 16, 1093.
- Measures, R. M., 1977. J. Appl. Phys. 48, 2673.
- Measures, R. M., Drewell, N. H., Cardinal, P., 1979a. J. Appl. Phys. 50, 2662.
- Measures, R. M., Drewell, N. H., Cardinal, P., 1979b. Appl. Opt. 18, 1824.
- Milne, E. A., 1926. J. London Math. Soc. 1, 40.
- Morgan, E. J., Morrison, R. D., 1965. Phys. Fluids, 8, 1608.

- Norton, B. A., Peacock, N. J., 1976. J. Phys. B: Atom & Molec. Phys. 47, 4535.
- Ralston, A., 1965. "A First Course in Numerical Analysis", McGraw-Hill.
- Ready, J. F., 1971. "Effects of High Power Laser Radiation", Academic Press, New York.
- Robinson, D. C., 1970. Nucl. Instr. & Meth. 79, 65.
- Rodrigo, A. B., 1972. "Experiments on the Application of Laser Selective Excitation Spectroscopy to the Diagnostics of a Potassium Plasma", UTIAS Report No. 180.
- Rodrigo, A. B., Measures, R. M., 1973. IEEE J. Quant. Electr. QE-9, 972.
- Rumsby, P. T., Paul, J. W. M., 1974. Plasma Physics, 16, 247.
- Schenck, P., Metcalfe, H., 1973. Appl. Opt. 12, 183.
- Seaton, M. J., 1962. "Atomic and Molecular Processes", Ed. Bates, D. R., Academic Press, New York.
- Seely, J. F., McKnight, W. B., 1977. J. Appl. Phys. 48, 3691.
- Shaver, L. A., Love, L. J. C., 1975. Appl. Spectrosc. 29, 485.
- She, C. Y., Fairbank, W. M. Jr., Billman, K. W., 1978. Opt. Lett. 2, 30.
- Shukhtin, A. M., Mishakov, V. G., Fedotov, G. A., Ganeev, A. A., 1975. Opt. Spectros. 39, 444.
- Sterlinski, S., 1967. Nucl. Instr. & Meth. 47, 329.
- Tam, A. C., Happer, W., 1977. Opt. Commun. 21, 403.
- Teague, M. R., Lambropoulos, P., 1976. J. Phys. B: Atom & Molec. Phys. 9, 1251.
- Tenenbaum, J., Smilanski, I., Gabay, S., Erez, G., Levin, L. A., 1978. J. Appl. Phys. 49, 2662.
- Waksberg, A. L., Carswell, A. I., 1965. Appl. Phys. Lett. 6, 137.
- Yamashita, M., 1978. Rev. Sci. Instrum. 49, 1336.
- Yonas, G., 1978. Scientific American, Nov. 1978.
- Zel'dovich, Ya. B., Raizer, Yu. P., 1966. "Physics of Shock Waves and High Temperature Hydrodynamic Phenomena", Vol. 1, Academic Press.

TABLE 1

OBSERVED WAVELENGTHS OF EMISSION LINES
FROM LASER ABLATION PLASMA

OBSERVED (nm)	TABULATED (nm)		INTENSITY (visual estimate*)
416.12	416.14	Cr I	3
416.31	416.36	Cr I	3
416.53	416.55	Cr I	3
416.97	416.98	Cr I	4
417.47	417.48	Cr I	5
417.90	417.93	Cr I	2
420.93	420.94	Cr I	4
422.14	422.16	Cr I	4
422.46	422.45	Cr I	3
424.23	424.24	Cr II	2
425.44	425.44	Cr I	1
426.18	426.14	Cr I	3
426.29	426.31	Cr I	3
426.89	426.88	Cr I	4
427.50	427.48	Cr I	1
428.04	428.04	Cr I	3
428.40	428.42	Cr I	4
428.99	428.97	Cr I	1
429.80	429.77	Cr I	4
433.76	433.76	Cr I	3
433.97	433.97	Cr I	2
434.46	434.45	Cr I	2
435.18	435.18	Cr I	2
436.00	435.96	Cr I	5
436.32	436.31	Cr I	6
437.12	437.13	Cr I	5

* 1 - strong

6 - weak

TABLE 1 (CONTINUED)

OBSERVED	TABULATED	INTENSITY
438.48	438.50	Cr I 6
440.35	440.35	Cr I 6
445.87	445.86	Cr I 6
449.71	449.69	Cr I 6
450.66	450.69	Cr I 6
451.22	451.19	Cr I 6
452.66	452.64	Cr I 5
453.09	453.07	Cr I 5
453.58	453.57	Cr I 5
454.07	454.05	Cr I 5
454.58	454.60	Cr I 6
455.53	455.53	Cr I 5
455.90	455.87	Cr II 1
458.84	458.82	Cr II 1
459.22	459.21	Cr II 3
459.57	459.55	Cr I 4
460.07	460.08	Cr II 4
461.64	461.61	Cr I 3
461.91	461.88	Cr II 2
462.19	462.20	Cr I 6
462.60	462.62	Cr I 5
463.41	463.41	Cr II 3
464.60	464.62	Cr I 4
465.16	465.13	Cr I 6
482.32		2
484.69		4

TABLE 2

RADIATIVE LIFETIMES FOR THE CHROMIUM RESONANCE LEVELS (NSEC)

AUTHORS	${}^7P_4^0$	${}^7P_3^0$	${}^7P_2^0$
COCKE ET AL 1971	35^{+3}_{-5}		
MAREK AND RICHTER 1973	31.4 ± 2.9	32.6 ± 2.6	30.5 ± 1.5
MAREK 1975	31.8 ± 2.5		
BIENIEWSKI 1976	32.9 ± 2.4	33.4 ± 2.5	33.4 ± 2.5
BECKER ET AL 1977	31.42 ± 0.8	32.28 ± 0.9	32.01 ± 0.9
PRESENT WORK	31.17 ± 0.87	32.22 ± 1.06	31.42 ± 1.18

TABLE 3

K_{1j} - RATE COEFFICIENT MATRIX

<u>K_{1j} - RATE COEFFICIENT MATRIX</u>	<u>K_{1,12}</u>	<u>K_{1,13}</u>	<u>K_{1,2}</u>	<u>K_{1,10}</u>	<u>K_{1,11}</u>
1.18D-10	2.19D-11	5.68D-11	1.46D-12	1.23D-12	1.53D-11
6.30D-12	2.07D-13	5.31D-14	2.17D-12	9.98D-14	4.36D-11
1.01D-07	2.18D-08	5.47D-10	2.99D-09	2.79D-11	7.84D-11
4.93D-11	2.91D-10	3.54D-12	1.43D-10	4.17D-10	2.16D-09
1.60D-06	2.91D-06	1.40D-07	2.98D-09	3.00D-08	2.05D-08
6.76D-09	2.15D-10	5.53D-11	2.25D-09	2.90D-10	2.33D-08
0.0	4.57D-06	1.13D-06	1.94D-08	1.38D-06	9.66D-08
2.70D-08	8.51D-10	1.71D-08	8.80D-09	2.78D-12	6.82D-08
9.06D-06	0.0	1.68D-06	2.24D-06	4.09D-07	2.35D-08
3.87D-09	2.25D-08	3.59D-10	1.45D-08	3.99D-08	9.91D-08
1.07D-05	8.03D-06	0.0	1.82D-06	1.27D-05	1.48D-06
4.58D-07	2.46D-07	7.36D-09	7.47D-08	1.97D-08	2.95D-07
1.67D-07	2.55D-08	1.89D-09	0.0	8.73D-05	7.34D-06
2.41D-09	4.55D-08	2.65D-06	2.05D-07	5.98D-10	1.36D-07
5.53D-09	7.14D-07	5.80D-07	2.04D-08	6.27D-05	6.95D-06
1.75D-08	3.32D-06	3.48D-07	2.27D-06	0.0	1.24D-05
7.40D-07	7.40D-07	2.00D-06	5.40D-09	2.12D-07	5.30D-07
1.69D-08	9.50D-10	1.41D-06	6.69D-05	3.19D-07	6.55D-07
4.16D-06	1.76D-07	7.39D-07	8.17D-09	7.69D-07	0.0
1.11D-07	1.51D-06	1.86D-07	4.90D-05	7.25D-05	4.59D-05
1.22D-04	6.51D-06	1.58D-07	4.01D-08	8.96D-07	1.26D-06
6.82D-10	8.74D-09	1.90D-07	1.23D-08	1.51D-06	1.73D-06
1.59D-01	5.34D-07	2.10D-05	4.83D-06	1.04D-05	1.82D-06
1.07D-01	2.60D-05	1.08D-09	7.20D-06	2.57D-08	1.46D-07
4.13D-11	6.08D-11	2.00D-07	5.06D-06	9.20D-06	1.84D-06
1.62D+00	2.82D-05	7.43D-07	1.49D-07	7.61D-06	1.84D-06
2.82D-09	5.35D-08	4.70D-08	6.96D-08	1.10D-06	6.67D-06
0.0	2.84D-05	5.63D-07	4.50D-05	9.25D-06	1.84D-06
3.20D-11	8.51D-11	3.45D-07	1.07D-07	5.27D-08	4.71D-05
2.89D-03	5.06D-05	4.65D-05	2.57D-07	1.48D-05	2.12D-06
4.17D-09	5.48D-07	3.97D-08	6.19D-06	8.92D-06	8.45D-06
4.74D-08	0.0	2.41D-05	1.53D-04	3.92D-04	3.34D-06
1.70D-04	3.67D-09	4.90D-08	3.75D-08	5.13D-06	4.36D-08
5.22D-09	3.20D-10	0.0	1.96D-01	4.31D-04	6.62D-07
1.28D-05	3.32D-05	5.11D-06	1.56D-01	9.01D-04	4.34D-06
3.36D-12	5.89D-11	5.27D-08	6.15D-10	9.89D-09	7.91D-09
1.84D-07	1.31D-07	8.83D-07	6.45D-04	2.39D-03	4.38D-06
8.75D-11	1.52D-09	1.73D-08	1.44D-08	2.47D-07	1.45D-04
3.99D-06	2.90D-06	1.48D-05	8.93D-02	2.52D-03	1.48D-07
1.51D-11	1.28D-08	7.37D-10	1.48D-07	2.29D-06	4.39D-06
2.72D-05	3.51D-05	1.42D-04	5.71D-03	0.0	4.22D-07
1.35D-08	2.10D-09	1.97D-06	1.35D-06	1.74D-05	4.86D-06
1.01D-04	1.30D-04	2.77D-06	5.78D-04	4.91D-04	7.06D-05
1.51D-29	1.35D-28	1.15D-27	8.43D-28	5.30D-27	6.83D-06
1.25D-26	1.60D-26	2.77D-27	1.70D-26	1.11D-26	1.35D-27
					0.0
					4.87D-27
					4.45D-13
					7.95D-10
					5.68D-10
					2.51D-09
					1.08D-07
					3.34D-08
					1.36D-07
					6.95D-06
					1.31D-05
					7.78D-06
					0.0
					2.48D-04
					5.95D-02
					2.76D-04
					1.56D-04
					6.62D-07
					1.86D-05
					2.73D-06
					9.58D-08
					7.06D-05
					6.83D-06
					8.80D-27

K_{2,j} - RATE COEFFICIENT MATRIX

0
K_{1,12}
K_{2,1}
K_{1,2}
K_{1,13}
0
K_{2,3}
K_{1,10}
K_{1,c}
....

TABLE 4

RELATIONS BETWEEN "COLLISIONAL BOTTLENECK" CROSS-SECTIONS, ELECTRON TEMPERATURE, AND LIBORS IONIZATION TIME

CASE	T_e ($^{\circ}\text{K}$)	IONIZATION TIME
REFERENCE	9050	398 NSEC
$K_{23} \times 10$	4850	5×10^{10} @ 600 NSEC
$K_{24} \times 10$	6420	1×10^{11} @ 600 NSEC
$K_{23}, K_{24} \times 10$	4610	4.8×10^{10} @ 600 NSEC
$K_{24} \div 10$	9770	314 NSEC
$K_{23}, K_{24} \div 2$	10700	243 NSEC

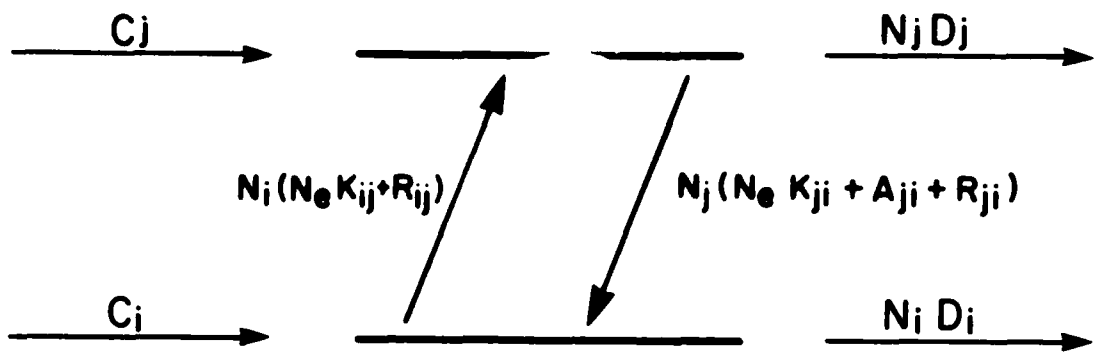


FIG. 1 PARTIAL ENERGY LEVEL DIAGRAM OF AN ATOM SHOWING THE TWO LASER-COUPLED LEVELS.

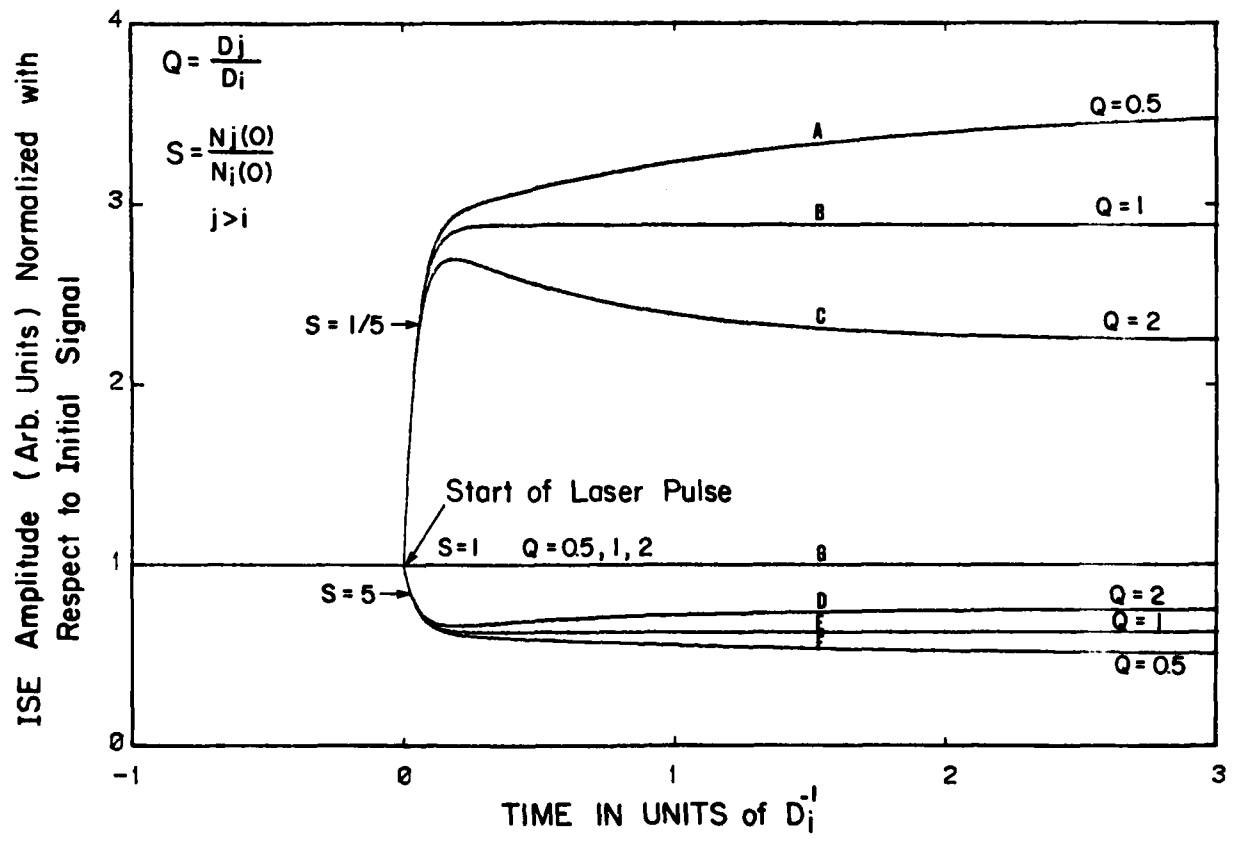


FIG. 2 ISE CURVES UNDER VARIOUS PLASMA CONDITIONS.

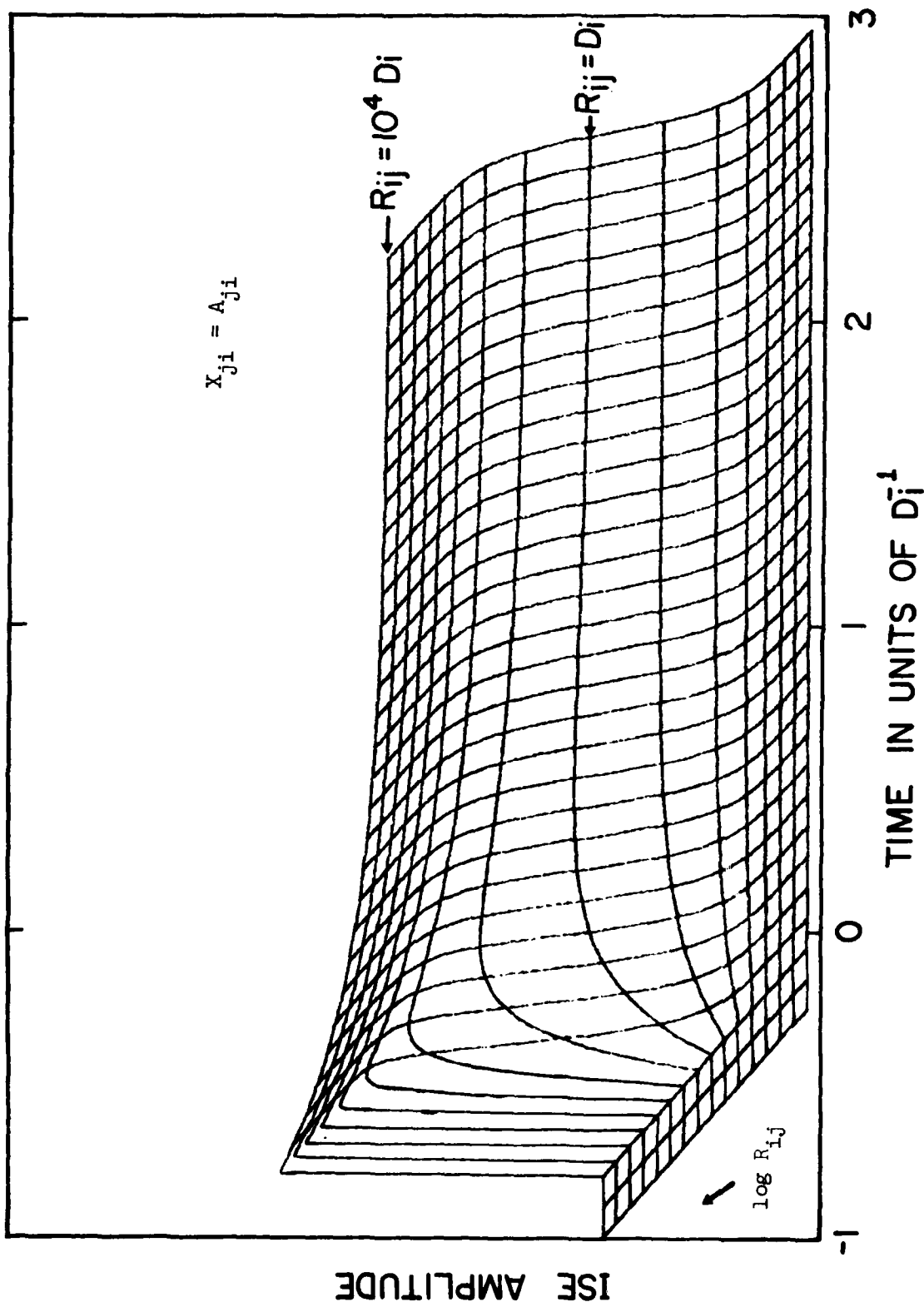


FIG. 3 ISE CURVES FOR VARIOUS LASER POWERS.

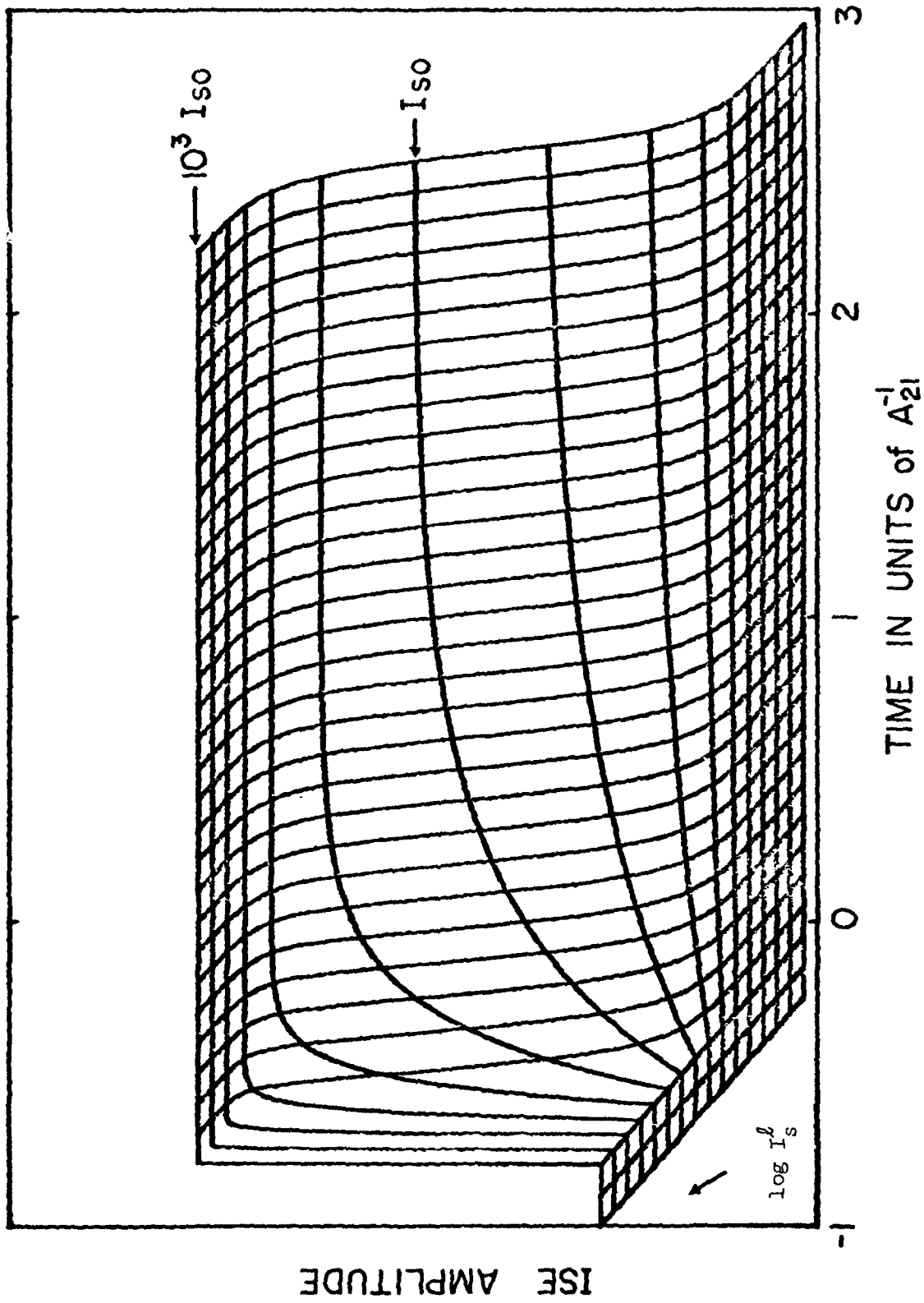


FIG. 4 ISE CURVES FOR RESONANCE PUMPING AT VARIOUS LASER POWERS.

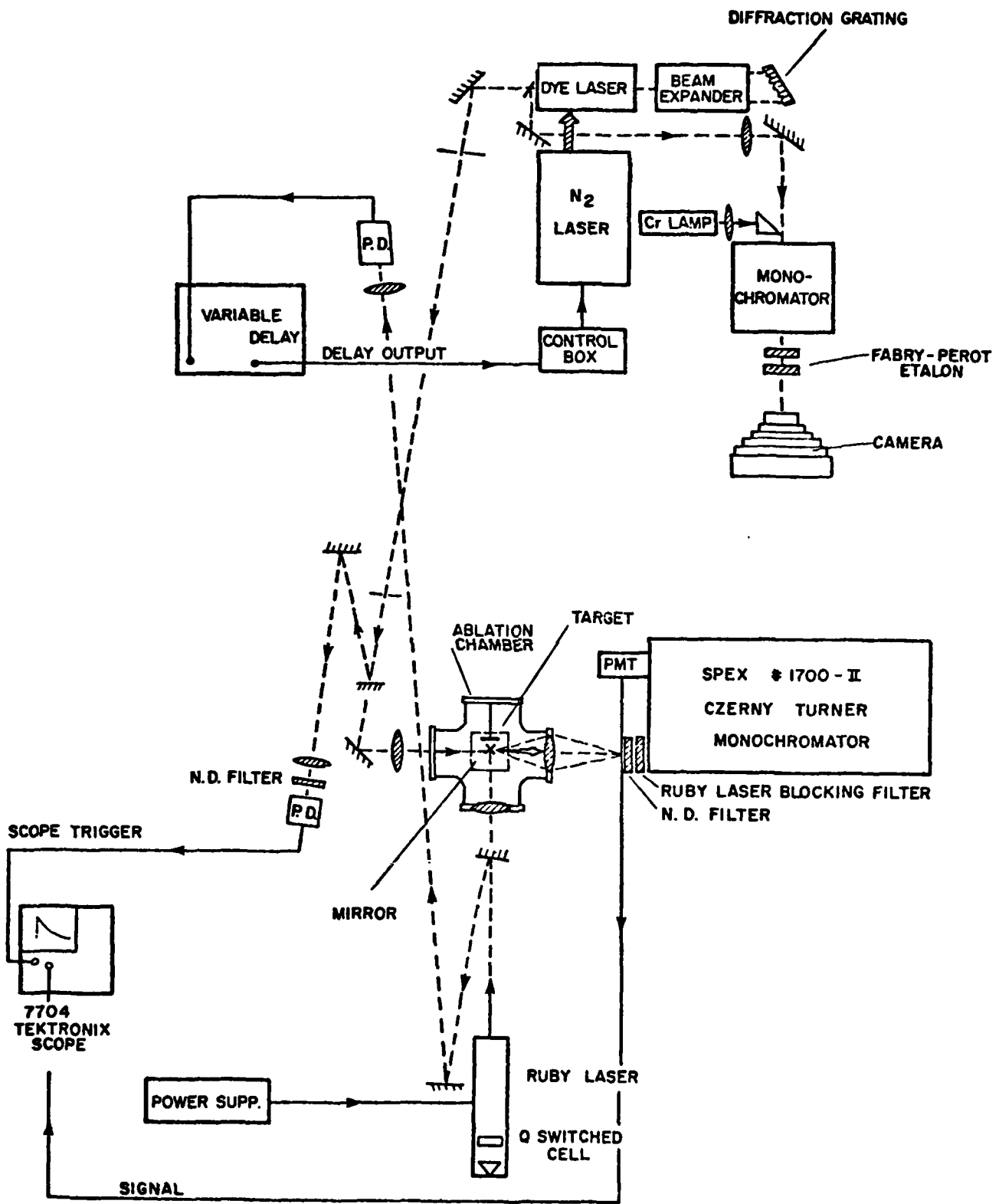


FIG. 5(a) GENERAL SCHEMATIC OF LASES FACILITY.

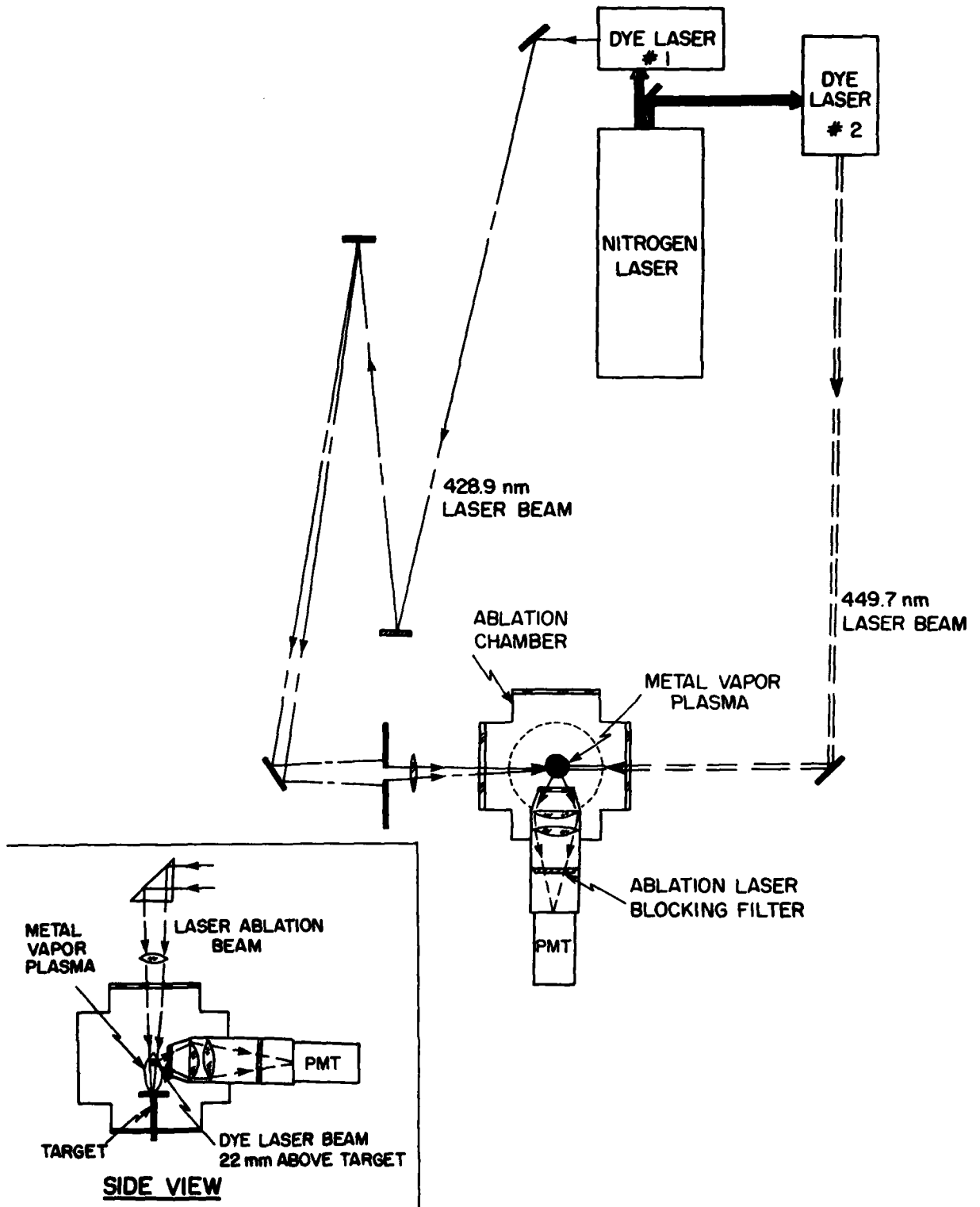


FIG. 5(b) SCHEMATIC OF LASES FACILITY AS USED DURING THE TWO-WAVELENGTH PUMPING EXPERIMENT (CHAPTER 6).

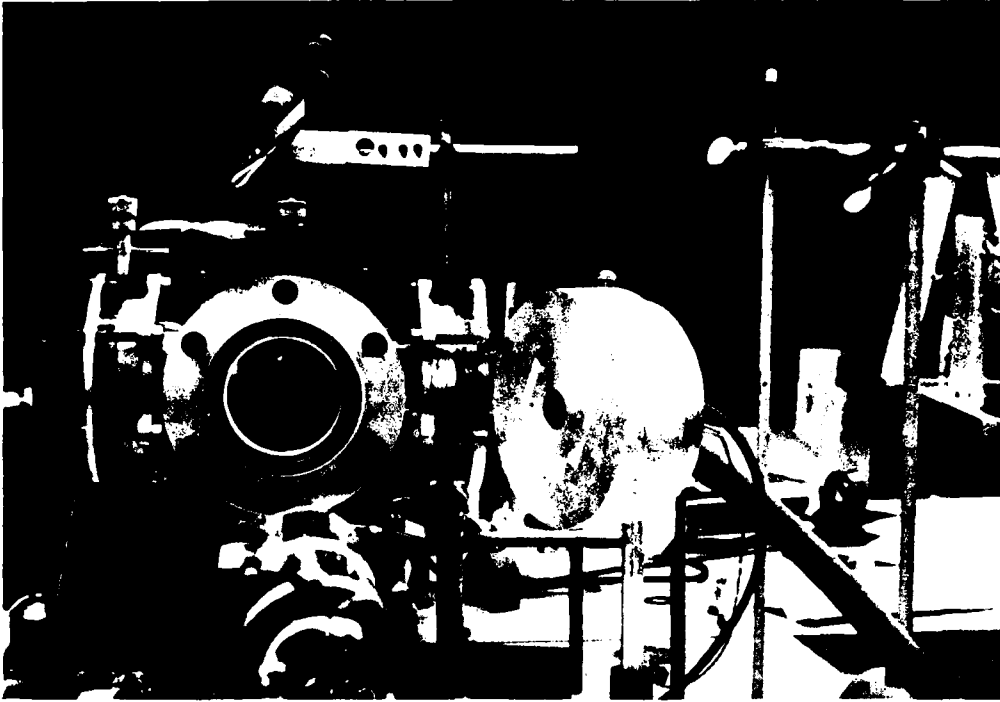


FIG. 6(a) 4-ARMED GLASS CROSS ABLATION FACILITY.

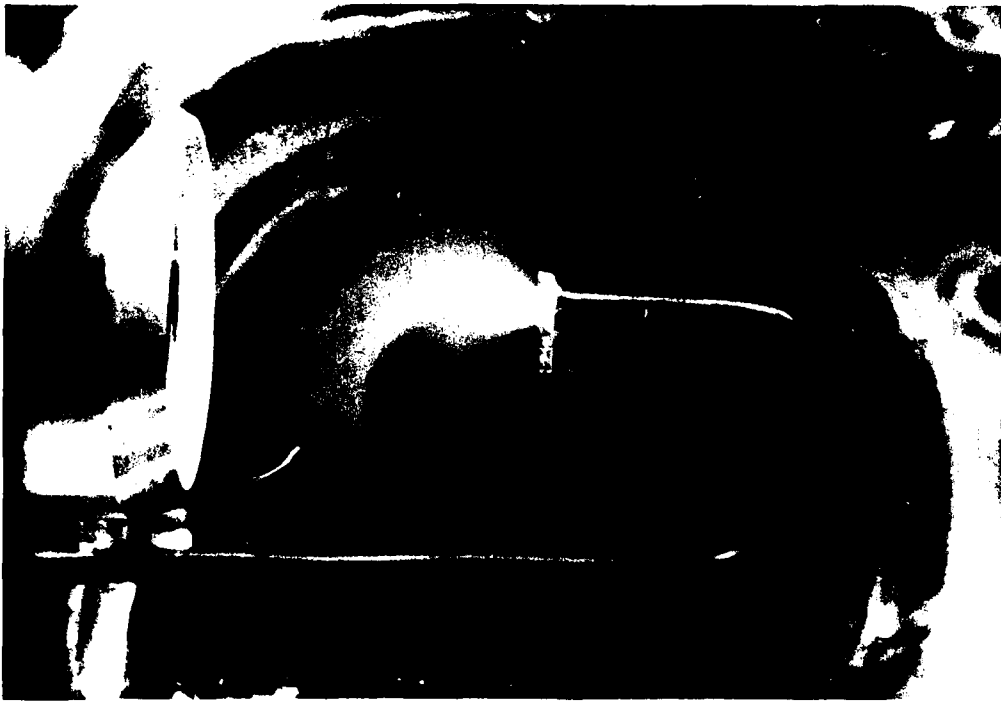


FIG. 6(b) ABLATION CLOSE-UP.

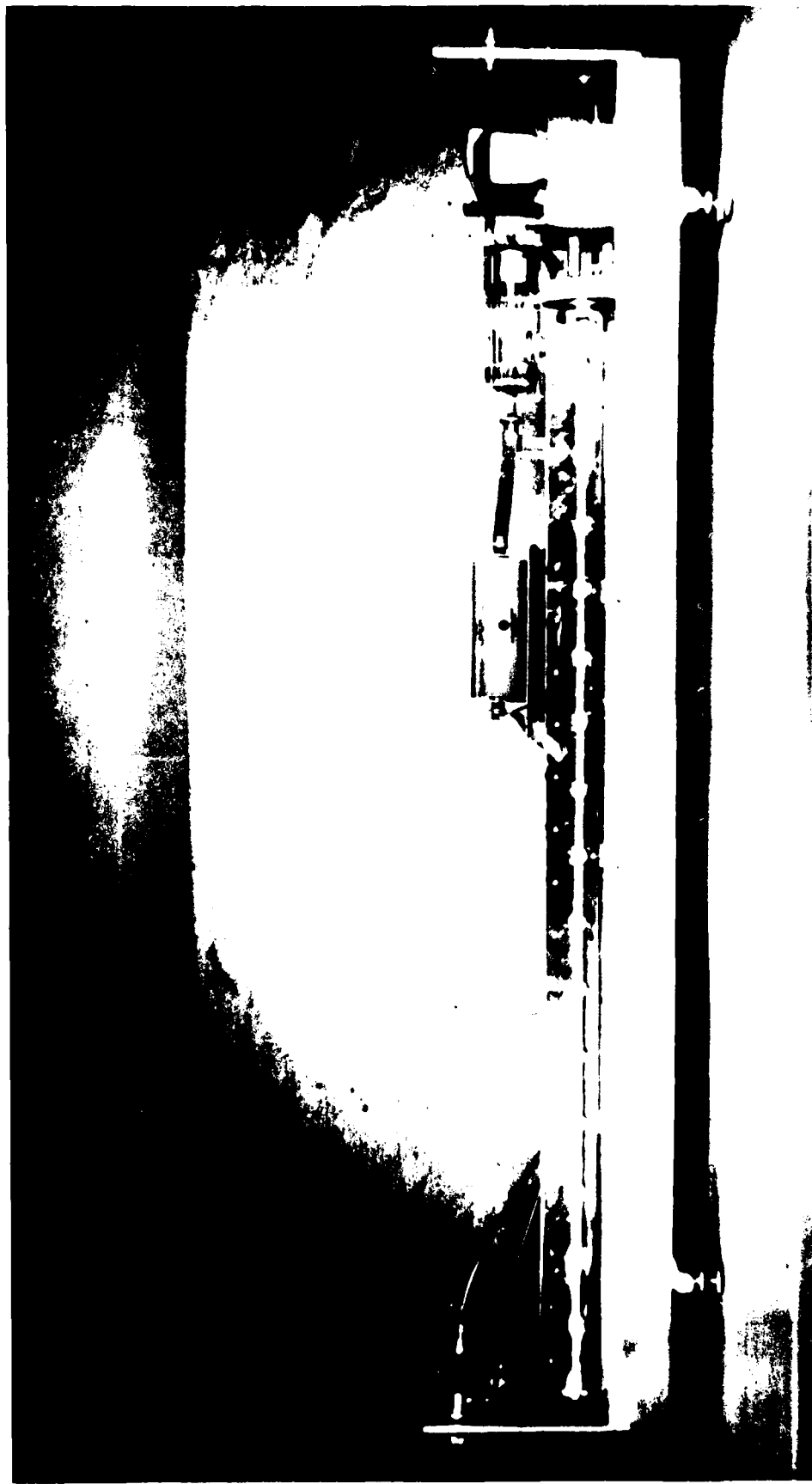


FIG. 7 NITROGEN LASER

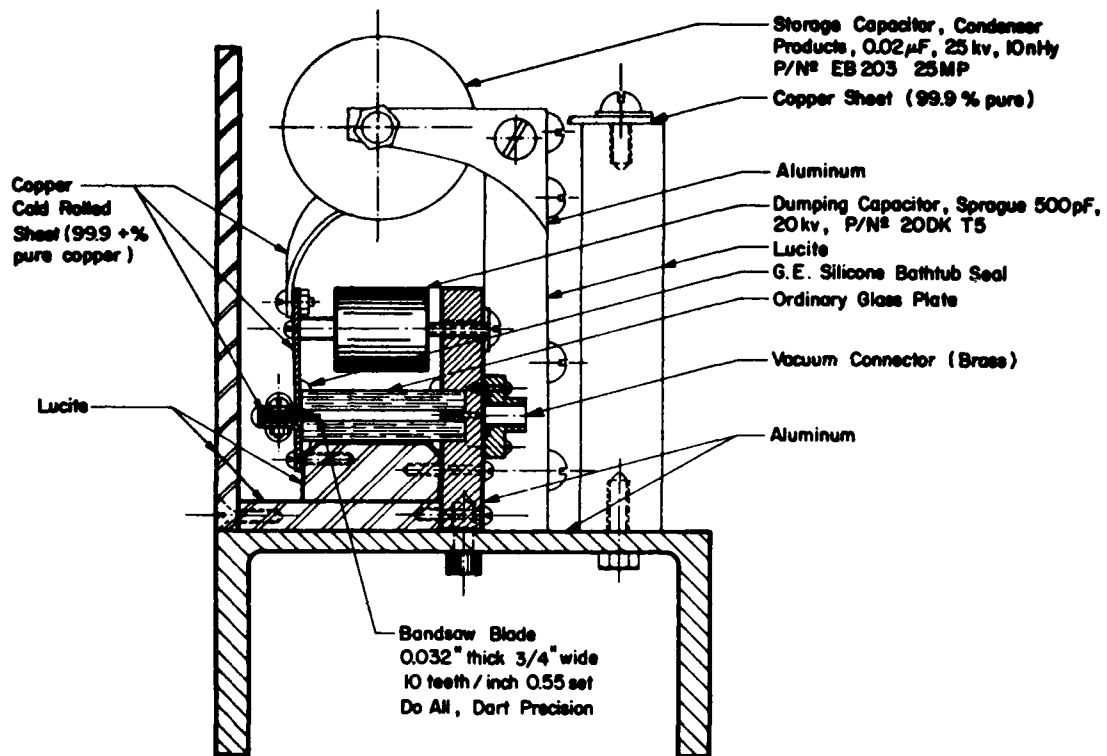


FIG. 8 NITROGEN LASER CONSTRUCTION DETAILS.

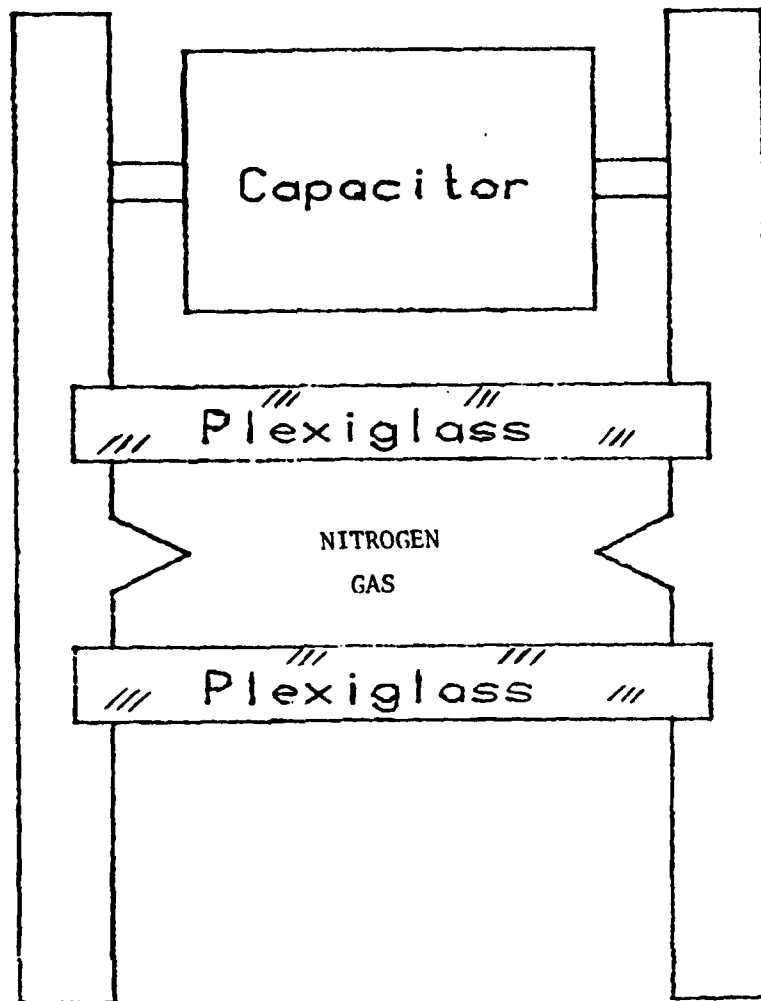


FIG. 9 NITROGEN LASER CHANNEL CROSS-SECTION.

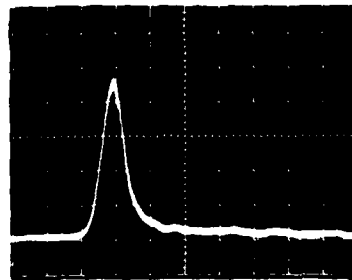


FIG. 10 NITROGEN LASER PULSE (10 NS/DIV AND 25 KW/DIV).



FIG. 11 DYE LASER NO. 1.

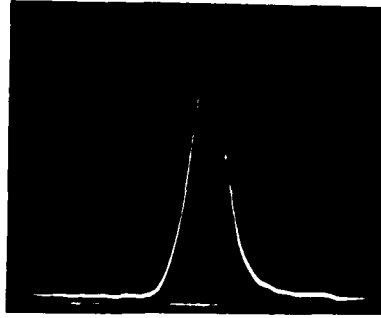


FIG. 12 DYE LASER PULSE (4 NS/DIV).

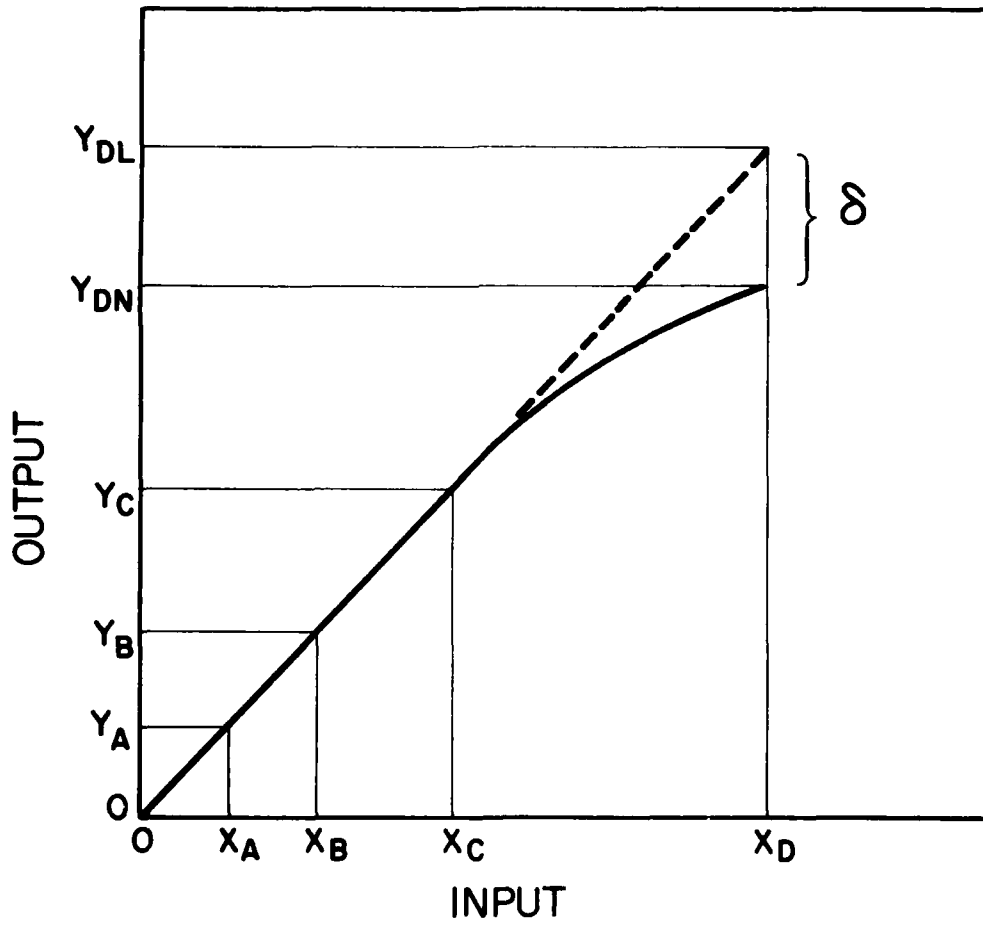


FIG. 13 PHOTOMULTIPLIER TUBE LINEARITY CURVE ILLUSTRATING TWO FILTER METHOD OF ESTIMATING PMT NONLINEARITY (SEE TEXT).

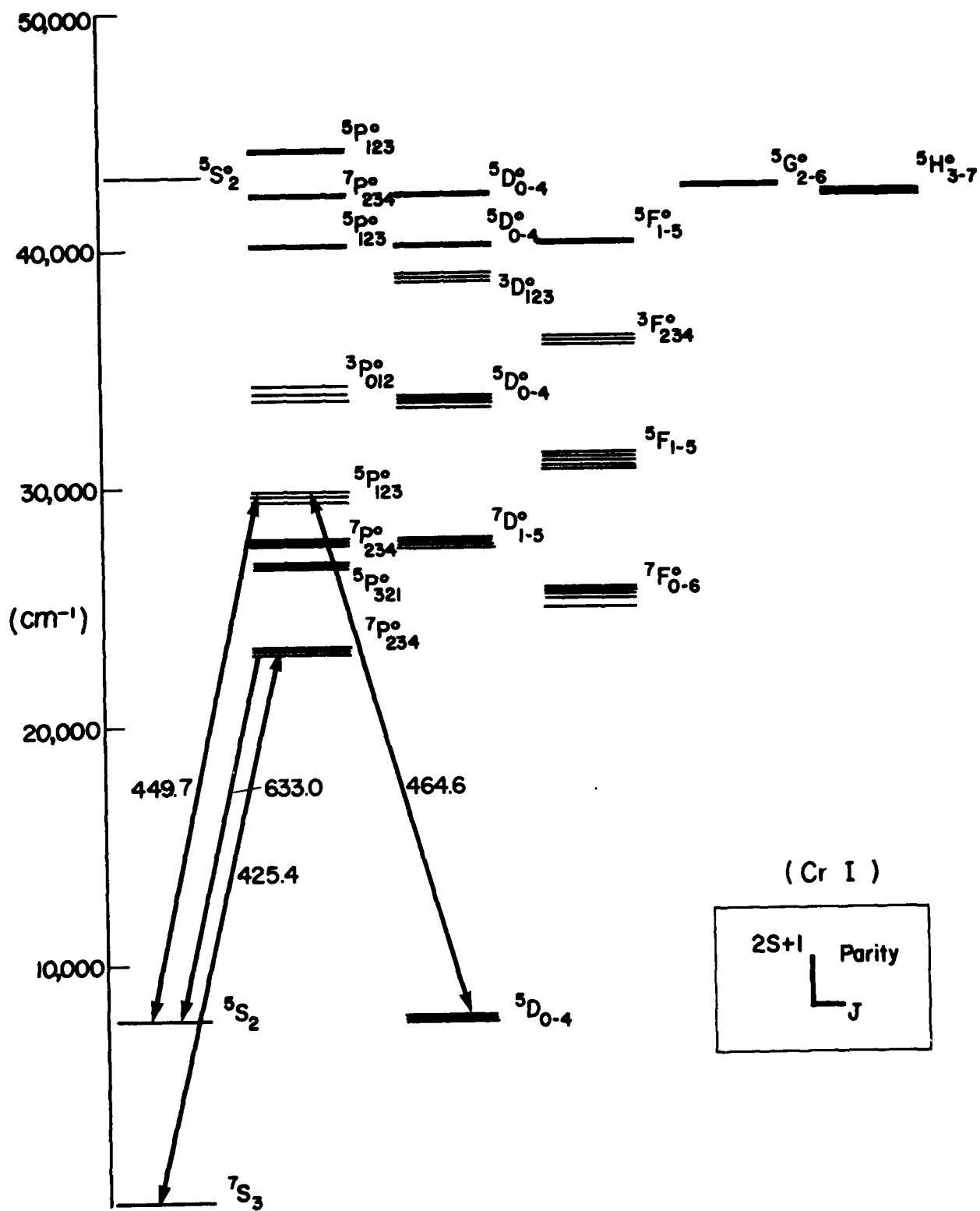


FIG. 14 PARTIAL ENERGY LEVEL DIAGRAM OF CHROMIUM I.

AD-A086 497

TORONTO UNIV DOWNSVIEW (ONTARIO) INST FOR AEROSPACE --ETC F/G 17/4
STUDIES OF LASER SELECTIVE EXCITATION OF ATOMS; (U)

DEC 79 N DREWELL

AFOSR-76-2902

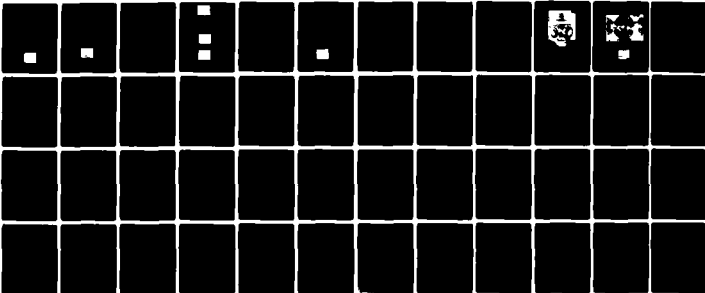
UNCLASSIFIED

UTIAS-229

AFOSR-TR-80-0507

NL

2 of 2
AD
A086 497



END
DATE
FILMED
8-80
DTIC

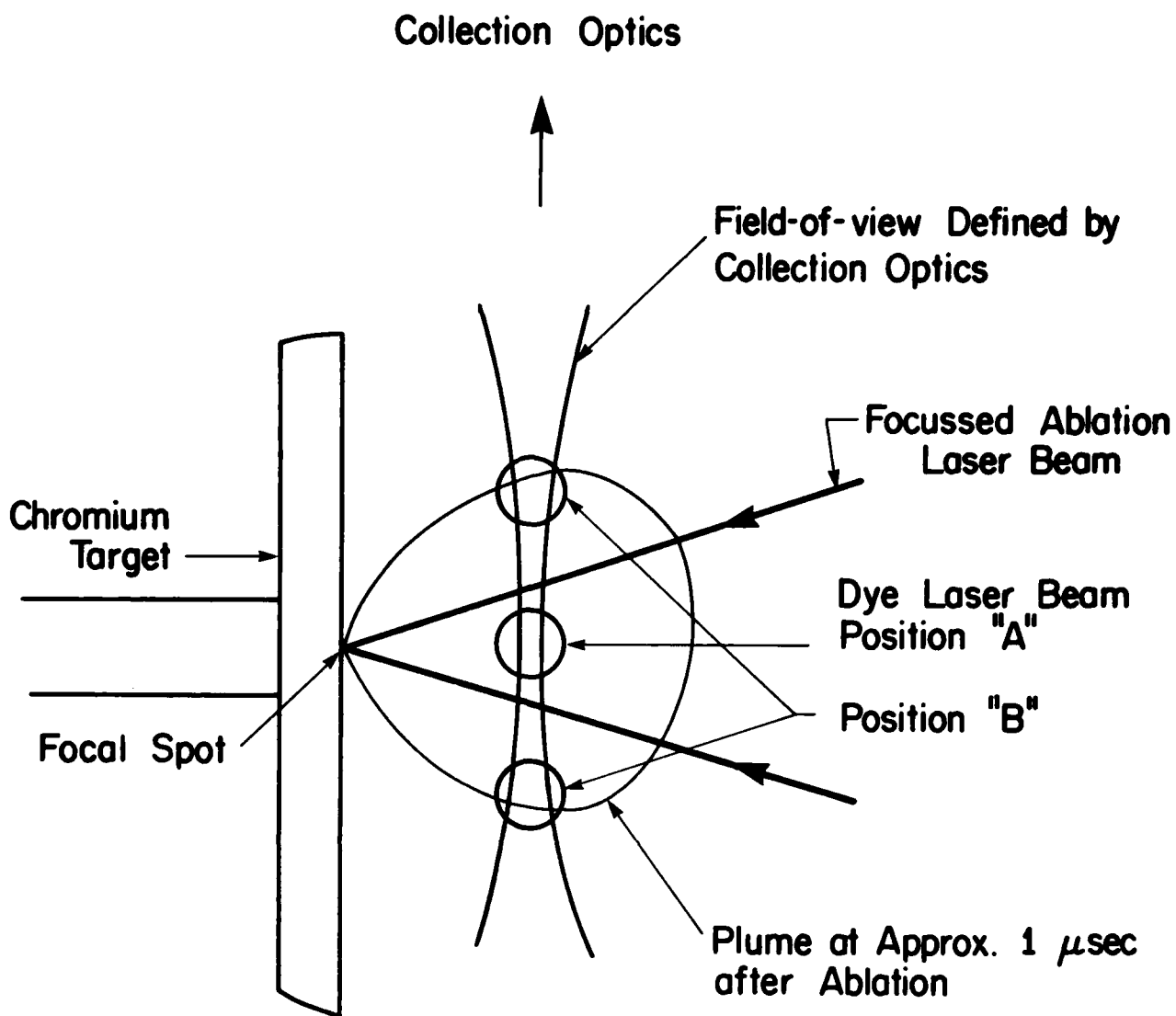


FIG. 15 ABLATION AND OPTICS GEOMETRY DURING PRELIMINARY EXPERIMENTS.



FIG. 16 TEMPORAL VARIATION OF 425 NM RADIATION AS DETECTED WITH THE GEOMETRY OF FIG. 15 (500 NSEC/DIV).

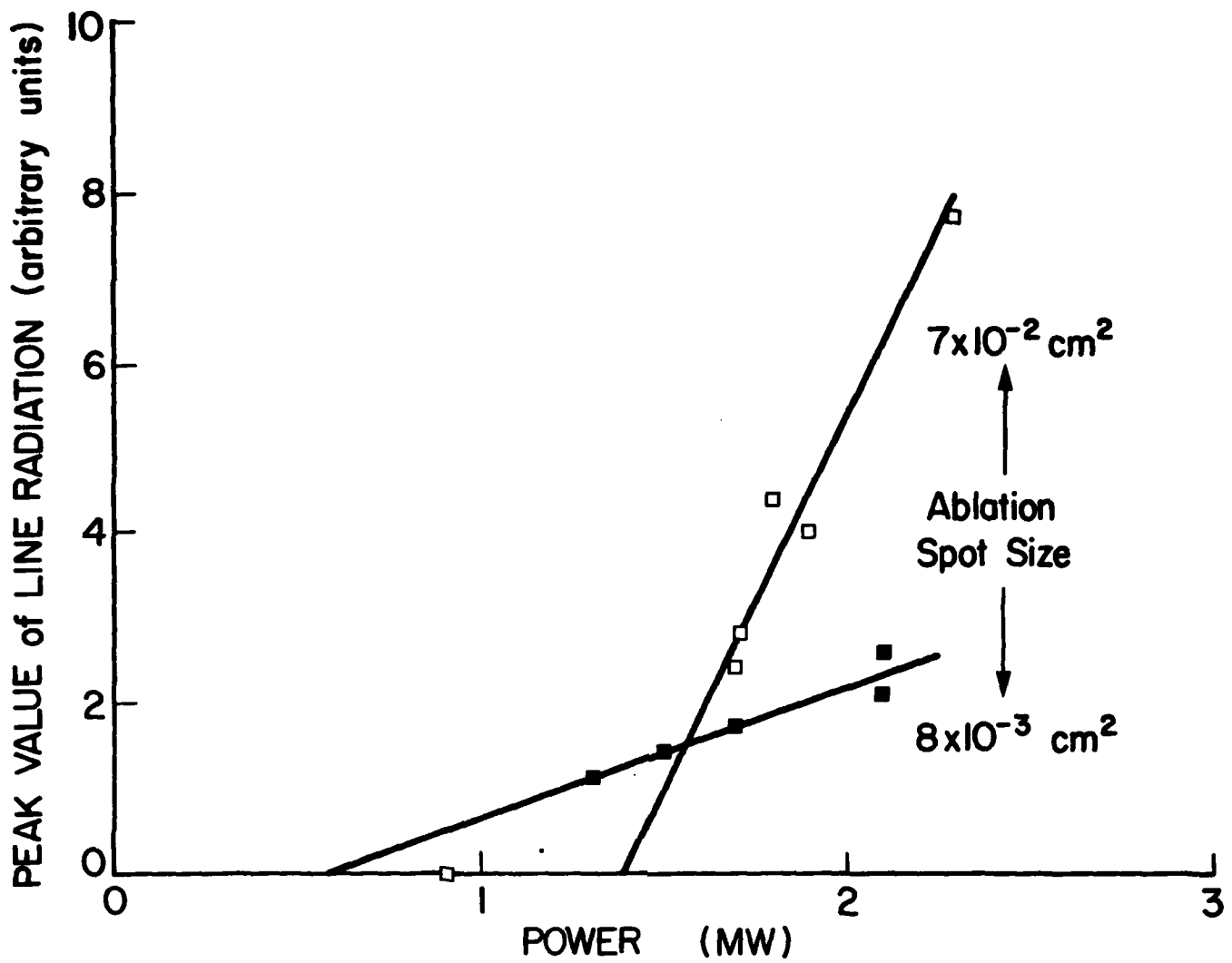


FIG. 17 427 NM LINE RADIATION PEAK VALUE VS LASER POWER.

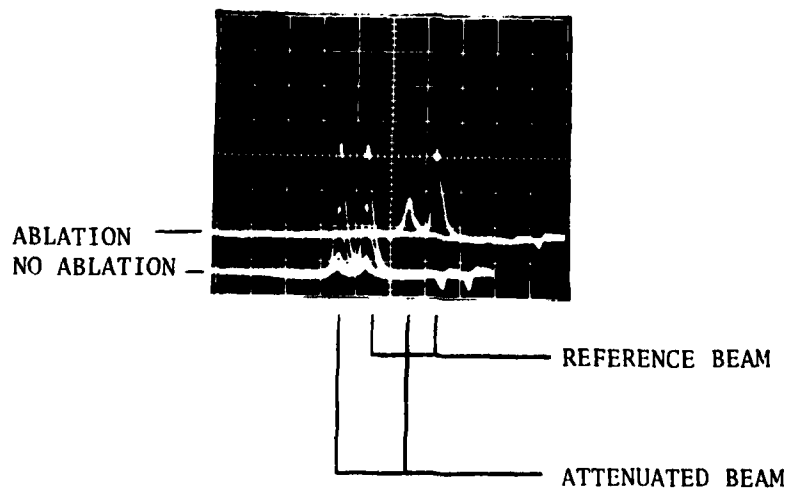


FIG. 18 ATTENUATION OF DYE LASER PULSE BY ABLATION PLUME 950 NSEC AFTER ABLATION EVENT (20 NSEC/DIV).

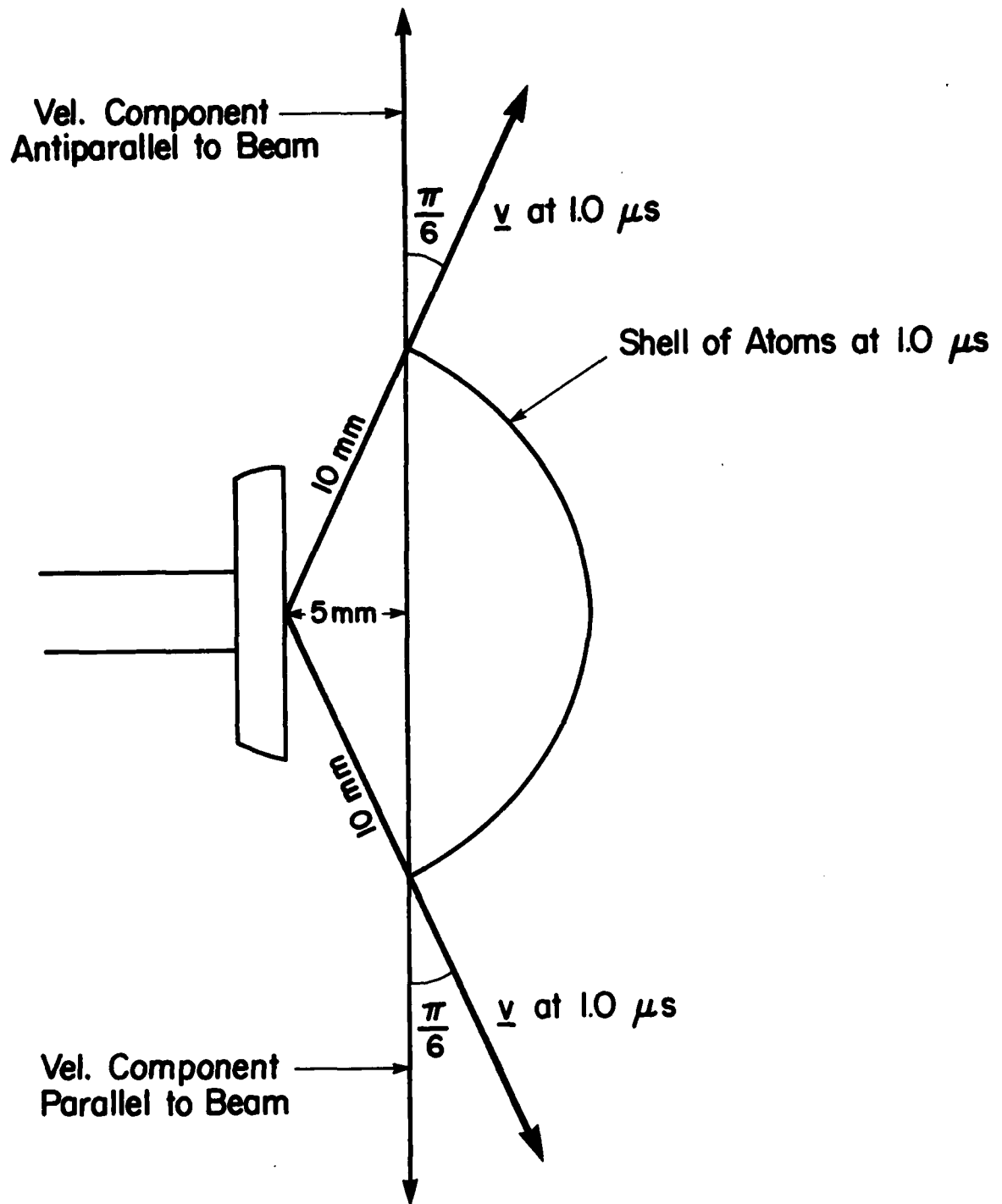


FIG. 19 GEOMETRY OF PLUME AND DYE LASER BEAM WHICH ILLUSTRATES POSSIBLE DOPPLER SHIFTS IN ABSORPTION.

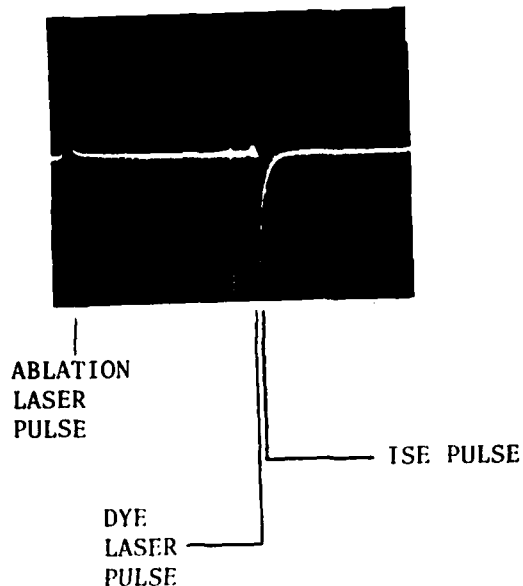


FIG. 20 THREE PULSES ELECTRICALLY SUPERIMPOSED ON A SINGLE TRACE TO SHOW "ISE" SIGNAL AND THE ABSENCE OF ABLATION PLASMA EMISSION, USING AN ABLATION IRRADIANCE OF $15 \text{ mJ}/0.07 \text{ cm}^2$ (200 NSEC/DIV).

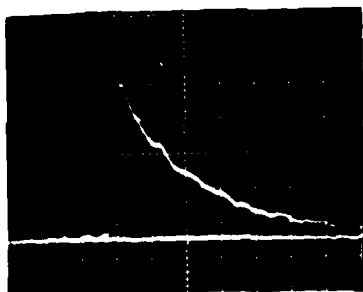


FIG. 21 ISE AT 427 NM WHEN LASER IS TUNED TO THE LINE. DELAY = $20 \mu\text{s}$ (20 NS/DIV).

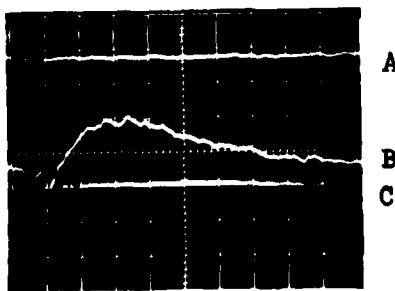


FIG. 22 "ISE" SIGNAL AT 427 NM WHILE THE LASER PUMPS THE 425 NM LINE AT A TIME DELAY OF $1.1 \mu\text{s}$, INDICATES CLEARLY COLLISIONAL MIXING BETWEEN FINE STRUCTURE STATES (20 NSEC/DIV). A: REFERENCE TRACE TO SHOW THE RELATIVE AMPLITUDES OF THE DYE LASER PULSES (NEGATIVE-GOING SIGNALS) RESPECTIVELY AFTER, AND BEFORE ENTERING ABLATION CHAMBER, WITHOUT ABLATION EVENT. B: "ISE" PULSE DURING ABLATION EVENT SUPERIMPOSED ON BACKGROUND LINE EMISSION. C: ZERO SIGNAL REFERENCE BASELINE.

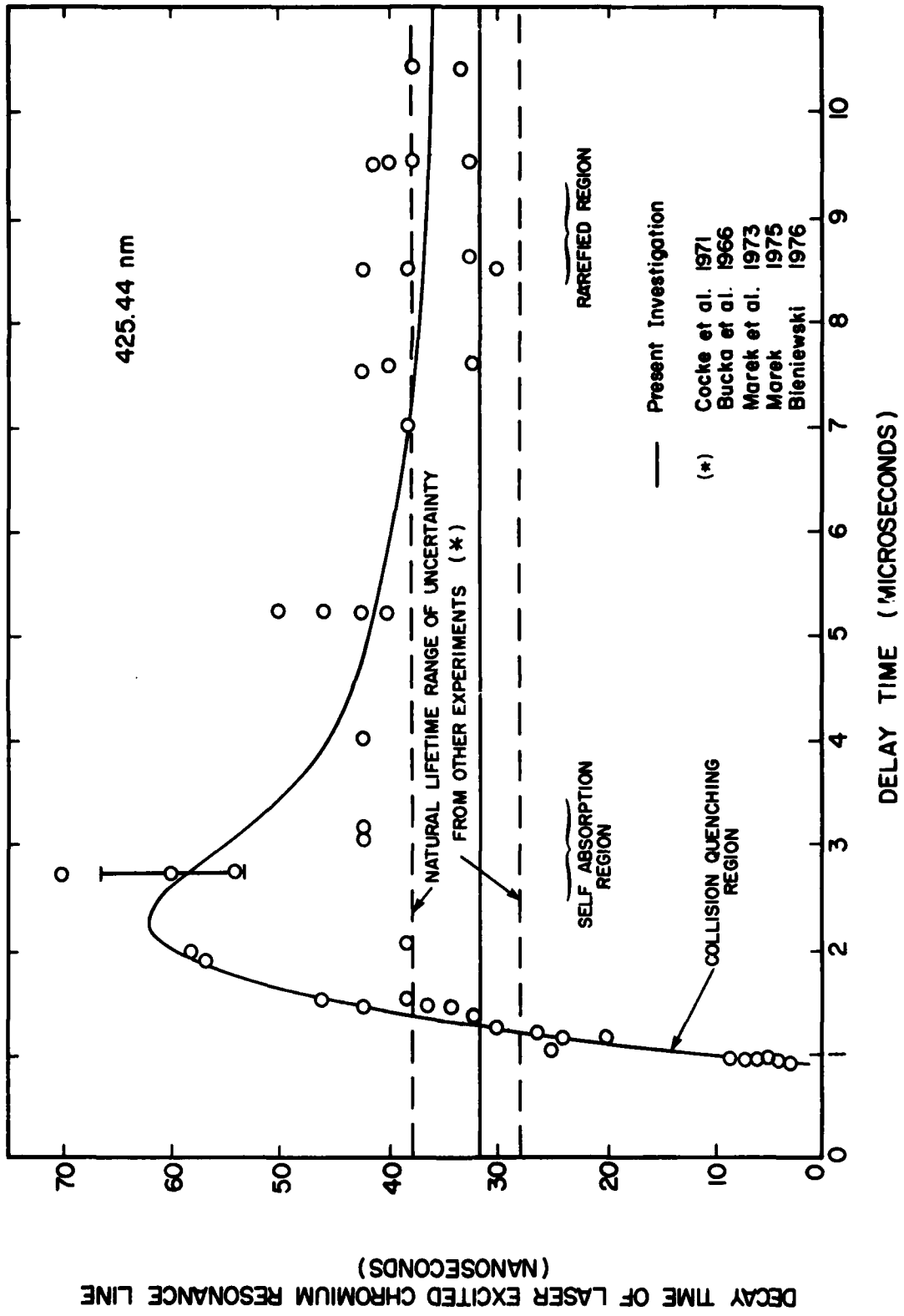


FIG. 23 DECAY TIME OF LASER EXCITED CHROMIUM RESONANCE LINE (NANOSECONDS).

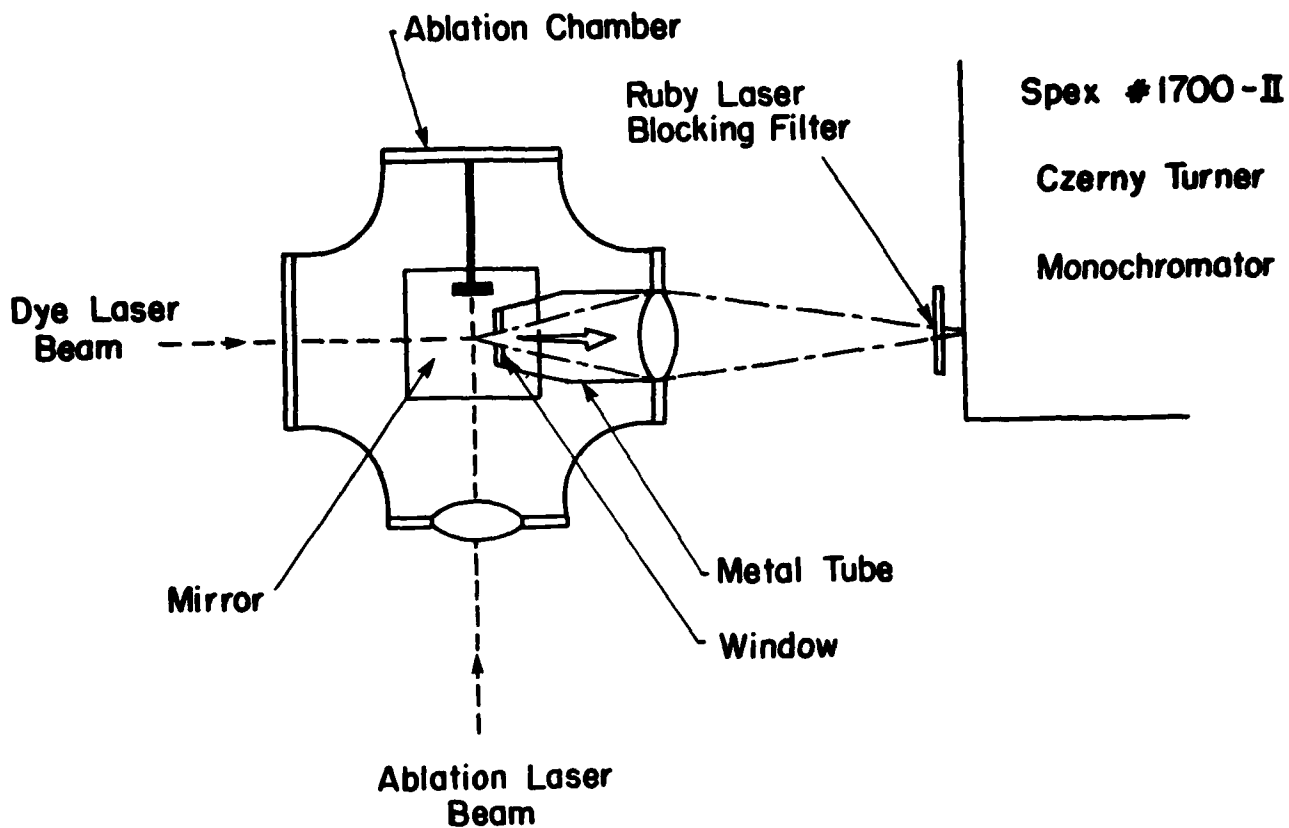


FIG. 24 EXPANDED PLAN VIEW OF VACUUM CHAMBER SHOWING THE METAL TUBE MODIFICATION TO REDUCE RADIATION TRAPPING EFFECTS ON THE ISE.

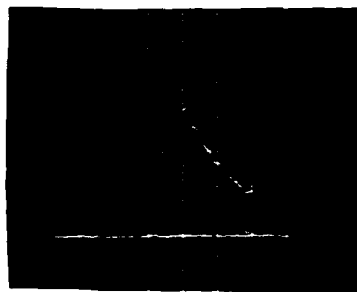


FIG. 25 TYPICAL "ISE" DECAY CURVE USED IN THE ATOMIC LIFETIME DETERMINATIONS (10 NSEC/DIV).

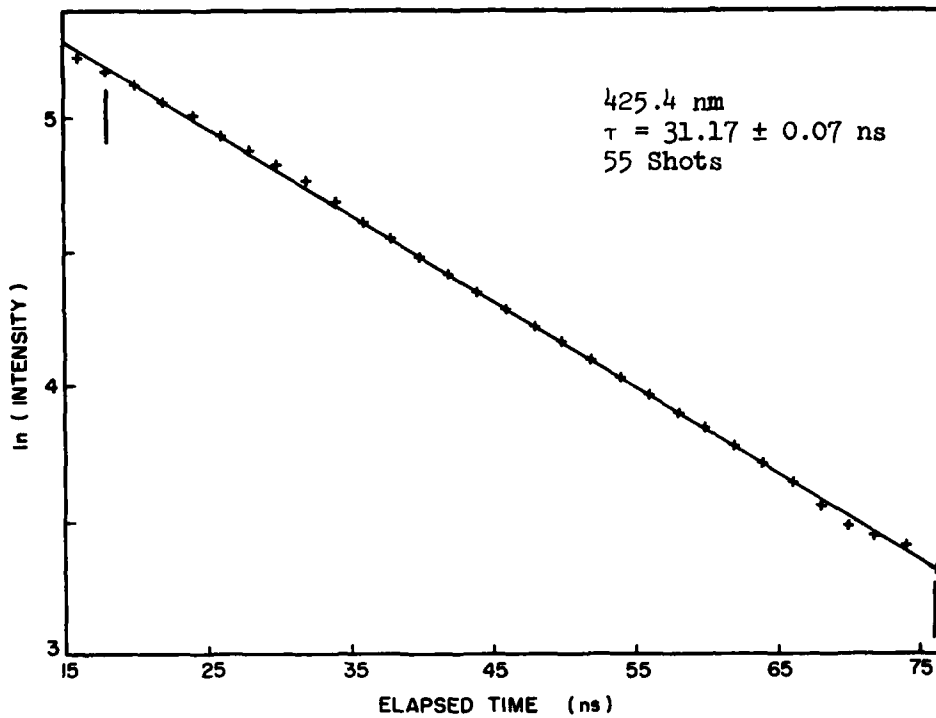


FIG. 26 DECAY OF ISE SIGNAL AT 425.4 NM (AVERAGED OVER 55 SHOTS).

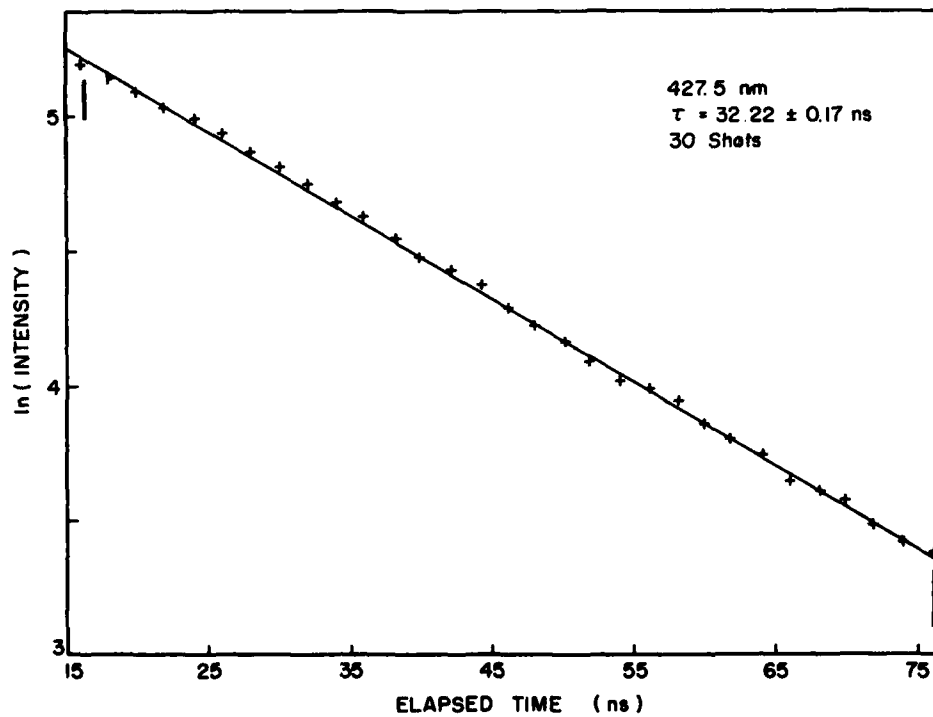


FIG. 27 DECAY OF ISE SIGNAL AT 427.5 NM (AVERAGED OVER 30 SHOTS).

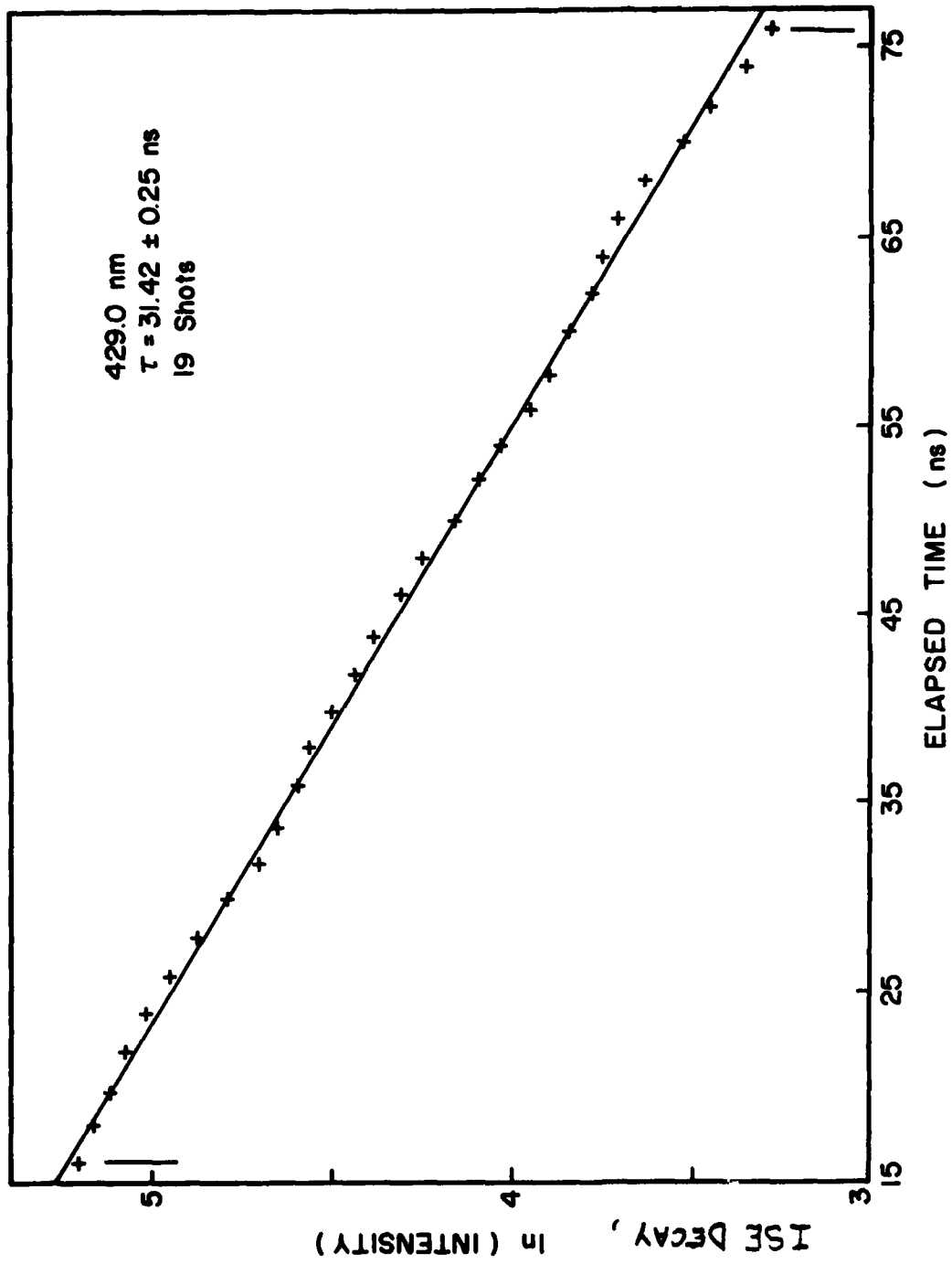


FIG. 28 DECAY OF ISE SIGNAL AT 429.0 NM (AVERAGED OVER 19 SHOTS).

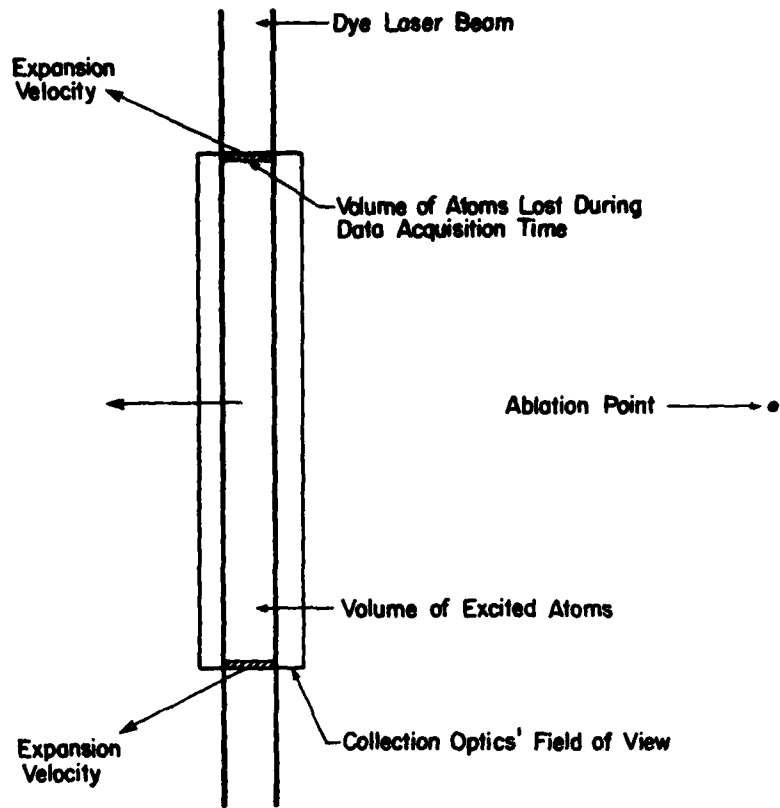


FIG. 29 SCHEMATIC REPRESENTATION OF THE BULK MOTION OF LASER-EXCITED ATOMS DURING THE DATA ACQUISITION TIME OF THE ATOMIC LIFETIME EXPERIMENT.

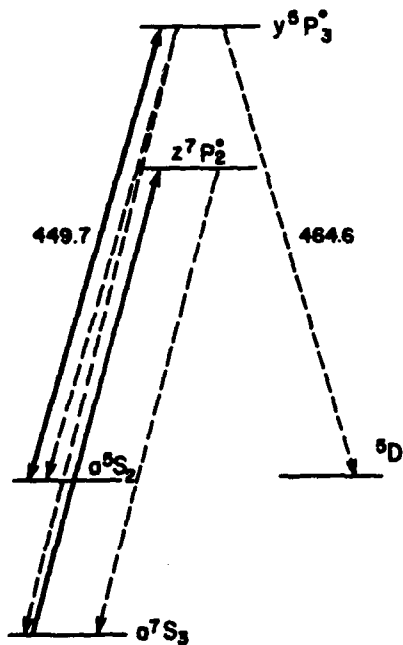


FIG. 30 PARTIAL ENERGY LEVEL DIAGRAM OF CHROMIUM SHOWING THE RELEVANT LEVELS AND TRANSITIONS OF THE TWO-WAVELENGTH PUMPING EXPERIMENT. ——— LASER PUMPING, - - - RADIATIVE DECAY.

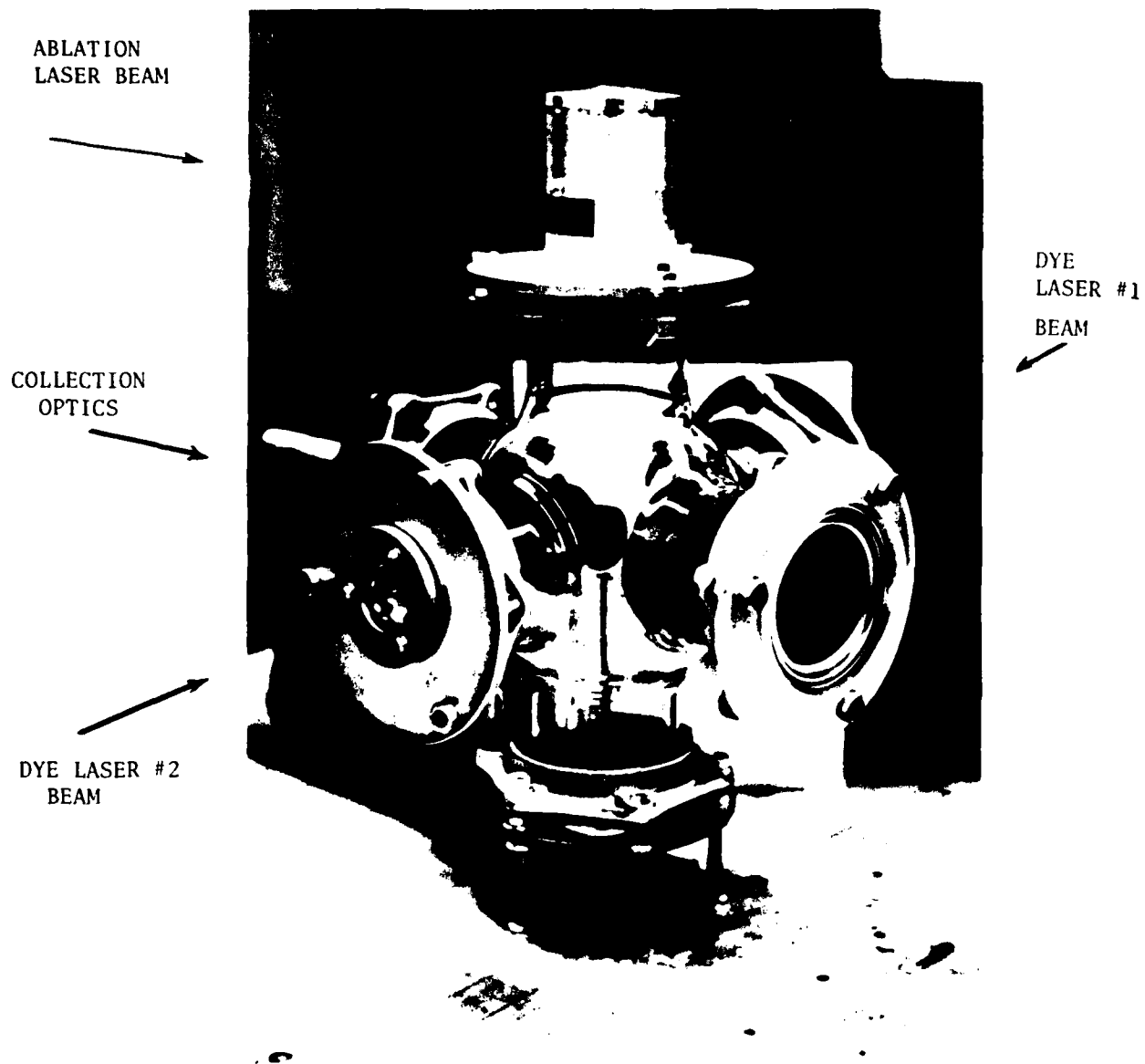


FIG. 31 ABLATION CHAMBER USED DURING THE TWO-WAVELENGTH PUMPING EXPERIMENT. TARGET IS THE HORIZONTAL SURFACE MOUNTED ON THE VERTICAL ROD. ABLATION PULSE HITS THE TARGET VERTICALLY AFTER PASSING THROUGH A TIR PRISM MOUNTED INSIDE THE METAL CYLINDER ABOVE THE CHAMBER.

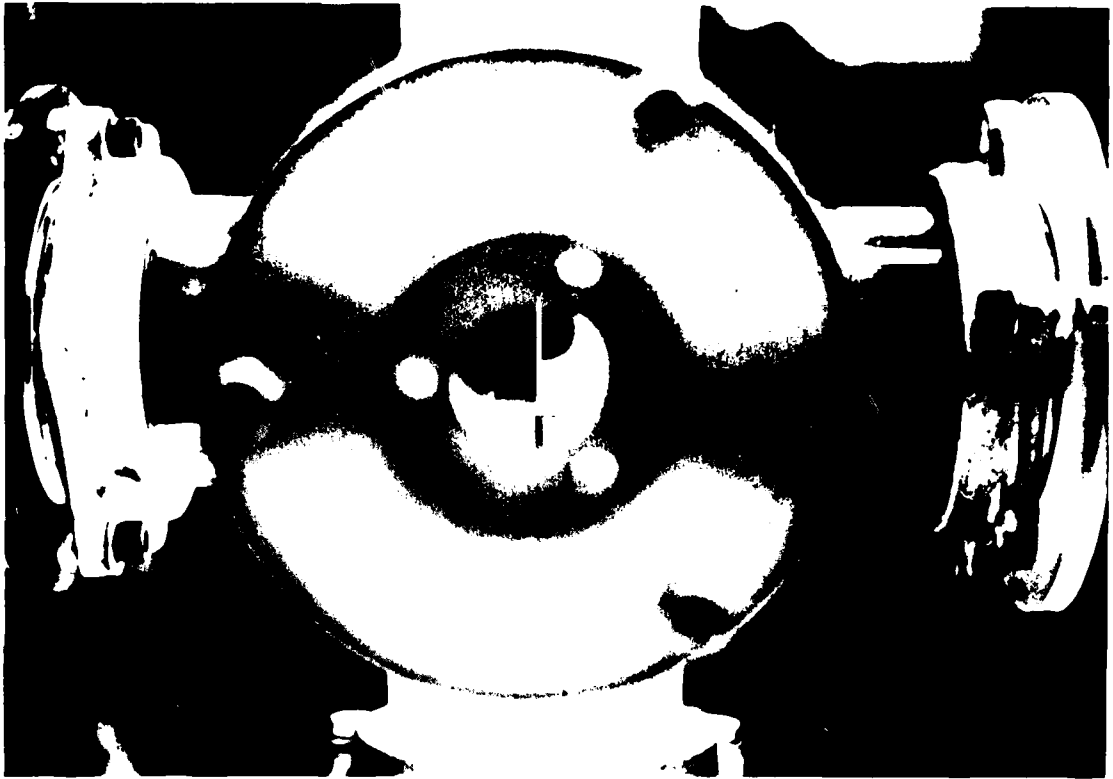


FIG. 32 CLOSE-UP VIEW OF TARGET AND COLLECTION OPTICS TUBE AS SEEN THROUGH ONE OF THE CHAMBER WINDOWS USED FOR DYE LASER NO. 2 BEAM.

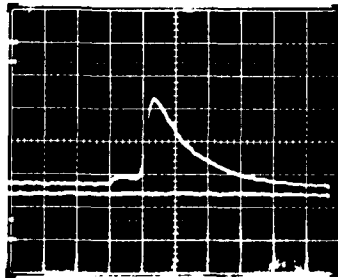


FIG. 33 TYPICAL COMPOSITE "ISE" SIGNAL SHOWING CONTRIBUTION FROM THE DECAY OF TWO SEPARATE EXCITED STATES OF CHROMIUM. TIME DIFFERENCE OF THE TWO SIGNALS HAS BEEN INTRODUCED ARTIFICIALLY IN ORDER TO SHOW BOTH COMPONENTS ON A SINGLE SWEEP USING A SINGLE PHOTOMULTIPLIER TUBE.

FIG. 36

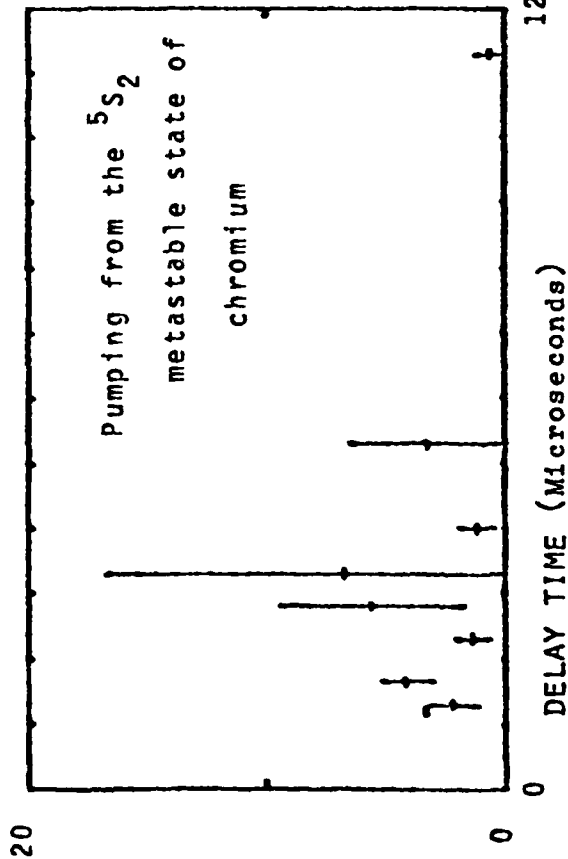
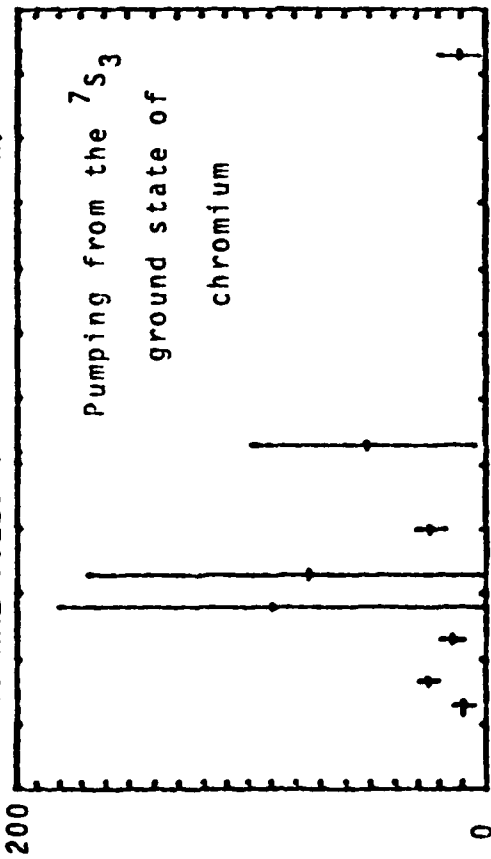


FIG. 34

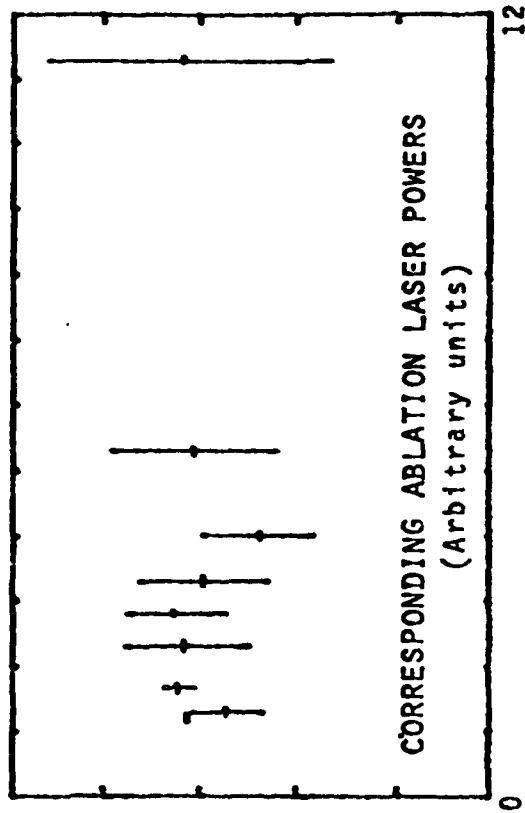
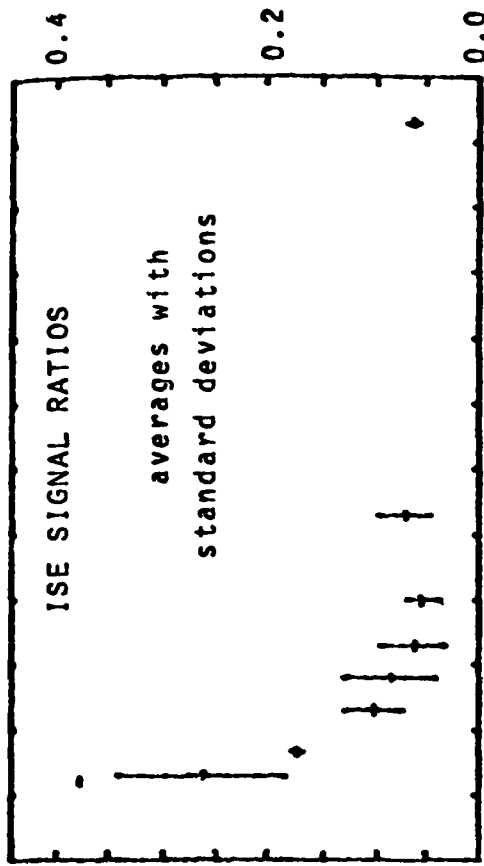


FIG. 35

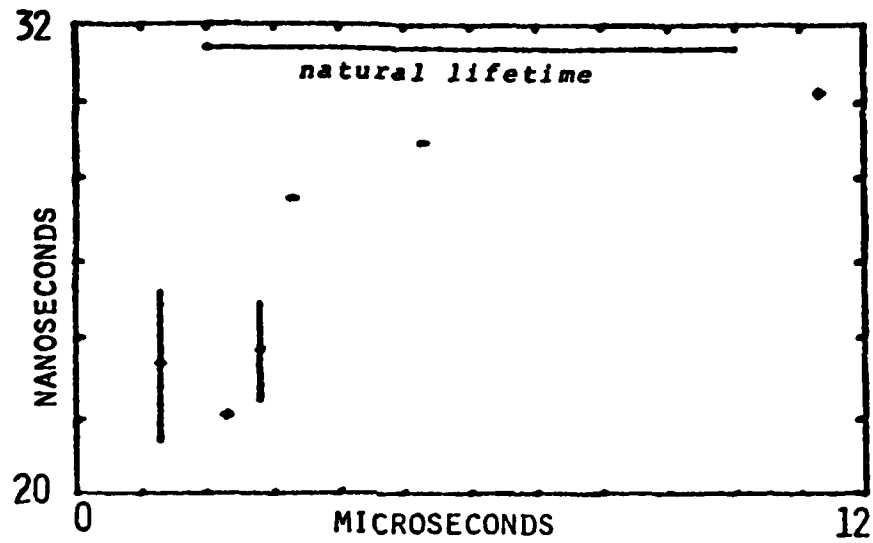


FIG. 37 ISE DECAY TIME CONSTANT VS DELAY TIME.

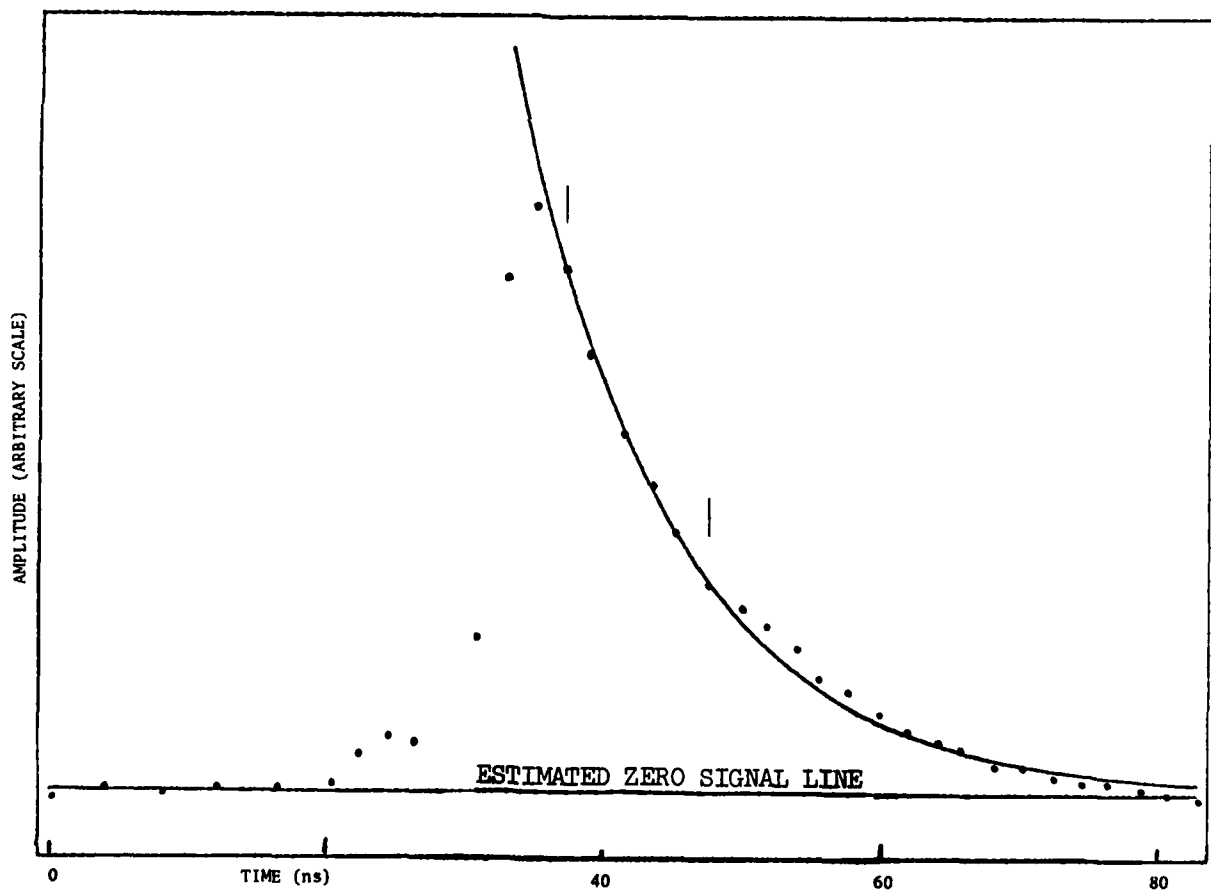


FIG. 38 CURVE FIT OF AN EXPONENTIAL DECAY TO THE DATA SHOWN IN FIG. 33.

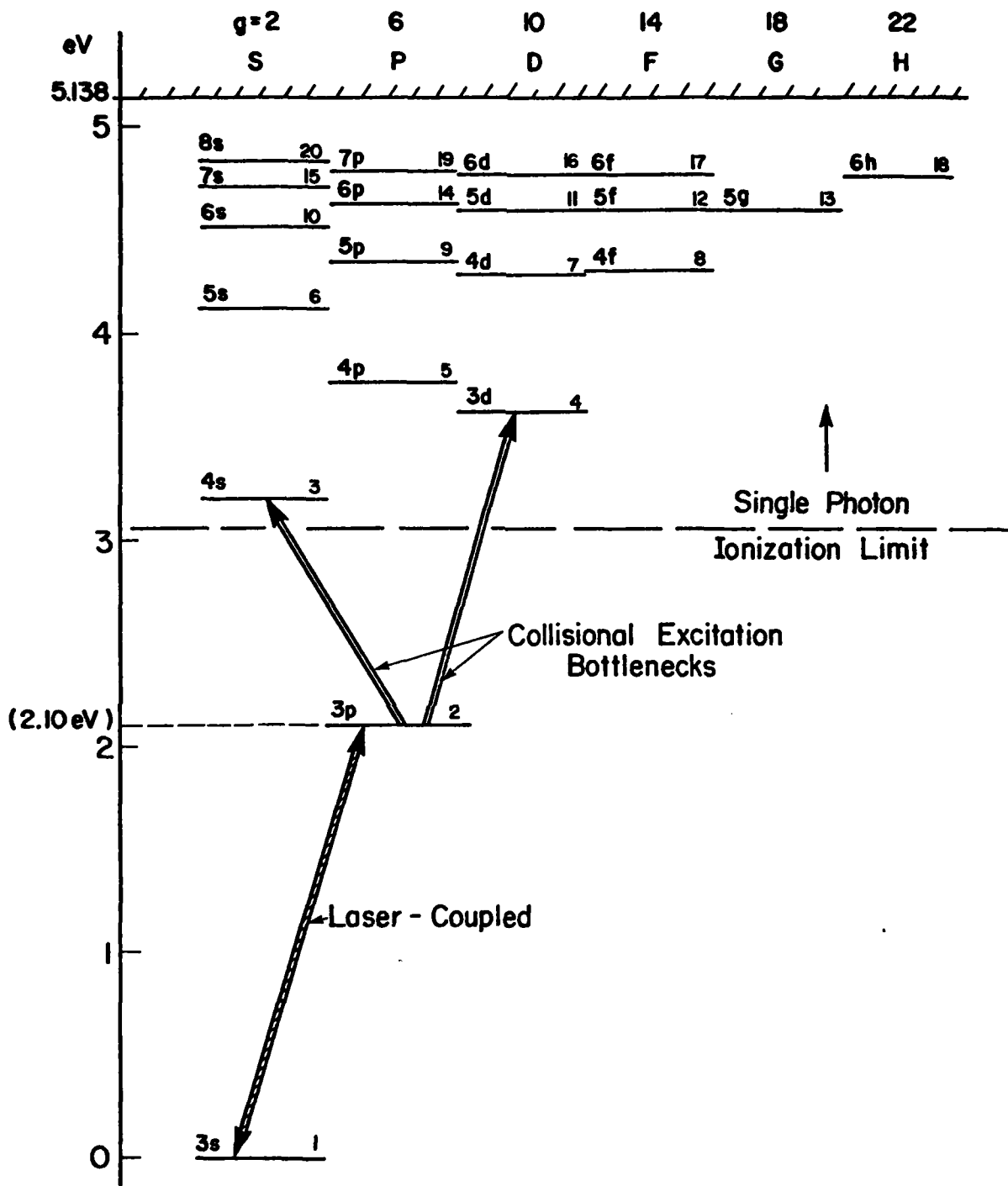


FIG. 39 SODIUM ENERGY LEVELS SCHEME USED IN LIBORS PROGRAM.

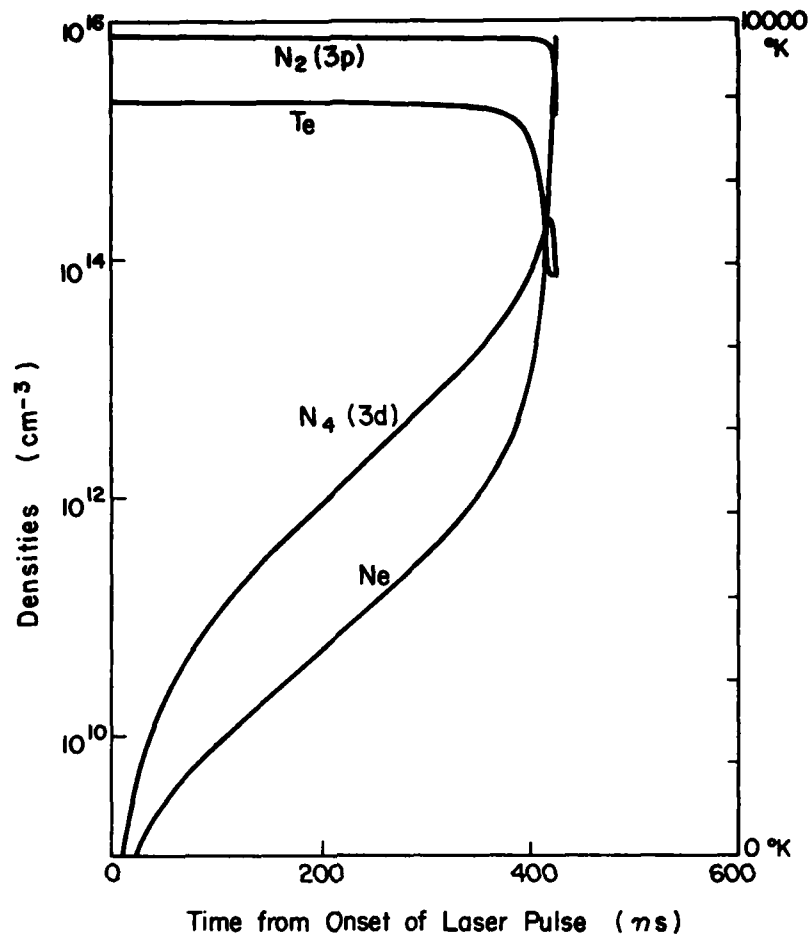


FIG. 40 LIBORS VARIATION OF POPULATION DENSITIES AND ELECTRON TEMPERATURE.

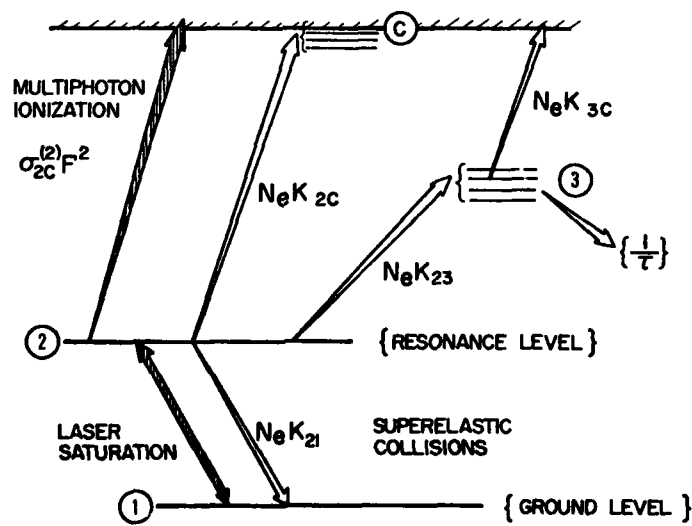


FIG. 41 SIMPLE MODEL OF LASER IONIZATION BASED ON RESONANCE SATURATION (LIBORS).

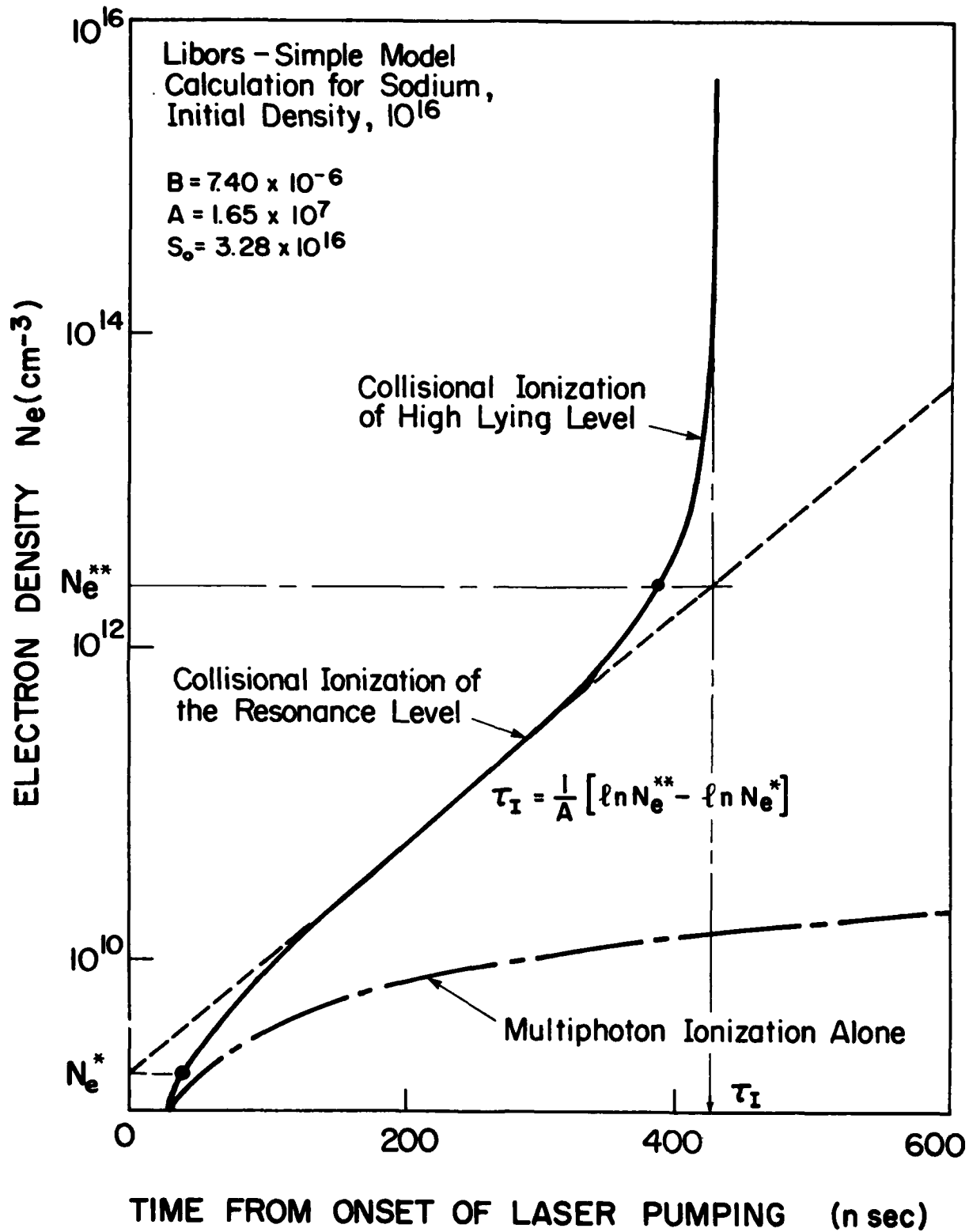


FIG. 42 "LIBORS" - SIMPLE MODEL IONIZATION CURVE.

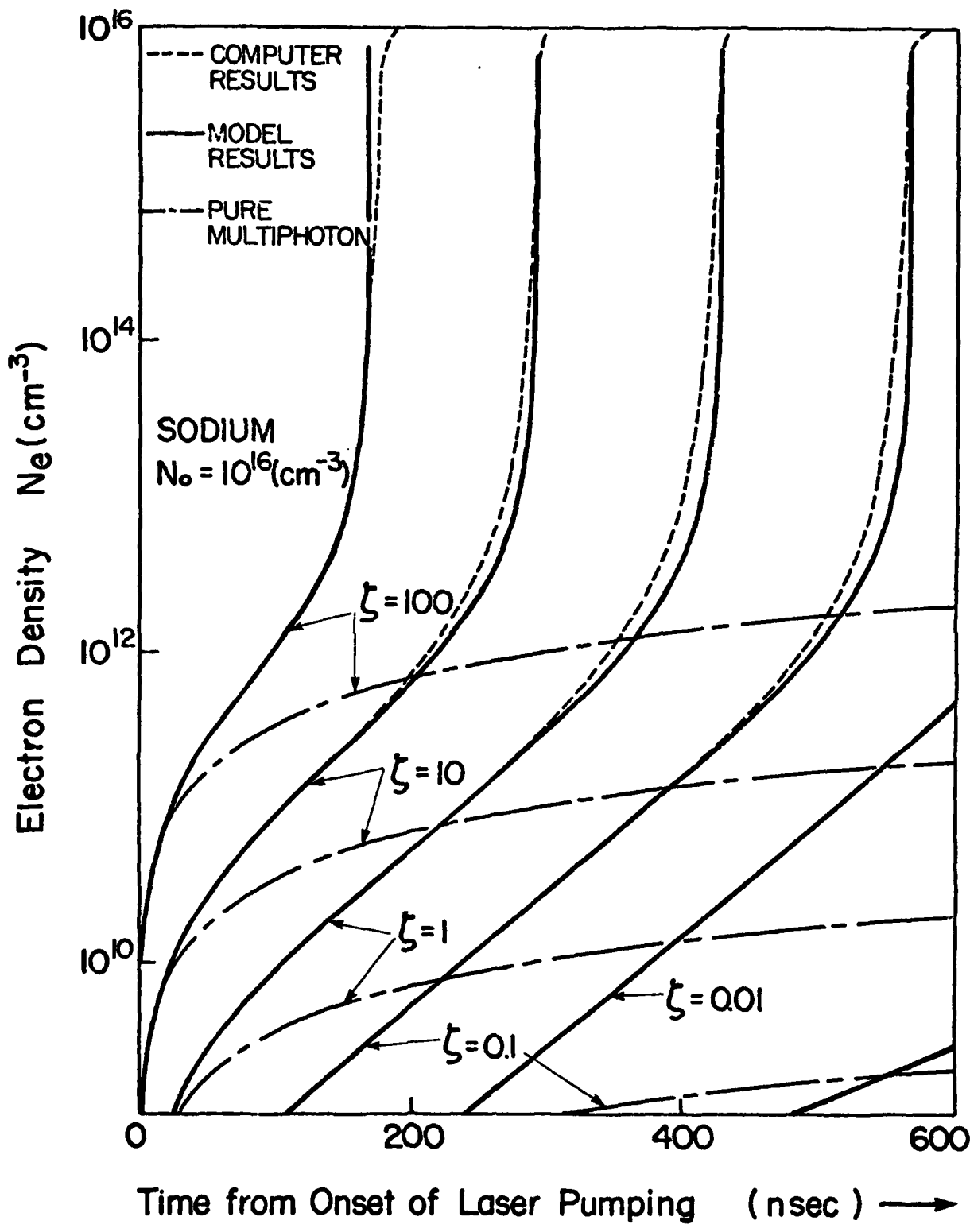


FIG. 43 COMPARISON OF SIMPLE MODEL AND COMPUTER CALCULATIONS.

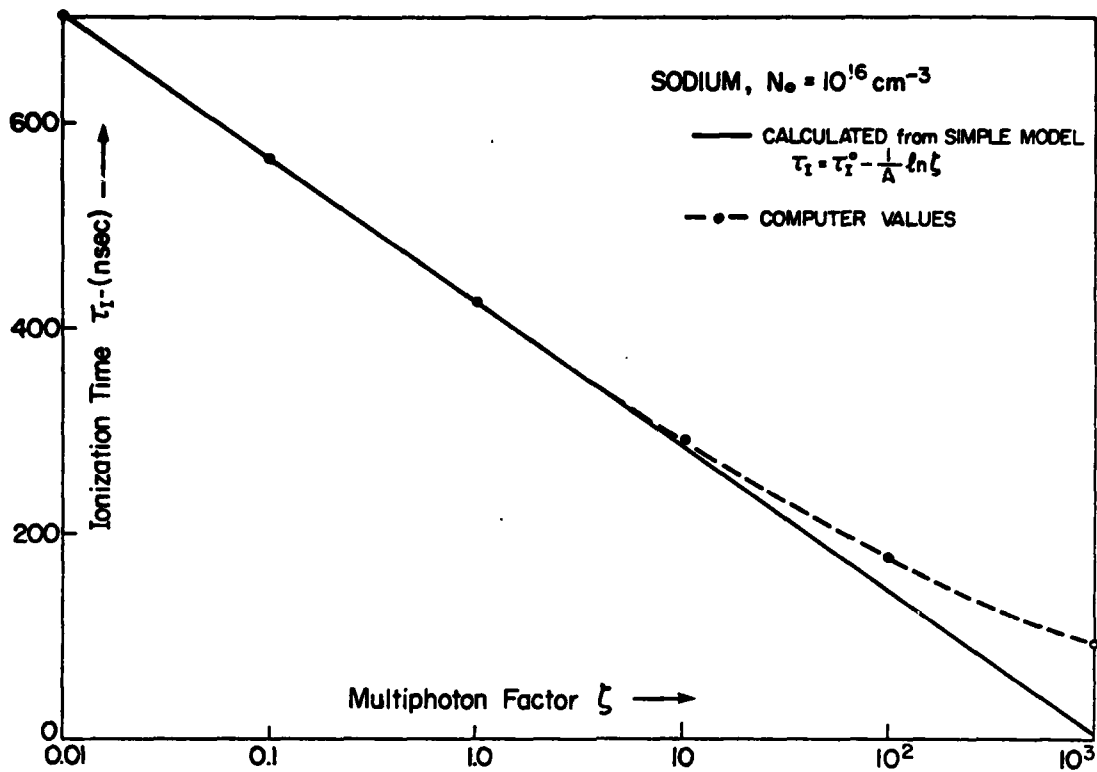


FIG. 44 VARIATION OF IONIZATION TIME WITH "MULTIPHOTON FACTOR ζ ".

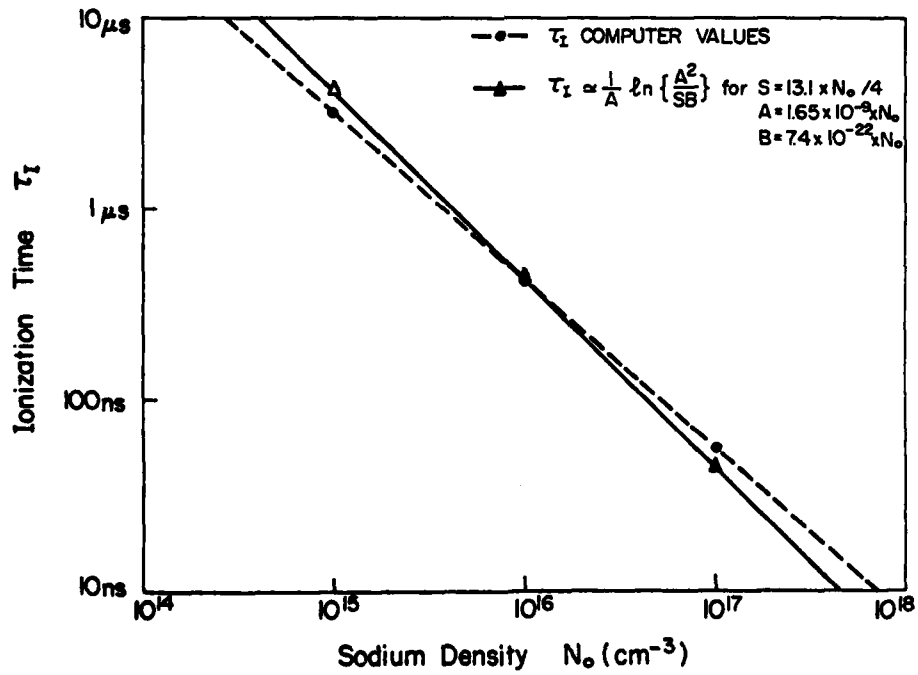


FIG. 45 VARIATION OF IONIZATION TIME WITH SODIUM DENSITY.

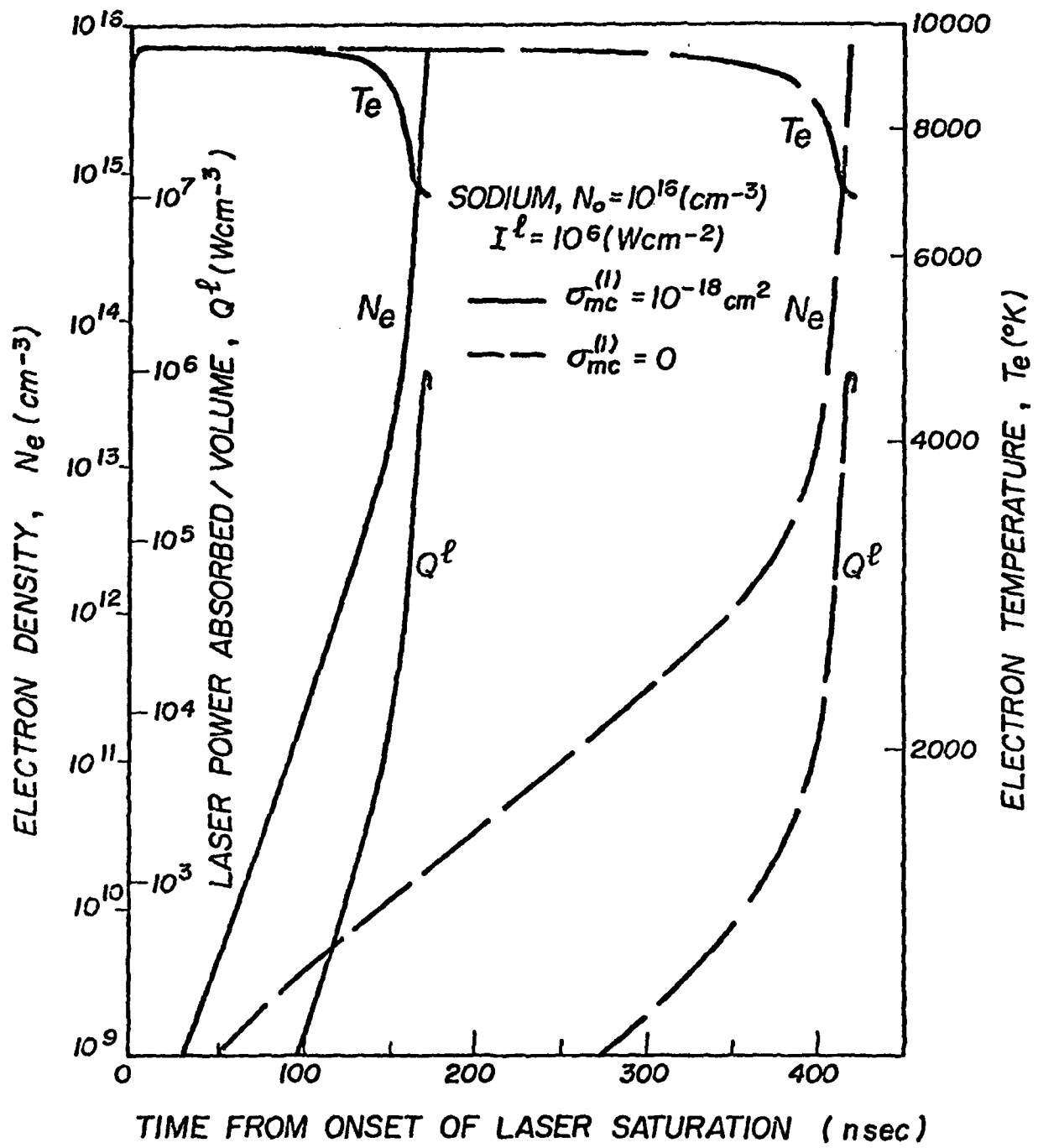


FIG. 46 LIBORS RESULTS SHOWING THE EFFECT OF INCLUDING SINGLE-PHOTON IONIZATION IN REDUCING IONIZATION TIME.

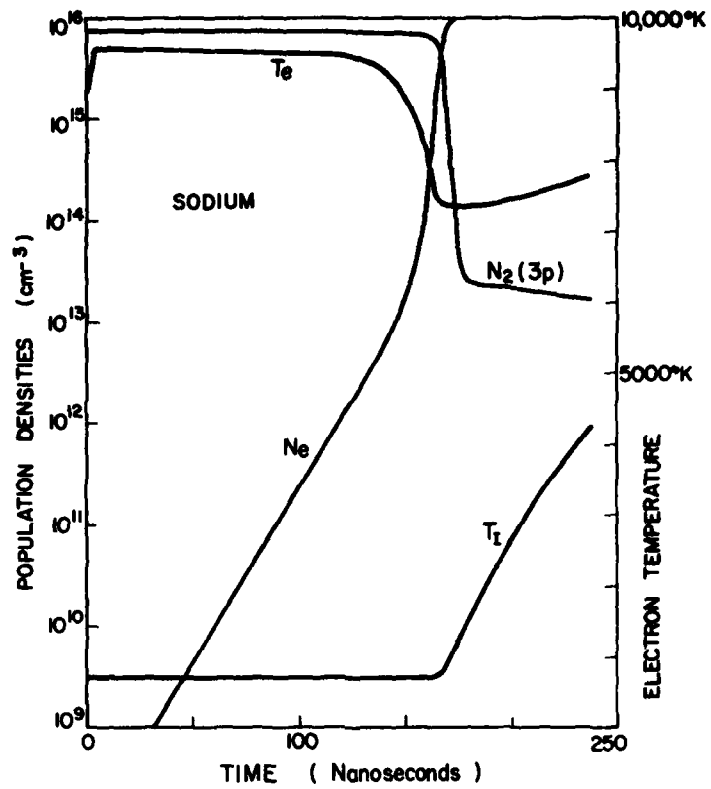


FIG. 47

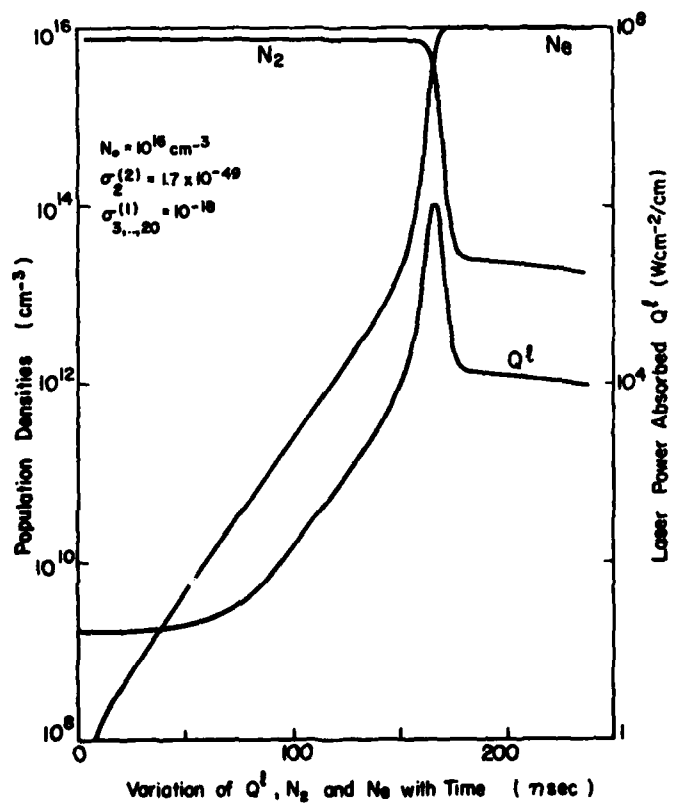


FIG. 48

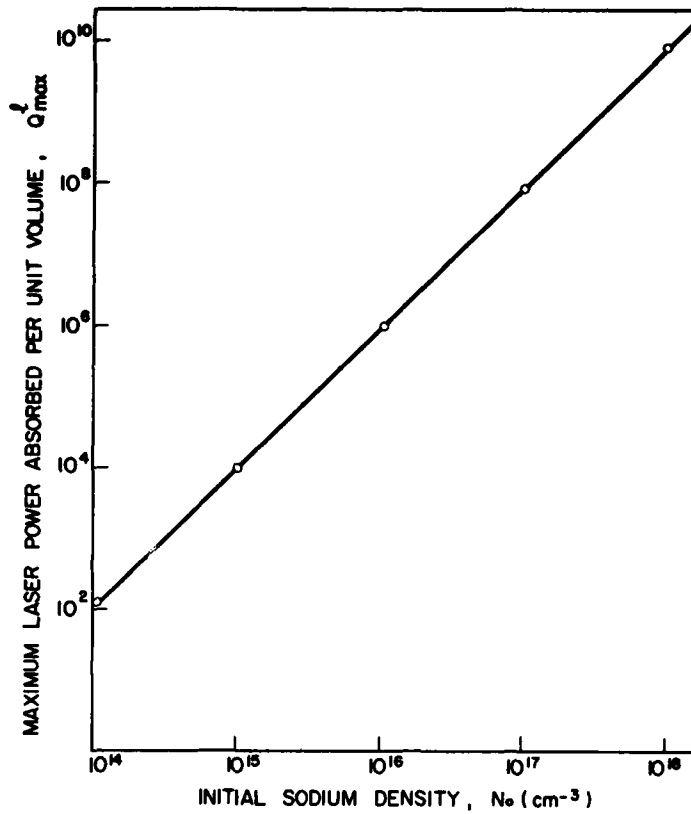


FIG. 49 PEAK POWER ABSORBED DURING IONIZATION BURN-OUT: LIBORS OUTPUT \circ , EQ. (7.5.3) —.

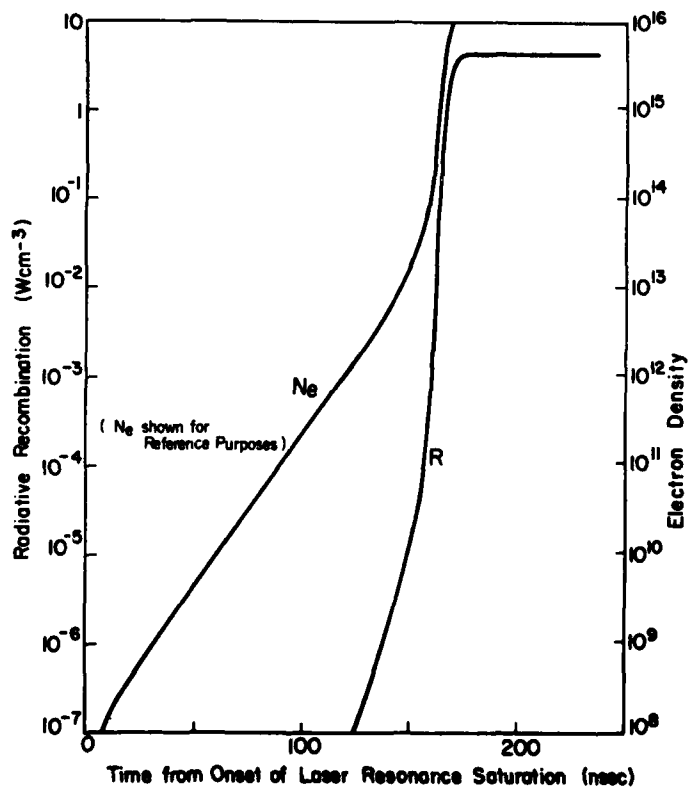


FIG 50 POWER EMITTED (W CM^{-3}) DUE TO RADIATIVE RECOMBINATION INTO RESONANCE LEVEL.

APPENDIX A

COLLISION RATE COEFFICIENTS

Collision rate coefficients for upward transitions describe phenomenologically the rate at which collision impact excitation and ionization occurs under various experimental conditions of a plasma. In general, collisions only between electrons and atoms (as opposed to atom-atom collisions) are considered because the relevant cross-sections are large and because the speed of the electrons is generally much higher (due to their smaller mass) than that of the atoms. For example, compared with sodium atoms of comparable kinetic energy, electron speeds are 200 times higher. Collision times for 700°K sodium atoms of 10^{16} cm^{-3} density are typically 100 ns (assuming a cross-section of 10^{-14} cm^2). This is of the same order as a typical LIBORS ionization time (see Chapter 7). Atom-atom collisions can therefore be neglected in the LIBORS context.

It is not our purpose to detail the calculation of the electron collision rate coefficients, but for the sake of completeness, we outline the calculation of these coefficients by Jaskolka (1969) and Cardinal (1979) using formulae provided in the literature as they apply to our LIBORS program. The theoretical work underlying these formulae is not exact and the resultant formulae are considered accurate only to within a factor of two (Elton, 1970).

Electron collision rate coefficients which apply to bound-bound transitions have been treated in the literature as belonging in general to two classes. One class contains those coefficients which apply to optically allowed transitions; the other class covers forbidden transitions. Elton (1970) cites a formula for the collision rate for allowed transitions under the assumption of a Maxwellian speed distribution for electrons:

$$K_{ij} (\text{cm}^3 \text{ sec}^{-1}) = \frac{1.6 \times 10^5 f_{ij} \langle \bar{g} \rangle}{\Delta E (kT)^{1/2}} \exp \left(- \frac{\Delta E}{kT} \right) \quad (\text{A1})$$

where ΔE is the threshold energy in eV,

kT_e is in eV,

f_{ij} is the oscillator strength of the transition

and $\langle \bar{g} \rangle$ is the effective Gaunt factor averaged over the Maxwellian.

Elton (1970) provides a graphical representation of $\langle \bar{g} \rangle$ as a function of $\Delta E/kT$. Cardinal (1979) has calculated the relevant excitation rate coefficients for sodium.

No formula as simple as (A1) is available for forbidden transitions (Elton, 1970), however, Gryzinski (1965) has treated classically the electron impact excitation and ionization of atoms taking no account of selection rules for dipole transitions. He derives an equation for the cross-section characterizing a collision where the incoming electron of energy ϵ loses energy

greater than U when encountering an atomic electron in level i with ionization energy ϵ_{ci} :

$$\sigma = \frac{\sigma_0}{U^2} f_E \left\{ \frac{U}{\epsilon_{ci}} + \frac{2}{3} \left(1 - \frac{U}{2\epsilon_{ci}} \right) \ln \left[2.7 + \left(\frac{\epsilon - U}{\epsilon_{ci}} \right) \right] \right\} \left(1 - \frac{U}{\epsilon} \right)^{1 + \frac{\epsilon_{ci}}{\epsilon_{ci} + U}} \quad (A2)$$

where $\sigma_0 = 6.56 \times 10^{-14} \text{ cm}^2 \text{ eV}^2$, U , ϵ , ϵ_{ci} are in eV, and

$$f_E = \frac{\epsilon_{ci}}{\epsilon} \left(\frac{\epsilon}{\epsilon + \epsilon_{ci}} \right)^{3/2}$$

By setting $U = \epsilon_{ci}$ in (A2) we get the cross section σ_{ic} for ionization from level i . The excitation cross-section from level i to j is obtained by taking the difference between two values of σ from (A2):

$$\sigma_{ij} = \sigma(U = \epsilon_{cj}) - \sigma(U = \epsilon_{ck}) \quad (A3)$$

where k refers to the next higher lying state above level j .

In order to evaluate the rate coefficients, the cross-sections must be integrated over the speed distribution of the free electrons. By assuming a Maxwellian distribution, Jaskolka (1969) has written a computer program to integrate the excitation and ionization cross sections numerically for any given electron temperature.

The equivalent downward rates were evaluated at a given T_e by detailed balancing. For bound-bound transitions, the Boltzmann factor and the ratio of degeneracies of the levels must be taken into account. For the case of impact ionization, the inverse process is three body recombination and this rate coefficient, K_{ci} , is evaluated from the ionization coefficient by making use of the Saha equation.

The excitation rate coefficient of the resonance level of sodium was calculated by Cardinal (1979) based on the paper by Crandall et al (1974) which in turn is based on the experimental work of others. The rate coefficient thus derived was assumed more accurate than any theoretical calculation.

APPENDIX B

PHOTOIONIZATION RATE COEFFICIENT $\sigma_i^{(k)}$ —

At the high spectral irradiances made possible with lasers, nonlinear interactions with atomic systems become an important component of the total interaction. One such nonlinear interaction is multiphoton ionization.

According to Bebb (1967), the frequency-integrated transition rate for three-photon ionization of sodium can be expressed in the form

$$W_{1c}^{(3)} = \sigma_1^{(3)} F^3 \quad (B1)$$

where 1 and c are the ground and continuum states, respectively,

$\sigma_1^{(3)}$ is the 3-photon ionization rate coefficient ($\text{cm}^6 \text{sec}^2$),

F is the laser photon flux density ($\text{cm}^{-2} \text{sec}^{-1}$).

Also implicit in (B1) is the assumption that three times the laser photon energy $3h\nu$ is in excess of the ionization energy ϵ_{c1} ; i.e., $3h\nu > \epsilon_{c1}$.

If the laser is tuned to the first resonance transition and the transition becomes saturated as a result, then the frequency-integrated transition rate will become a function of F^2 :

$$W_{2c}^{(2)} = \sigma_2^{(2)} F^2 \quad (B2)$$

where $\sigma_1^{(3)}$ and $\sigma_2^{(2)}$ are related by

$$\sigma_1^{(3)} = \sigma_2^{(2)} R$$

where R depends only on the properties of the resonance transition (Cardinal, 1979).

By using the above equations, Cardinal (1979) has calculated $\sigma_2^{(2)}$ for the sodium resonance D lines. The values thus obtained were used in the LIBORS calculations (see Chapter 7).

APPENDIX C

OSCILLOSCOPE PHOTOGRAPH ANALYSIS FOR ISE DECAY TIMES

The analysis of the oscilloscope photos of the ISE signal was done by digitizing the ISE signal with the Tektronix 4662 Interactive Plotter, and processing the data with the Tektronix 4051 Graphic Display System to which the Plotter was interfaced. Due to the random access memory limitations of our 4051 Display System, the analysis was split into two programs. Program 1 controlled the Plotter for purposes of digitizing the ISE signal. This program also had the capability to execute a linear regression routine on the logarithm of the ISE signal, but its primary function, after digitization, was to record the data on the magnetic tape cassette which is an integral part of the 4051 Display System. Program 2 read the data from the tape and calculated decay time constants using the same linear regression routine as used by Program 1. In addition, Program 2 had the capability of accumulating the data from any number of oscilloscope photos stored on the cassette. A given set of data could also be subtracted out from a set of accumulated data. Program 1 is described first, followed by a description of Program 2. A listing of the two programs appears in Fig. C2. In what follows, it is assumed that the reader is familiar with the operation of the Display System and the Plotter.

Before continuing, it is worth stressing two points: (a) extensive use is made of the User Definable Keys (UDK's) which allow the operator to control program flow to a large extent. In certain parts of the program, operations follow an automatic sequence, whereas at other points, an operator decision is implemented through the use of the UDK's; (b) a subroutine is provided in the program which correctly positions the cursor at the start of each message appearing on the screen, in order that these messages be placed in an orderly fashion. This subroutine will not be explicitly referred to in the following discussion.

The digitization procedure is started by checking data statement 130 to ensure that the ten horizontal deflection factors of the oscilloscope photo are correct (i.e., ns per major division for each of the ten major divisions). The photo is then attached to the plotter surface such that the vertical and horizontal axes are aligned with the corresponding plotter axes. The plotter viewport is set to comfortably bracket the graticule on the photograph, and RUN is typed in on the keyboard.

The System draws two graph outlines on the screen and asks for an identifier (20 character label) which will be attached to the particular ISE signal. The reason for the outlines will become obvious later. The System then asks for the number, U, of major divisions (maximum 6) required to span the region of the ISE from which data will be digitized. It is understood that the first data point to be digitized corresponds on the time axis to a major vertical line of the graticule. The last parameter to be entered from the keyboard is the number, U1, of the major division along the time axis at which digitization starts. An instruction to enter the zero signal reference line then appears on the screen. Figure C1 shows the points to be entered from the plotter (by pressing the CALL button) in relation to the data entered earlier from the keyboard.

During this sequence, the Display System samples the plotter status immediately after each CALL to ensure that the cursor is "down", in contact with the photograph. If the cursor is "up", a message appears on the screen, if "down", the Display System buzzer sounds to indicate its acceptance of the data point, and the number of the point in the sequence appears on the screen. After the total number, $U + 1$, have been entered, another message appears and the buzzer rings once again.

These entered data points serve two functions. First, they serve as accurate time benchmarks because the distance between them (on the time axis) is given by the appropriate quantities in DATA statement 130. Second, the Display System, upon entry of the last point of the zero reference line, immediately calculates the linear regression coefficients (see Baird, 1962) which define a line best fitting these points in a least squares sense. The routine is contained in a subroutine starting at line 1230.

The slope $T1$ of this line is stored, and the intercept $B1$ of the line (using vertical graticule line 1 in Fig. C1 as a reference) is also stored. Both quantities are expressed in plotter graphic display units (GDU's).

After $T1$ and $B1$ are stored, the program goes into a data acquisition mode. Vertical graticule line 1 in Fig. C1 is used as the $t = 0$ reference point (which equals the x-coordinate of the first time benchmark).

The x-coordinate of the first data point is calculated in GDU's and the position of an "error" band 0.8 ns wide is also calculated in GDU's using the time benchmarks read in previously, and the horizontal deflection factors appearing in DATA statement 130. The Display System continually samples the plotter cursor position while the operator moves the cursor to point A (see Fig. C1). Once the cursor x-position is within 0.4 ns of the desired x-position (i.e., within the error band), the buzzer alerts the operator and the Display System waits for a data point entry (by the operator pressing the CALL button on the Plotter). If the cursor at this time is in the "up" position, the operator is instructed to lower the cursor.

The operator moves the cursor vertically until the cross-hairs are centred on the trace, then enters the point. If the cursor x-position is still within 0.4 ns of the desired point, the x and y positions are accepted and the buzzer notifies the operator of such acceptance. If the x-coordinate is out of bounds, the Display System reverts to sampling the x-position of the cursor until the operator has correctly positioned the cursor within 0.4 ns of the desired point. The data entry procedure must then be repeated until the data point is accepted. Upon acceptance the GDU's are converted to height and time coordinates. The time coordinate is calculated by linear interpolation from the two nearest benchmarks. The time coordinate is then used to calculate the vertical position in GDU's of the zero signal line by using the regression coefficients $T1$ and $B1$. This coordinate is subtracted from the y coordinate read in to arrive at a true ISE signal height in arbitrary units. The datum point thus generated is immediately plotted on the screen, the left hand graph using a linear scale, and the right hand graph using a logarithmic vertical scale.

At this point the calculation of the new x-position of the cursor and the error band proceeds, followed by the Display System sampling the plotter to

find the true cursor x-position. The operator then positions the cursor to enter the next point, following the procedure outlined above. In this way, all the points are entered, at which time the buzzer sounds and an appropriate message appears on the screen. The program execution stops and one of the UDK's must be depressed to continue the program.

A discussion of the options available through the UDK's is helpful in indicating the scope and flexibility of the program. These UDK's will function at any point during or after the data digitization procedure.

Key No. 9 allows the operator to repeat an entry if a mistake was made the first time the entry occurred. Repeatedly depressing key No. 9 allows backstepping through the points to any previous point. This key works only for the ISE signal digitization, not for the zero signal line.

Key No. 20 allows the operator to re-enter the entire ISE signal, using the zero reference line already stored in the Display System.

Key No. 10 allows the operator to restart the entire procedure, including the zero reference line.

Key No. 16 allows the operator to draw a new graph outline on the screen.

Key No. 11 allows the operator to replot the data points already in the machine.

Key No. 13 instructs the Display System to calculate the decay constant of the data in the machine by using a linear regression routine which gives equal weight to all data points. The corresponding standard deviation is also calculated (Baird, 1962).

Key No. 14 allows the operator to store the data on the cassette tape, along with other variables for purposes of cataloging and further data analysis. The decay constant is automatically calculated with standard deviation before transfer to tape takes place. The organization of the cassette tape is discussed below.

Files 1 and 2 contain Programs 1 and 2 respectively. File 3 is a catalogue of the data sets stored on the rest of the files 4, ..., n. For each data set on tape, file 3 contains the file number, identifier, and decay constant with standard deviation, respectively as a listing in a catalogue.

The sequence of events which occurs when key No. 13 is depressed is as follows. The linear regression routine is called to calculate decay constant and standard deviation. The standard deviation is coded into the number representing the decay constant so that, for example, 32.07 ± 0.35 becomes 32.070035. This encoding was necessary in order to keep new versions of the program which calculated standard deviations compatible with older versions with respect to tape formatting. File 3 is searched by the program for an "end of file" (EOF) mark, at which point the new file number is calculated by incrementing the last read file number by one. The new file number, identifier, and coded decay constant are then written on file 3. The new file is then located, marked, and the data is then stored in the following order. The identifier, encoded decay constant, and number of data points are recorded first, followed by the time benchmarks, zero line regression

coefficients, the ISE heights (i.e., y-coordinates), and the ISE time coordinates. Finally a message appears on screen indicating the new file number.

Program 2 extends the data manipulation capabilities of Program 1, but no plotter operations are possible. A brief description of the program is given, followed by a description of the UDK's useable with this program.

Program 2 is used to call up a given record from the tape, identified by its file number. The data are automatically stored in a temporary register. The data can be added to, or subtracted from the accumulation register, which may contain the sum of other records from the tape. The data from a given record are weighted before being added into the accumulation register, each y-coordinate of the record is normalized by dividing it by the sum of all y-coordinates of that record. The data from a given record are subtracted from the accumulation register by simply changing the sign of each datum point in the temporary register, then adding the contents to the accumulation register. The end points of the set of data used by the regression routine are adjustable, and the regression routine can be applied to the data in the temporary or accumulation register. The contents of either register can be plotted on the screen on a log scale, and at the termination of the regression routine, the calculated line is automatically drawn through the points on the screen.

The functions of the user-definable keys (UDK's) are as follows.

Key No. 10 allows the operator to call up a new record from the tape. After the file number is entered, the appropriate record from the tape is stored in the temporary register, and the record is identified on the screen.

Key No. 16 draws the outline of the graph on the screen.

Key No. 11(1) plots the data in the temporary (accumulation) register.

Key No. 13(3) executes the linear regression routine on the data in the temporary (accumulation) register.

Key No. 15 resets the accumulation register to zero.

Key No. 8(18) adds (subtracts) the data in the temporary register to the accumulation register.

Key No. 6 allows the operator to select the end points to be used in the regression routine. After use of this key, bash marks appear below the appropriate data points on the screen whenever the data are plotted from either register. When the program is first run, the end point numbers assume their default values (1 and 31).

Key No. 7 allows the operator to revert the end points to their default values.

Key No. 14 allows the operator to store the contents of the accumulation register on the cassette tape. The Display System first requests a label to be attached to the record (maximum 20 characters). The process involved in writing on tape is the same one used by Program 1.

Key No. 12 displays the label of the record currently in the temporary register.

Key No. 4 displays the labels of all records on the tape including the calculated lifetimes and standard deviations.

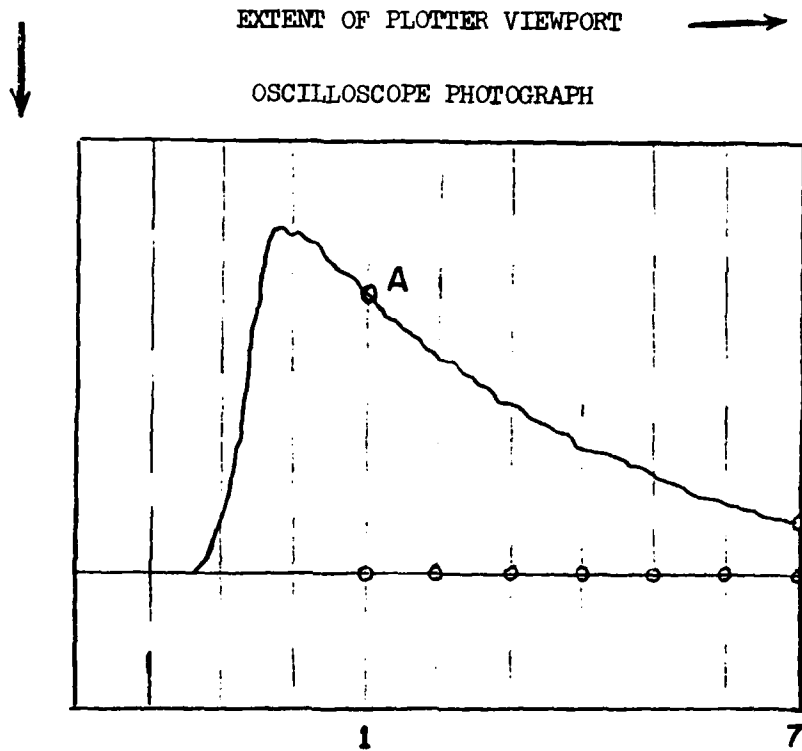


FIG. C1 OSCILLOSCOPE PHOTO ON PLOTTER SURFACE SHOWING DATA POINTS ENTERED WHICH DEFINE THE ZERO SIGNAL REFERENCE LINE. ALSO SHOWN IS THE FIRST, "A", AND LAST DIGITIZED DATA POINTS OF THE "ISE" SIGNAL. HERE $U = 6$, $U_1 = 5$. FOR CLARITY, THE HORIZONTAL GRATICULE LINES ARE NOT SHOWN.

```

1 GO TO 100
36 SET NOKEY
37 J=J-1
38 GO TO 1800
40 GO TO 320
44 SET NOKEY
45 GO TO 2000
46 SET KEY
47 RETURN
52 GOSUB 1230
53 T0=-1/T0
54 PRINT USING 1650:T0,S0
55 RETURN
56 GOSUB 1230
57 T0=0.01*INT(100*(-1/T0))+50/10000
58 GOSUB 1660
59 RETURN
64 GOSUB 200
65 RETURN
68 GO TO 440
100 INIT
110 SET KEY
120 DIM C$(20),D$(20),A(31),T(31),Z0(7),E$(13),K0(6)
130 DATA 10.1,10.1,10.1,10.1,10.1,10.1,10.1
140 E$="Lower the pen"
230 PAGE
260 GOSUB 200
270 GO TO 920
280 R1=0
282 GOSUB 1600
284 R1=0
290 MOVE 0,100
300 DRAW 0,50
310 DRAW 130,50

```

```

320 DRAW 130,100
330 DRAW 0,100
340 MOVE 65,100
350 DRAW 65,50
360 MOVE 0,45
380 RETURN
440 RESTORE
450 READ K0
460 Z0(I)=0
470 I=0
480 A=0
490 O=1
500 J=0
510 P=0
520 S=1
510 FOR I=1 TO U
520 Z0(I+1)=Z0(I)+K0(I)
530 NEXT I
545 XI=X0
546 GO TO 560
550 GOSUB 1300
560 J=J+1
570 L=2*G1/K0(Q)/5
580 INPUT #1,24: X,Y,Z
590 IF ABS(X-XI)>L THEN G10
600 GO TO 580
610 PRINT "G1"
620 IF Z=1 THEN G70
630 GOSUB 1600
640 PRINT E$1
650 INPUT #1,27: X,Y,Z
660 GO TO 580
670 INPUT #1,27: X,Y,Z
680 IF ABS(X-XI)>L THEN G70
690 GO TO 580

```

```

700 PRINT "G1"
710 GOSUB 1500
720 GOSUB 750
730 IF J>30 THEN G50
740 GO TO 350
750 VIEWPORT 0,65,50,100
760 WINDOW 0,60,0,100
770 IF J<2 THEN G80
780 MOVE T(J-1),A(J-1)
790 DRAW T(J),A(J)
800 VIEWPORT 65,130,50,100
810 WINDOW 0,60,1,LOG(100)
820 MOVE T(J),LOG(A(J))
830 DRAW T(J),LOG(A(J))
840 RETURN
850 GOSUB 1600
855 PRINT "GGGGG"
860 PRINT "31 Points read"
870 J=32
900 EMO
910 GO TO 900
920 GOSUB 1600
930 PRINT "Identifier"
940 INPUT C$
950 GOSUB 1600
960 GOSUB 1600
961 PRINT "No. of div? max 6  "
962 INPUT U
963 IF U>6 THEN G950
965 GOSUB 1600
970 PRINT "New zeroes ?"
975 J=1
980 INPUT #1,27:T(J),A(J)
985 INPUT #1,24: X,Y,Z
1000 IF Z=1 THEN 1035

```

```

1010 GOSUB 1600
1020 PRINT E$1
1030 GO TO 990
1035 PRINT "G1"
1036 PRINT J1
1037 A(J)=EXP(A(J))
1038 J=J+1
1040 IF J<U+2 THEN G990
1042 GOSUB 1230
1045 T1=T0
1048 X0=T(I)
1050 G1=(T(U+1)-T(I))/U
1052 B1=B0+T0*X0
1060 RESTORE
1070 READ K0
1080 Z0(I)=0
1090 FOR I=1 TO U
1100 Z0(I+1)=Z0(I)+K0(I)
1110 NEXT I
1120 GOSUB 1600
1130 PRINT "Zero line entered"
1135 PRINT "G1"
1140 GO TO 440
1230 SET NOKEY
1235 S1=0
1240 S2=0
1250 X=0
1260 Y=0
1265 Z=0
1270 FOR I=1 TO J-1
1280 S1=S1+T(I)
1290 S2=S2+LOG(A(I))
1300 X=X+T(I)*LOG(A(I))
1305 Z=Z+T(I)*T(I)
1310 NEXT I

```

```

1320 FOR I=1 TO J-1
1330 Y=Y+(S1/(J-I)-T(I))/2
1340 NEXT I
1350 T0=(X-S1*S2/(J-1))/Y
1360 B0=(S2-S1*T0)/(J-1)
1361 IF J=4 THEN 1364
1362 S0=99.99
1363 GO TO 1379
1364 Y=0
1365 FOR I=1 TO J-1
1366 Y=Y+(LOG(A(I))-T(I)*T0-B0)/2
1367 NEXT I
1368 S0=0.01*INT(100*S0*(Y/(J-1)-(Z/(J-1)-S1*S2)/(J-3))/T0/T0)
1372 VIEWPORT 65,130,50,100
1373 WINDOW 0,60,1,LOG(100)
1374 MOVE -10,-10*T0+B0
1375 DRAW 100,100*T0+B0
1378 GOSUB 1600
1379 SET KEY
1380 RETURN
1390 XI=XI+2*G1/K0(Q)
1400 R=2*G1/K0(Q)
1410 IF R<G1 THEN 1450
1415 IF Q>U-1 THEN 1450
1420 O=O+1
1430 XI=XI-(R-G1)*(1-K0(O-1))/K0(O)
1440 R=(R-G1)*K0(O-1)/K0(O)
1450 RETURN
1500 T(J)=Z0(S)+K0(S)*X-X0-(S-1)*G1/G1
1510 IF T(J)<Z0(S+1) THEN 1540
1520 S=S+1
1530 GO TO 1500
1540 A(J)=Y-T1*(X-X0)-B1
1550 RETURN
1600 WINDOW 0,130,0,100

```

```

1610 VIEWPORT 0,130,0,100
1620 MOVE 35*INT(R1/11),46-4*R1+44*INT(R1/11)
1630 R1=R1+1
1640 RETURN
1650 IMAGE "Tau=-,2D.2D,X,(", 2D.2D,") nsec"
1660 SET NOKEY
1665 FIND 3
1670 CN EOF (0) THEN 1700
1675 Z=1
1680 READ #33: Y,D$,X
1685 IF Z=2 THEN 1790
1690 GO TO 1680
1700 WRITE Y+1,C$,T0
1705 OFF EOF (0)
1710 FIND Y+1
1720 MARK 1,1000
1730 FIND Y
1735 Z=2
1740 FIND Y+1
1750 WRITE C$,T0,J-1,Z0,B1,T1,A,T
1760 FIND Y
1770 GOSUB 1600
1780 PRINT "In file no. "Y+1
1785 SET KEY
1790 RETURN
1800 O=1
1810 R=0
1815 X1=X0
1820 FOR I=1 TO J-1
1830 GOSUB 1390
1840 NEXT I
1850 SET KEY
1860 GO TO 580
2000 K=J
2002 FOR J=1 TO K-1
2010 GOSUB 750
2020 NEXT J
2025 J=K
2030 GO TO 46

```

FIGURE C2

PROGRAM 1

```

1 GO TO 100
4 GOSUB 000
5 RETURN
12 GOSUB 1600
13 PRINT "Acc. Date"
14 GO TO 500
15 RETURN
16 GOSUB 2200
17 RETURN
24 GO TO 600
25 RETURN
28 J1=1
29 J2=31
30 GO TO 750
31 RETURN
32 M=1
33 GOSUB 1900
34 PRINT "Summed"
35 RETURN
40 GO TO 920
41 GOSUB 1630
42 GO TO 850
44 GOSUB 1870
45 GOSUB 800
46 GOSUB 1870
47 RETURN
48 GOSUB 1600
49 PRINT C$1 ("J1")
50 RETURN
52 GO TO 450
53 RETURN
56 GOSUB 2000
57 RETURN
60 GO TO 170

```

```

61 RETURN
64 PAGE
65 GOSUB 1600
66 GOSUB 180
67 RETURN
72 M=-1
73 GOSUB 1800
74 PRINT "Subtracted"
75 RETURN
76 GOSUB 1600
77 RETURN
100 INIT
103 PRINT @33,0,0,0,0
110 SET KEY
120 DIM C$(20),A(31),T(31),U(31),M(31)
140 PAGE
150 GOSUB 200
155 GOSUB 170
160 GOSUB 20
165 GO TO 40
170 A=0
180 T=0
210 I1=0
215 I5=100
216 GOSUB 1600
217 PRINT "Acc. Reset"
220 RETURN
228 R1=-1
229 GOSUB 1600
230 MOVE -1,4,0
300 DRAM -1,2,4
310 DRAM 61,2,4
320 DRAM 61,4,0
330 DRAM -1,4,0

```

```

380 RETURN
400 GOSUB 1600
410 PRINT "Nothing in acc. "
420 GO TO 900
430 GOSUB 1870
440 GOSUB 1230
470 GOSUB 1870
480 PRINT INT(T0$100)/100 ("INT(100$0)/100") nsec"
490 GO TO 53
500 GOSUB 1230
501 PRINT INT(T0$100)/100 ("INT(100$0)/100") nsec"
510 GO TO 15
600 GOSUB 1600
610 PRINT "End-pts"
620 INPUT J1,J2
630 GOSUB 836
640 GO TO 25
700 GOSUB 1600
760 PRINT "Default gnd-pts"
770 GO TO 31
800 IF A(1)=0 THEN 400
811 FOR J=1 TO 31
820 MOVE T(J),LOG(A(J))
830 DRAM T(J),LOG(A(J))
832 NEXT J
835 RETURN
836 MOVE T(J2),LOG(A(J2))-0.1
837 DRAM T(J2),LOG(A(J2))-0.2
838 MOVE T(J1),LOG(A(J1))-0.2
839 DRAM T(J1),LOG(A(J1))-0.1
840 RETURN
850 GOSUB 1600
860 PRINT C$1
890 END
910 GO TO 900

```

```

920 GOSUB 1600
930 PRINT "File No.?"
940 INPUT N
950 GO TO 41
1000 Z=11
1002 IF I1>0 THEN 1006
1004 I1=1
1006 Y=Z*M$F19
1007 IF Y<0 THEN 1009
1008 Y=1
1009 FOR Q=1 TO 31
1010 A(Q)=(A(Q)*I1+M$S19M(Q))/Y
1020 T(Q)=(T(Q)*I1+M$S19T(Q))/Y
1030 NEXT Q
1040 I1=Z*M$F19
1050 GOSUB 1600
1060 RETURN
1070 FOR Q=1 TO 31
1080 Y=A(Q)
1090 A(Q)=M(Q)
1100 M(Q)=Y
1110 X=T(Q)
1120 T(Q)=U(Q)
1130 U(Q)=X
1140 M(Q)=Y
1150 NEXT Q
1160 RETURN
1230 S1=0
1235 IF A(1)=0 THEN 400
1240 S2=0
1250 M=0
1260 Y=0
1262 Z=0
1265 Q=Z-J1+1
1270 FOR I=1 TO J2
1280 S1=S1+T(I)

```

```

1290 S2=S2+LOG(A(I))
1300 N=N+T(I)*LOG(A(I))
1305 Z=Z+T(I)*S1(I)
1310 NEXT I
1315 S0=S1/Q
1320 FOR I=J1 TO J2
1330 Y=Y+(S0-T(I))*I^2
1340 NEXT I
1350 S3=C*(S0S2)/Y
1360 S0=S2/Q-S0*F19
1362 MOVE -10,-10*F19+00
1364 DRAM 100,100*F19+00
1365 T0=-1/F19
1366 IF Q>3 THEN 1370
1367 S0=S0*F19
1368 GO TO 1376
1370 S0=Y
1371
1372 FOR I=J1 TO J2
1373 Y=Y+LOG(A(I))-T(I)*F19+00*I^2
1374 NEXT I
1375 S0=S0*Y/(S0*(Q-2))/T0/F19
1376 T0=INT(T0$100)/100+INT(100$0)*1.0E-6
1379 GOSUB 1600
1380 RETURN
1600 HINDON 0,130,0,100
1610 VIEWPORT 0,130,0,100
1620 G=INT(R1/15)
1625 MOVE 3300,46-30R1+4500
1630 R1=R1+G
1634 HINDON 0,130,50,100
1634 VIEWPORT -1,51,2,4,4,0
1640 RETURN
1650 IMAGE 2T,3D,6T,20A,30T,3D,2D,36T,2A,30T,2D,2D,43T,1A
1690 FIND H

```

```

1695 I9=1
1699 READ @33:C0,T0,J,Z,Y,N,X,K,X,K,B1,T1,M,U
1700 N=RUN(N)/1450
1701 IF Y<0 THEN 1702
1702 I9=2
1703 FOR Q=1 TO 31
1704 M(Q)=M(Q)/X
1705 NEXT Q
1706 IF J>15 THEN 1710
1708 I5=J
1710 RETURN
2000 GOSUB 1600
2001 PRINT "Ident acc. data?"
2002 GOSUB 1600
2003 INPUT C$
2005 FIND 05
2010 ON EOF (0) THEN 2040
2015 Z=1
2020 READ @33:Y,D0,X
2025 IF Z=2 THEN 2140
2030 GO TO 2020
2040 WRITE Y,I,C0,T0
2045 OFF EOF (0)
2050 FIND Y+1
2060 MARK 1,700
2070 FIND Y
2075 Z=2
2080 FIND Y+1
2085 X=0
2090 WRITE C$,T0,I5,I1,X,Z,2,Z,2,Z,2,Z,A,T
2100 GOSUB 1600
2110 PRINT "File #? Y+1"
2120 RETURN
2200 FIND 05
2200 PAGE

```

```

2210 ON EOF (0) THEN 2260
2215 Z=1
2220 READ @33:Y,D0,X
2225 IF Z=2 THEN 2260
2230 G=100000*(X-INT(X$100))/100
2240 Q=0.01*INT(100$0)
2242 PRINT USING 1650:Y,D0,0.01*INT(100$0), ("I0")
2250 GO TO 2220
2255 OFF EOF (0)
2270 Z=2
2280 RETURN

```

FIGURE C2

PROGRAM 2

APPENDIX D

RAY TRACING ROUTINE

A ray tracing routine was developed in order to evaluate the sensitivity of the receiving optics (employed in the two-wavelength pumping experiment) to variations in dye laser beam radius and distance along the optical axis in the region of the system focal point. An analytical approach to this problem was abandoned because the distortions produced by the fast lens are of the same dimensions as the region of observation as defined by the diameter of the laser beam. The geometry is shown in Fig. D1. Light is considered to emanate from a uniform spatial distribution of points located inside a cylindrical volume representing a uniform distribution of atoms pumped by the dye laser beam. Part of this light will find its way through the system and onto the PMT photocathode by passing through the lenses and field stop. Losses at a lens-air interface are not considered. Coherence effects (such as diffraction) are not considered; nor are polarization effects considered. The problem is considered as one of geometrical optics, using Snell's law of refraction.

The obvious method of solution is to create a three-dimensional uniform grid inside the dye laser beam and from each grid point generate uniformly distributed (in angle) rays. The number of rays passing through the field stop as a function of dye laser beam position and radius is then a measure of the variation in system response as beam position and radius are changed. This method is inefficient because the grid used is three-dimensional, and because at each grid point many more rays are generated (and have to be traced at least partially through the system) than are actually used.

It is more efficient to create a uniform two-dimensional grid at the field stop and generate a uniform distribution (in angle) of rays at each grid point to pass through lens L_1 . The resultant ray emerging from L_2 is then sent through the focal region. The length of intersection of this ray with the cylindrical zone representing the laser beam is proportional to the relative efficiency of the system to the given beam geometry. For the given ray which has been calculated, the intersection distance is calculated for various beam radii and various beam positions, and the results are stored as elements of a matrix. With each additional ray calculated, the intersection distances are accumulated in the matrix. When all the rays have been processed, the matrix elements then represent the relative system efficiency as a function of beam position (along the optical axis of the system) and beam radius.

The efficiency of the program is further improved by making use of symmetry in the geometry. There are two planes of symmetry, each containing the optical axis of the system (see Fig. D1); we need therefore to construct a grid on only one quarter of the field stop, as shown in Fig. D1.

A development of a set of ray tracing equations is given below, followed by a brief discussion of the computer implementation and results.

The position of a general ray passing through the point x_0, y_0, z_0 is represented in a Cartesian coordinate system parametrically as,

$$x_0 + m, \quad y_0 + mk, \quad z_0 + ml \quad (D1)$$

where m is the free parameter,

x -axis is the optical axis (assumed horizontal),

y -axis is horizontal, perpendicular to the optical axis,

z -axis is vertical,

k is the slope of the ray projected on the x, y plane, and

l is the slope of the ray projected on the x, z plane.

The light is assumed to be moving in the positive x direction. The intersection point x_1, y_1, z_1 of this ray with an optical surface is calculated by substituting (D1) into the equation for the surface. A plane surface is rather uninteresting and will not be considered here. For a spherical surface, we define the radius as positive if the centre of curvature lies beyond the surface (is seen by the approaching ray), and negative otherwise. The equation of the surface is

$$(x - a)^2 + y^2 + z^2 = r^2 \quad (D2)$$

where the centre of curvature is located on the optical axis at $x = a$ and where the radius of curvature is r . For later convenience we define

$$c = a - r \quad (D3)$$

where c is the x -coordinate of the intersection of the surface and the optical axis. In fact the intersection point is $(c, 0, 0)$.

On substituting (D1) into (D3) we get

$$m = \frac{-B - \text{SIGN}(r)(B^2 - 4AS)^{1/2}}{2S} \quad (D4)$$

where $A = (x_0 - c)(x_0 - c - 2r) + y_0^2 + z_0^2$,

$B = 2(x_0 - a + y_0 k + z_0 l)$,

$S = 1 + k^2 + l^2$.

By substituting this value of m into (D1) we get (x_1, y_1, z_1) , the point of intersection. The equation of the new ray can now be written,

$$x_1 + m, \quad y_1 + mk_1, \quad z_1 + ml_1$$

where we need find only the new values for k and l (i.e., k_1 , l_1) due to refraction at the surface using Snell's law,

$$N_0 \sin \theta_0 = N_1 \sin \theta_1 \quad (D5)$$

where N_0 and N_1 are the respective refractive indices and θ_0 and θ_1 are the respective angles of incidence and refraction. To find $\sin \theta_0$, we first construct the vector normal to the surface at x_1 , y_1 , z_1 :

$$\underline{W} = (x_1 - a, y_1, z_1)$$

and without loss of generality define the incident vector

$$\underline{V}_0 = (1, k, l)$$

and calculate their cross product, whose components are t , u , v , where

$$t = kz_1 - ly_1, \quad u = l(x_1 - a) - z_1, \quad v = y_1 - k(x_1 - a)$$

It follows from the definition of the cross product that

$$\sin \theta_0 = \frac{(t^2 + u^2 + v^2)^{1/2}}{s^{1/2} |r|}$$

Again without loss of generality, we define the emerging ray propagating in the positive x direction

$$\underline{V}_1 = (1, k_1, l_1) \quad (D6)$$

Two conditions on \underline{V}_1 serve as a basis for calculating k_1 and l_1 :

$$\underline{V}_1 \cdot \underline{V}_0 \times \underline{W} = 0$$

which requires that the emerging ray lie in the plane defined by \underline{V}_0 and \underline{W} , and which reduces to

$$t + k_1 u + l_1 v = 0 \quad (D7)$$

and

$$\sin \theta_1 = \frac{|\underline{V}_1 \times \underline{W}|}{(1 + k_1^2 + l_1^2)^{1/2} |r|} = \frac{N_0}{N_1} \sin \theta_0 \quad (D8)$$

From (D7) we have

$$l_1 = -(t + k_1 u)/v \quad \text{for } v \neq 0 \quad (D9)$$

If $v = 0$, then we define

$$k_1 = -(t + l_1 v)/u \quad \text{for } u \neq 0 \quad (D10)$$

and if u is also zero, we use the plane surface solution.

Substituting (D9) for l_1 into (D8) we get

$$k_1 = k_{\pm} = [-D \pm (D^2 - 4EF)^{1/2}]/2E \quad (D11)$$

where D , E , F are complicated functions of S , x_1 , y_1 , z_1 , $\sin\theta_0$, t , u , and v . The expressions for D , E , and F are very long and are not reproduced here. Details of an efficient way to calculate these are given in the program listing between lines 1100 and 1320 in Fig. D3. It will suffice to say that the value of k_1 is not unique and a method of finding the correct choice of sign in (D11) is required. The geometrical meaning of the choice of sign is illustrated in Fig. D2 where the plane of the paper is chosen to contain the vector W which is the normal to the interface, and V_0 , the incident ray. The "possible" emerging rays V_1 and V_1' are shown for the cases of $N_1 > N_0$ and $N_1 < N_0$ respectively. The reason for the two mathematically possible orientations of the refracted ray in each case is that only the magnitudes of θ_0 and θ_1 were compared using Snell's law. One way of separating the real ray V_1 from the mathematical artifact V_1' is to use the fact that

$$\frac{V_1 \cdot V_0}{|V_1|} > \frac{V_1' \cdot V_0}{|V_1'|} \quad (D12)$$

which requires V_1 to be "more parallel" to V_0 than is V_1' . This is easily visualized by referring to Fig. D2. Equation (D12) can be rewritten as

$$\frac{1 + kk_1 + ll_1}{(1 + k_1^2 + l_1^2)^{1/2}} > \frac{1 + kk_1' + ll_1'}{1 + k_1'^2 + l_1'^2}$$

where we have used (D9) to evaluate the appropriate l_1 and l_1' . Once the proper value of k_1 is chosen from k_+ and k_- , the appropriate l_1 is chosen and the entire procedure is repeated, starting at Eq. (D1), through the next surface.

Once the final ray has been calculated emerging from the last surface, we calculate the intersection distance Ml through the cylinder which represents the dye laser beam. The equation of a cylinder parallel to the y axis, on the optical axis, with centre at $x = P$ and radius B is:

$$(x - P)^2 + z^2 = B^2 \quad (D13)$$

Solving this simultaneously with (D1) for m yields

$$m = \frac{-D \pm \sqrt{D^2 - 4EF}}{2E}$$

where $D = 2(x_0 - P + z_0 l)$,

$$E = 1 + l^2,$$

$$F = (x_0 - P)^2 + z_0^2 - B^2.$$

The change in m , which is proportional to the intersection length is simply

$$\Delta m = (D^2 - 4EF)^{1/2} / E$$

and finally, the intersection length Ml is found by multiplying Δm by the ray length per unit m :

$$Ml = \Delta m (1 + k^2 + l^2)^{1/2}$$

The ray tracing program was written in BASIC to run on the Tektronix 4051 Graphic Display System and required less than 8k of memory. A listing is shown in Fig. D3. Three user-definable keys are used by the program:

- No. 1 generates a display on the Graphic System screen of the current PMT output normalized by the dye laser beam radius, along with the current values of the running variables which generate the rays.
- No. 5 generates the same display as No. 1 but draws the output on the plotter.
- No. 6 prints on the screen the number of rays processed up to that point in time.

The results of the ray tracing program, as applied to the optical system shown in Fig. D1 are shown in Fig. D4, which graphs the PMT signal amplitude (when recording the ISE) versus distance from lens L_2 , and versus dye laser beam radius. Due to the strong dependence of the PMT signal on the beam radius, the PMT signal represented in Fig. D4 has been normalized by the beam radius before being plotted.

We note from Fig. D4 that the signal is maximum when the dye laser beam axis lies about 42 mm from the plane surface of L2. The distance at which the maximum occurs becomes less well defined as the laser beam radius becomes large. The r^2 dependence of PMT signal on beam radius, obvious at small beam radii, also changes to a r^x dependence ($x < 2$) as the radius is increased beyond about 0.3 mm. The region near the peak as shown in Fig. D4 has been expanded and plotted in Fig. D5 to show finer detail. The slight amount of noise in the graph is undoubtedly due to the finite number of rays used to generate the graphical information presented as Figs. D4 and D5 (3354 rays).

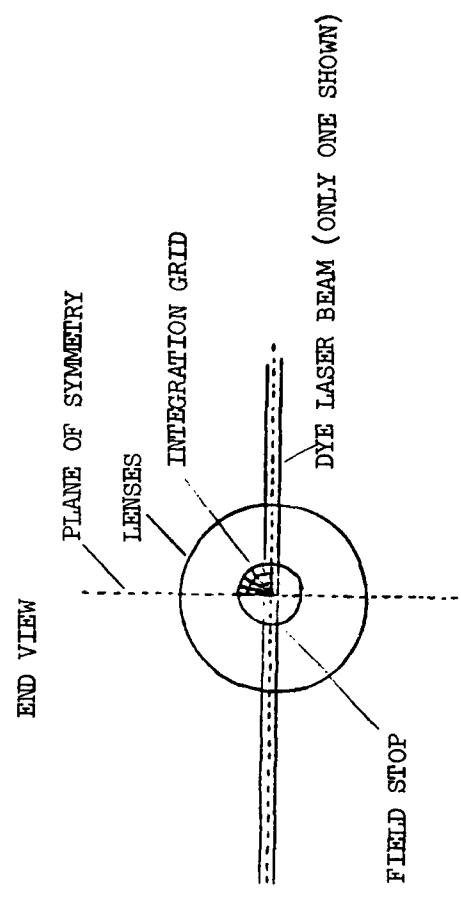
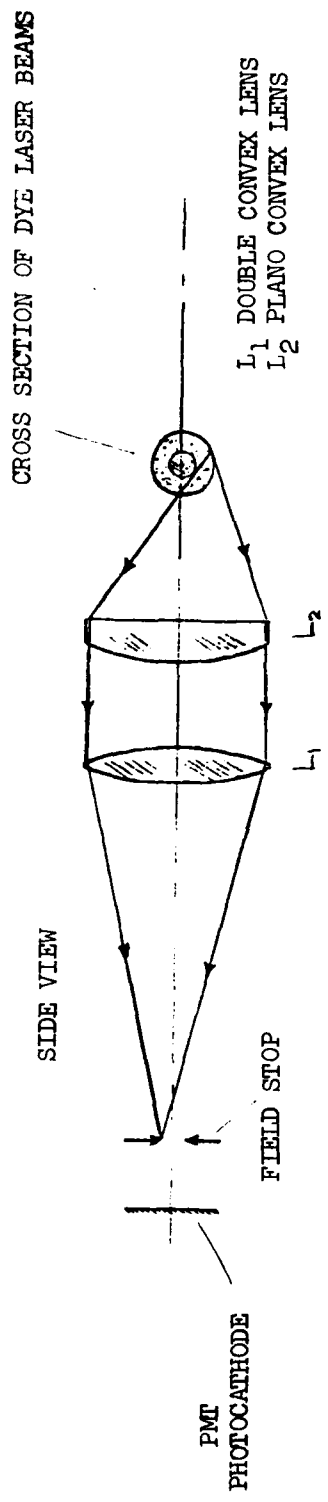


FIG. D1 SCHEMATIC OF COLLECTION OPTICS.

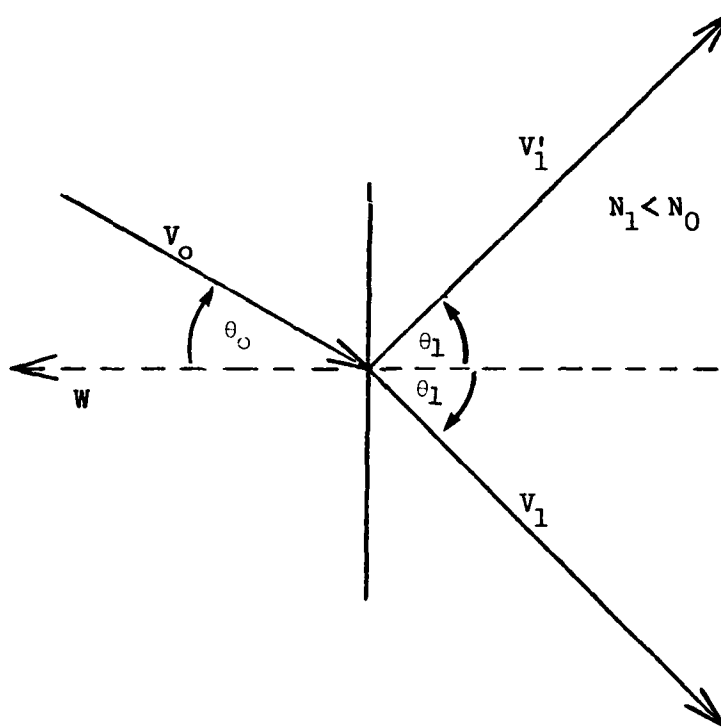
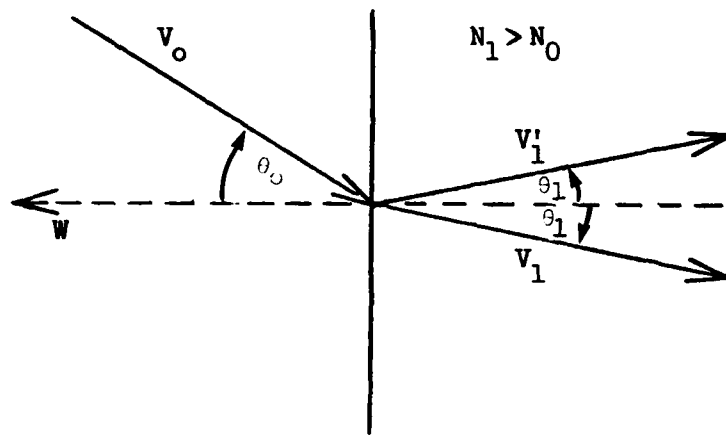


FIGURE D2 REFRACTION AT AN INTERFACE
(DEFINITION OF THE VECTORS)

```

1 GO TO 100
2 S9=32
3 GOSUB 710
4 RETURN
5 S9=1
6 GOSUB 710
7 RETURN
8 HOME
9 PRINT C1
10 RETURN
110 SET KEY
120 WINDOW -1.374,1.374,-4,4
130 DIM X(4),Y(3),M(12,10)
140 O1=3.3/230
150 C1=0
160 M1=0
170 REM SWEEP X0
180 FOR I6=-0.95 TO 0.95 STEP 0.1
190 IS=SQR(1-16*I6)
200 REM SWEEP Z0
210 FOR I7=0.05 TO 15 STEP 0.1
220 REM SWEEP Y0
230 FOR I2=0.15 TO 10 STEP 0.1
240 REM SWEEP THETA
250 FOR I3=0.5 TO 6 STEP 1
260 K1=TAN(13901)
270 REM SWEEP AZIMUTH
280 FOR I4=0 TO 2*PI-O1/2/K1 STEP O1/K1
290 K2=SIN(14)
300 Y0=I2
310 Z0=I3
320 X0=I6
330 K=K1*K2

```

```

340 L=K1*SQR(1-K2*K2)
350 IF I4<PI/2 THEN 380
360 IF I4>PI*1.5 THEN 380
370 L=-L
380 C=61.5
390 R1=1.0E+8
400 N0=1
410 N1=1.46
420 GOSUB 970
430 C=C*9.8
440 R1=-26.72222222
450 N0=N1
460 N1=1
470 GOSUB 970
480 C=C*3
490 R1=193.2
500 N0=1
510 N1=1.4
520 GOSUB 970
530 C=C*4
540 R1=-193.2
550 N0=1.4
560 N1=1
570 GOSUB 970
580 M=C*197.4-Y0
590 Y0=Y0+M*K
600 Z0=Z0+M*L
610 R0=SQR(Y0*Y0+Z0*Z0)
620 IF R0>2 THEN 650
630 MOVE Y0,Z0
640 DRAW Y0,Z0
650 C1=C1+1
660 NEXT I4
670 NEXT I3
680 NEXT I2

```

```

690 NEXT I6
700 END
710 HOME @S9:
720 PRINT @S9:C1:" STEPS"
730 PRINT @S9:"Y0 ="I6,"Z0 ="I12
740 PRINT @S9:"THETA ="I3*O1*180/PI," AZIM ="I4*180/PI
750 SS=SUM(N1)/100
760 IF SS=0 THEN 960
770 WINDOW 0,130,-10,100
780 FOR A1=1 TO 12
790 MOVE @S9:10*8*A1,20*H1(A1,10)/SS/1+10
800 IF A1<12 THEN 820
810 DRAW @S9:10*8*A1,10
820 FOR B1=10 TO 1 STEP -1
830 DRAW @S9:B1*8*A1,20*H1(A1,B1)/SS<(B1/10)+B1
840 NEXT B1
850 DRAW @S9:8*A1,0
860 NEXT A1
870 MOVE @S9:10*8*(A1-1),10
880 DRAW @S9:8*(A1-1),0
890 DRAW @S9:8,0
900 FOR B1=1 TO 10
910 MOVE @S9:B1*8,20*H1(1,B1)/SS<(B1/10)+B1
920 FOR A1=1 TO 12
930 DRAW @S9:B1*8*A1,20*H1(A1,B1)/SS<(B1/10)+B1
940 NEXT A1
950 NEXT B1
960 RETURN
970 IF ABS(R1)>9999 THEN 1410
980 A=(X0-C)*I2-2*(Y0-C)*R1+Y0*I2+20*I2
990 B=2*(Y0-C)*R1+Y0*K+20*K
1000 S=1+K*K+L*L
1010 H=B*I2-4*A*B
1020 IF H=0 THEN 660
1030 M=(-B-SGN(H)*SQR(M)*SQR(M))/2/S

```

```

1040 X1=X0+M
1050 Y1=Y0+M*K
1060 Z1=Z0+M*L
1070 F=X1-C-R1
1080 T=K*Z1-L*Y1
1090 U=L*F-F*Z1
1100 U=Y1-K*F
1110 S=(T*U+U*U+U*U)/S*(N0/M1/I2)
1120 IF ABS(U)<1.0E-7 THEN 1230
1130 A=S-2*I*Z1-F*K
1140 B=Y1*M1+U*F-S
1150 G=S-2*I*Z1-Y1*K
1160 T=U/U
1170 U=U/U
1180 A=A-2*Y1*Z1*U-U*U*B
1190 S=C-B*A*I-2*F*Z1*I
1200 B=2*Y1*(F-Z1*I)-2*8*B*U-2*F*Z1*U
1210 M=1
1220 GO TO 1250
1230 IF ABS(U)<1.0E-7 THEN 1410
1240 STOP
1250 FOR I1=1 TO 2
1260 X(I1+1)+M)=(-B-SGN(I1-1.5)*SQR(B*I2-4*A*B))/2/A
1270 X(I1+1)-M)=(-F+M*I1+2)*U)
1280 U(I1)=SQR(1+X(I1)*I2+X(I1+2)*I2)
1290 NEXT I1
1300 Z9=SGN(ABS(1+K*K*(3)+L*L*(1)))/U3(1)-ABS(1+K*K*(4)+L*L*(2))/U3(2)
1310 IF Z9<0 THEN 1350
1320 K=K*(Z9)
1330 L=L*(Z9)
1340 GO TO 1370
1350 K=K*(4)
1360 L=L*(2)
1370 Y0=Y1
1380 Y0=Y1

```

```

1390 Z0=Z1
1400 RETURN
1410 M=C-X0
1420 X1=C
1430 Y1=Y0+M*K
1440 Z1=Z0+M*L
1450 M=SQR(K*K+L*L)
1460 T=K/M
1470 B=L/M
1480 A=H0/M1*M/SQR(1+M*M)
1490 M=M/SQR(1+A*A)
1500 K=T*M
1510 L=B*M
1520 X0=X1
1530 Y0=Y1
1540 Z0=Z1
1550 RETURN
1560 IMAGE 2X,D,3D,3X,4D

```

```

FIND12
SAVE
FIND0

```

FIGURE D3

RAY TRACING PROGRAM

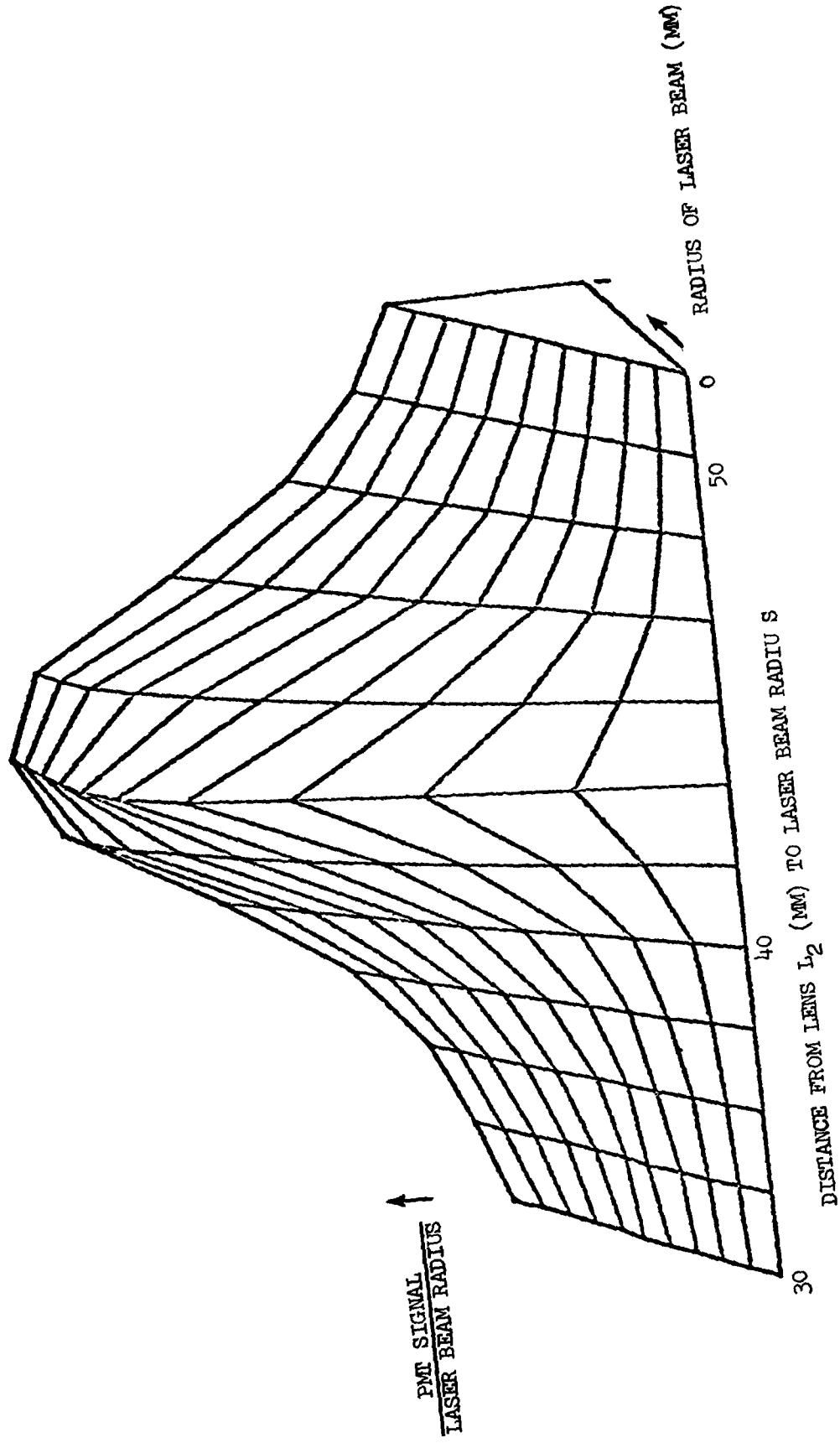
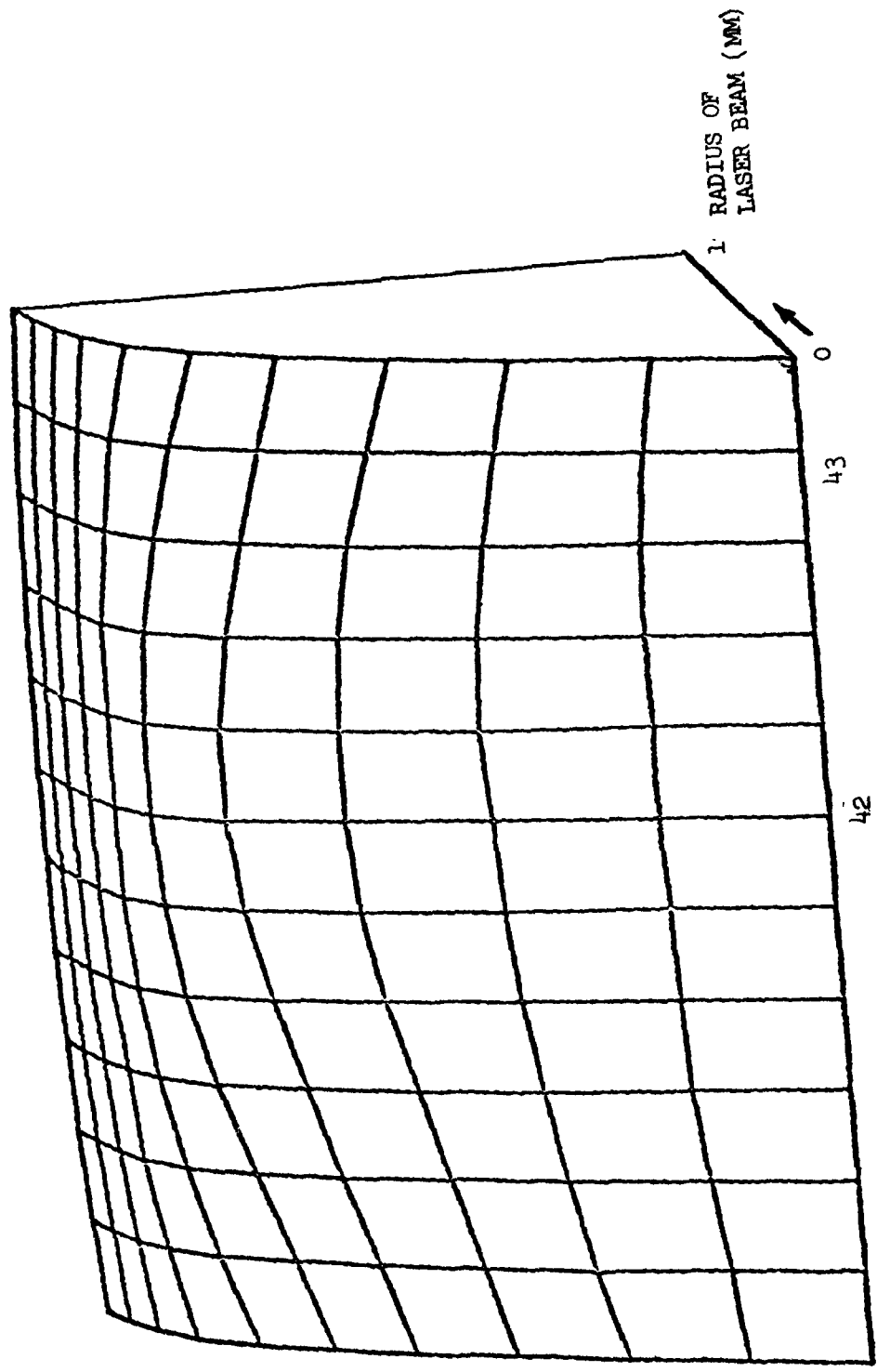


FIG. D4 CALCULATED PMT SIGNAL DIVIDED BY LASER BEAM RADIUS.



PMT SIGNAL
LASER BEAM RADIUS

RADIUS OF
LASER BEAM (MM)

DISTANCE FROM LENS L_2 (MM) TO LASER BEAM AXIS

FIG. D5 CALCULATED PMT SIGNAL DIVIDED BY LASER BEAM RADIUS.

APPENDIX E

LIBORS COMPUTER PROGRAM

The LIBORS program was used to integrate simultaneously the rate equations of the 24 variables as described in Section 2.5, i.e., the twenty bound-state population densities, the free-electron density N_e , and the energy of the neutrals, ions, and electrons. For purposes of computational ease, the time was also treated as a variable but its derivative was always set equal to one; 25 rate equations were integrated using double precision (16 decimal digits). This appendix, in conjunction with Fig. E1 (the source program listing in IBM FORTRAN IV) describes the important features of the program in detail. A quick overview of the program is given first, followed by a detailed discussion.

The set of first order differential equations was solved using a fourth-order Runge-Kutta numerical integration routine (Ralston, 1965) on the University of Toronto IBM System 370/165 computer. Straightforward application of the routine would, however, have resulted in a very long execution time (hours) due to the very small step sizes required at certain stages. This arises because the typical time constants involved were very much smaller than the time of interest (i.e., the time to ionize). Thus the integration routine developed by Fournier (1972) was modified to allow the use of a more reasonable step size. Unfortunately, these caused instability in the electron temperature solution (this is perhaps obvious after considering the discussion of r_c and r_H in Section 7.4). Further modifications were then required in order to remove the instability.

The detailed discussion of the program begins with a description of the main program, which will serve to indicate the strategy employed to speed up program execution, and to reduce to a minimum the number of punched cards - source program, data, and output - which must be handled. A description of the subroutines then follows.

Program execution starts by initializing certain variables and flags (line 5), and reading of data cards (line 25) which describe the conditions of the experiment to be simulated. Atomic data is then read in (line 44) for the particular element under consideration (sodium, in this case). The electron collision excitation rate coefficient is assumed to have the form

$$K_{ij} = A_{ij} T_e^{B_{ij}} C_{ij} / T_e \quad (E1)$$

where A_{ij} , B_{ij} and C_{ij} are constants unique for each transition, including those to the continuum. For a twenty level atom, there are 210 possible upward transitions. Thus there are a total of 630 numbers, which are read in as a single vector. These numbers had been previously calculated (Cardinal, 1979) using the experimentally-based electron collision rate coefficient for the resonance transition and a combination of Gryzinski (1965) and Seaton (1962) cross sections for evaluating the electron collision rates for optically forbidden and allowed transitions, respectively (see Chapter 7 and Appendix A).

The radiative transition probabilities are read in as half a matrix (line 49). To conserve space on the data cards, the logarithm of the transition probabilities are used; they are exponentiated after being read in, and used to fill a square, symmetric matrix (line 55). At this point the elements in the upper half of the matrix are equal to the corresponding elements in the lower half, but during the integration procedure, some of the elements in the upper half are overwritten in subroutine DERIV with corresponding effective transition probabilities calculated to take into account radiation trapping.

Execution in the main program continues by calculating various constants that are used repeatedly in the integration procedure (line 63). By doing these calculations only once, and storing the results, execution time is reduced.

Initial energies are calculated (line 84) based on the given temperatures and densities of the neutrals, ions and electrons, followed by a calculation (line 98) of the multiphoton ionization rates from each level (i.e., $\alpha_1^{(k)} F^k$) and the rate of excess electron energy production due to these ionization rates. At this point the electron temperature is recalculated (line 111) if the initial electron density has been set equal to zero. The calculation is based on the excess electron energy produced (per electron) by two-photon ionization from the resonance level.

The ground and resonance levels are then "locked" together (line 114) according to their degeneracies, to simulate laser turn-on. This locking of levels is simply a manifestation of the laser saturation of a transition (2.3.9). The associated time constant τ_p is so small for the laser irradiances in question that an extremely small step size would be required to keep the numerical integration stable and the execution time would consequently be prohibitive.

Subsequently a short routine is executed (line 117) which detects the presence of additional data cards. These additional cards will exist if it is intended that the present computer run be a continuation of a previous run. In this case the 21 population densities, 3 kinetic energies, and the time are read in and new kinetic temperatures are calculated.

Execution of the main program continues with a calculation of, and storage of $\ln T_e$ (line 125), and a calculation of electron collision rate coefficients by calling subroutine DERIV (line 130). Also calculated in DERIV at this time are the effective radiative transition probabilities to take into account radiation trapping where applicable. In the main program, the electron collision rate coefficients and the radiative transition probabilities are then printed out in matrix form (line 133) along with other variables such as the energies of energy levels and the various constants calculated earlier.

DERIV is called again (line 145), this time to calculate the instantaneous rates of the variables to be integrated, and execution proceeds to the loop (line 150) which contains the integration subroutine RKCLA. At this point various flags are employed to control the frequency of the punched-card output, and the termination of the program. Termination occurs if (a) integration has proceeded to a preset time (line 174), or (b) a preset level of ionization has occurred (line 152), or (c) a preset execution time has been reached (line 154). Punched-card output is executed by calling subroutine OUTPUT and occurs only if the output has changed significantly since OUTPUT was last called; i.e., if (a)

the accumulated integration time exceeds 1% of the preset total integration time (line 157), or (b) flag IP exceeds 1000 (line 155). IP is described in connection with subroutine RKCLA in Section E.4.

Each time OUTPUT has been called, the computer calls DERIV (line 162) in order to re-evaluate resonance trapping effects and thus modify the spontaneous transition probabilities. Subsequently, if certain conditions are met, the main program calls subroutine COAL (line 168), which coalesces certain energy levels into single levels in much the same way as, and for the same reason that, the ground and resonance levels are "locked". The "conditions" are discussed in connection with subroutine COAL in Section E.1.

E.1 Subroutine COAL

Subroutine COAL systematically compares (line 16) electron collision de-excitation rate coefficients (K_{ji} for $j > i$) between adjacent levels for all levels between 7 and 20 inclusive with $(XN_e)^{-1}$ where X is scaled according to N_0^{-1} and equals 0.5 ns at $N_0 = 10^{16}$. If K_{ji} exceeds $(XN_e)^{-1}$, then levels j and i are coalesced in the sense that all rate processes between levels j and i are no longer considered explicitly by the program. This condition is signaled by setting $K_{ji} = K_{ij} = 0$. The criterion for coalescing also includes the case $K_{ji} = 0$ (line 16), which simply means that a set of levels, once coalesced, stays coalesced. The redistribution of populations, and population rates, among levels that are coalesced is done automatically by subroutine REDIST.

During the process of coalescing levels, this subroutine generates a vector ICO describing the levels which have been coalesced. Thus if $ICO = 12, 13, 15, 18$, then level 12 is coalesced with 13 and levels 15 through and including 18 are coalesced into a single level. Two other numbers are generated by this subroutine for reference by other parts of the program: ICON (= 4 in the above example) is the number of components in the ICO vector, and ICOT (= 6 in the above example) is the number of levels that are coalesced.

At the end of the subroutine, ICOT and ICON are compared with their previous values and if a change has occurred in the value of either, then the new ICO vector is printed out.

The main program calls this subroutine within the integration loop only if $ICO \neq 7, 20$ in line 166, and if the laser power density is nonzero.

E.2 Subroutine REDIST

This subroutine calculates the equilibrium distribution of populations or population rates within sets of coalesced levels according to the prevailing electron temperature and calculates the change in free electron energy required to effect such a change in distribution. The quantity A_i in question (i.e., population density or its time derivative) is summed over all levels within a manifold (line 11), and a weighted sum (weighted with respect to the energy of the level) is also calculated for the manifold (line 12). Inside the same loop, a third sum over i of $B_i = g_i e^{-\epsilon_i/kT_e}$ is calculated (line 13). A constant, $C = (\sum A_i / \sum B_i)$ is then used to re-apportion the A_i to form new A_i^* 's according to $A_i^* = CB_i$ (line 16). A new weighted sum (with respect to energy of the level) then determines the change in kinetic energy (or its time derivative) of the free electrons; and this change is automatically applied to the electron kinetic energy.

E.3 Subroutine DERIV

This subroutine performs various functions according to the value of the dummy index IGO.

If IGO = 1, then radiation trapping effects are calculated according to the equations of Holstein (1947, 1951) for all bound-bound allowed radiative transitions that terminate on either the resonance or ground state. Only these two levels are sufficiently populated over most of the time span to render radiation trapping an important effect. The execution proceeds as follows:

The effective transition probabilities [see Eq. (2.1.2)] are calculated and stored in the upper half of the A matrix in line 61 after multiplying the spontaneous emission coefficients (stored in the lower half of the A matrix) by appropriately calculated escape factors.

If IGO = 3, then, besides calculating radiation trapping effects, the subroutine calculates the electron collision rate coefficients K_{ij} ($j > i$) following the functional form (E1). However, to reduce execution time, (E1) is reformulated as

$$K_{ij} = A_{ij} e^{B_{ij} \ln T_e + C_{ij}/T_e} \quad (E2)$$

where $\ln T_e$ is constant for all elements of the K matrix, and as a result need be calculated only once. Note that in the case of (E2), only one exponentiation is required for each K_{ij} versus two exponentiations and one logarithm in the case of (E1). The fact that T_e was nearly constant throughout most of the time span was used to advantage by employing a second order Taylor expansion of (E2) which did not require any exponentiation or logarithms (line 41). After having calculated K_{ij} exactly, the Taylor expansion was used for the next 100 steps before another exact calculation of K_{ij} was done, as long as T_e was within 1°K of the expansion point. An independent calculation on the Tektronix 4051 system determined that the typical error in K_{ij} evaluated 1° away from the expansion point was less than the resolution of the 4051, i.e., 10⁻¹²%.

The K_{ij} values had to be recalculated at each integration step when the electron temperature T_e changed, therefore this location in the DERIV subroutine was also the logical place to calculate the Boltzmann factors relevant to each energy level. Since exponentiation was involved here also (line 30) a Taylor series was similarly used (line 25).

After K_{ij} has been calculated, K_{ji} is calculated using the principle of detailed balance. Following this, the two-body recombination rate coefficient is calculated using (2.1.5).

If IGO = 4, then the subroutine calculates the derivatives of the 21 population densities and the 3 kinetic energies (lines 64 to 108). After calculation of the time derivatives of the 20 population densities of bound states, REDIST is called in order to properly apportion the derivatives of the coalesced levels according to their degeneracies and Boltzmann factors. The required change in the free-electron kinetic energy derivative is generated at the same time, and this value is used to correct the free-electron kinetic energy derivative as calculated from other considerations.

E.4 Subroutine RKCLA

Subroutine RKCLA implements the fourth-order Runge-Kutta routine as described by Ralston (1965). This routine requires four calculations of all derivatives for each integration step. The routine is quite simple (located between lines 18 and 53), but the subroutine is long because various routines have been included in order to keep the electron temperature stable. In addition, a routine has been included which determines the step size to be used in the following integration step.

A major feature of the subroutine is the determination of the electron temperature to be used in the following integration step. Straightforward integration of the electron energy equation resulted in electron temperature instabilities because the typical step sizes (0.1 ns) used at a certain point of the ionization curve were much larger than the relaxation time of the processes which determine the temperature.

The electron temperature to be used in evaluating the derivatives during the next integration step (i.e., the step following the current step which the subroutine is executing) is determined at the end of the current step by choosing a suitably weighted mean of two differently derived temperatures. One temperature T_0 is derived by the normal integration of the electron energy and density, and dividing their quotient by $3/2 k$. (This is the procedure, if used alone, which results in the instability.) The other temperature T_x is derived by linear extrapolation of the temperatures used during the previous five steps to that point in time corresponding to the end point of the current integration step. The extrapolation is done by using a linear regression routine.

The following variable weighting scheme was found to work very well:

$$T_e = pT_0 + (1 - p)T_x \quad (\text{E.4.1})$$

where T_e is the final result of executing RKCLA, and

$$p = m(m + 1)/30, \quad 3 \leq m \leq 5 \quad (\text{E.4.2})$$

where m is an integer and depends on the recent history of T_0 and T_x in the following manner.

If, at the current integration step, T_0 deviates from T_x in the same direction as it did in the previous step, then m is incremented by 1, subject to the restriction (E.4.2). If the opposite case is true, then m is decremented by 1, subject to (E.4.2).

This procedure applies only after the 10th integration step. Earlier steps use $m = 5$. The calculation of T_x is contained between lines 6 and 13, and between lines 79 and 89. The weighting scheme is implemented between lines 90 and 103.

Note that the scheme used to establish an electron temperature does not introduce any cumulative error in the electron energy due to the admixture of

T_x , because the kinetic energy is at all times calculated by integrating the kinetic energy rate equation. The electron temperature is calculated from the kinetic energy, not vice versa.

For purposes of computer output, the ion and neutral kinetic temperatures are also calculated from the respective kinetic energies. This is done at lines 110 and 111.

Another important feature of the subroutine is the calculation of the step size to be used in the subsequent integration step. The step size Δt was made variable in order to keep the size consistent with a required integration accuracy, and with a reasonable execution time. The procedure for choosing a step size is best explained by illustration. Consider a typical output of the LIBORS program such as shown for example in Fig. 47. Note the curve for N_e . At the end of each integration step i , the instantaneous slope of the N_e curve,

$$S = \frac{\log(N_e)_i - \log(N_e)_{i-1}}{\Delta t}$$

was determined, and converted to an angle relative to the horizontal axis as it would appear in Fig. 47. A similar angle was calculated for the 20 other population densities. The changes in the angles from the previous step were then computed and the largest such change ΔC was selected. The new step size $(\Delta t)_n$ (i.e., the one to be used in the following integration step) was then calculated (at line 57):

$$(\Delta t)_n = (\Delta t)K/(\Delta C)$$

where K is a constant and ΔC is expressed in radians.

A value of 0.001 for K gave good results, however, it was found that $(\Delta t)_n$ had to be restricted:

$$(\Delta t)_n \geq K_1 = 5000/N_0$$

in order to prevent the execution time from getting too large; and

$$(\Delta t)_n \leq 1.05 (\Delta t)$$

was imposed in order to keep the solution stable.

A check of the integration accuracy was made by reducing K by a factor of 10. Ionization time changed by less than 1 ns. The step size for the first integration step was set equal to K_1 in line 127 of the main program.

The value of the flag IP, which in the main program is used to determine frequency of punched card output, is determined in this subroutine by accumulating

the angle changes for each population density as described above. When the curve of a population has changed by 0.2 radians, IP is set, and this in turn triggers an output in the main program.

E.5 Subroutine OUTPUT

Subroutine OUTPUT produces punched-card output whenever it is called by the main program. Twenty-six encoded numbers are punched, occupying 78 of the 80 columns available on the card. Encoding of the numbers was desirable due to the large number of cards otherwise required for a typical LIBORS graph; in order to achieve a reasonable time resolution in the final graphs, at least 200 values of any particular variable are required, and there are 27 variables which should be output. With the usual format of LPE9.2, which yields an adequate minimum resolution of 1% for graphing purposes, well over 1000 cards would be required for a typical LIBORS output. Encoding reduces this number to 200 cards.

Encoding of the numbers is accomplished by using a base 36 number system and using as characters the ten decimal numbers and the 26 letters of the alphabet. This is a simple extension of hexadecimal notation commonly seen in computer work. The dynamic range available in the base 36 number system, when using a single character exponent of 36, is approximately 10^{50} . Furthermore, three significant "digits" in base 36 numbers yield a minimum resolution of $1/36^2 \cong 0.1\%$. These properties were exploited in the encoding scheme: Each number to be output is first multiplied by 10^{25} in order to shift the apparent dynamic range of the output to about 10^{-25} to 10^{31} (line 25), then a search procedure is executed to find the three significant "digits" and the single exponent. The three significant "digits" are punched for each of 26 variables; the last two columns of the card are used to sequence the cards - also using base 36 numbers.

The twenty-six variables which are punched are, in order, the population densities of levels 1 to 16 inclusive, recombination radiation, levels 18 to 20 inclusive, electron density, and temperature, the ion and neutral temperatures, the time, and the power absorbed from the laser beam.

The relevant exponents corresponding to the data on the first three punched cards are punched as three sets of 26 characters after the third card has been punched (line 40). It was found that after the third punched output card, the punched data varied slowly enough between punched cards that a change in exponent could be detected as a discontinuity in the decoded graph. The exponents therefore did not have to be punched after the third data card. The program which decoded and graphed the LIBORS output simply detected the discontinuity in any given variable and corrected the value of the relevant exponent accordingly.

UTIAS REPORT NO. 229

Institute for Aerospace Studies, University of Toronto (UTIAS)
429 Dufferin Street, Downsview, Ontario, Canada, M3H 5T6

STUDIES OF LASER SELECTIVE EXCITATION OF ATOMS

Drewell, Norbert 136 pages (approx.) 40 figures

1. Laser induced fluorescence, 2. Selective excitation spectroscopy, 3. Saturation spectroscopy, 4. Radiative lifetimes, 5. Laser resonance saturation, 6. Laser ionization, 7. Laser heating, 8. Plasma formation, 9. Laser plasma formation, 10. Laser ablation, 11. Atomic lifetime measurement, 12. Laser pumping, 13. Laser diagnostics of plasmas, 14. Laser spectroscopy, 15. Atomic spectroscopy.

I. Drewell, Norbert II. UTIAS Report No. 229

Sample preparation through laser ablation of a solid target under vacuum has been combined with short-pulsed laser selective excitation to create a new and convenient experimental technique for measuring atomic radiative lifetimes. The lifetimes of the three resonance states of chromium determined in this way compare very favourably with those found through other experimental means.

In addition, the technique has been extended to demonstrate experimentally the potential for plasma diagnostics using two-wavelength selective excitation with short laser pulses. The ratio of population densities of two energy states of chromium atoms has been measured as a function of time during the expansion of the ablation plasma.

Extended saturation pumping of the resonance transition in sodium vapour has been investigated theoretically. Rate equations for 20 energy levels in the sodium atom and the rate equations for the free electrons were integrated numerically. It has been found that multiphoton ionization combined with supercritical heating of free electrons can account for the rapid and complete ionization of an un-ionized vapour, as reported in the literature. The detailed theoretical results have led to the development of a simple model which accurately predicts the temporal variation of electron density.

Available copies of this report are limited. Return this card to UTIAS, if you require a copy.



UTIAS REPORT NO. 229

Institute for Aerospace Studies, University of Toronto (UTIAS)
429 Dufferin Street, Downsview, Ontario, Canada, M3H 5T6

STUDIES OF LASER SELECTIVE EXCITATION OF ATOMS

Drewell, Norbert 136 pages (approx.) 40 figures

1. Laser induced fluorescence, 2. Selective excitation spectroscopy, 3. Saturation spectroscopy, 4. Radiative lifetimes, 5. Laser resonance saturation, 6. Laser ionization, 7. Laser heating, 8. Plasma formation, 9. Laser plasma formation, 10. Laser ablation, 11. Atomic lifetime measurement, 12. Laser pumping, 13. Laser diagnostics of plasmas, 14. Laser spectroscopy, 15. Atomic spectroscopy.

I. Drewell, Norbert II. UTIAS Report No. 229

Sample preparation through laser ablation of a solid target under vacuum has been combined with short-pulsed laser selective excitation to create a new and convenient experimental technique for measuring atomic radiative lifetimes. The lifetimes of the three resonance states of chromium determined in this way compare very favourably with those found through other experimental means.

In addition, the technique has been extended to demonstrate experimentally the potential for plasma diagnostics using two-wavelength selective excitation with short laser pulses. The ratio of population densities of two energy states of chromium atoms has been measured as a function of time during the expansion of the ablation plasma.

Extended saturation pumping of the resonance transition in sodium vapour has been investigated theoretically. Rate equations for 20 energy levels in the sodium atom, and the rate equations for the free electrons were integrated numerically. It has been found that multiphoton ionization combined with supercritical heating of free electrons can account for the rapid and complete ionization of an un-ionized vapour, as reported in the literature. The detailed theoretical results have led to the development of a simple model which accurately predicts the temporal variation of electron density.

Available copies of this report are limited. Return this card to UTIAS, if you require a copy.



UTIAS REPORT NO. 229

Institute for Aerospace Studies, University of Toronto (UTIAS)
429 Dufferin Street, Downsview, Ontario, Canada, M3H 5T6

STUDIES OF LASER SELECTIVE EXCITATION OF ATOMS

Drewell, Norbert 136 pages (approx.) 40 figures

1. Laser induced fluorescence, 2. Selective excitation spectroscopy, 3. Saturation spectroscopy, 4. Radiative lifetimes, 5. Laser resonance saturation, 6. Laser ionization, 7. Laser heating, 8. Plasma formation, 9. Laser plasma formation, 10. Laser ablation, 11. Atomic lifetime measurement, 12. Laser pumping, 13. Laser diagnostics of plasmas, 14. Laser spectroscopy, 15. Atomic spectroscopy.

I. Drewell, Norbert II. UTIAS Report No. 229

Sample preparation through laser ablation of a solid target under vacuum has been combined with short-pulsed laser selective excitation to create a new and convenient experimental technique for measuring atomic radiative lifetimes. The lifetimes of the three resonance states of chromium determined in this way compare very favourably with those found through other experimental means.

In addition, the technique has been extended to demonstrate experimentally the potential for plasma diagnostics using two-wavelength selective excitation with short laser pulses. The ratio of population densities of two energy states of chromium atoms has been measured as a function of time during the expansion of the ablation plasma.

Extended saturation pumping of the resonance transition in sodium vapour has been investigated theoretically. Rate equations for 20 energy levels in the sodium atom, and the rate equations for the free electrons were integrated numerically. It has been found that multiphoton ionization combined with supercritical heating of free electrons can account for the rapid and complete ionization of an un-ionized vapour, as reported in the literature. The detailed theoretical results have led to the development of a simple model which accurately predicts the temporal variation of electron density.

Available copies of this report are limited. Return this card to UTIAS, if you require a copy.



UTIAS REPORT NO. 229

Institute for Aerospace Studies, University of Toronto (UTIAS)
429 Dufferin Street, Downsview, Ontario, Canada, M3H 5T6

STUDIES OF LASER SELECTIVE EXCITATION OF ATOMS

Drewell, Norbert 136 pages (approx.) 40 figures

1. Laser induced fluorescence, 2. Selective excitation spectroscopy, 3. Saturation spectroscopy, 4. Radiative lifetimes, 5. Laser resonance saturation, 6. Laser ionization, 7. Laser heating, 8. Plasma formation, 9. Laser plasma formation, 10. Laser ablation, 11. Atomic lifetime measurement, 12. Laser pumping, 13. Laser diagnostics of plasmas, 14. Laser spectroscopy, 15. Atomic spectroscopy.

I. Drewell, Norbert II. UTIAS Report No. 229

Sample preparation through laser ablation of a solid target under vacuum has been combined with short-pulsed laser selective excitation to create a new and convenient experimental technique for measuring atomic radiative lifetimes. The lifetimes of the three resonance states of chromium determined in this way compare very favourably with those found through other experimental means.

In addition, the technique has been extended to demonstrate experimentally the potential for plasma diagnostics using two-wavelength selective excitation with short laser pulses. The ratio of population densities of two energy states of chromium atoms has been measured as a function of time during the expansion of the ablation plasma.

Extended saturation pumping of the resonance transition in sodium vapour has been investigated theoretically. Rate equations for 20 energy levels in the sodium atom, and the rate equations for the free electrons were integrated numerically. It has been found that multiphoton ionization combined with supercritical heating of free electrons can account for the rapid and complete ionization of an un-ionized vapour, as reported in the literature. The detailed theoretical results have led to the development of a simple model which accurately predicts the temporal variation of electron density.

Available copies of this report are limited. Return this card to UTIAS, if you require a copy.

UTIAS REPORT NO. 229

Institute for Aerospace Studies, University of Toronto (UTIAS)
4925 Bufferyn Street, Downsview, Ontario, Canada, M3H 5T6

STUDIES OF LASER SELECTIVE EXCITATION OF ATOMS

Drewell, Norbert 136 pages (approx.) 40 figures

1. Laser induced fluorescence, 2. Selective excitation spectroscopy, 3. Saturation spectroscopy, 4. Radiative lifetime, 5. Laser resonance saturation, 6. Laser ionization, 7. Laser heating, 8. Plasma formation, 9. Laser plasma formation, 10. Laser ablation, 11. Atomic lifetime measurement, 12. Laser pumping, 13. Laser diagnostics of plasmas, 14. Laser spectroscopy, 15. Atomic spectroscopy.

I. Drewell, Norbert II. UTIAS Report No. 229

Sample preparation through laser ablation of a solid target under vacuum has been combined with short-pulsed laser selective excitation to create a new and convenient experimental technique for measuring atomic radiative lifetimes. The lifetimes of the three resonance states of chromium determined in this way compare very favourably with those found through other experimental means.

In addition, the technique has been extended to demonstrate experimentally the potential for plasma diagnostics using two-wavelength selective excitation with short laser pulses. The ratio of population densities of two energy states of chromium atoms has been measured as a function of time during the expansion of the ablation plasma.

Extended saturation pumping of the resonance transition in sodium vapour has been investigated theoretically. Rate equations for 20 energy levels in the sodium atom, and the rate equations for the free electrons, were integrated numerically. It has been found that multiphoton ionization combined with superelastic heating of free electrons can account for the rapid and complete ionization of an un-ionized vapour, as reported in the literature. The detailed theoretical results have led to the development of a simple model which accurately predicts the temporal variation of electron density.

Available copies of this report are limited. Return this card to UTIAS, if you require a copy.

UTIAS REPORT NO. 229

Institute for Aerospace Studies, University of Toronto (UTIAS)
4925 Bufferyn Street, Downsview, Ontario, Canada, M3H 5T6

STUDIES OF LASER SELECTIVE EXCITATION OF ATOMS

Drewell, Norbert 136 pages (approx.) 40 figures

1. Laser induced fluorescence, 2. Selective excitation spectroscopy, 3. Saturation spectroscopy, 4. Radiative lifetime, 5. Laser resonance saturation, 6. Laser ionization, 7. Laser heating, 8. Plasma formation, 9. Laser plasma formation, 10. Laser ablation, 11. Atomic lifetime measurement, 12. Laser pumping, 13. Laser diagnostics of plasmas, 14. Laser spectroscopy, 15. Atomic spectroscopy.

I. Drewell, Norbert II. UTIAS Report No. 229

Sample preparation through laser ablation of a solid target under vacuum has been combined with short-pulsed laser selective excitation to create a new and convenient experimental technique for measuring atomic radiative lifetimes. The lifetimes of the three resonance states of chromium determined in this way compare very favourably with those found through other experimental means.

In addition, the technique has been extended to demonstrate experimentally the potential for plasma diagnostics using two-wavelength selective excitation with short laser pulses. The ratio of population densities of two energy states of chromium atoms has been measured as a function of time during the expansion of the ablation plasma.

Extended saturation pumping of the resonance transition in sodium vapour has been investigated theoretically. Rate equations for 20 energy levels in the sodium atom, and the rate equations for the free electrons, were integrated numerically. It has been found that multiphoton ionization combined with superelastic heating of free electrons can account for the rapid and complete ionization of an un-ionized vapour, as reported in the literature. The detailed theoretical results have led to the development of a simple model which accurately predicts the temporal variation of electron density.

Available copies of this report are limited. Return this card to UTIAS, if you require a copy.

UTIAS REPORT NO. 229

Institute for Aerospace Studies, University of Toronto (UTIAS)
4925 Bufferyn Street, Downsview, Ontario, Canada, M3H 5T6

STUDIES OF LASER SELECTIVE EXCITATION OF ATOMS

Drewell, Norbert 136 pages (approx.) 40 figures

1. Laser induced fluorescence, 2. Selective excitation spectroscopy, 3. Saturation spectroscopy, 4. Radiative lifetime, 5. Laser resonance saturation, 6. Laser ionization, 7. Laser heating, 8. Plasma formation, 9. Laser plasma formation, 10. Laser ablation, 11. Atomic lifetime measurement, 12. Laser pumping, 13. Laser diagnostics of plasmas, 14. Laser spectroscopy, 15. Atomic spectroscopy.

I. Drewell, Norbert II. UTIAS Report No. 229

Sample preparation through laser ablation of a solid target under vacuum has been combined with short-pulsed laser selective excitation to create a new and convenient experimental technique for measuring atomic radiative lifetimes. The lifetimes of the three resonance states of chromium determined in this way compare very favourably with those found through other experimental means.

In addition, the technique has been extended to demonstrate experimentally the potential for plasma diagnostics using two-wavelength selective excitation with short laser pulses. The ratio of population densities of two energy states of chromium atoms has been measured as a function of time during the expansion of the ablation plasma.

Extended saturation pumping of the resonance transition in sodium vapour has been investigated theoretically. Rate equations for 20 energy levels in the sodium atom, and the rate equations for the free electrons, were integrated numerically. It has been found that multiphoton ionization combined with superelastic heating of free electrons can account for the rapid and complete ionization of an un-ionized vapour, as reported in the literature. The detailed theoretical results have led to the development of a simple model which accurately predicts the temporal variation of electron density.

Available copies of this report are limited. Return this card to UTIAS, if you require a copy.

UTIAS REPORT NO. 229

Institute for Aerospace Studies, University of Toronto (UTIAS)
4925 Bufferyn Street, Downsview, Ontario, Canada, M3H 5T6

STUDIES OF LASER SELECTIVE EXCITATION OF ATOMS

Drewell, Norbert 136 pages (approx.) 40 figures

1. Laser induced fluorescence, 2. Selective excitation spectroscopy, 3. Saturation spectroscopy, 4. Radiative lifetime, 5. Laser resonance saturation, 6. Laser ionization, 7. Laser heating, 8. Plasma formation, 9. Laser plasma formation, 10. Laser ablation, 11. Atomic lifetime measurement, 12. Laser pumping, 13. Laser diagnostics of plasmas, 14. Laser spectroscopy, 15. Atomic spectroscopy.

I. Drewell, Norbert II. UTIAS Report No. 229

Sample preparation through laser ablation of a solid target under vacuum has been combined with short-pulsed laser selective excitation to create a new and convenient experimental technique for measuring atomic radiative lifetimes. The lifetimes of the three resonance states of chromium determined in this way compare very favourably with those found through other experimental means.

In addition, the technique has been extended to demonstrate experimentally the potential for plasma diagnostics using two-wavelength selective excitation with short laser pulses. The ratio of population densities of two energy states of chromium atoms has been measured as a function of time during the expansion of the ablation plasma.

Extended saturation pumping of the resonance transition in sodium vapour has been investigated theoretically. Rate equations for 20 energy levels in the sodium atom, and the rate equations for the free electrons, were integrated numerically. It has been found that multiphoton ionization combined with superelastic heating of free electrons can account for the rapid and complete ionization of an un-ionized vapour, as reported in the literature. The detailed theoretical results have led to the development of a simple model which accurately predicts the temporal variation of electron density.

Available copies of this report are limited. Return this card to UTIAS, if you require a copy.

—8
DTIC